UNIVERSITY OF MICHIGAN
MAY 5 1958
PHYSICS LIBRARY

Journal of Research

of the

National Bureau of Standards

MARCH 1958

VOLUME 60 NUMBER 3

U. S. DEPARTMENT OF COMMERCE
Sinclair Weeks, Secretary
NATIONAL BUREAU OF STANDARDS
A. V. Astin, Director

MARCH • 1958
VOLUME • 60
NUMBER • 3

JOURNAL OF RESEARCH
of the
NATIONAL BUREAU OF STANDARDS

The National Bureau of Standards

Functions and Activities

The functions of the National Bureau of Standards are set forth in the Act of Congress, March 3, 1901, as amended by Congress in Public Law 619, 1950. These include the development and maintenance of the national standards of measurement and the provision of means and methods for making measurements consistent with these standards; the determination of physical constants and properties of materials; the development of methods and instruments for testing materials, devices, and structures; advisory services to Government Agencies on scientific and technical problems; invention and development of devices to serve special needs of the Government; and the development of standard practices, codes, and specifications. The work includes basic and applied research, development, engineering, instrumentation, testing, evaluation, calibration services, and various consultation and information services. Research projects are also performed for other Government agencies when the work relates to and supplements the basic program of the Bureau or when the Bureau's unique competence is required. The scope of activities is suggested by the listing of divisions and sections on the inside of the back cover.

Publications

The results of the Bureau's work take the form of either actual equipment and devices or published papers. These papers appear either in the Bureau's own series of publications or in the journals of professional and scientific societies. The Bureau itself publishes three monthly periodicals, available from the Government Printing Office: The Journal of Research, which presents complete papers reporting technical investigations; the Technical News Bulletin, which presents summary and preliminary reports on work in progress; and Basic Radio Propagation Predictions, which provides data for determining the best frequencies to use for radio communications throughout the world. There are also five series of nonperiodical publications: The Applied Mathematics Series, Circulars, Handbooks, Building Materials and Structures Reports, and Miscellaneous Publications.

Information on the Bureau's publications can be found in NBS Circular 460, Publications of the National Bureau of Standards ($1.25) and its Supplement ($0.75), available from the Superintendent of Documents, Government Printing Office, Washington 25, D. C.

Order all publications from the Superintendent of Documents
U. S. Government Printing Office, Washington 25, D. C.

Use of funds for printing this publication approved by the Director of the Bureau of the Budget (May 14, 1956).

Journal of Research of the National Bureau of Standards Vol. 60, No. 3, March 1958 Research Paper 2833

Current and Potential Relations for the Cathodic Protection of Steel in Salt Water

W. J. Schwerdtfeger

A laboratory investigation was made pertaining to the cathodic protection of steel specimens that were exposed for 60 days to both stagnant and aerated city water, to which was added 3 percent by weight of sodium chloride.

Major consideration was given to the significance of potential as a criterion for protection. Optimum protection was achieved when specimens were controlled at −0.77 volt with reference to the saturated calomel half cell. Although a good degree of protection was obtained at controlled potentials more noble than −0.77 volt, that is, at the potentials associated with the breaks in cathodic polarization curves, this lesser degree of protection could not be obtained at lower mean current densities.

1. Introduction

Cathodic protection is applied primarily to iron and steel structures exposed to corrosive soils and waters. Despite the numerous publications on this subject, there still remains a diversity of opinion concerning the criteria for such protection. The fundamental requirements for cathodic protection were established by Mears and Brown [1, 2] [1] who concluded that in solutions of high conductivity a metal must be cathodically polarized to the open-circuit potential of the most anodic element on its surface in order to have complete protection.

In an earlier study of cathodic protection at the Bureau, it was observed that the potential of steel exposed to one relatively air-free soil (pH 9.5) was about −0.77 v with reference to a saturated calomel half cell [3]. It was also observed that a composite curve of pH versus potential of steel, as obtained from measurements in 20 air-free soils, intersected the pH-potential curve of the standard hydrogen electrode at pH 9 and approximately −0.77 v. In tests which followed, steel maintained for 60 days at about −0.77 v lost very little weight in 5 severely corrosive soils. This potential is equivalent to −0.85 v referred to the copper-copper sulfate electrode. These laboratory results thus confirmed the field experience of Kuhn [4] and many others. A pertinent observation was made by Sudrabin [5] in that iron in an air-free sea water environment was found to have a potential of −0.77 v with reference to the saturated calomel half cell.

Some engineers are of the opinion that −0.85 v with reference to a copper-copper sulfate electrode sometimes represents overprotection and excessive current demands. In order to investigate the matter further, the present work was undertaken. Cathodic polarization curves are logically associated with any study in cathodic protection. The current at the break (change-in-slope) in the curve, which occurs at the open-circuit potential of the anode of a corrosion cell or at the composite open-circuit potential of all the anodes on a corroding steel surface, has been found to bear a relatively direct relationship to the corrosion current [6]. This current is the minimum value necessary for cathodic protection, based on the corrosion rate existing at the instant of measurement and has been previously discussed in connection with the cathodic protection of steel in soils [3]. The minimum current for cathodic protection has also been discussed by Pope [7]. In order to relate the current at the break in the curve with the currents and the potential required to maintain optimum protection, an investigation was conducted with a water environment containing 3 percent of sodium chloride. This environment was chosen as the IR drop is negligible in such a medium and therefore potentials measured with the equipment used would be significant.

2. Experimental Procedures

2.1. General

All specimens used in these experiments were cut from one piece of 0.5 in. diameter cold-rolled steel to lengths of 16 in. They were degreased, smoothed with emery cloth, washed in hot water, and then weighed to the nearest 5 mg.

The exposure medium was Washington, D. C., city water to which had been added 3 percent by weight of sodium chloride, each specimen being exposed for a period of 60 days. Exposure was under two conditions, one with the electrolyte in Pyrex jars (approximately 12 in. in diameter by 12 in. high) representing a stagnant condition, and the other in the electrolyte in an aerated condition when contained in a wooden vat about 66 in. in diameter and 18 in. high. Air was continually passed into the salt water in the vat from a perforated rubber hose which rested on the bottom. In both cases, water lost by evaporation was replaced weekly. No attempt was made to control the temperature of the electrolyte, and exposure of the specimens in the jars was not simultaneous with exposure of those in the vat. All of the specimens were positioned normal to the surface of the electrolyte with 0.1 ft² of bare surface under exposure. Specimens were protected from waterline corrosion by plastic insulating tape extending about 1.5 in. above and below the waterline thus allowing about 9 in. of the steel to be exposed. The surface of the specimens above the tape was protected

[1] Figures in brackets indicate the literature references at the end of this paper.

against atmospheric corrosion with a thin coating of oil.

At the conclusion of exposure all specimens were removed from the electrolyte, washed under hot running water, and examined. Tightly adherent corrosion products were loosened by cathodically cleaning the specimens in the same electrolyte at a current density of 1 amp/ft^2 for periods ranging from 1 to 3 hr. This was followed by brushing with a stiff brass bristle brush under hot running water. When dry, the specimens were again wire brushed and reweighed to measure the loss of metal.

2.2. Arrangement for Stagnant Exposure

Five jars were filled to within 1 in. from the top with the sodium chloride solution. Four of the jars were each fitted with three 0.5 in. diameter carbon anodes mounted vertically 0.5 in. from the inner wall so as to form the corners of a triangle and extending about 3 in. above the waterline. One specimen was located at the vertical center line of each jar and held by a perforated rubber stopper with a clamp, so that its lower end did not quite reach the bottom of the jar. Electrical connections to the anodes and specimens were made with battery clips, the 3 anodes being interconnected. Wires from the clips were securely fastened to the outside of the jars so as to avoid disturbing the specimens when making electrical connections. The fifth jar was not fitted with carbon anodes but contained two control specimens, No. 1 centrally mounted and No. 6 off to the side about 1 in. from the inside wall of the jar. Three of the four jars with the carbon anodes contained specimens that were held under different degrees of cathodic protection. The fourth jar contained control specimen No. 2. Sleeves of insulating material were vertically mounted near the inner wall of each jar with one end of the sleeve extending about 5.5 in. below the waterline in order to hold an agar salt bridge. The bridge consisted of a flexible plastic tube containing a cotton string saturated with potassium chloride and filled with a saturated potassium chloride-agar mixture. This connected the test solution with the reference cell.

2.3. Arrangement for Aerated Exposure

The location of specimens Nos. 8 through 12 in the wooden vat, A, is shown in figure 1. They too were fitted with perforated rubber stoppers for clamping to a supporting bar which spanned the open top of the vat. The electrolyte, B, was maintained to a depth of 17 in. and the exposed ends of the specimens were about 6.5 in. from the tank bottom. Anodes, C, consisting of 0.5 in. diameter steel rods mounted as shown, were used to supply current for the specimens as needed. Two anodes were used in conjunction with each specimen as indicated by the arrows. Steel rather than carbon anodes were used in order to avoid excessive anodic polarization of the anodes when obtaining cathodic polarization curves automatically on the specimens. Electrical connections with the specimens and anodes were made as previously described. The air hose,

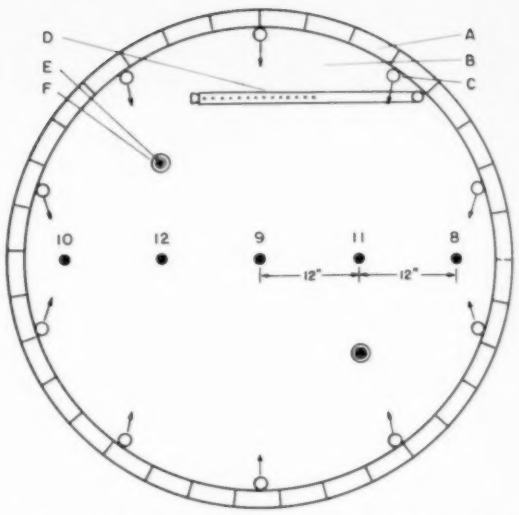

FIGURE 1. *Experimental arrangement in the wooden vat.*
Control specimens, Nos. 8, 9, and 10; cathodically protected specimens, Nos. 11 and 12.

D, end sealed, contained 15 holes 1 in. apart. In anticipation of the likelihood of uneven water movement around the 5 specimens, the cathodically protected specimens (Nos. 11 and 12) were symmetrically arranged with respect to the air supply. Visual observation and later experimental results indicated maximum agitation in the center of the tank, with decreasing agitation toward the tank wall. The flexible agar-salt bridges, E, used in conjunction with the potential-control equipment for specimens Nos. 11 and 12, were held by insulated sleeves, F, as previously mentioned.

2.4. Instrumentation

All potentials were measured with reference to the saturated calomel half cell using an indicating potentiometer. Some specimens were held at a constant current in the stagnant water while others were held at constant potential. The constant current was supplied from 4 series-connected heavy duty 1.5 v dry cells and appropriate series resistance. After the initial polarization of the carbon anodes, the current remained within about 2 percent of the desired value. The constant potential was controlled by the circuit shown in figure 2 to within ± 5 mv of the adjusted value. The voltage divider, A, was set at the desired potential with reference to the half cell, C. Any difference of potential between terminals PS caused the balancing motor, M, to operate the voltage divider, B, until the difference of potential was reduced to zero. As previously stated, the *IR* drop through the electrolyte was negligible. Two agar-salt bridges, E, connected the test solution with the reference cell, C, through a container of saturated potassium chloride, D. When specimens were protected at a designated potential, the polarizing current was continuously recorded by a strip chart recorder, R.

Cathodic polarization curves were obtained on most of the controls at significant times throughout the exposure periods and occasionally on some of

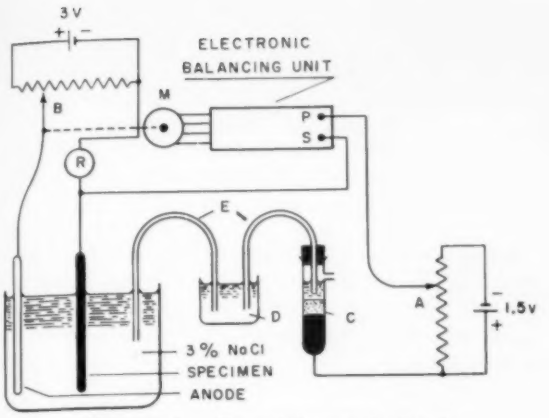

FIGURE 2. *Potential-control circuit.*

the specimens under cathodic protection. The polarizing current and potential of the specimen were recorded with a two-pen strip chart electronic recorder, the potential measuring circuit of which has a high imput impedance. The polarizing current was supplied by a 4 v storage battery shunted by a voltage divider which was manually controlled during stagnant exposure and synchronously driven during aerated exposure.

3. Experimental Results

3.1. Exposure to Stagnant Salt Water

For the first 24 hr of exposure all of the specimens corroded freely. It was assumed that all six would corrode at approximately the same rate as the exposed areas were equal and the environment the same. On the second day, cathodic polarization curves were obtained on the control specimens Nos. 1 and 2. The current, I_p, at the break in the curve, approximately the same value being measured for both specimens, was applied to specimen No. 4. A current equal to 50 percent of this value of I_p was applied to specimen No. 3. Potential control was placed on specimen No. 5, the controller being adjusted to −0.775 v. The potential of specimens 3 and 4 and the current to specimen 5, measured daily or less frequently throughout the exposure period, are plotted in figure 3. Also shown in figure 3 are the values of current, I_p, from curves obtained less frequently on control specimen No. 1 at significant times during the exposure period. The values of current shown in figure 3 and wherever later mentioned have been converted to current densities.

The plots of the potentials of specimens Nos. 3 and 4 and of the current to specimen No. 5 (fig. 3) show that fluctuations such as occurred in the corrosion rates, due chiefly to temperature changes of the electrolyte, happened more or less simultaneously. For example, any depolarization of specimens No. 3 and 4, indicative of increases in corrosion rate, was generally accompanied by increased current to specimen No. 5, while increased polarization of specimens Nos. 3 and 4 was usually associated with decreased current to specimen No. 5. That the current at the break

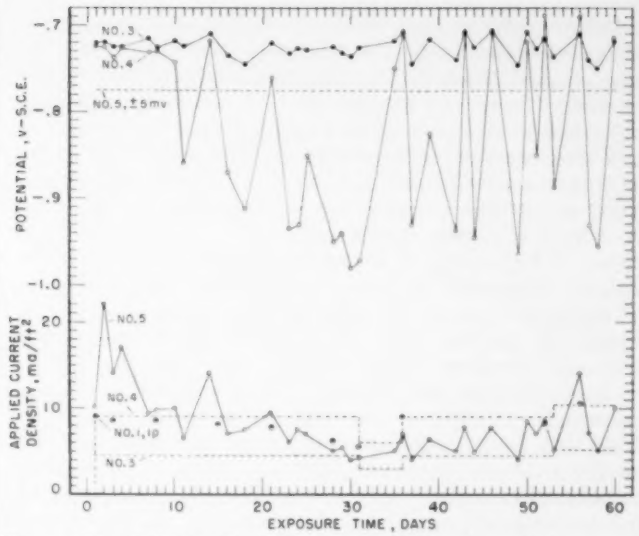

FIGURE 3. *Relationship between potential and applied current density for different degrees of cathodic protection on steel specimens Nos. 3, 4, and 5 exposed to stagnant water containing 3 percent of sodium chloride.*

I_p, protective current requirement as indicated by control specimen No. 1; No. 5, specimen at constant potential −0.77 volt; No. 4, specimen at constant current, except as indicated; No. 3, specimen at constant current equal to 50 percent of that on No. 4.

in the polarization curve is a critical value, as related to polarization, is shown by the values of current I_p (No. 1 specimen) and the potential changes of specimen No. 4, presumably held fairly close to a mean value of I_p considered applicable to all specimens. It will be observed that an over-all lowering of the corrosion rate occurred up to about the 31st day of exposure, as indicated by the decreasing values of I_p for specimen No. 1. The low rates of corrosion on the 28th and 31st days of specimen No. 1 are reflected in the potential of specimen No. 4, which at the time had more protective current applied than was then required. Accordingly, it was decided to reduce the current to specimen No. 4 and also to specimen No. 3 as shown (fig. 3). On the 36th day, it was noticed that considerable depolarization had occurred on specimen No. 4, some on specimen No. 3, and that the current to specimen No. 5 had increased. That these observations were indicative of increased rates of corrosion was verified by an increase in current I_p from the curve on control specimen No. 1, obtained on the 36th day, to approximately its original value. Accordingly therefore, the currents to specimens Nos. 3 and 4 were again raised, No. 4 to the value indicated by the then currently measured I_p and No. 3 to 50 percent of that value. On the 52d day, an unusually large amount of depolarization had occurred on specimen No. 4. Therefore, on the following day, the current applied to this specimen was again raised slightly. During the remainder of the test, the potential of specimen No. 4 and the current to specimen No. 5 continued to fluctuate. However, a cathodic polarization curve obtained on control specimen No. 1 on the 56th day indicated I_p to be very nearly the same as the current applied to specimen No. 4. During this period the current to specimen No. 3 was increased accordingly.

All specimens were subject to fluctuations in temperature of the salt water because the room temperature varied from 60° to 92° F during the exposure period. As would be expected, increases in temperature were accompanied by increased rates of corrosion and decreases in temperature resulted in lower rates of corrosion. The effect was particularly noticeable by the potential changes that occurred on specimen No. 4. Although these effects were not premeditated, the changes in corrosion rate on specimen No. 4 made it possible to observe the effects, on potential, of applied current less and greater than the critical value, I_p, as this value fluctuated above and below the applied value.

At the end of the 60-day exposure period, in turn, protective currents were removed from specimens Nos. 3, 4, and 5 and depolarization allowed to proceed to the most noble potentials. In each instance, the depolarization time was about 20 min, specimen No. 5 reaching the most noble potential of the three specimens, followed in the order of potential by specimens Nos. 4 and 3. Based on previous experience with the cathodic protection of steel in soils [3], these relative changes in potential indicated that specimen No. 5 had probably received the best degree of protection. That this was true will be shown later with reference to the weight losses measured on these specimens.

Table 1 shows pertinent data resulting from the experiment. The weight losses of the cathodically protected specimens have been adjusted to allow for the first 24 hr of exposure when all specimens were corroding freely. This adjustment was made by substituting the value of I_p, measured on the controls during the second day of exposure, in the Faraday equation and deducting the calculated weight loss from the total measured weight loss. The data show virtually complete protection of specimen No. 5 maintained at the protective potential and also at a lesser average current than was applied to specimen No. 4, which was not as effectively protected. These data show that steel must be continuously polarized at least to the potential at the break in the cathodic polarization curve in order to achieve a good degree of protection. Based on the cathodic polarization curves (table 1) this value, E_a, peculiar to the type of environment, was around −0.765 v (mean of specimens Nos. 1 and 2). Although the mean polarized potential of specimen No. 4 was −0.843 v (overprotection), there were times when the potential was more noble than −0.765 v, probably accounting for most of the additional weight loss over specimen No. 5, By referring to figure 3, and considering −0.775 v as a datum line, it will be observed how often the potential of specimen No. 4 reflected insufficient protection. It is believed that the greatest weight loss on specimen No. 4 occurred during the first 10 days when polarization was inadequate. Other important points brought out by these data, which are in agreement with results previously obtained for soil exposure, are that the current I_P is a measure of the minimum value required to produce adequate polarization (with time) and that lesser values initially applied, for example as on No. 3 specimen, result in only partial protection.

The ratio between the corrosion current and the current required to prevent corrosion is about 0.85. This ratio is based on the average corrosion current figured for the three controls and the mean current applied to specimen No. 5 (table 1). For steel in soils, this ratio varied from 0.78 to 0.88, based on the current I_p [6].

3.2. Exposure to Aerated Salt Water

For the experiment in aerated water it was decided to hold one specimen No. 11, at about the potential corresponding to that at the break in the cathodic polarization curve (designated E_a), and the other at −0.77 v. This experiment was designed primarily to determine whether it is advantageous to protect at a potential more noble than −0.77 v, and also to determine the comparative protective currents required in stagnant and agitated waters. The average water temperature during exposure was 74° F, ranging between 66° and 88° F and never varied more than 5 degrees in 24 hr.

TABLE 1. *Exposure for 60 days to stagnant water containing 3 percent of sodium chloride*

Exposure period	Specimen number	Protective criterion	Cathodic polarization curve: Current at break, I_p: Range Min.	Range Max.	Mean	Cathodic polarization curve: Potential at break, E_a [a]: Range Min.	Range Max.	Mean	Protective current to specimen: Range Min.	Range Max.	Mean	Potential of specimen [a]: Range Min.	Range Max.	Mean	Corrosion current [b] I	Weight loss of specimen 60 days	Effectiveness of protection [c]
1st 24 hr	All specimens corroding freely																
			ma/ft²	*ma/ft²*	*ma/ft²*	*v*	*v*	*v*	*ma/ft²*	*ma/ft²*	*ma/ft²*	*v*	*v*	*v*	*ma/ft²*	*mg*	%
Remainder, 59 days	1	Control	5.5	10.5	8.0	−0.740	−0.775	−0.763	---	---	---	−0.685	−0.735	−0.719	6.1	920	------
	2	do	8.5	10.5	9.1	−.760	−.775	−.768	---	---	---	−.710	−.730	−.722	6.9	1035	------
	3	Current	----	----	----	----	----	----	3.0	5.2	4.4	−.706	−.750	−.726	----	[c] 435	54
	4	do	----	----	----	----	----	----	6.0	10.4	8.8	−.688	−.980	−.843	----	[c] 120	87
	5	Potential	----	----	----	----	----	----	4.0	22.0	[d] 7.4	−.770	−.780	−.775	----	[c] 20	98
	6	Control	----	----	----	----	----	----	---	---	---	−.690	−.733	−.720	5.8	865	------

[a] Saturated calomel scale.
[b] Based on Faraday's law, $W=KIt$, where $K=2.8938\times10^{-4}$ grams per coulomb, W=wt loss of control.
[c] Effectiveness of protection $=\frac{Wc-Wp}{Wc}\times100$, where Wc=avg. wt. loss of controls, Wp=wt. loss of the cathodically protected specimen.
[d] Based on hourly values from the strip chart record.
[e] Corrected for freely corroding period.

Unlike the test in stagnant water, the protective currents were initially applied to specimens Nos. 11 and 12 immediately upon immersion. A preliminary polarization curve obtained upon a control specimen furnished the basis for the initial control of specimen No. 11 at about −0.7 v while specimen No. 12 was adjusted for control at −0.775 v. After applying protection it soon was observed that the protective currents, automatically recorded, were unusually high. These currents, plotted in figure 4, are daily averages based on hourly values from the strip charts. The potentials shown are the mean measured values. It will be noted that, even after 8 days, the current densities are still high. On the previous day (7th day), cathodic polarization curves had been recorded on the freely corroding controls Nos. 8, 9, and 10. The values of I_p from these curves, tabulated in table 2, showed that protection of the controls could have been accomplished at less than half the current applied to specimens Nos. 11 and 12, even after the latter two had been under cathodic protection for 8 days. On the 8th day of exposure, the current to specimen No. 12 was removed and in a period of 60 sec the specimen potential rose to −0.46 v and then began to slowly drift back again in the less noble direction. After a lapse of 50 min the potential was −0.57 v, changing very little compared to previous changes. A cathodic polarization curve was then obtained on specimen No. 12, resulting in the values of I_p and E_a tabulated in table 2 (1st 8 days). One hour later, an anodic polarization curve was recorded on this specimen (not recorded in table 2). These curves revealed that the corrosion process was cathodically controlled and at a relatively high corrosion rate, as indicated approximately by the cathodic polarization current I_p.

Apparently the protective currents to specimens Nos. 11 and 12 were high, for the first 8 days at least, because no time was allowed for a normal corrosion rate to become established. After obtaining the polarization curves on specimen No. 12, both specimens were left without any protection for 3 days by removing the protective currents. After corroding freely during this time, cathodic polarization curves were again obtained (11th day). The new values of I_p (28 ma/ft², table 2) were more consistent with the values previously obtained for the controls and the intermediate values of I_p seem reasonable when considering the positions in the vat of specimens Nos. 11 and 12 relative to the controls. On the 11th day of exposure, these specimens were again placed under cathodic protection. Because the potentials E_a (table 2), previously obtained from curves of the controls, were all more anodic than −0.70 v it was expedient to readjust the control potential for specimen No. 11. Accordingly, specimen No. 11 was adjusted to −0.725 v and No. 12 again at −0.775 v. The currents applied to these specimens, automatically recorded for 60 days, are tabulated in table 2 and daily averages are plotted in figure 4. The potential of specimen No. 12 was also automatically recorded for the 60 days and, in addition, daily measurements of potential were made on all other specimens, including No. 12. Minimum, maximum, and mean values are tabulated in table 2.

The values of I_p and E_a shown for the controls (table 2, 11th to 60th day) are based on all curves, that is, those recorded on the 7th, 39th, and 57th days of exposure. Judging from the mean values of E_a for the controls, it would be expected that the composite open-circuit potential, E_a, of the anodes of specimen No. 11, and for that matter also specimen No. 12, was probably between −0.715 and −0.728 v. Thus, this range gave assurance that the potential, −0.725 v, to which specimen No. 11 was controlled, was about right, the value −0.73 v shown in table 2 for this specimen being based on only one measurement made the 11th day. On the 60th day, when the protective currents were removed, the rise in potential, as previously described for the cathodically protected specimens in the stagnant water, indicated that specimen No. 12 received the best degree of protection.

TABLE 2. *Exposure for 60 days to aerated water containing 3 percent of sodium chloride*

Exposure period	Specimen number	Protective criterion	Cathodic polarization curve						Protective current to specimen [d]			Potential of specimen [a]			Corrosion current [b] I	Weight loss of specimen 60 days	Effectiveness of protection [c]
			Current at break, I_p			Potential at break, E_a											
			Range		Mean	Range		Mean	Range		Mean	Range		Mean			
			Min.	Max.		Min.	Max.		Min.	Max.		Min.	Max.				
			ma/ft²	*ma/ft²*	*ma/ft²*	*v*	*v*	*v*	*ma/ft²*	*ma/ft²*	*ma/ft²*	*v*	*v*	*v*	*ma/ft²*	*mg*	%
1st 8 days	8	Control	.....	.....	20.0	.....	.....	−0.725	.....	.....	.....	−0.655	−0.700	−0.686	.....	.....	.....
	9	do	.....	.....	30.0	.....	.....	−.730	.....	.....	.....	−.652	−.695	−.681	.....	.....	.....
	10	do	.....	.....	22.5	.....	.....	−.730	.....	.....	.....	−.647	−.700	−.684	.....	.....	.....
	11	Potential	.....	.....	.....	.....	.....	.....	60.0	95.0	70.7	−.685	−.700	−.697	.....	.....	.....
	12	do	.....	.....	51.0	.....	.....	−.680	56.0	90.0	70.2	−.770	−.780	−.772	.....	.....	.....
8th to 11th day	Specimens 11 and 12 corroding freely for 72 hours																
11th to 60th day	8	Control	20.0	22.5	21.2	−0.725	−0.735	−0.728	.....	.....	.....	−0.690	−0.715	−0.705	13.9	2,090	.....
	9	do	27.5	33.0	30.2	−.705	−.730	−.715	.....	.....	.....	−.670	−.702	−.689	19.7	2,955	.....
	10	do	19.0	22.5	20.5	−.725	−.730	−.728	.....	.....	.....	−.680	−.712	−.704	15.3	2,300	.....
	11	Potential	.....	.....	28.0	.....	.....	−.730	13.5	34.2	27.5	−.720	−.733	−.725	.....	[e] 238	90
	12	do	.....	.....	28.0	.....	.....	−.730	20.0	36.0	27.6	−.770	−.780	−.776	.....	[e] 108	95

See footnotes to table 1.

The weight loss data (table 2) indicate that the effectiveness of the cathodic protection was best on specimen No. 12 and also favorable from the standpoint of applied current over the latter portion of the exposure period (fig. 4). While investigating the reasons for the high currents initially required to protect specimens Nos. 11 and 12, it was decided to hold control specimen No. 8 at a protective potential of −0.775 v overnight and automatically record the protective current required. After 20 hr of cathodic protection, the potential was changed progressively over a period of 10 min to a value of −0.700 v (fig. 5). Within 1 hr, the initially reduced current had increased until it was almost as high as previously. Upon again gradually readjusting the potential to −0.775 v, which required an initial increase of current, a gradual reduction followed, the current once again approaching the original value. This experiment confirmed the comparative currents applied to the cathodically protected specimens Nos. 11 and 12. In fact, the data seem to indicate that protection at the potential −0.77 v not only assures virtually complete protection but also optimum current requirements.

The average weight loss of the controls in aerated water was about 2.6 times that in stagnant water whereas 3.7 times as much current was required for protection. Had the exposure of the steel in the aerated water been prolonged until the protective current on specimen No. 12 (fig. 4) was stabilized, the ratio of the currents might have been more in agreement with the ratio of the weight losses. It is believed that the higher protective current ratio may be attributed in part, to a difference in the degree of cathodic control of the corrosion rates under the two conditions of exposure. A somewhat analogous comparison of protective currents was made by Waldron and Nelson [8] in reference to the cathodic protection of ship hulls. They found that approximately twice as much current was required to maintain a given potential when a ship was moving as when it was stationary.

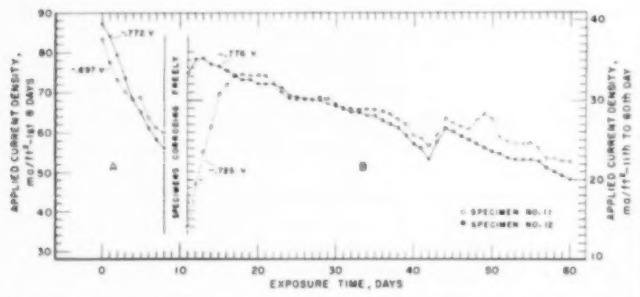

FIGURE 4. *Protective current densities on steel specimens exposed to aerated water containing 3 percent of sodium chloride when controlled at constant potentials.*

A, protective current applied immediately upon exposure; B, protective current applied to the same specimens after an intermediate freely corroding period of 3 days.

4. Summary

Cold-rolled steel specimens were exposed for 60 days to both stagnant and aerated city water, to which was added 3 percent by weight of sodium chloride.

Under both stagnant and aerated exposure, the best degree of cathodic protection was achieved when the specimens were held at a potential −0.77 v with reference to the saturated calomel electrode (equivalent to −0.85 v with reference to the copper-copper sulfate electrode). Although a good degree of protection was obtained at controlled potentials more noble than −0.77 v, that is, at the potentials associated with the breaks in cathodic polarization curves, this lesser degree of protection could not be obtained

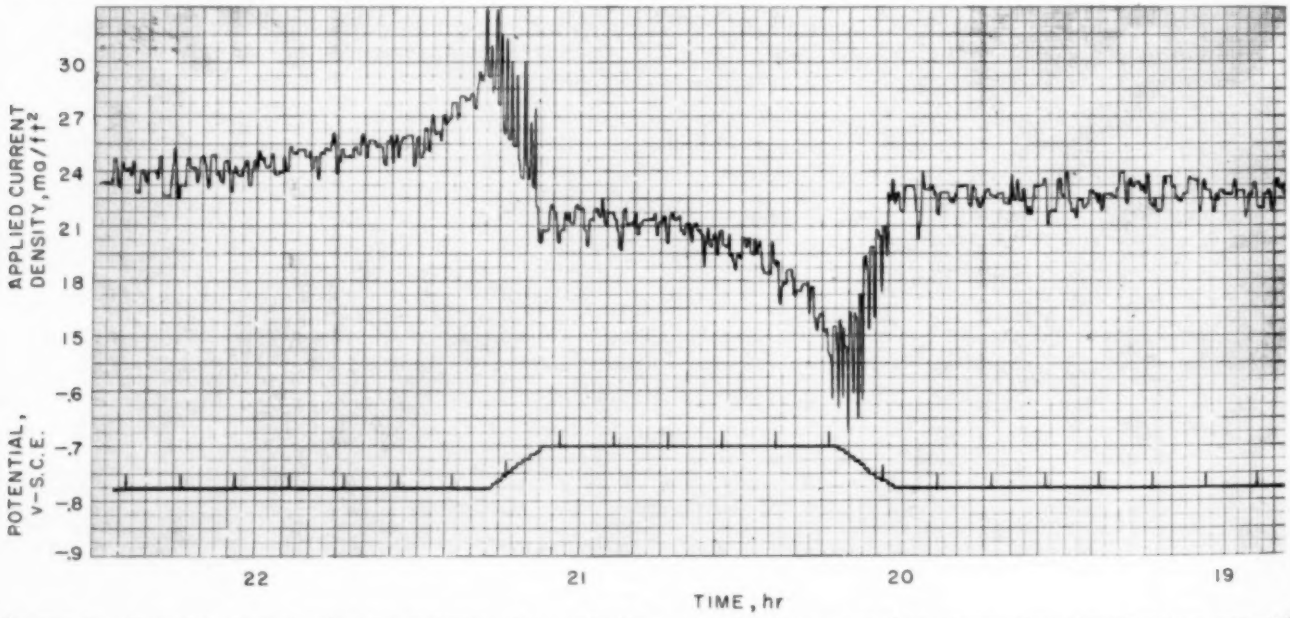

FIGURE 5. *Recorded chart showing the variation of the cathodic current density on a steel specimen when changing from potential control at −0.775 volt to control at −0.700 volt and back again.*

The potential was initially −0.775 volt for 20 hours.

at lower mean current densities. Therefore, −0.77 v was found to be the optimum protective potential.

Applied currents indicated by the breaks in cathodic polarization curves agreed reasonably well with the currents required to maintain polarization at the optimum potential. The break current, therefore, which was observed to be related to the rate of corrosion, is considered a good measure of the current required for optimum protection.

A short preliminary period of exposure without protective current was observed to greatly reduce the amount of current initially required for cathodic protection.

WASHINGTON, August 14, 1957.

5. References

[1] R. B. Mears and R. H. Brown, A theory of cathodic protection, Trans. Electrochem. Soc. **74,** 519 (1938).

[2] R. H. Brown and R. B. Mears, Cathodic protection, Trans. Electrochem. Soc. **81,** 455 (1942).

[3] W. J. Schwerdtfeger and O. N. McDorman, Potential and current requirements for the cathodic protection of steel in soils, J. Research NBS **47,** 104 (1951) RP2233; Corrosion **8,** 391 (1952).

[4] Robert J. Kuhn, Cathodic protection of underground pipe lines from soil corrosion, Proc. Am. Petroleum Inst. **14,** Sec. IV, 153 (Nov. 1933).

[5] L. P. Sudrabin, A study of protective criteria on a pipe section in a uniform environment, Corrosion **12,** 16 (Feb. 1956).

[6] W. J. Schwerdtfeger and O. N. McDorman, Measurement of the corrosion rate of a metal from its polarizing characteristics, J. Electrochem. Soc. **99,** 407 (1952).

[7] Robert Pope, Cell currents and potentials, Corrosion **11,** 189 (April 1955).

[8] L. J. Waldron and E. E. Nelson, The performance of a cathodic protection system on the USS Sumner–DD 692, NRL Mem. Rept. 291, Naval Research Laboratory (June 1954).

Journal of Research of the National Bureau of Standards Vol. 60, No. 3, March 1958 Research Paper 2834

Joule-Thomson Process in the Liquefaction of Helium[1]

Edmund H. Brown and John W. Dean

A dimensionless, normalized, correlating function is introduced for the specific enthalpy of helium. Using this function, the consistency of various enthalpy data is determined. These data are then used to obtain curves of helium liquefaction yield in the region of variable specific heat in terms of heat-exchanger efficiency.

1. Introduction

Many different devices and cycle arrangements can be used in partially cooling gas for helium liquefaction. With the exception of the Simon free-expansion type liquefier, however—which is suitable only for small-yield, batch production—all such arrangements have a final stage at the lowest temperatures, in which a so-called Joule-Thomson process takes place. This process may be considered to include cooling of the high-pressure gas by the unliquefied return gas in a "Joule-Thomson heat exchanger", as well as cooling of the high-pressure gas by the Joule-Thomson effect, that is, isenthalpic expansion through a "Joule-Thomson valve." If the initial state of the high-pressure gas at the top of the J-T heat exchanger (which is most conveniently defined by its pressure and temperature) is fixed within a certain region, a definite mass fraction α of the gas passing through the J-T valve will be liquefied.

To determine the yield α of a liquefier, the specific enthalpies at certain points in the J-T process must be known as functions of P and T. The most readily available data on the specific enthalpy, h, of helium is from the monograph of Keesom [1],[2] or the temperature-entropy diagram of Keesom published by the International Institute of Refrigeration [2]. The errors and inconsistencies of these sources below about 20° K, however, have been pointed out in a series of papers by Zelmanov [3, 4, 5, 6]. In addition, Zelmanov [6] has recalculated and redrawn both T–s and h–P diagrams which, as indicated later, appear to be of good accuracy and consistency. The Zelmanov T–s diagram is reproduced by Zemansky [7]; and the h–P diagram, by Collins [8]; who, however, also reproduces the Keesom T–s diagram. Because of the crowded nature of the isobars in the region of interest for the J-T process on a T–s diagram, the h–P diagram is more convenient for liquefier calculations.

At the beginning of this study there was no easy way to judge the relative value of various conflicting sets of data. In order to determine, at least, the consistency of such data, a new dimensionless, normalized correlating function $w(P, T)$ was introduced. With this function, the consistency of Zelmanov's work was evident, and both the lack of self-consistency of the T–s diagrams of Keesom, and the inconsistency of these diagrams in certain regions with Keesom's own density data was apparent. In addition, it appears that there may be some value in this new function $w(P, T)$ in theoretical studies, since it implies that, above certain pressures, the enthalpy of a real gas may be approximately given by the sum of two linearly independent functions, one of the pressure alone, the other, of the temperature alone. However, not enough time was available in this study for further investigations in this direction.

A second factor which complicates the design of helium liquefiers is the behavior of the specific heat c_p of the real gas at low temperatures. At high temperatures c_p of a gas gradually increases with increasing pressure; but, at a lower temperature, dependent on the pressure, this trend is reversed. Ignorance of this effect has occasionally led the unwary to design liquefiers in which the temperature difference ΔT at the bottom of the J-T heat exchanger would have to be reversed. This phenomenon, which has been hinted at by Keesom and discussed qualitatively by Zelmanov, is investigated further in this study. In order to determine performance, a method of analyzing J–T heat exchangers in terms of one parameter—the heat exchanger efficiency η—is presented, and graphs of yield curves for helium based on this method are included.

The purpose of this paper, then, consists of three things: First, and most important, to affirm the work of Zelmanov (an adaptation of Zelmanov's h–P diagram is included as figure 1); second, to present the correlating function $w(P, T)$ and discuss some of its properties; and third, to show quantitatively the effect of the variation of c_p in the J–T heat-exchanger on the liquefied fraction α.

2. Correlating Function $w(P,T)$

The enthalpy of a gas can be expressed as

$$h(P,T)=\int^{T} c_p(P,T)dT+G(P)$$

where G is a constant of integration. For an ideal gas, $c_p(0,T)=c_p^\circ$; and, for helium, which is a monatomic gas, $c_p^\circ=(5R/2)=5.193$ j/g-° K. In defining the enthalpy of the ideal gas, $h^\circ=h(0,T)$, the constant of integration $G(0)$ was equated with the latent heat of evaporation at 0° K, L°, which is equivalent to fixing the enthalpy (which at this point is equal to the internal energy) of the liquid at $P=0$, $T=0$ as zero. According to Swenson [9], the extrapolated

[1] This work was supported by the Department of the Navy, Bureau of Aeronautics, Helium Branch.
[2] Figures in brackets indicate the literature references at the end of this paper.

value of L° is 14.95 j/g. Thus, the expression used for helium in the ideal gas state is

$$h^\circ = c_p^\circ T + L^\circ = 5.193T + 14.95 \text{ j/g}.$$

Just as an enthalpy in an "ideal gas" state can be defined by extrapolating to zero pressure, so an enthalpy in an "ideal condensed phase" state, $h_0 = h(P,0)$, can be defined by extrapolating to zero temperature. If $V(P,0)$ is the specific volume at zero temperature, then

$$\left(\frac{\partial h_0}{\partial P}\right)_{T=0} = V(P,0) = V(0,0)\epsilon^{-\int_0^P k(P,0)dP}.$$

An attempt was made to express the extrapolated isothermal compressibility at 0° K, $k(P,0) = -(1/V)\cdot[(\partial V)/(\partial P)]_T$, by an empirical equation which would have led to an expression for h_0 as a function of exponential integrals, $Ei(k)$. However, since this required some simplifying assumptions, was not particularly suited for engineering calculations, and lacked theoretical justification, h_0 was finally determined by extrapolating Keesom's density data [1] with the aid of expansivity and compressibility data of Atkins and Edwards [10]. The resulting curves for h_0, $V(P,0)$, and also $k(P,0)$, are included as figures 2, 3, and 4. It should be mentioned that Swenson's extrapolated value [9] of $V(0,0)$, for the liquid seems to be in error.

Having, now, both $h^\circ = h(0,T)$ and $h_0 = h(P,0)$, the remaining "anomalies" of both the real gas and the condensed phases can all be contained in a function $w(P, T)$ defined by

$$w(P,T) = \frac{h(P,T) - h_0(P)}{h^\circ(T)}$$

which is not only dimensionless, as is evident from the definition, but has a total range of zero to one; zero, for the condensed phases as $T \to 0°$ K; one, for the gas as $T \to \infty$; one, for the gas as $P \to 0$; and zero, for the condensed phase as $P \to \infty$.

Here, we use the symbols $T \to \infty$ or $P \to \infty$ merely for convenience to indicate relatively high and increasing temperature and pressure, but not so high that the character of the "elementary" particles implied by the choice of L° and $h^\circ(T)$ is destroyed. Thus, we assume, for instance, that the pressure is not so high as to force an electron from the atomic shell, converting the solid into *metallic* helium (estimated required pressure 1,000,000 atm), or that the temperature is so high as to form a gas mixture of ionized particles. This restriction would be of even greater importance for diatomic gases, such as hydrogen, which begin to dissociate from molecular to atomic particles at relatively low temperatures. Presumably, all the properties of the w function could be reobtained in such cases by a redefinition of L° and $h^\circ(T)$. For example, $h^\circ(T)$ would, then, have to be the enthalpy of the gas in the atomic ideal gas state and L° the difference between the energy of isolated atoms at 0° K and the energy of (for hydrogen) the crystal at 0° K and 0 atm. Some of these effects, such as dissociation, however, are so large that the introduction of a more general w function would result in characteristics in the regions of interest for cryogenic processes too small to be useful.

From the theoretical point of view this function does have the disadvantage that a discontinuity in $[(\partial w)/(\partial P)]_T$—though *not* in w—is introduced by the liquid-solid transformation for h_0 at 25 atm. However, this change in slope of w is slight, being given approximately by $\Delta[(\partial h)/(\partial P)]_T = 0.0524$j/g-atm (from the data of Swenson [9]). It would probably be of considerable interest to compare curves of w (P_r, T_r) as functions of reduced temperature T_r and pressure P_r for several gases.

Further insight into the characteristic behavior of $w(P,T)$ can be obtained by examination of the graphs (at end of paper). From figure 6 which gives w as a function of P with T as a parameter, it can be seen that all isotherms start with the same value, $w=1$, $P=0$; that outside of the liquid II region, all isotherms are everywhere decreasing functions of P; that the isotherms are continuous except on passing through phase changes; that no two isotherms cross; that the slopes of all isotherms approach zero with increasing pressure; and that, although the total percent change in w along an isotherm is greater the smaller the temperature, the pressure at which the slope of an isotherm becomes effectively zero increases with increasing temperature (for the 0° K isotherm the slope becomes zero at zero atmosphere, the value of w changing discontinuously from *one* to *zero* through the vapor dome, and then remaining *zero* for all nonzero pressures).

From figure 7, giving w as a function of T with P as a parameter a similar set of statements can be made; all isobars start with the same value, $w=0$ $T=0$; all isobars are everywhere increasing functions of T; the isobars are continuous except on passing through phase changes; outside of the liquid II region no two isobars cross; the slopes of all isobars outside the liquid II region approach zero with increasing temperature, and approach zero more rapidly the lower the pressure (the slope of the zero atmosphere isobar being zero for all nonzero temperatures); the value of w for all isobars approaches *one* with increasing temperature, and approaches more rapidly the lower the pressure (the zero atmosphere isobar changing discontinuously from *zero* to *one* at zero atmosphere). The liquid II region sketched on this diagram is somewhat uncertain, due principally to lack of time for more extended calculations in an area of little interest for liquefier design.

The limiting behavior of $w(p,T)$ can also be determined by considering its definition. It is obvious that for $T \to 0$, $p \neq 0$, $w \to 0$; for $p \to 0$, $T \neq 0$, $w \to 1$; while for $T \to 0$, $p = 0$, or $p \to 0$, $T = 0$, w becomes undefined, but lies within the range 0 to 1. This is the region of liquid-vapor coexistence at 0° K and zero atmospheres.

When T increases without limit at constant and finite p,

$$\lim_{T\to\infty} w(p,T) = \frac{\lim_{T\to\infty} h(p,T)}{\lim_{T\to\infty} h^\circ(T)} = 1.$$

The second equality of this equation may be obtained on the assumption that no matter how high the pressure the system will become a "gas" for a sufficiently large increase in temperature, with enthalpy h approaching the enthalpy of an ideal gas h°. This may be seen for a region in which a virial equation of state applies, where the higher virial type coefficients in the pressure series are sometimes taken as decreasing approximately as increasing power of $1/T$.

For increasing pressure, however,

$$\lim_{p\to\infty} w(p,T) = \lim_{p\to\infty} \frac{1}{h^\circ}\int_0^T c_p(p,T)\,dT$$

$$= \frac{1}{h^\circ}\int_0^T \lim_{p\to\infty} c_p(p,T)\,dT = 0,$$

since $\lim_{p\to\infty} c_p(p,T)\to 0$, as can be deduced from the fact that the slopes of the isobars with fixed T on a temperature entropy diagram, $[(\partial T)/(\partial S)]_p = (T/c_p)$, approach infinity with increasing pressure (recall, however, our restriction on the meaning of $P\to\infty$).

The above combination of well-defined behavior and range of magnitude makes the checking and cross checking of enthalpy data with w–P and w–T diagrams relatively easy. In particular, it has indicated many errors and inconsistencies in the T-s diagrams of Keeson, and affirmed the consistency of the T-s and h-P diagrams of Zelmanov.

Since the enthalpy of helium can be expressed as

$$h(P,T) = h_0(P) + w(P,T)h^\circ(T),$$

the fact that the isotherms on the w–P diagram shown in figure 6 become approximately horizontal at pressures that are not extremely high is of some theoretical interest; for this behavior of the isotherms is equivalent to stating that $w(P,T)$ becomes practically a function of temperature, alone, even for large pressure ranges; thus, since h° is also a function of the temperature, alone, the enthalpy can be expressed approximately as the sum of a function of the pressure h_0 (which might be considered a *strain energy* term), and a function of the temperature $w(T)h^\circ(T)$ (which might be considered a *thermal energy* term).

3. Liquefier Performance and Heat-Exchanger Efficiency

Before discussing the J-T heat exchanger for helium use, it is desirable to review a few general relations. Heat exchanger efficiency is defined as the ration of actual heat flow to the ideal heat flow, $\eta = \dot{Q}_{\text{actual}}/\dot{Q}_{\text{ideal}}$, where the ideal is that which would occur if the product of the total effective heat exchange area and the over-all coefficient of heat transfer, AK, is made infinite. However, in obtaining η, $\dot{Q}_{\text{actual}}$ and $\dot{Q}_{\text{ideal}}$ must be evaluated for the same conditions; that is, the flows, pressures, and inlet temperatures of both streams must be held constant. Thus, for an arbitrarily defined heat exchanger, the efficiency will be an explicit function of the flows, and—if the fluid properties are not constant—an implicit function of temperatures and pressures as well.

The efficiency of a two-stream, counter-flow, heat exchanger can be expressed analytically in three different forms, depending on the flow conditions. If $\dot{m}_1$, $\dot{m}_2$ are the mass flows, c_{p1}, c_{p2}, the specific heats, $W_1 = -\dot{m}_1 c_{p1}$, $W_2 = \dot{m}_2 c_{p2}$, the heat capacity flows in the two streams, and writing, for convenience, $(1/W) = [(1/W_1) + (1/W_2)]$, the expressions for efficiency are

$$\eta = \frac{1 - e^{-A\left(\frac{\overline{K}}{\overline{W}}\right)}}{1 + \frac{\overline{W}_2}{\overline{W}_1} e^{-A\left(\frac{\overline{K}}{\overline{W}}\right)}}, \quad W > 0,$$

$$\eta = \frac{1 - e^{+A\left(\frac{\overline{K}}{\overline{W}}\right)}}{1 + \frac{\overline{W}_1}{\overline{W}_2} e^{+A\left(\frac{\overline{K}}{\overline{W}}\right)}}, \quad W < 0$$

$$\eta = \frac{1}{1 + \left(\frac{\overline{W}_2}{\overline{W}}\right)\left(\frac{\overline{W}}{AK}\right)} = \frac{1}{1 - \left(\frac{\overline{W}_1}{\overline{W}}\right)\left(\frac{\overline{W}}{AK}\right)}, \quad W_1 = -W_2, W \to \infty,$$

where bars above quantities indicate that some kind of integrated average over the heat exchanger must be taken. However, obtaining such averages requires a knowledge of the temperature distributions in the streams, and if these were known, there would be no problem in the first place. Thus, for heat exchangers with variable fluid properties, the above formulas can only be used to obtain approximations for efficiencies.

It is our purpose, however, to show how liquefier performance depends on an arbitrarily assigned efficiency, rather than analyzing how the efficiency of a given heat exchanger may be determined. Thus, our results will be correct for any exchanger that has the assigned efficiency under the assumed flow conditions. Since the efficiency of a given exchanger varies with the flow, an important question is, to what extent may a curve of constant efficiency also be considered a curve of performance with fixed exchanger characteristics? To this we can only give a qualitative answer; since the efficiencies of J-T heat exchangers are ordinarily very high, even with equal heat capacity flows in the streams, the efficiency will not be a very strong function of the flows. To justify this statement, we use an example, based on an approximation of constant and equal fluid properties in the streams of a typical counter-flow heat exchanger.

Remembering that the film coefficients are given by equations of the form $\text{Nu} = \text{C Re}^{0.8} \text{Pr}^n$, writing K_0 for the over-all coefficient of transfer for the particular case where equal flow exists and $\sigma_0 = [(AK_0)/W_2)]$ and introducing the liquefied fraction α to specify the relation between the mass flows.

$W_1 = -(1-\alpha)W_2$, the efficiency is given by the equation

$$\frac{1}{\eta} = 1 - \frac{\alpha}{1 - \exp \frac{2\sigma_0 \alpha}{1-\alpha+(1-\alpha)^{0.2}}}, \quad 0 \leq \alpha \leq 1$$

or, in the limit as $\alpha \to 0$, as evaluated by l'Hospital's Rule,

$$\frac{1}{\eta} = 1 + \frac{1}{\sigma_0}, \quad \alpha = 0.$$

From these it is easy to see that, for any α, η increases with increasing σ_0; and, for any σ_0, η increases with α. However, in the limit, as $\sigma_0 \to \infty$, the limiting curve $\eta(\alpha)$ becomes merely the horizontal line $\eta = 1$. For large, but finite σ_0, $\eta(\alpha)$ will remain nearly horizontal and nearly straight, so that—as mentioned before—η is not a very strong function of α for J-T heat exchangers

To get an idea of the magnitude of the change we assume some arbitrary values. Suppose $K_0 = 50$ w/ft²-°K and $A = 25$ ft². Also, let $\dot{m}_2 = 0.01$ kg/sec, $c_{p2} = 5000$ j/kg-°K, so that $W_2 = 50$ w/°K, and $\sigma_0 = 25$. Substitution of these values in the above equations shows that the efficiency varies from 96 percent at $\alpha = 0$, to 100 percent at $\alpha = 1$. In real liquefiers the variation would be even less, since α would ordinarily be in the range 0.2 to 0.5.

4. Calculation of Performance From Efficiency

The liquefaction rate α will now be determined from the inlet, high-pressure stream pressure and temperature and the heat exchanger efficiency using only specific enthalpies from an h–P diagram. In making an enthalpy balance, the specific enthalpy h_i at the inlet of the high-pressure stream is determined by the assumed pressure and temperature, and the specific enthalpy h_g at the inlet of the low-pressure stream is assumed to be that of the saturated vapor at 1 atm. Thus, only two quantities, the specific enthalpy h_j above the J-T valve, and the specific enthalpy h_r of the return gas at the outlet of the low-pressure stream, are available, and only one of these is independent since

$$h_i - h_j = (1-\alpha)(h_r - h_g).$$

Furthermore, if h_j' and h_r' are the values of h_j and h_r when $\eta = 100$ percent, the efficiency in any other case is given by

$$\eta = \frac{h_r - h_g}{h_r' - h_g} = \frac{h_i - h_j}{h_i - h_j'},$$

so that we can write

$$h_j = h_i - \eta(h_i - h_j')$$

and

$$h_r = h_g + \eta(h_r - h_{rg}').$$

It should be reemphasized here that the efficiency is defined in terms of two heat flows (or enthalpy changes) under the same conditions of inlet pressures and temperatures and the same mass flows.

Since enthalpies must balance for the whole J-T process, as well as just the heat-exchanger, we can also write

$$h_i = \alpha h_L + (1-\alpha)h_r$$

where h_L is the specific enthalpy of the saturated liquid at one atmosphere. Thus α can be expressed by either of the equations

$$\alpha = \frac{h_r - h_i}{h_r - h_L} = \frac{h_g - h_j}{h_g - h_L}.$$

Substituting for h_r and h_j their expressions in terms of h_r' and h_j', and writing $L_v = h_g - h_L$, these equations become

$$\alpha = \frac{\eta - \frac{h_i - h_g}{h_r' - h_g}}{\eta + \frac{L_v}{h_r' - h_g}} = \eta \frac{h_i - h_j'}{L_v} - \frac{h_i - h_g}{L_v}.$$

Now, a reasonable assumption is that, for $\eta = 100$ percent the temperature difference between streams ΔT becomes zero at some point in the heat exchanger. We should not naively assume that, in the most general case, this might not be in the middle of the exchanger, since this is exactly what would happen if c_p for the high-pressure stream were lower than that for the low-pressure stream at the higher temperatures, and conversely at lower temperatures. For helium in the J-T process range, however, the reverse is the case, and thus, ΔT must diminish towards the top of the exchanger, and—for suitable initial pressure and temperature—diminish again towards the bottom of the exchanger. Thus, the ideal case will be characterized by having $\Delta T = 0$ at either the top or the bottom of the exchanger. If we write h_r'' for the value of h_r' when $\Delta T = 0$ at the top, and h_j'' for the value of h_j' when $\Delta T = 0$ at the bottom, then—since both h_r'' and h_j'' can be determined immediately from an h-P diagram—there will be two different possible equations for the liquefaction rate α in which all the quantities are known:

$$\text{(a)} \quad \alpha = \frac{\eta - \frac{h_i - h_g}{h_r'' - h_g}}{\eta + \frac{L_v}{h_r'' - h_g}}, \ \Delta T \to 0 \text{ at the top;}$$

$$\text{(b)} \quad \alpha = \eta \frac{h_i - h_j''}{L_v} - \frac{h_i - h_g}{L_v}, \ \Delta T \to 0 \text{ at the bottom.}$$

In case (a) we can determine h_j' by an enthalpy balance and see whether $h_i' > h_j''$; if not, the assumption $\Delta T = 0$ at the top must be wrong, and we would have to change to case (b). Similarly, in case (b) we can determine h_r' and check that $h_r' < h_r''$. Actually, however, such a check is unnecessary, since the two assumptions will result in two curves inter-

secting where $\Delta T=0$ simultaneously at the top and bottom of the exchanger, and it will be immediately evident which branch should be used to form the composite curve for the liquefaction rate.

Such composite curves of α as a function of P with η as a parameter, for helium, are shown in figures 9, 10, and 11. The discontinuities in the slopes of these curves would be disturbing if one did not recall that, even for the case of *constant* fluid properties, the efficiency of an exchanger is expressed by *two* different formulas, depending on whether W is positive or negative. It is just the change of the total average value of W from positive to negative with the variation of specific heat of helium, which produces two independent branches in the curves shown.

The differing way α varies with η for these two branches should be especially noted. For lower pressures, relatively large changes in η have only a small effect on α. If, however, a pressure is chosen at or slightly above the "optimum" pressure, α will not only decrease rapidly with increasing pressure, but at a given pressure, will drop drastically with slight reductions in heat-exchanger efficiency. Therefore, it is desirable to be somewhat conservative in the design pressure for a liquefier in order to allow for possibly too optimistic estimates of heat-exchanger performance.

5. References

[1] W. H. Keesom, Helium (Elsevier, Amsterdam, 1940).
[2] International Institute of Refrigeration, T–S diagram for helium (Paris, 1941).
[3] J. L. Zelmanov, On some peculiarities observed in the liquefaction of helium, Compt. rend. acad. sci. USSR **19,** 469 (1938).
[4] J. L. Zelmanov, On the liquefaction of helium by means of the Joule-Thomson effect, Compt. rend. acad. sci. USSR **20,** 537 (1938).
[5] J. L. Zelmanov, A new method of helium liquefaction by means of the Joule-Thomson effect, Compt. rend. acad. sci. USSR **22,** 25 (1939).
[6] J. L. Zelmanov, The entropy diagram for helium at low temperatures, J. Phys. USSR **8,** 135 (1944).
[7] M. W. Zemansky, Heat and thermodynamics (McGraw-Hill Book Co., Inc., New York, N. Y., 1951).
[8] S. C. Collins, Helium liquefiers and carriers, Handbuch der physik, **14,** 112 (Springer, Berlin, 1956).
[9] C. A. Swenson, The liquid-solid transformation in helium near absolute zero, Phys. Rev. **79,** 626 (1950).
[10] K. R. Atkins and M. H. Edwards, Coefficient of expansion of liquid helium II, Phys. Rev. **97,** 1429 (1955).

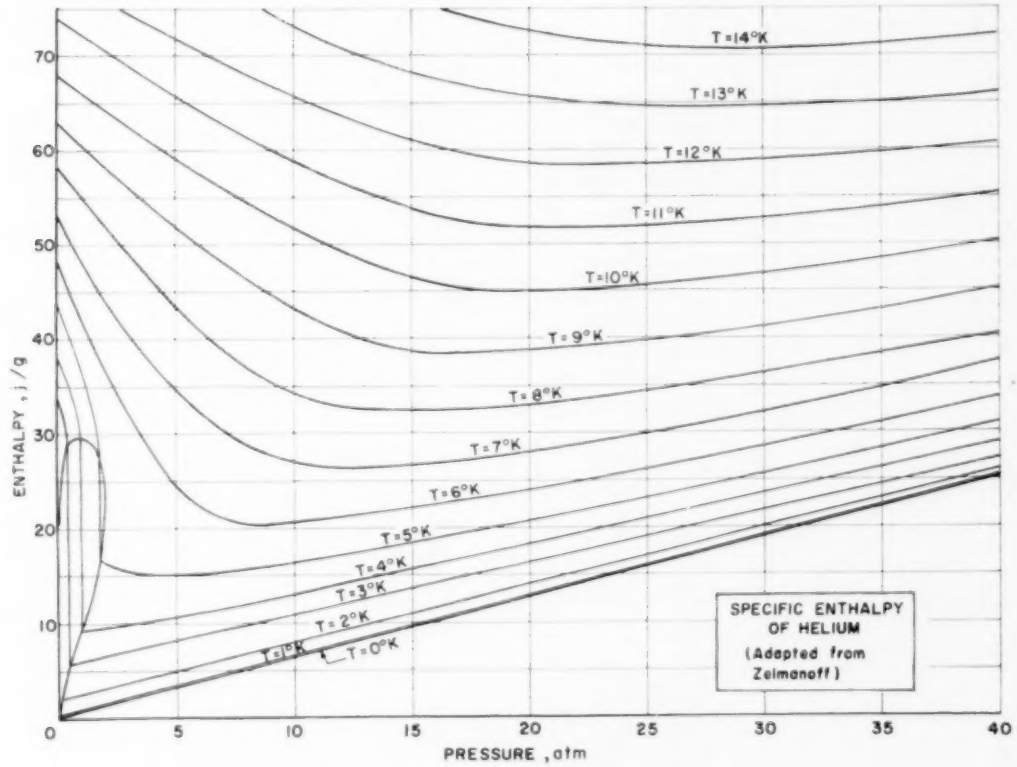

FIGURE 1. *Specific enthalpy of helium.*

Adapted from Zelmanov

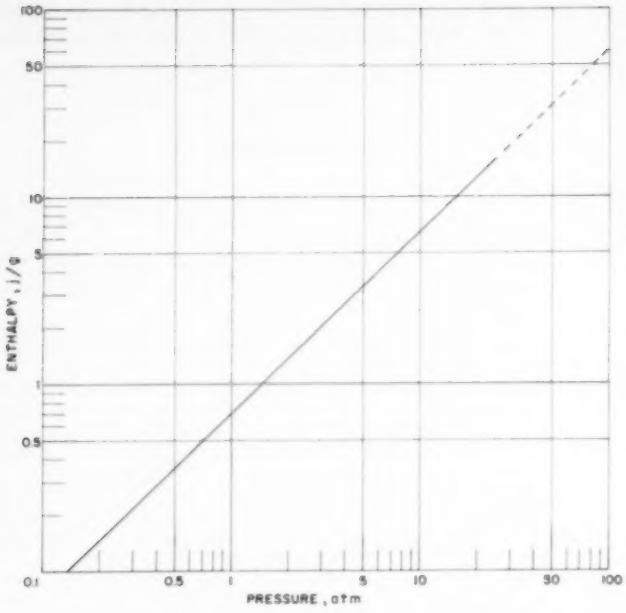

FIGURE 2. *Specific enthalpy of helium at 0° K, $h_0(p)$ versus pressure.*

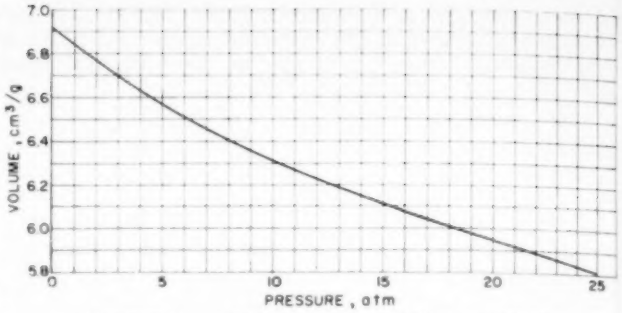

FIGURE 3. *Specific volume of helium at 0° K.*

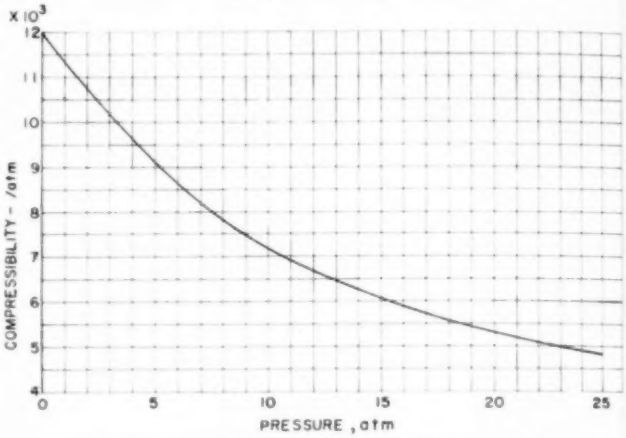

FIGURE 4. *Compressibility of helium at 0° K.*

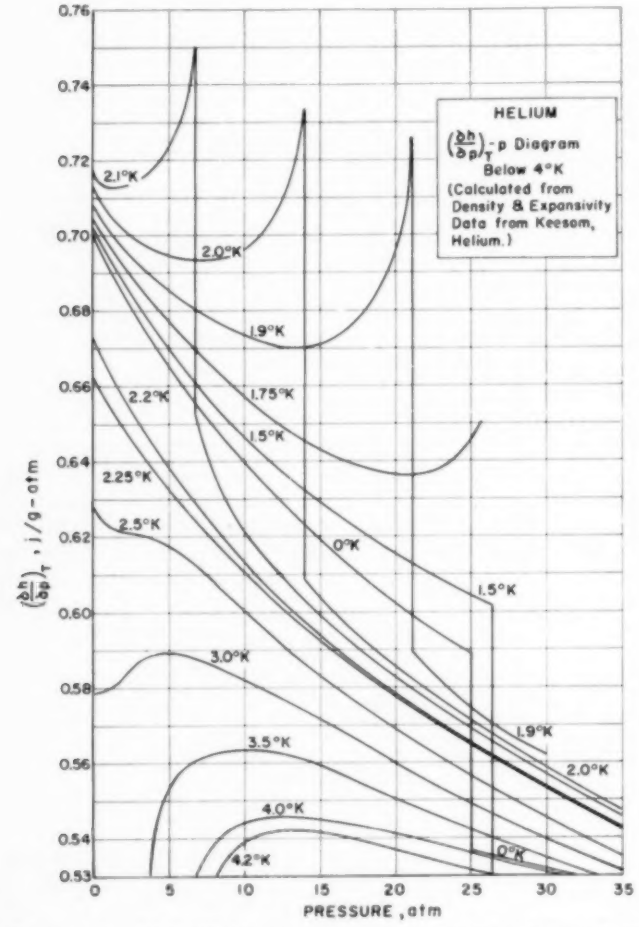

FIGURE 5. $[(\partial h)/(\partial p)]_T$ *versus pressure of helium below 4° K.*
Calculated from density and expansivity data from Keesom, helium.

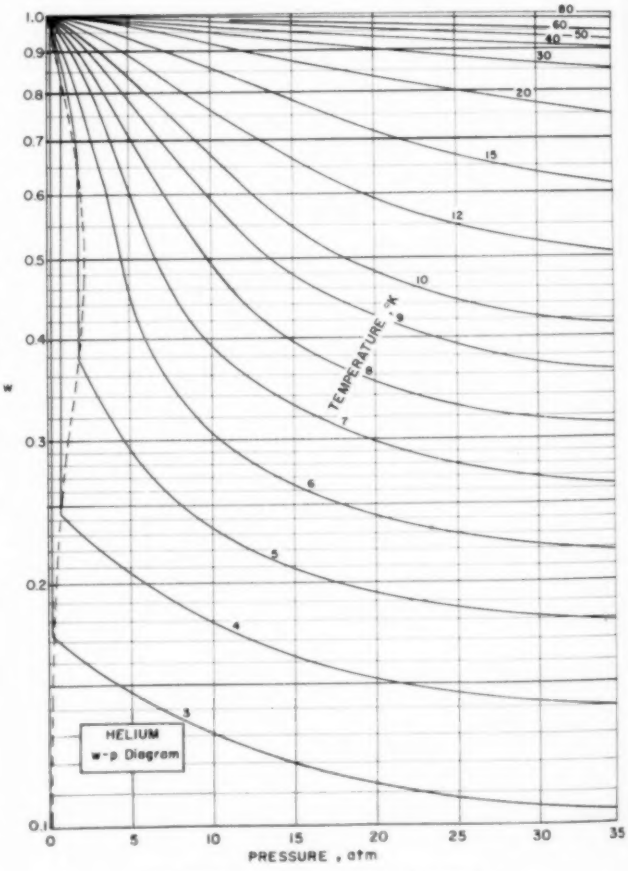

FIGURE 6. *Helium w-p diagram.*

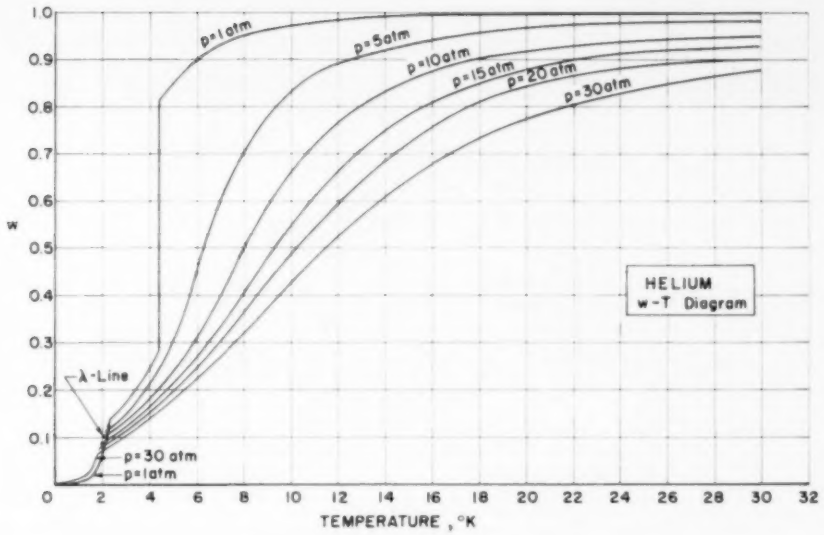

FIGURE 7. *Helium w-T diagram.*

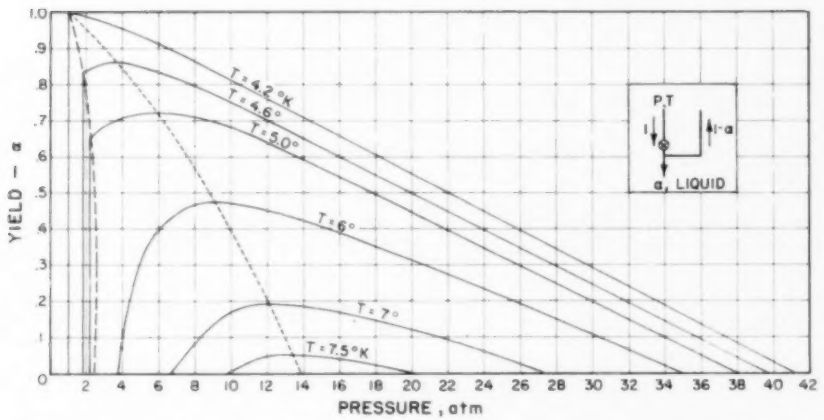

FIGURE 8. *Yield α as a function of pressure and temperature at the J-T valve.*

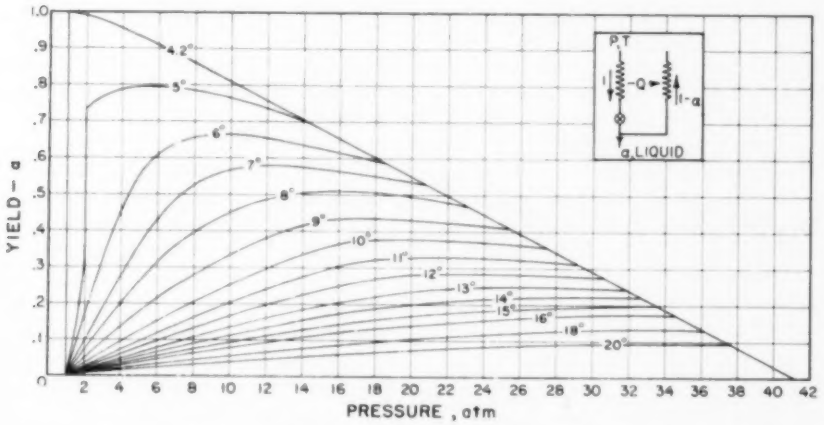

FIGURE 9. *Yield α with J-T heat exchanger efficiencies η equals 100 percent as a function of HP inlet temperature and pressure.*

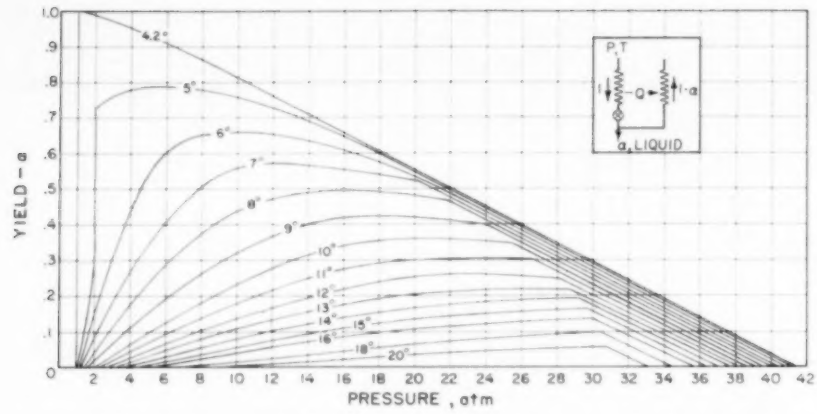

FIGURE 10. *Yield α with J-T heat exchanger efficiency η equals 95 percent as a function of HP inlet pressure and temperature.*

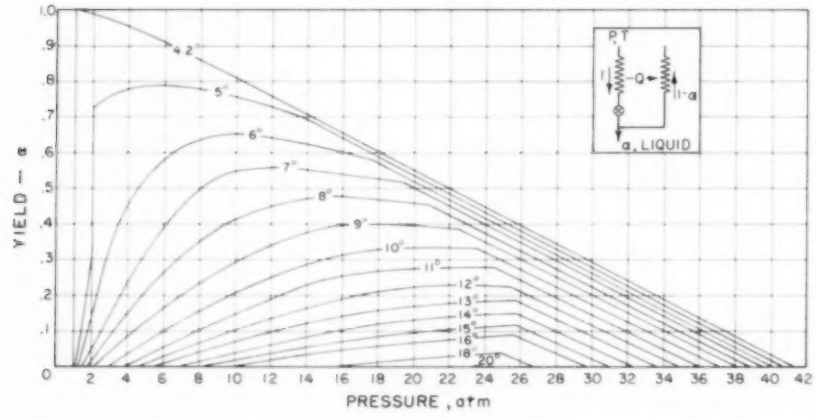

FIGURE 11. *Yield α with J-T heat exchanger efficiency η equals 90 percent as a function of HP inlet pressure and temperature.*

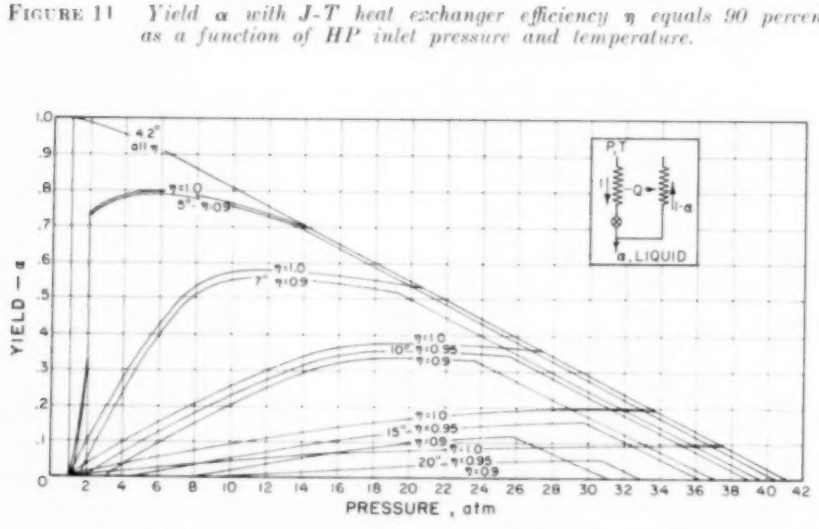

FIGURE 12. *Yield α for several heat exchanger efficiencies as a function of inlet temperature and pressure.*

BOULDER, COLO., August 30, 1957.

Journal of Research of the National Bureau of Standards Vol. 60, No. 3, March 1958 Research Paper 2835

Changes in the Properties of an Asphalt During the Blowing Operation

L. R. Kleinschmidt and H. R. Snoke

The physical characteristics and component distribution of an asphalt flux and of asphalt products taken at six two-hour intervals during the conversion, by air blowing, of the flux to a coating-grade asphalt, were determined. The softening point and asphaltene content of the asphalt products increased linearly with time during the blowing operation There was essentially no change in percentage, refractive index, and viscosity of the water-white oils during blowing. The percentage and refractive index of the dark oils decreased progressively during the blowing operation.

1. Introduction

The National Bureau of Standards, in cooperation with the Asphalt Roofing Industry Bureau, is engaged in the study of the constitution of asphalt and the mechanism of degradation of asphalt on weathering. A method has been published for the chromatographic separation of asphalt into groups of components [1].[1]

Asphalt fluxes are the residues from refinery processes that remove the lower-boiling fractions from petroleum. Asphalts used in the manufacture of roofings are made by blowing air through the fluxes at elevated temperatures. Normally, the softening point of the asphalt products is increased and the ductility and penetration decreased by blowing for longer periods of time.

As part of the study of the constitution and degradation of asphalt, it seemed desirable to determine the effect of the blowing process on the physical characteristics and component distribution of an asphalt to correlate any changes, if possible, with the mechanism of degradation.

2. Experimental Procedure

2.1. Materials and Methods

A 50-ton charge of a typical asphalt flux was blown at 375° to 400° F for a period of 11¾ hr, at the rate of 500 ft³ of air per minute. The laboratory examinations were carried out within 1 month after the blowing operation. The differences in the physical characteristics of the original flux and of the asphalt products removed at 2-hr intervals and the differences in the distribution and physical characteristics of similar components in these products were determined.

The following methods of the American Society for Testing Materials were used in determining the chemical and physical characteristics of the asphalt flux, asphalt products, and their components:

Softening point	D36–26
Penetration	D5–52
Ductility	D113–44
Viscosity	D445–53T
Sulfur	D129–52
Iodine number	D555–54
Coke residue	D168–30

Refractive indices of the oily constituents were determined with an Abbe-type refractometer for the wavelength of the sodium D line.

2.2. Separation Into Components

The asphalt components separated were those described in reference [1], namely, asphaltenes, asphaltic resins, water-white oils, and dark oils. Because the chromatographic method described in [1] did not provide specimens large enough for further work, the following method was substituted:

a. Asphaltenes

One hundred and fifty grams of the asphalt products were digested in 6 liters of *n*-pentane for 18 hr. The *n*-pentane was contained in a glass cylinder, 15 cm in diameter and 45 cm high, and the asphalt sample was suspended in a wire basket just under the surface of the *n*-pentane. The difference between the specific gravity of the asphalt (approximately 1) and the *n*-pentane (0.63) set up convection currents which facilitated greatly the extraction of the *n*-pentane soluble components. At the end of the digestion period the insoluble matter in the basket was transferred to a 2-liter beaker and digested with 1 liter of *n*-pentane for 1 hr, then transferred to a Buchner funnel and washed with *n*-pentane until the washings were light straw in color. This insoluble matter, designated as asphaltenes, was air-dried until free from the odor of *n*-pentane, heated at 212° F for 1 hr, cooled, and weighed.

b. Total Oily Constituents

The volume of the filtrate from the *n*-pentane insoluble was adjusted to contain approximately 45 ml of *n*-pentane for each gram of asphalt processed. To this solution 100- to 200-mesh fuller's earth was added, with rapid stirring, until the color

[1] Figures in brackets indicate the literature references at the end of this paper.

of the solution changed from a blackish-brown to a light yellowish-green. The more viscous (longer blown) asphalts required from 1 to 1½ g of fuller's earth for each gram of asphalt processed. This procedure has several advantages over that of Strieter [2] who used a fixed ratio [2] of fuller's earth to asphalt. It establishes a control for the quantity of fuller's earth; it gives a more definite separation between the groups of components, and it reduces greatly subsequent extraction operations.

The fuller's earth was recovered by filtration, using a Buchner funnel, transferred to extraction thimbles, and extracted in Soxhlet extractors for 10 hr with *n*-pentane, using a 6-min cycling rate. The filtrate and washings from the fuller's earth were combined with the Soxhlet extractions and the *n*-pentane was evaporated. The nonvolatile residue has been designated the total oily constituents.

c. Asphaltic Resins

The fuller's earth from the determination of total oily constituents was air dried and extracted with ethyl ether in Soxhlet extractors until the washings were colorless. The nonvolatile residue from the extract constituted the asphaltic resins.

d. Fractionation of Total Oily Constituents

The total oily constituents were fractionated into water-white and dark oils by a modification of the procedure described in reference [1], as follows:

e. Water-White Oils

A 15-g sample of the total oily constituents, dissolved in approximately 100 ml of *n*-pentane, was placed in a column containing 225 g of fuller's earth and eluted as described in [1]. The nonvolatile residue from the eluate has been designated water-white oils.

f. Dark Oils

The components adsorbed by the fuller's earth during the elution of the water-white oils were recovered by eluting with 50 ml of chloroform, followed by methyl ethyl ketone. The nonvolatile residue from this eluate has been designated dark oils.

3. Results

3.1. Physical Characteristics

The softening points, ductilities, and penetrations of the asphalt products taken at 2-hr intervals during the blowing operation are shown graphically in figures 1 to 3, inclusive. During the blowing operation the softening point increased linearly with time. Practically all of the change in ductility of the asphalt products occurred during the first 6 hr of blowing (fig. 2). Practically all of the change in penetration occurred during the first 8 hr of blowing (fig. 3).

[2] Five grams of fuller's earth to 1 g of asphalt.

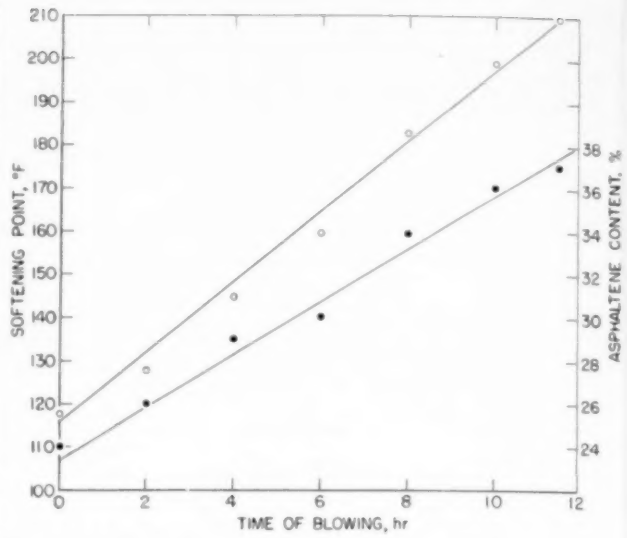

FIGURE 1. *Softening point and percentage asphaltenes of asphalt products.*

O, Softening point; ●, percent asphaltenes.

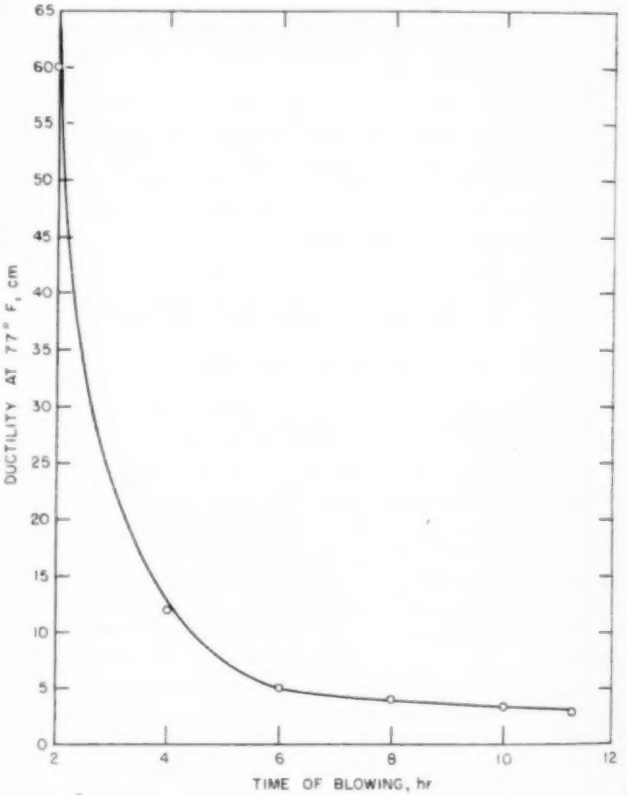

FIGURE 2. *Ductility of asphalt products.*

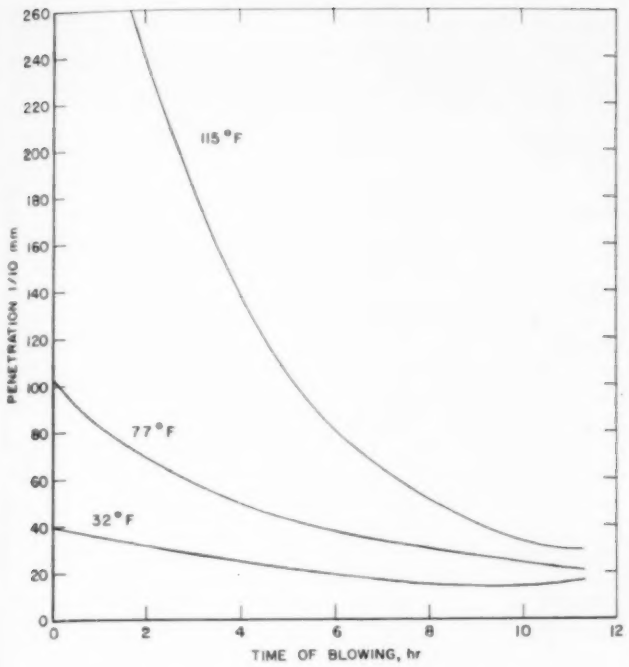

FIGURE 3. *Penetration of asphalt products.*

3.2. Component Distribution

The percentages of asphaltenes, asphaltic resins, and total oily constituents in the original flux and in the asphalt products are shown in table 1. The percentages of oily constituents and asphaltic resins decreased as blowing proceeded, while the percentage of asphaltenes recovered increased linearly with the time of blowing as shown in figure 1.

TABLE 1.—*Component distribution in asphalt products*

Time of blowing.....hr	0	2	4	6	8	10	11¾
Components:							
Asphaltenes.....%	24	26	29	30	34	36	37
Asphaltic resins.....%	17	15	14	14	13	13	13
Total oily constituents.....%	58	58	56	56	53	51	49
Total recovery.....%	99	99	99	100	100	100	99

The percentage of asphaltic resins decreased 2 percent during the first 2 hrs of blowing and only 2 percent during the remainder of the blowing operation. The precision of the asphaltic resin determination is ± 0.5 percent.

In table 2 are reported the percentages and some physical characteristics of the total oily constituents, water-white oils, and dark oils, recovered from the flux and the asphalt products. Changes that occurred in the percentages of the total oily constituents resulted primarily from changes of the dark oil components. These decreased from 32 to 24 percent during the blowing period. The following significant differences in the physical characteristics of the total oily constituents from the different products were observed: the refractive index decreased from 1.513 to 1.505 and the viscosity from 448 to 305 centistokes. The percentages, refractive indices, and viscosities of the water-white oils remained essentially constant during the blowing operation.

TABLE 2.—*Characteristics of oily constituents*

Time of blowing.....hr	0	2	4	6	8	10	11¾
Total oily constituents.....%	58	58	56	56	53	51	49
Refractive index at 100° F.	1.513	1.512	1.511	1.511	1.507	1.507	1.505
Viscosity at 140° F.....cs.	448	438	372	409	302	298	305
Water-white oils:							
Percentage [a]	24	26	26	26	28	26	25
Refractive index at 100° F.	1.488	1.487	1.488	1.488	1.487	1.487	1.488
Viscosity at 140° F.....cs.	109	109	110	110	112	111	109
Dark oils:							
Percentage [a]	32	31	29	30	25	24	24
Refractive index at 100° F.	1.543	1.540	1.538	1.540	1.543	1.536	1.536

[a] Calculated on asphalt products.

3.3. Coke Residue

In table 3 are reported the coke residues determined on asphalt products, asphaltenes, and several of the total oily constituents and asphaltic resins. The percentage of coke residue of the asphaltenes, of the asphaltic resins, and of the total oily constituents differed greatly. Although the conversion of the flux into an asphalt product having a softening point of 210° F increased the asphaltenes 24 to 37 percent, the coke residue of the asphaltenes remained essentially the same. If the increase in the asphaltenes was due to an adsorption of the maltenes,[3] marked changes occurred in the structure of the adsorbed maltenes. Physical adsorption alone would have resulted in a progressively lower coke residue of the asphaltenes as blowing progressed.

The percentages of coke residue in the asphalt products increased progressively during the blowing operation and approximately linearly with the asphaltene content of the asphalt products as shown in figure 4.

TABLE 3. *Coke residue of asphalt products and components*

Time of blowing	Coke residue				
	Asphaltenes	Asphaltic resins	Total oily constituents	Asphalt products	
				Determined	Calculated
Hours	%	%	%	%	%
0	39.5	12.2	0.8	12.0	12.0
2	38.5	.....	.....	12.5	.....
4	37.1	.....	.....	12.9	.....
6	38.4	.....	.....	13.4	.....
8	37.6	11.3	0.3	14.4	14.3
10	37.4	.....	.....	15.0	.....
11¾	38.2	12.4	0.5	15.9	16.1

[3] The *n*-pentane soluble constituents of asphalt.

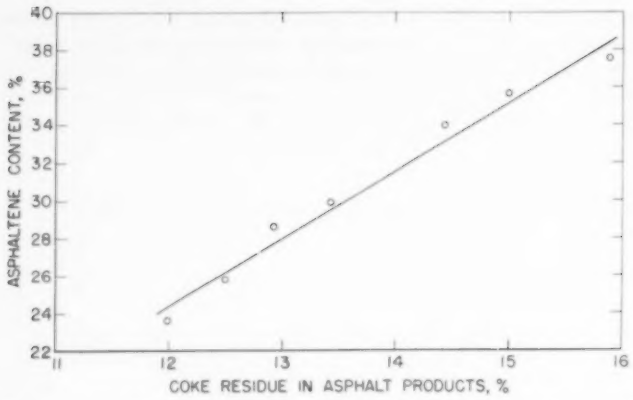

FIGURE 4. *Relationship between asphaltene formation and coke residue.*

3.4. Iodine Value and Sulfur Content

In table 4 are reported the iodine values and the percentages of sulfur determined in the flux and in the asphalt product blown 11¾ hr. Also reported in this table are similar determinations made on the asphaltenes, asphaltic resins, and water-white and dark oils derived from these products. The slight differences in the iodine value, between the flux and the blown product and of the components separated from these two materials showed that no marked changes occurred in the halogen reactivity of the flux during blowing.

The sulfur content of the flux and of the asphalt product blown 11¾ hr were the same (2.0%), showing that no sulfur was lost during the blowing operation. The differences in the sulfur content of the asphaltenes, asphaltic resins, water-white oils, and dark oils determined in the flux and the product blown 11¾ hr were of such small magnitude that it was apparent the sulfur content could not be used to determine changes in components during the blowing operation.

TABLE 4. *Iodine value and percentage sulfur—flux and asphalt product blown 11¾ hours*

Material	Iodine value[a]		Sulfur	
	Asphalt flux	11¾ hr asphalt product	Asphalt flux	11¾ hr asphalt product
			%	%
Asphalt	49	41	2.0	2.0
Asphaltenes	51	53	3.0	3.8
Asphaltic resins	48	45	2.4	2.3
Water-white oils	10	8	0.2	0.2
Dark oils	42	39	2.4	2.3

[a] Centigrams of iodine combining with 1 g of material.

4. Summary

During the conversion of a 50-ton charge of asphalt flux to produce asphalt products with properties suitable for use in roofing, samples were taken at 2-hr intervals during the blowing operation which was carried out at 375° to 400° F for 11¾ hr. The distribution of the components in the flux and in the asphalt products and the properties of the flux, products and components were determined as part of a study of the constitution and degradation of asphalt.

The softening point of the asphalt products increased linearly from 118° to 210° F during the blowing operation. The penetration and ductility decreased rapidly during the first 6 hr of blowing and relatively little thereafter.

The asphaltene content of the asphalt products increased linearly with the time of blowing. The percentage of coke residue from the asphaltenes of the different products remained essentially constant, indicating that polymerization occurred in the adsorbed maltenes. The mechanism by which the asphaltenes were formed was not established. No changes were found in the percentage or physical characteristics of the water-white oils in samples taken during the blowing operation.

The close agreement between the iodine values of the asphalt flux and the final blown product indicated no marked change in halogen reactivity during the blowing operations.

The authors are indebted to George W. Clarvoe, Asphalt Research, Johns-Manville Corporation, who furnished the specimens for this investigation.

5. References

[1] L. R. Kleinschmidt, J. Research NBS **54,** 163, (1955) RP2577.
[2] O. G. Strieter, J. Research NBS **26,** 415, (1941) RP1387.

WASHINGTON, September 10, 1957

Journal of Research of the National Bureau of Standards Vol. 60, No. 3, March 1958 Research Paper 2836

Creep of Annealed Nickel, Copper, and Two Nickel-Copper Alloys

William D. Jenkins and Carl R. Johnson

Creep tests were made in tension under constant loads at temperatures of 300°, 700°, and 900° F on initially annealed specimens of nickel, copper, and 70-percent-nickel–30-percent-copper and 30-percent-nickel–70-percent-copper alloys. Tests at 1,200° F were also made on the nickel and the two alloys, but not on the annealed copper as the resistance to creep of copper is relatively low at this temperature. The investigation included a study of the influence of rate of loading on the creep stress and of prior thermal-mechanical history on the creep behavior of the alloys at several selected temperatures. Contour and hardness surveys and metallographic examinations were also carried out on some of the fractured specimens to ascertain the effect of creep on the necking characteristics, hardnesses, and structures of the metals.

1. Introduction

The effects of temperature on the short-time tensile and some other properties of the same lots of nickel, copper, and nickel-copper alloys initially in the annealed and cold-drawn condition were discussed in previous publications [1 to 7].[1] Parker and Hazlett [8] made a comprehensive survey of the literature on the principles of solution hardening in relation to the tensile properties of nickel-copper alloys. Hazlett and Hansen [9] showed that the shape of the creep curves for nickel extended in tension was markedly altered by either prestraining or alloying. French and Hibbard [10] discussed the changes in lattice parameters and mechanical properties of copper introduced by alloying with nickel.

According to Barrett [11] nickel and copper form a continuous series of substitutional solid solutions. All alloys of the system consist of a face-centered-cubic lattice with copper and nickel atoms distributed at random on the lattice points. Nickel has nearly the same atomic size as copper and the presence of nickel atoms alter only slightly the copper lattice. However, Averbach [12] pointed out that recent researches show that solid solutions are not random; that the atoms are displaced from their lattice sites; and that the atoms neither retain their pure metal sizes nor assume the average size calculated from the alloy lattice parameter. There is considerable uncertainty concerning the role of strain energy in solutions containing atoms of disparate sizes; the solutions, however, may be randomized by plastic flow.

The present study was made of the creep characteristics of nickel, copper, and two alloys of these metals as a part of a comprehensive investigation designed to evaluate the rheological properties of samples of these metals at temperatures ranging from −320° to +1,700° F. Special attention was directed towards an evaluation of the resistance to creep of the alloys in relation to that of the component metals.

2. Metals, Apparatus, and Procedure

The chemical composition and average grain size of the metals used in this investigation are shown in table 1. All the bars of each metal were processed from a single heat. The creep specimens of each metal were machined from one annealed bar to an 0.505-in. diameter over a 2-in. gage length. The preparation of the specimens and the apparatus used were described previously [1]. Essentially, each creep specimen was heated in air to the desired temperature and held at temperature 48 hr before loading. Load increments, each equivalent to a stress value of 5,333 lb/in.^{2}, were applied at 1-hr intervals (hereafter designated as the "standard" rate of loading) until the desired stress was attained. This standard loading procedure was modified in those tests made to determine the influence of prior-strain history on the subsequent creep behavior. The prior history and procedures used in this series of experiments are described in tables 5 and 6.

[1] Figures in brackets indicate the literature reference at the end of this paper.

TABLE 1. *Chemical composition (percentage by weight) of the metals and alloys used as determined by chemical, spectrochemical, and vacuum fusion analyses*

Metal	C	Cu	Ni	Co	Fe	Mn	Si	S	Zn	O_2	N_2	H_2	Average [c] grain diameter
													mm
Copper [a] (OFHC)	.....	99.99+	.....	.....	.....	.....	.....	.....	.....	.....	.....	.....	0.025
30%-Ni–70%-Cu	0.023	68.84	29.89	0.04	0.50	0.65	0.003	0.004	0.09	0.001	0.001	0.0002	.040
70%-Ni–30%-Cu	.017	29.71	70.08	[b]	.01	.01	.12	.002	----	.001	.0015	.0003	.025
Nickel	.007	0.009	99.85	[b]	.04	.03	.11	.002	----	.002	.001	.0002	.045

[a] The arc spectrum of the copper was examined for the sensitive lines of Ag, Al, B, Be, Co, Fe, In, Ir, Mg, Mo, Na, Ni, Pb, Sb, Si, Sn, Ti, V, and Zn. The lines for Ag, Al, Mg, and Si were identified and there was some indication of the presence of Fe, Ni, and Pb.
[b] Not detected.
[c] Values obtained on specimens prepared from the annealed bars.

The temperatures of the creep furnaces were controlled within ±1° F of the desired temperatures over the specimen length and the probable error in measuring the extensions was less than 0.00002 in. Specimen contours were determined by measuring the diameter of the specimens at various distances from a fractured end. Rockwell hardness determinations were made along the longitudinal axis of specimens prepared by the usual procedures for making these measurements [1].

3. Results and Discussion

The results of creep tests made on specimens loaded at the standard rate are summarized in figures 1 to 20, and in tables 2, 3, and 4. Data obtained on specimens tested to determine the effect of prior-strain history on the creep properties are presented in figures 21 to 27 and in tables 5 and 6. Values for the copper at 110° and 300° F and for the nickel are not tabulated, as they were presented previously [1, 2, and 5].

3.1. Influence of Temperature and Stress on Creep Behavior of Specimens Loaded at the Standard Rate

a. Stress-Strain Relations During Loading

The effect of temperature on the stress-strain relations during loading is shown in figure 1. At each temperature, the general shape of the family of curves show that, after the start of deformation, the incremental changes of strain increased with each successive increment of stress. These values also increased with an increase in temperature. Thus, it is apparent that the strain hardening becomes less pronounced as the temperature is raised.

At each of the temperatures and at equal strains the strengths of the alloys were greater than those of the component metals. Furthermore, the differences in the rate of strain hardening between the component metals and the alloys were strongly dependent on temperature. A strengthening effect due to small strains associated with alloying the component materials has been described by Fisher [13].

b. Effect of Temperature and Composition on Strain-Time and Creep Rate-Strain Relations

The shape of the creep curves for all the specimens used in this investigation was, with a few exceptions, similar to those shown previously for copper [1, 2] and nickel [5].

Some of the strain-time curves of specimens of different compositions tested under identical conditions at 700°, 900°, and 1,200° F are shown in figures 2, 3, and 4. Due to differences in strengths of the metals, no identical tests were run at 300° F. It is apparent that the resistance to deformation (fig. 2) of the alloys was greater than that of the pure nickel. Furthermore, the alloy containing 30 percent of copper was more creep resistant at all values of time than the alloy containing 70 percent of copper. Other examples of the effect of alloying the nickel with 70 percent of copper are shown in figure 3 for specimens tested at 700° and 900° F. These data indicate that the strengthening effects due to alloying are more pronounced as the time at stress is

TABLE 2. *Summary of conditions used and results of creep tests on 70-percent-nickel–30-percent-copper alloy, initially as annealed*

Test			Plastic strain			Beginning of third stage			End of test					
Number	Temperature	Creep stress	1 hr after application of load	Intercept	Average creep rate, second stage	Time	Plastic strain	True stress	Time	Plastic strain or elongation	Contraction of area or reduction of area	$\log_e(A_0/A)$ at fracture	True stress	Remarks
	°F	lb/in.²	Percent	Percent	%/1,000 hr.	hr	Percent	lb/in.²	hr	Percent	Percent		lb/in.²	
B–11	300	56,030	15.73	16.04	0	.....	.....	.....	2,202	16.04	13.9	.....	65,000	Test stopped in second stage.
B–12	300	58,670	20.28	20.37	0	.....	.....	.....	1,699	20.37	17.0	.....	70,600	Do.
B–15	300	61,000	27.03	27.1	0.006	.....	.....	.....	2,036	27.11	21.3	.....	77,500	Do.
B–17	300	61,840	27.59	27.61	0	.....	.....	.....	1,871	27.61	21.6	.....	78,900	Do.
B–18	300	62,500	.....	30.75	220,000	0.03	39.5	87,200	0.043	55.5	85.4	1.925	427,000	Tested to complete fracture.
B–1	700	37,330	3.97	5.83	0.12	.....	.....	.....	5,034	6.45	6.1	.....	39,800	Test stopped in second stage.
B–6	700	42,670	6.74	8.27	.52	.....	.....	.....	3,357	10.39	9.4	.....	47,100	Do.
B–9	700	48,000	10.18	16.22	1.09	.....	.....	.....	3,051	19.61	16.4	.....	57,400	Do.
B–13	700	56,030	21.20	21.14	59.0	5.1	21.6	68,100	243	60.5	74.2	1.356	217,300	Tested to complete fracture.
B–14	900	18,670	0.26	0.523	0.61	.....	.....	.....	2,468	2.23	2.15	.....	19,100	Test stopped in second stage.
B–4	900	21,330	.31	1.32	1.4	2,200	4.4	22,300	9,927	53	48.6	0.666	41,500	Tested to complete fracture.
B–2	900	26,670	2.11	3.90	11.1	.....	.....	.....	408	8.42	7.8	.....	28,900	Test stopped in second stage.
B–7	900	28,000	3.02	5.75	14.3	650	15.0	32,200	1,696	54.5	45.3	.604	51,200	Tested to complete fracture.
B–10	900	32,000	5.03	8.5	51.8	315	24.5	39,800	480	56.5	47.3	.641	60,800	Do.
B–16	1,200	2,665	0	0.70	0.34	.....	.....	.....	1,414.5	1.18	1.16	.....	2,700	Test stopped in second stage.
B–8	1,200	5,330	0.09	5.07	6.6	2,200	19.6	5,800	4,048	43.5	31.7	.381	7,800	Tested to complete fracture.
B–5	1,200	8,000	.186	0.18	41	68	2.9	8,200	643	61.5	47.9	.651	15,300	Do.
B–3	1,200	10,670	.256	.12	125	23	3.0	11,000	165	61.3	54.6	.790	23,500	Do.

TABLE 3. *Summary of conditions used and results of creep tests on 30-percent-nickel–70-percent-copper alloy, initially as annealed*

Test			Plastic strain			Beginning of third stage			End of test					Remarks
Number	Temperature	Creep stress	1 hr after application of load	Intercept	Average creep rate, second stage	Time	Plastic strain	True stress	Time	Plastic strain or elongation	Contraction of area or reduction of area	$\log_e (A_0/A)$ at fracture	True stress	
	° F	*lb/in.²*	*Percent*	*Percent*	*%/1,000 hr.*	*hr*	*Percent*	*lb/in.²*	*hr*	*Percent*	*Percent*		*lb/in.²*	
C-24	300	37,330	7.71	7.74	0				1,507	7.74	7.2		40,200	Test stopped in second stage.
C-6	300	42,670	13.07	13.16	0				2,370	13.16	11.7		48,300	Do.
C-11	300	46,000	19.69	19.84	0				2,182	19.84	16.5		55,200	Do.
C-15	300	47,000	20.18	20.42	0				2,340	20.42	16.9		56,600	Do.
C-23	300	47,200	20.6	20.7	0				1,484	20.7	17.2		57,000	Do.
C-22	300	47,370	23.57	23.45	510				13	39.5	23.4		61,800	Do.
C-26	300	47,650	47.0	23.1	6000	0.67	27.1	60,600	1	47.0	80.1	1.612	238,900	Tested to complete fracture.
C-19	700	26,670	3.58	6.43	0.27				3,330	7.73	6.8		28,600	Test stopped in second stage.
C-4	700	32,000	6.39	11.35	3.63	4,020	26	40,300	5,346	46.0	51.7	0.728	66,300	Tested to complete fracture.
C-20	700	34,670	8.49	15.2	33.3	490	31.5	45,600	692	56.0	65.0	1.045	98,600	Do.
C-10	700	37,330	11.92	16.0	83.0	200	32.6	49,500	250	53.0	66.5	1.092	111,300	Do.
C-16	700	40,000	15.13	18.0	290	35	28.2	51,300	56	59.5	71.5	1.253	140,000	Do.
C-21	900	10,670	0.034	0.11	0.19				2,345	0.57	0.57		10,700	Test stopped in second stage.
C-17	900	13,335	.21	.8	2.1	1,800	4.6	13,900	3,860	10.12	9.2		14,700	Test stopped in third stage.
C-14	900	16,000	.91	2.6	2.6	1,310	6.0	17,000	6,864	49.0	49.2	0.513	26,700	Tested to complete fracture.
C-8	900	18,670	1.03	2.3	9.5	1,300	14.7	21,400	2,752	49.0	44.5	0.590	33,700	Do.
C-7	900	21,330	3.58	6.6	73.6	220	22.8	26,200	344	61.0	52.5	0.744	44,900	Do.
C-18	900	24,000	6.32	9.2	286	55	26.0	30,200	97	72.0	66.5	1.088	71,300	Do.
C-25	1,200	1,450	0.03	0.15	1.54				1,439	2.37	2.3		1,500	Test stopped in second stage.
C-13	1,200	1,700	0.13	.29	2.2	795	2	1,750	5,206	10.22	9.3		1,900	Test stopped in third stage.
C-9	1,200	2,665	.07	.34	4.9	860	4.6	2,800	944	5.3	5.0		2,800	Do.
C-5	1,200	5,330	.10	.03	58	45	2.65	5,470	215	23	23.2	0.265	6,950	Tested to complete fracture.
C-12	1,200	8,000	.66	.22	425	1.2	0.75	8,000	29	28	28.6	0.336	11,200	Do.

TABLE 4. *Summary of conditions used and results of creep tests on copper, initially as annealed*

Test			Plastic strain			Beginning of third stage			End of test					Remarks
Number	Temperature	Creep stress	1 hr after application of load	Intercept at zero time	Average creep rate, second stage	Time	Plastic strain	True stress	Time	Elongation	Reduction of area	Log ε (A_0/A) at fracture	True stress	
	° F	*lb/in.²*	*Percent*	*Percent*	*%/1000 hr*	*hr*	*Percent*	*lb/in.²*	*hr*	*Percent*	*Percent*		*lb/in.²*	
25	700	2,100	0.02	0.06	2.43	450	1.15	2,100	1,485	11	6.0	0.06	2,250	Tested to complete fracture.
34	700	2,765	.07	.14	5.04	400	2.23	2,850	797	11	6.9	0.07	2,950	Do.
31	700	5,330	1.08	1.11	77	15	2.25	5,450	62.5	11	8.8	0.09	5,850	Do.
30	700	10,670	10.52	6.32	4,200	1.5	12.7	12,000	2.4	25.5	21.3	0.24	13,600	Do.
27	900	725	0.02	0.02	2.4	610	1.5	750	2,806	21	13.1	0.14	850	Do.
33	900	1,450	.04	.05	9	140	1.3	1,500	452	15	8.9	0.09	1,600	Do.
35	900	2,100	.20	.21	39.6	30	1.4	2,150	119	12.5	9.5	0.10	2,300	Do.
32	900	2,755	.41	.6	80	6.5	1.17	2,800	39	14	10.3	0.11	3,100	Do.

increased and as the temperature is decreased. These observations agree with the results obtained on specimens of the two alloys tested at 700° or 1,200° F (fig. 4). If the strengthening effects associated with alloying were due wholly to the lattice distortion or short-order arrangements, then it appears that the magnitude of these differences would not be as great. Apparently, some additional mechanism is partly responsible for this behavior. Cottrell [14] describes a process of this type and relates the properties found in substitutional solid solution alloys to the relative degree of interaction of moving dislocations with moving solute atoms. The solute atoms may act as barriers to the motion of dislocations. The Cottrell theory accounts for the alternating of dislocations between slow and fast motions and may be applied to the serrated creep rate-strain curves shown in figures 5 and 6. An additional prediction in this theory based on the creation of vacancies during straining at constant load, is that these curves (figs. 5 and 6) should be at first rather smooth, should become serrated as the strain is increased, and, at large strains, should again be comparatively smooth. An inspection of these data reveals that these effects do occur. Moreover, it appears that increasing the temperature from 900° to 1,200° F, increasing the stress at constant temperature, or increasing the copper content of the alloys tends to decrease the magnitude of the serrations.

It was not possible to deduce a simple mathe-

TABLE 5. *Effect of prior-strain history on creep of 70-percent-nickel–30-percent-copper alloy at 700°, 900°, and 1,200° F*

Test			Creep stress	Plastic strain		Average creep rate, second stage	Beginning of third stage			End of test				Remarks
Number	Temperature	Prior history		1 hr. after application of load	Intercept		Time	Plastic strain	True stress	Time	Plasic strain or elongation	Contraction of area or reduction of area	True stress	
	° F		*lb/in.²*	*% in 2 in.*	*% in 2 in.*	*%/1,000 hr*	*hr*	*% in 2 in.*	*lb/in.²*	*hr*	*% in 2 in.*	*Percent*	*lb/in.²*	
B–1	700	Loaded 5,333 lb/in.² hr to 37,330 lb/in.² at 700° F; stress changed to 42,670 lb/in.² after 5,034 hr.	42,670	8.44	8.9	0.52	.....	.....	.....	1,511	9.74	8.9	46,800	Test stopped in second stage.
B–1	700	Same specimen as B–1 (above). Stress changed to 48,000 lb/in.² after 1,511 hr.	48,000	12.47	15	.99	.....	.....	.....	5,796	20.76	17.2	58,000	Do.
B–6	700	Loaded 5,333 lb/in.² hr at 700° F to 42,670 lb/in.². Stress changed to 48,000 after 3,357 hr.	48,000	12.54	12.9	1.75	.....	.....	.....	1,700	16.25	13.9	55,800	Do.
B–1	700	Same specimen as B–1 (above). Stress changed to 56,030 lb/in.² after 5,796 hr at 48,000 lb/in.² and 1 hr at 53,330 lb/in.²	56,030	27.26	27.2	52	35	29	72,300	165	56	61.8	146,600	Tested to complete fracture.
B–6	700	Same specimen as B–6 (above). Stress changed to 56,030 lb/in.² after 1,700 hr at 48,000 lb/in.² and 1 hr at 53,330 lb/in.²	56,030	22.61	22.0	74.5	122	31.1	73,500	235.5	66	65.8	163,800	Do.
B–14	900	Loaded 5,333 lb/in.² hr at 900° F to 18,670 lb/in.². Unloaded after 2,468 hr and temperature held at 900° F. Reloaded (after 216 hr) 5,333 lb/in.² hr to 21,330 lb/in.²	21,330	2.26	2.46	1.64	.....	.....	.....	1,259.3	4.47	4.3	22,300	Test stopped in second stage.
B–14	900	Same specimen as B–14 (above). Stress changed to 28,000 lb/in.² after 1,259 hr at 21,330 lb/in.² and 1 hr at 26,670 lb/in.²	28,000	5.46	6.8	11.8	1,150	20.6	33,800	2,133	58	43.2	49,300	Tested to complete fracture.
B–9	900	Loaded 5,333 lb/in.² hr to 48,000 lb/in.² at 700° F. Unloaded after 3,051 hr. Temperature raised to 900° F; loaded 5,333 lb/in.² hr to 28,000 lb/in.²	28,000	19.48	18.6	19	540	28.8	36,100	847.5	48	38.1	45,200	Do.
B–16	900	Loaded instantaneously to 2,665 lb/in.² at 1,200° F; load removed and temperature changed to 900° F after 1,414.5 hr; loaded 5,333 lb/in.² hr to 28,000 lb/in.²	28,000	9.32	14.1	42.6	220	23.5	34,600	499	63	70.9	96,100	Do.
B–17	900	Loaded 5,333 lb/in.² hr to 61,840 lb/in.² at 300° F; load removed and temperature changed to 900° F after 1,871 hr; loaded 5,333 lb/in.² hr to 28,000 lb/in.²	28,000	27.65	27.6	17	250	32	37,000	762.5	56.5	52.4	58,900	Do.
B–2	1,200	Loaded 5,333 lb/in.² hr to 26,670 lb/in.² at 900° F; load removed; temperature raised to 1,200° F; reloaded in 2 increments (5,333 and 2,667 lb/in.²) to 8,000 lb/in.²	8,000	10.8	11.15	27.2	210	16.9	9,350	375.3	27	21.3	10,200	Do.

matical formula for describing the complete strain-time curves. This observation is attributed to the fact that adequate parameters have not been determined for describing the complex structural changes that occur during the different stages of creep. Therefore, it was considered to be more fruitful to tabulate the data, as in tables 2, 3, and 4, and then to analyze separately the data as applied to each of the various stages.

c. First Stage of Creep

The nature of the strain-time curve during the first stage (flow at a decelerating rate) has resulted in a number of mathematical analyses of this stage of the creep process. In general, a period of decreasing creep rate with increasing time was obtained in specimens used in this investigation. Several of the specimens used indicated the existence of an incubation period similar to those shown previously for some specimens of initially annealed nickel at 300° F [5]. The existence of this period in the alloys is also partly attributed to the magnitude of the final applied stress.

Probably the most complete analysis of the creep curves has been made by Andrade [15] who indicated that his data could be described by the equation:

$$l = l_0(1 + Bt^{1/3})e^{Kt}$$

TABLE 6. *Effect of prior-strain history on creep of 30-percent-nickel–70-percent-copper alloy, initially as annealed*

Test			Creep stress	Plastic strain		Average creep rate, second stage	Beginning of third stage			End of test			
Number	Temperature	Prior-strain history		1 hr after application of load	Intercept zero time		Time	Plastic strain	True stress	Time	Elongation	Reduction of area	True stress
	°F		lb/in.²	Percent	Percent	%/1,000 hr	hr	Percent	lb/in.²	hr	Percent	Percent	lb/in.²
C-6	300	Loaded 5,333 lb/in.² hr to 42,670 lb/in.² Stress changed to 46,000 lb/in.² after 2,370 hr; to 47,000 lb/in.² after 3,499 hr; to 47,900 lb/in.² after 4,318 hr at 300° F.	47,900	20.54						10	49.5	80.6	246,500
C-11	300	Loaded 5,333 lb/in.² hr to 46,000 lb/in.² Stress changed to 47,900 lb/in.² after 2,182 hr at 300° F.	47,900	19.82						10	46.5	80.7	248,100
C-15	300	Loaded 5,333 lb/in.² hr to 47,000 lb/in.² Stress changed to 47,900 lb/in.² after 2,340 hr; to 48,440 lb/in.² after 3,373 hr; to 48,980 lb/in.² after 4,693 hr at 300° F.	48,980	20.42						1.5	47.5	80.2	247,500
C-24	900	Loaded 5,333 lb/in.² hr to 37,330 lb/in.² at 300° F; unloaded after 1,707 hr; temperature changed to 900° F; loaded 5,333 lb/in.² hr to 18,670 lb/in.² at 900° F.	18,670	7.80	7.6	18	600	18.2	22,100	1,123	52	56	42,600
C-23	900	Loaded 5,333 lb/in.² hr to 47,200 lb/in.² at 300° F.; unloaded after 1,484 hr; temperature changed to 900° F, loaded 5,333 lb/in.² hr to 18,670 lb/in.² at 900° F.	18,670	21.04	20.9	19.2	260	26	23,500	696	78	63	49,800
C-19	900	Loaded 5,333 lb/in.² hr to 26,670 lb/in.² at 700° F, unloaded after 3,330 hr; temperature changed to 900° F; loaded 5,333 lb/in.² hr to 18,670 lb/in.² at 900° F.	18,670	7.36	7.1	21.5	600	20	22,400	1,065	51	49.5	37,000
C-21	900	Loaded 5,333 lb/in.² hr to 10,670 lb/in.² at 900° F; stress changed to 18,670 lb/in.² (2 increments) after 2,345 hr at temperature under stress.	18,670	1.56	4.5	11.6	730	12	20,900	1,214	40	45	34,000
C-17	900	Loaded 5,333 lb/in.² hr to 13,335 lb/in.² at 900° F; stress changed to 18,670 lb/in.² (1 increment) after 3,830 hr at temperature under stress.	18,670	10.6	11	57	210	23	23,000	342	48	51	38,000
C-25	900	Load corresponding to a stress of 1,470 lb/in.² applied instantaneously at 1,200° F; unloaded after 1,439 hr; temperature changed to 900° F; loaded 5,333 lb/in.² hr to 18,670 lb/in.² at 900° F.	18,670	6.4	9.7	60	267	25.5	23,400	380	55	50.5	37,800
C-13	900	Load corresponding to a stress of 1,700 lb/in.² applied instantaneously at 1,200° F.; unloaded after 5,205 hr; temperature changed to 900° F; loaded 5,333 lb/in.² hr to 18,670 lb/in.² at 900° F.	18,670	18.3	18.15	905	13.5	30.3	24,300	18	41	43	33,000

Where l is the length of the specimen at time, t, and l_0, B, and K are constants. The term, $Bt^{\frac{1}{3}}$, was considered as representative of transient creep (essentially first stage) and the term, Kt, represented the steady-state component (second stage of creep). If no steady-state component exists then K would equal 0 and

$$l=l_0(1+Bt^{\frac{1}{3}})$$

or

$$\frac{dl}{dt}=1/3l_0Bt^{-\frac{2}{3}}$$

whence

$$\log \dot{e}=-2/3 \log t+C_1$$

where

$$\dot{e}=\frac{1}{l_0}\frac{dl}{dt}=\text{creep rate.}$$

With the exception of the data for several specimens, previously mentioned, a linear relation was obtained when the logarithm of the creep rate was plotted against the logarithm of the time during the first stage of creep. The relations between the slopes of the curves and the initially applied creep stresses are shown in figures 7A and 8. It is apparent that transient creep, as described by Andrade, did not exist as the slopes are dependent on stress, temperature, and nickel content. Obviously, the slopes are displaced to higher values (fig. 7A) as the temperatures are increased. No general trend was observed to describe the influence of alloying the nickel with copper (fig. 8).

The modified exhaustion theory of Davis and Thompson [16] is described by the equation

$$\log(t\dot{e})=A+B\log e$$

where t=time, e=creep rate, and e=strain. Attempts were made to apply this formula to the data obtained for the 70-percent-Ni–30-percent-Cu alloy. However, the agreement was not as good as that previously recorded for nickel [5] as shown by the curves in figures 7B and 9. The values for the slopes in this analysis should be between $+1$ and $-\frac{1}{2}$. The effect of stress on the values of the slopes, for the 70-percent-Ni–30-percent-Cu alloy is shown in figure 7B, and the influence of alloying the nickel

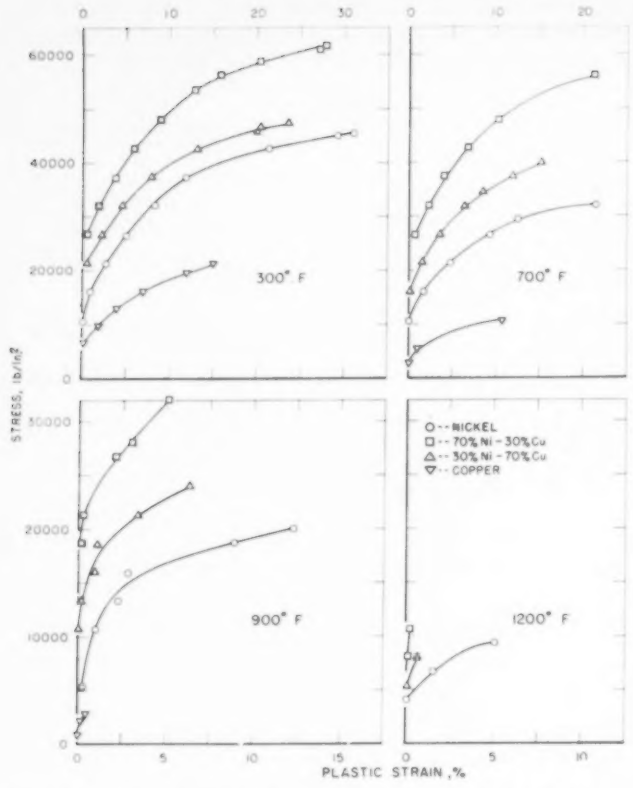

FIGURE 1. *Stress-strain relations of specimens tested at different temperatures.*

The strain values shown were those measured 1 hr after application of the corresponding stress.

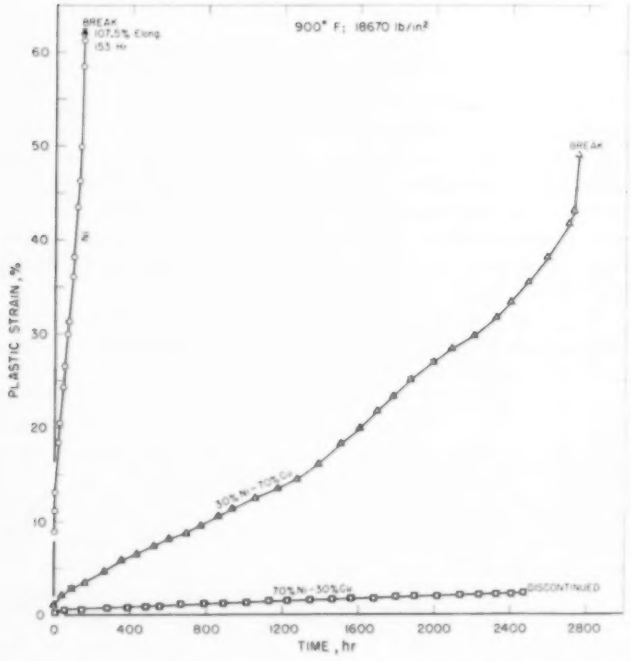

FIGURE 2. *Strain-time relations of specimens tested at 900° F with a stress of 18,670 lb/in².*

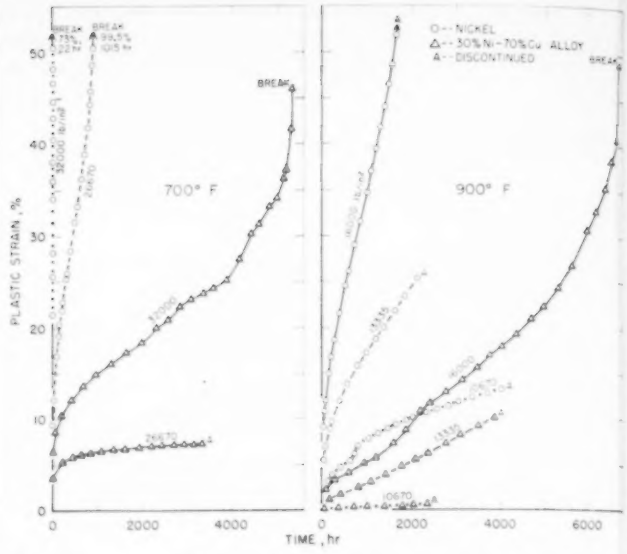

FIGURE 3. *Strain-time relations of specimens tested at 700° a 900° F.*

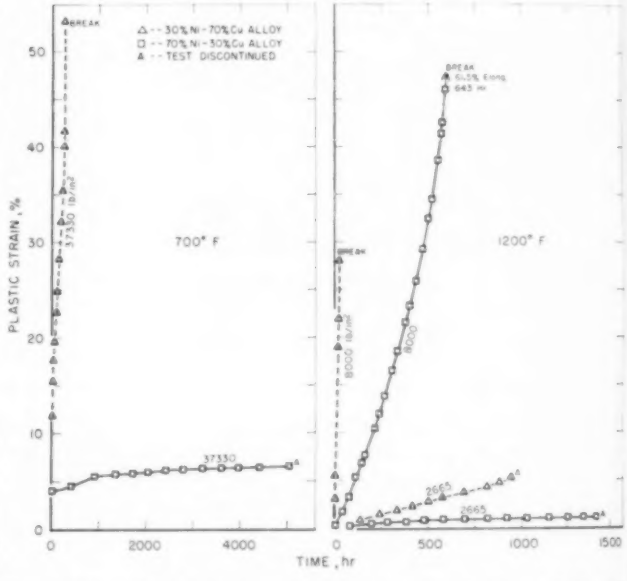

FIGURE 4. *Strain-time relations for two specimens of* Cu-Ni *alloys tested at 700° or 1,200° F with different stresses.*

with 30 percent of copper is shown by the data reproduced in figure 9. For the alloy (fig. 7B), it appears that the slopes increase with increasing temperature (stress constant) or with increasing stress (temperature constant).

The shapes of the curves appear to indicate that the deformation process changes somewhat with variations in temperature and stress. With the exception of the data obtained at 1,200° F (fig. 9), alloying the nickel displaced the values of the slopes to lower values. Apparently, the solute atoms that cause a strengthening effect in the alloy at low temperatures are less effective strengtheners as the temperature is raised.

The stress dependence of creep rate in the first stage of the 70-percent-Ni–30-percent-Cu alloy is shown in figure 10. Nadai and McVetty [17] indicated that this relation could be expressed by an equation of the form

$$\dot{\epsilon}=\dot{\epsilon}_0 \sinh\left(\frac{\sigma}{\sigma_0}\right)$$

where $\dot{\epsilon}$=the creep rate, σ=stress, and $\dot{\epsilon}_0$ and σ_0 are material constants. At low stresses this equation becomes

$$\dot{\epsilon}=\dot{\epsilon}_0\left(\frac{\sigma}{\sigma_0}\right).$$

This suggests that at low stresses the material behaves like a Newtonian fluid. At high stresses, however, the expression may be shown to exist in the form

$$\dot{\epsilon}=\left(\frac{\dot{\epsilon}_0}{2}\right)\exp\left(\frac{\sigma}{\sigma_0}\right)$$

or

$$\log \dot{\epsilon}=K\left(\frac{\sigma}{\sigma_0}\right)+k.$$

The data were plotted on semilog paper and reproduced in figure 10. The curves at 300° F indicate an approach to linearity as the time at stress is increased. At 900° F, the shape of the curves indicates that the flow mechanisms, although temperature-sensitive, are less affected by the time at which the creep rate was measured for any stress value employed. The positions of the curves, however, indicate that the short-time (5 to 20 min) strain hardening occurring at 700° F is equal to or greater than that occurring at 300° F. This phenomenon is in agreement with another prediction of the theory of the effect of solute atoms as proposed by Cottrell [14]. In the short-time tensile tests of this alloy [7], the magnitude of the serrations in the stress-strain curve attained a maximum in the temperature range 600° to 800° F.

d. Second Stage of Creep

It was previously pointed out in Andrade's creep equation [15] that one of the components described a steady state of flow. This would indicate that when $B=0$,

$$l=l_0\epsilon^{Kt}$$

or

$$\frac{1}{l}\frac{dl}{dt}=K.$$

The region to which this formula applies is generally called the second stage of creep. The apparent balance between the competing mechanisms of strain hardening and recovery of metals during this stage has caused a number of theories to be proposed to describe this steady state. Generally, the analyses of the relations between stress, temperature, and second stage creep rate are based on Eyring's chemical-rate theory [18] or are a result of curve fitting.

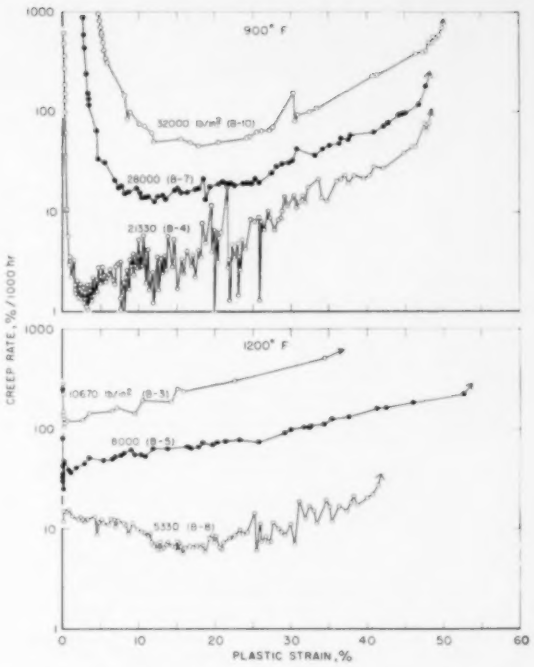

FIGURE 5. *Creep rate-strain characteristics of 70 percent* Ni-*30-percent*-Cu *alloy at 900° and 1,200° F.*

Specimen numbers correspond to those found in the tables.

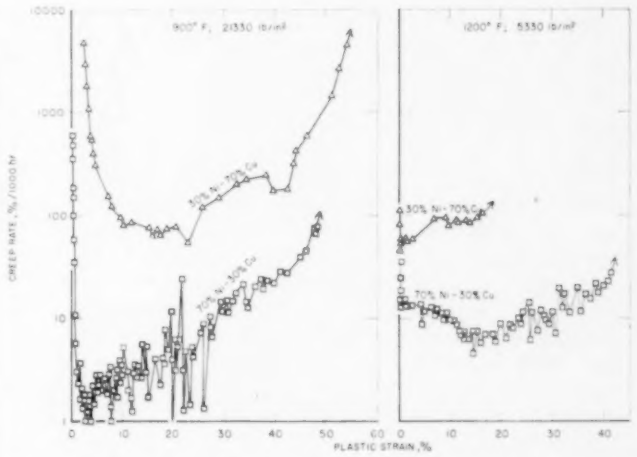

FIGURE 6. *Creep rate-strain relations for specimens of two nickel-copper alloys tested at 900° or 1,200° F.*

Essential features of each of these proposals have been incorporated into a logarithmic rate law in which the second stage creep rate is considered to be proportional to a power function of the stress. The relations between stress and creep rate of the specimens used in the present investigation are shown in figures 11 and 12. At 300°, 700°, and 900° F the curves for the alloys are at higher stress levels than those for the component metals although at 300° F the creep strength of the nickel was only slightly

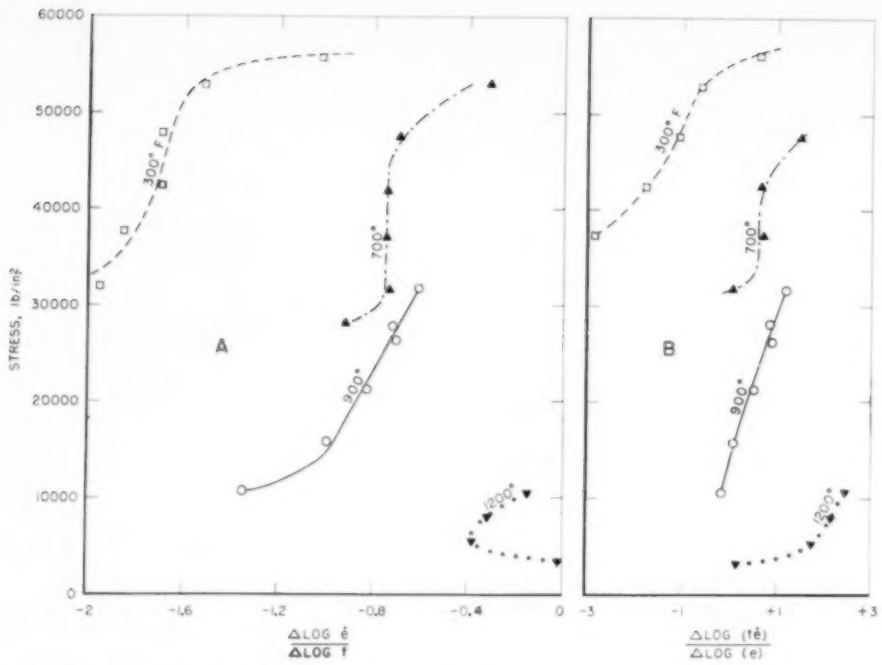

FIGURE 7. *Relations of stress to the slopes of the log creep rate-log time curves and of the log product of time and creep rate-log strain curves during the first stage of creep of 70-percent-Ni–30-percent-Cu specimens at different temperatures.*

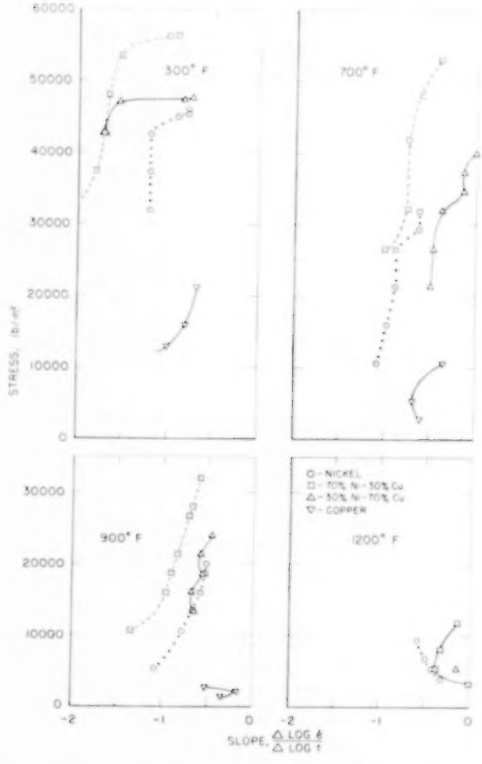

FIGURE 8. *Relation of stress to the slopes of the log creep rate-log time curves during first stage of creep at different temperatures.*

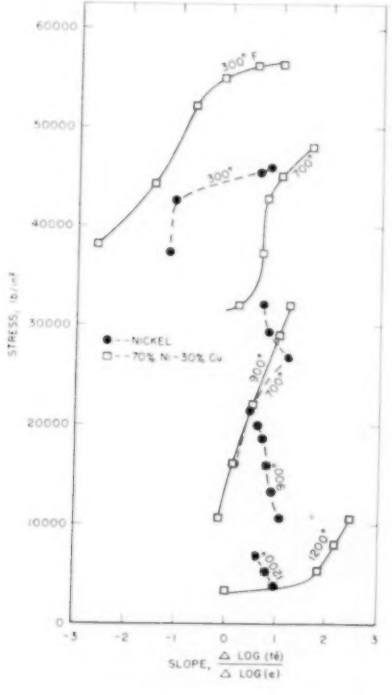

FIGURE 9. *Relation of stress to the slopes of the log product of the time and creep rate-log strain curves during the first stage of creep.*

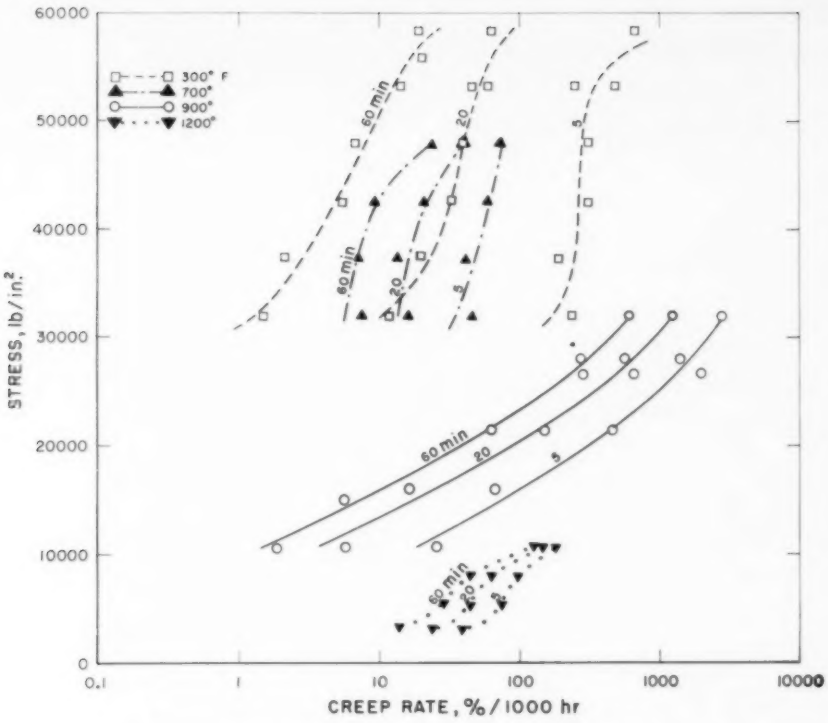

FIGURE 10. *Relation of stress to first stage creep rate of 70-percent-Ni–30-percent-Cu alloy at different temperatures and times.*

less than that of the 30-percent-Ni–70-percent-Cu alloy. Thus, the strengthening effects due to alloying that was observed in the first stage are still evident during the second stage of creep. At 1,200° F, however, the nickel specimens appeared stronger than those of the 30-percent-Ni–70-percent-Cu alloy, indicating that factors affecting the strengths at low temperatures are not necessarily as effective at the higher test temperatures. Similar strengthening effects were obtained previously in short-time tensile tests on high-purity and commercial grades of the 70-percent-Ni–30-percent-Cu alloy [6]. Above the threshold stresses at which creep begins at 300° F (fig. 11), small changes in stress caused a marked change in creep rate. However, the relatively high threshold stresses at 300° may be attributed to a combination of a high degree of strain hardening and aging accompanied by a low rate of recovery. As the temperature is raised, (figs. 11 and 12) recovery predominates and the threshold stresses needed to produce equal second stage rates become less.

The relations between temperature and stress necessary to produce different second-stage creep rates are shown for the 70-percent-Ni–30-percent-Cu alloy in figure 13. As the shape of this family of curves is typical of the behavior of all the metals used in this investigation, the data for the other metals are not shown. However, the short-time tensile strengths of the 70-percent-Ni–30-percent-Cu alloy are included for comparison. In the temperature range 300° to 700° F, the rate of change in stress with temperature increases with increasing creep rates; whereas, the reverse is true in the 900° to 1,200° F range. However, within the 700° to 900° F range, these slopes appear to be independent of creep rate. Apparently, both high- and low-temperature mechanisms are active within this latter range of temperatures.

The relation between stress and nickel content to produce various second-stage creep rates at different temperatures is shown in figures 14 and 15. In general, the slopes of the stress-nickel content curves to produce second-stage creep rates of 0.5 percent, 1 percent, 10 percent, or 100 percent per 1,000 hr are a maximum as the nickel content is increased from zero to 30 percent. It is observed that the variation of stress with nickel content at any creep rate is generally greater at 700 ° F than at other test temperatures. Several phenomena are considered to be responsible for the latter observation. Of the temperatures used, simultaneous straining and recrystallization of copper have been reported at 700° F [7]; this temperature is within the vicinity of the Curie point of nickel [3]; serrated stress-strain curves are obtained for specimens of the alloys in short-time tensile tests [7].

The relation between stress and nickel content to produce different creep rates at different temperatures is shown in figure 15. Although the 70-percent-nickel alloy specimens showed the best creep resistance at all temperatures and stresses, the parallelism of some of the line segments indicated that the strengthening effects of nickel were practically independent of the second-stage creep rate.

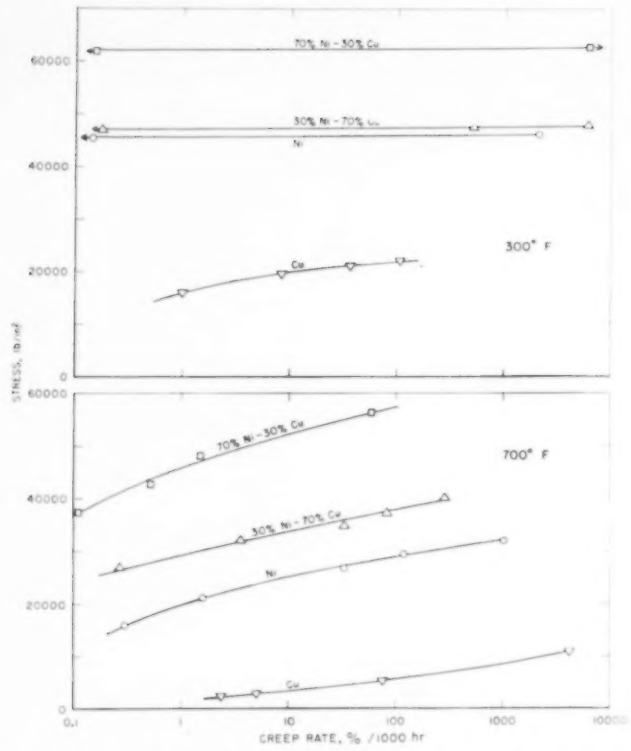

FIGURE 11. *Influence of stress on the average creep rate during the second stage at 300° and 700° F.*

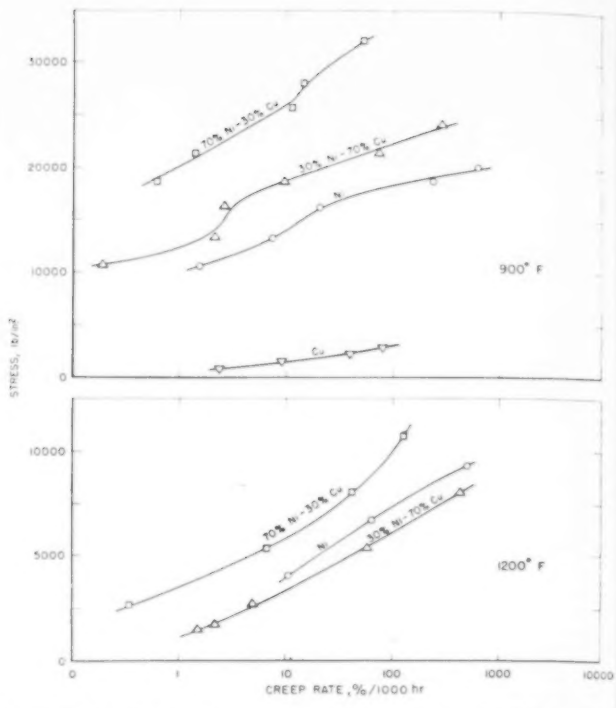

FIGURE 12. *Influence of stress on the average creep rate during the second stage at 900° and 1,200° F.*

Larson and Miller [19] have proposed time-temperature relationships for describing creep behavior and rupture strength. For any given stress

$$T_R(20+\log t)=K$$

or

$$T_R(20-\log r)=C$$

where T_R=temperature in degrees Rankine, t=fracture time in hours, r=second-stage creep rate in percent per 1,000 hr and C and K are constants. Also if the logarithm of the stress is plotted against C or K, all values for specimens of each material should fall on a single curve in the absence of major structural changes. Conformance to these predictions is obtained for the materials used in this investigation as shown in figure 16. The discontinuous curves for copper are attributed, in part, to recrystallization and extensive grain growth during creep. Moreover, the relative positions of the nickel and the 30-percent nickel alloy indicate the factors contributing to the strengthening of the nickel due to alloying are most effective within the parameter values of 16 to 26×10^3.

e. Creep Rate-Ductility Relations

One of the most important structure-sensitive properties of metals is ductility. Previous investigations have shown that no consistent trend existed between ductility values and the rate of straining at different temperatures. Therefore, predictions of ductility values, based on fundamental concepts, does not appear possible at this time. However, it is generally conceded that the ductility of metals depends on the initial concentration of lattice defects and the formation and motion of new defects throughout the crystals. Apparently, as observed in short-time tensile tests on materials of the nickel-copper system [7], substantial changes in the ductility-temperature relations are made by alloying. Changes of this type have been analyzed by Cottrell [14] who considered them to be related to the creation of vacancies and interstitial defects during cold-working.

The relation between strain values, obtained one hour after application of load and the logarithm of the second-stage creep rates for specimens tested at 700°, 900°, and 1,200° F is shown in figure 17. Sufficient data were not available for analyzing the behavior of the specimens at 300° F. The initial strain values, corresponding to equal second-stage creep rates at 700° and at 900° F, increase as the copper content of the specimens is decreased from 100 to 30 percent. The strain values at 700° F for the nickel are approximately the same as those of the 30-percent-Ni–70-percent-Cu alloy; whereas, at 900° F the corresponding strain values for the nickel are greater than those of the 30-percent-nickel alloy. Moreover at 1,200° F, the strain values of the nickel are higher than those for either of the alloys. These observations indicate that the flow characteristics of these metals are strongly dependent on the copper content.

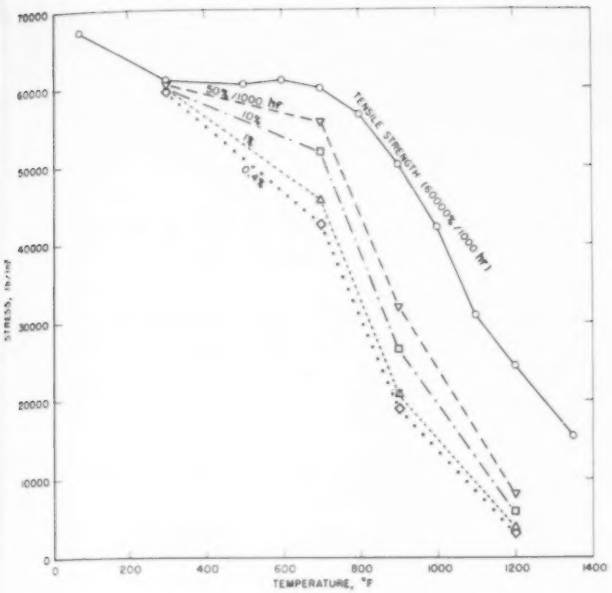

FIGURE 13. *Variation of stress with temperature required to produce various second-stage rates of 70-percent-Ni–30-percent-Cu alloy.*

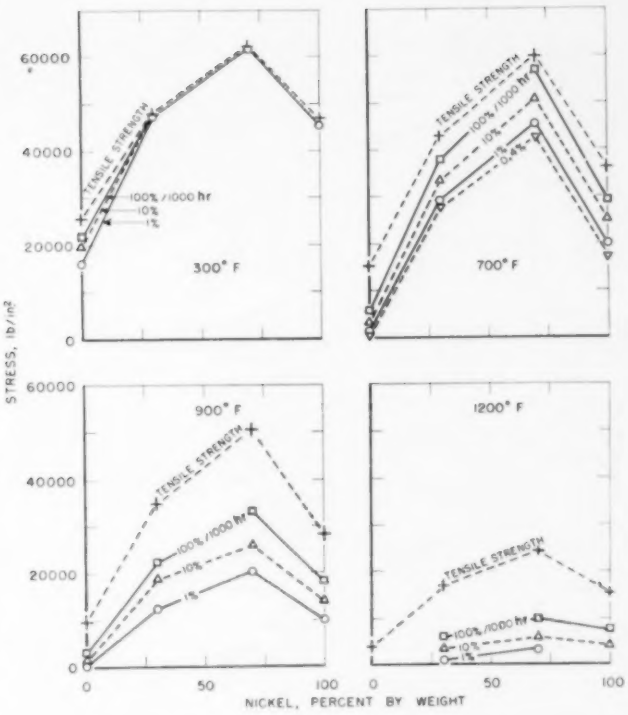

FIGURE 15. *Variation of stress with nickel content to produce different second-stage creep rates at various temperatures.*

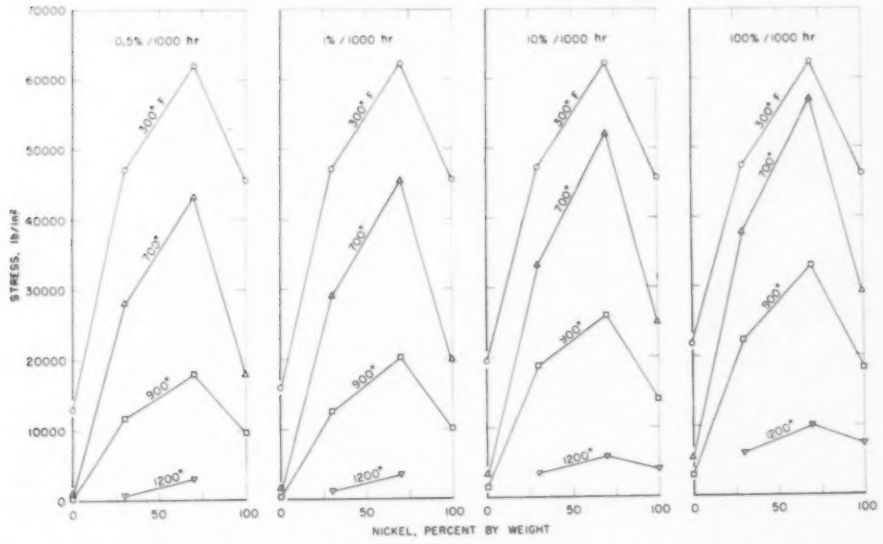

FIGURE 14. *Variation of stress with nickel content to produce equal second-stage creep rates at different temperatures.*

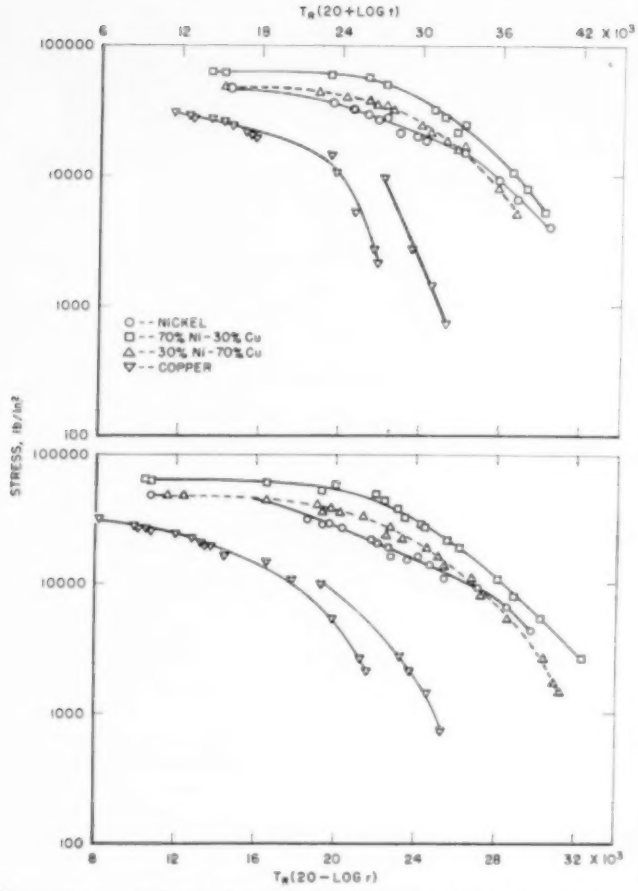

FIGURE 16. *Relation between creep stress and fracture time or creep-rate parameters.*

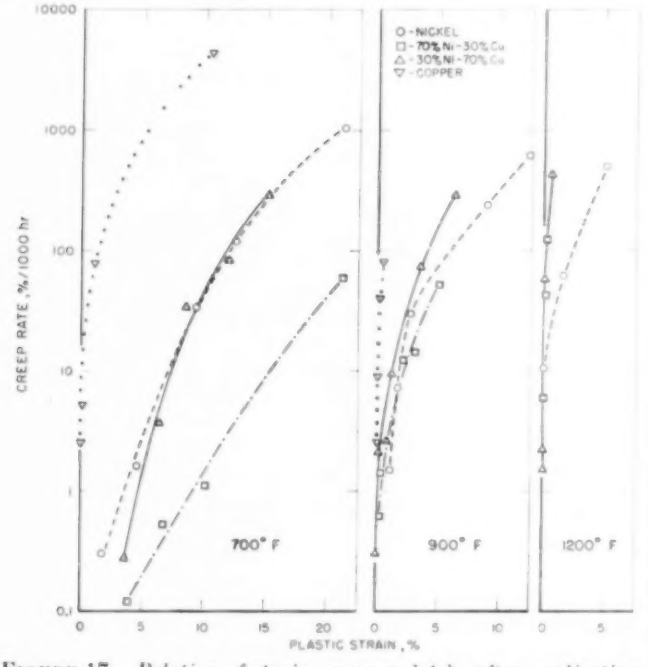

FIGURE 17. *Relation of strain, measured 1 hr after application of load, to the second-stage creep rate at different temperatures.*

The relation between second-stage creep rate and elongation or reduction of area values for specimens tested to complete fracture at 700°, 900°, and 1,200° F is shown in figure 18. It is noteworthy that the ductility of the specimens of the alloys was intermediate between the low values for copper and the high values of the nickel.

f. Third Stage of Creep, Specimen Contour, and Post-Test Hardness

Several processes are discussed in the literature as being the causes of the initiation and the propagation of accelerating creep in the third stage. Among these processes are the following: rising stresses resulting from a decrease in cross-sectional area of the specimen, structural changes, extensive recovery or recrystallization, and nucleation and density of void nuclei. Machlin [20] has recently developed a theory based on the probability of the growth of pre-existent voids by vacancy condensation. Each of the above concepts are applicable to a limited extent to the data for the present investigation. No local contraction (necking) nor voids of a microscopic size were observed for any of the specimens that were examined after stopping the tests prior to the third stage. Therefore, it is concluded that the necking and the growth of cracks, were a consequence of accelerating creep in the third stage. Similar observations were made previously for the copper [1] and for the nickel [5]. With the exception of nickel, previously discussed [5], the degree of necking, in general, decreased with increase in temperature and with decrease in creep rate. This typical behavior is illustrated by the curves shown for the 70-percent-Ni–30-percent-Cu alloy specimens in figure 19A. Moreover, the specimens exhibiting the greatest tendency to contract locally (B–18 and B–13) both showed a tendency toward an increase in hardness with increase in contraction of area values (fig. 19B).

For the specimens tested at 1,200° F (B–3, B–5 and B–8), the opposite effect on hardness was observed. The tendency to soften as the contraction of area values increased was attributed both to the relatively high temperature and decrease in creep rate. This behavior was accompanied by a progressively increasing number of microscopic cracks both near the surface and in the interior of the specimens.

The relations between maximum post-test hardness and second-stage creep rate are shown in figure 20 for specimens of the nickel and the two alloys. The general trends were for the hardness to increase with a decrease in test temperature (creep rate constant) or with increase in creep rate (temperature constant). This same observation was made for the copper; however, the hardness values were too low to be included in the figure. Alloying the copper tended to raise the hardness values markedly; however, with one exception the maximum hardness value for the nickel was higher than the corresponding values of the 30-percent-Ni–70-percent-Cu alloy.

Apparently, some of these and previous data are consistent with the observations on the lattice param-

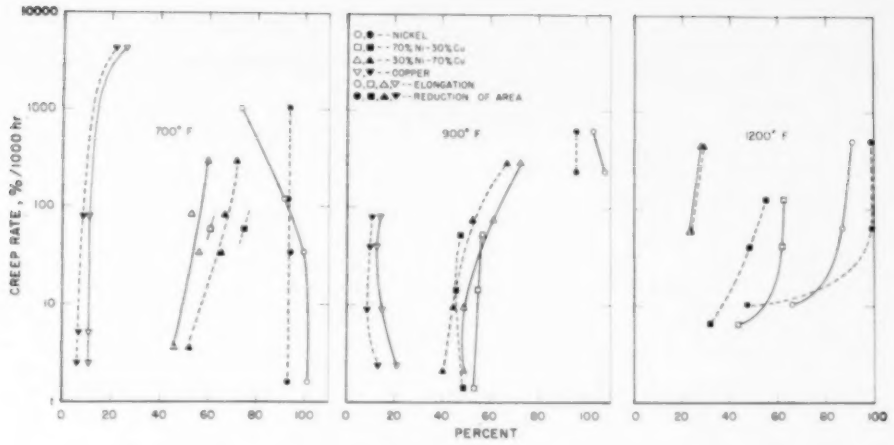

FIGURE 18. *Effect of second-stage creep rate on elongation or reduction of area.*

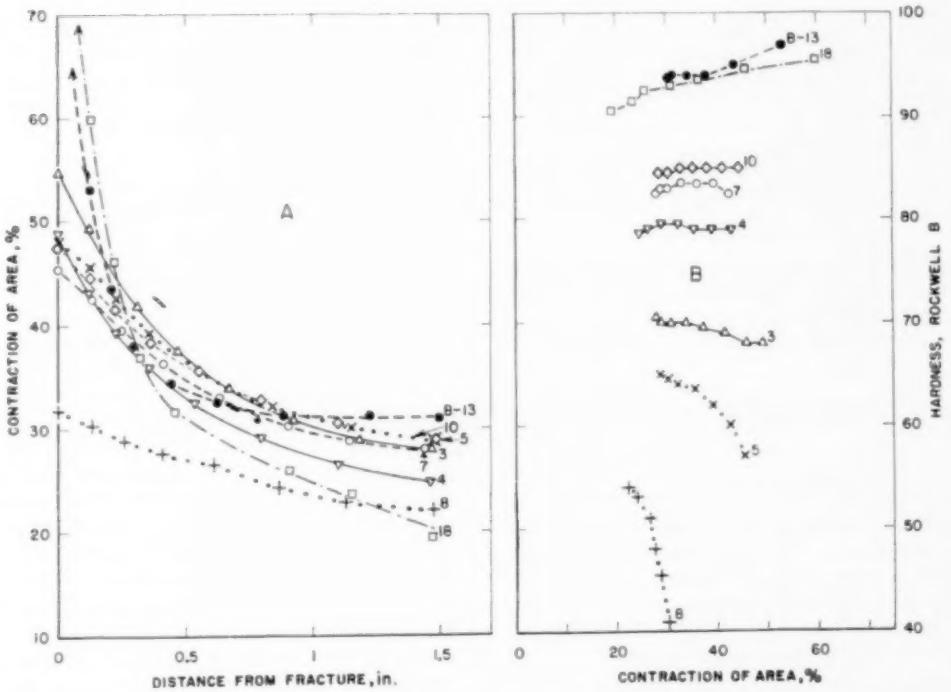

FIGURE 19. *Specimen contours and hardness distributions of specimens of 70-percent-Ni–30-percent-Cu alloy tested to complete fracture*

Specimen number	Temperature	Average creep rate, second stage
	° F	%/1,000 hr
B–18	300	220,000
B–13	700	59
B–10	900	51.8
B– 7	900	14.3
B– 4	900	1.4
B– 3	1,200	125
B– 5	1,200	41
B– 8	1,200	6.6

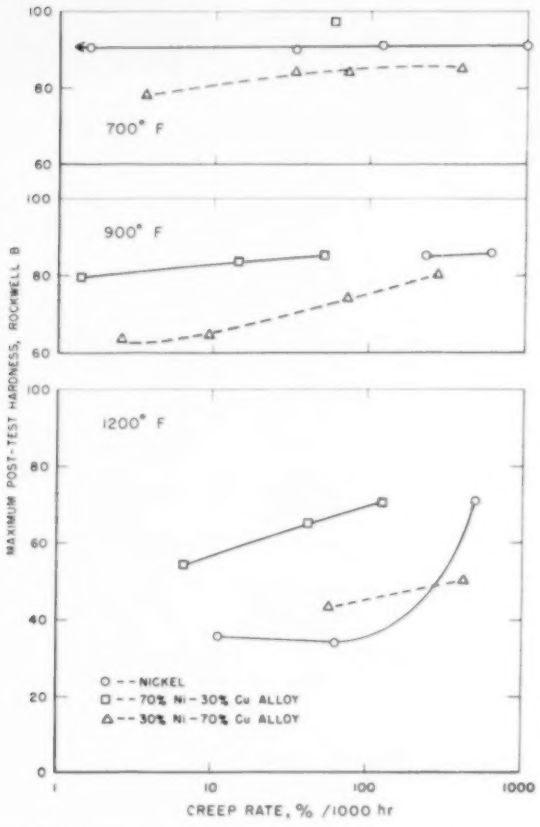

FIGURE 20. *Effect of second-stage creep rate on the maximum post-test hardness values of specimens tested to complete fracture at different temperatures.*

eters of the copper-nickel system recently presented by Coles [21].

g. Activation Energy

Determinations of activation energies from data obtained in creep tests on different metals have been made in recent years. Some investigators have found that the activiation energy associated with creep is approximately equal to that for self-diffusion of the material. Other data depart rather markedly from this observation. Also controversial are the influences of prior-strain history, strain, temperature, grain and subgrain sizes, and the metallurgical changes occurring during creep. In addition, differences in values of activation energy may be attributed to the use of different basic assumptions in the calculations. For example, the activation energy for creep of the nickel used in this investigation was calculated as about 53,500 calories per mole according to the analysis of Manjoine and Mudge [23] and about 65,000 calories per mole by using the dislocation climb mechanism proposed by Weertman and Shahinian [22]. It was, therefore, thought unfruitful to pursue further any analysis of activation energy until a more complete appraisal of the basic factors affecting the calculations can be made.

3.2. Effect of Prior-Strain History on Creep Behavior

a. Strain-Time and Stress-Strain Curves

An analysis of experimental data led Ludwik [24] to propose that the strain-hardening characteristics of a material were a function of the instantaneous strain, strain rate, and temperature and were practically independent of the prior strain history. Many fundamental data have since been accumulated to test the validity of this equation of state. It is now the generally accepted view that this relation is generally invalid and that the data tending to confirm this and similar proposals may be considered as only special cases of the general problem of plastic flow.

Wood [25], in summarizing the factors affecting the structural changes in metals during deformation, indicated that the parent grains are fragmented. The size of the substructures so formed increases with increase in test temperature and with decrease in rate of straining. The boundaries of the substructures can act as barriers to the motion of dislocations or as sites where stable barriers form. During a constant-stress creep test the substructure tended toward an equilibrium size characteristic of the stress and test temperature. Systematic changes in subgrain size, accompanied by changes in resistance to deformation, was predicted for specimens as the test temperature or strain rate was altered. A quantitative test of this hypothesis was recently made by Hazlett and Hansen [10] who indicated that the shape of the creep curve could be materially altered by changes in the initial substructure of the base material and further altered by alloying. The prestraining of the nickel in that investigation was done exclusively at room temperature and followed by a recovery treatment at 1,290° F.

The influence of prior straining in creep on the subsequent creep behavior at elevated temperature and tensile properties at room temperature of nickel and copper has been discussed in previous publications [1, 2, 3, 5]. The present paper is concerned with similar effects on the 70-percent-Ni–30-percent-Cu and 30-percent-Ni–70-percent-Cu alloys. The test conditions and results are summarized in tables 5 and 6 and analyzed graphically in figures 21 to 27, inclusively.

The effect of the magnitude of the initial stress and the subsequent rate of loading on the creep behavior of specimens of 70-percent-Ni–30-percent-Cu alloy at 300° F is shown in figure 21. If the only modes of deformation, existing for these specimens, were the ones suggested by Wood [25], then the curves for specimens tested at equal stresses should merge after a time. Apparently, an aging phenomenon, such as was shown for nickel [5] existed for this alloy under these test conditions. Although the reduction of area values are approximately independent of the rate of loading, elongation and the true stress at fracture appear to be dependent on this factor.

The influence of alloying the nickel with copper on the resistance to creep at 300° F of slowly loaded specimens can be deduced from a comparison of the difference in stresses, in excess of the tensile strengths,

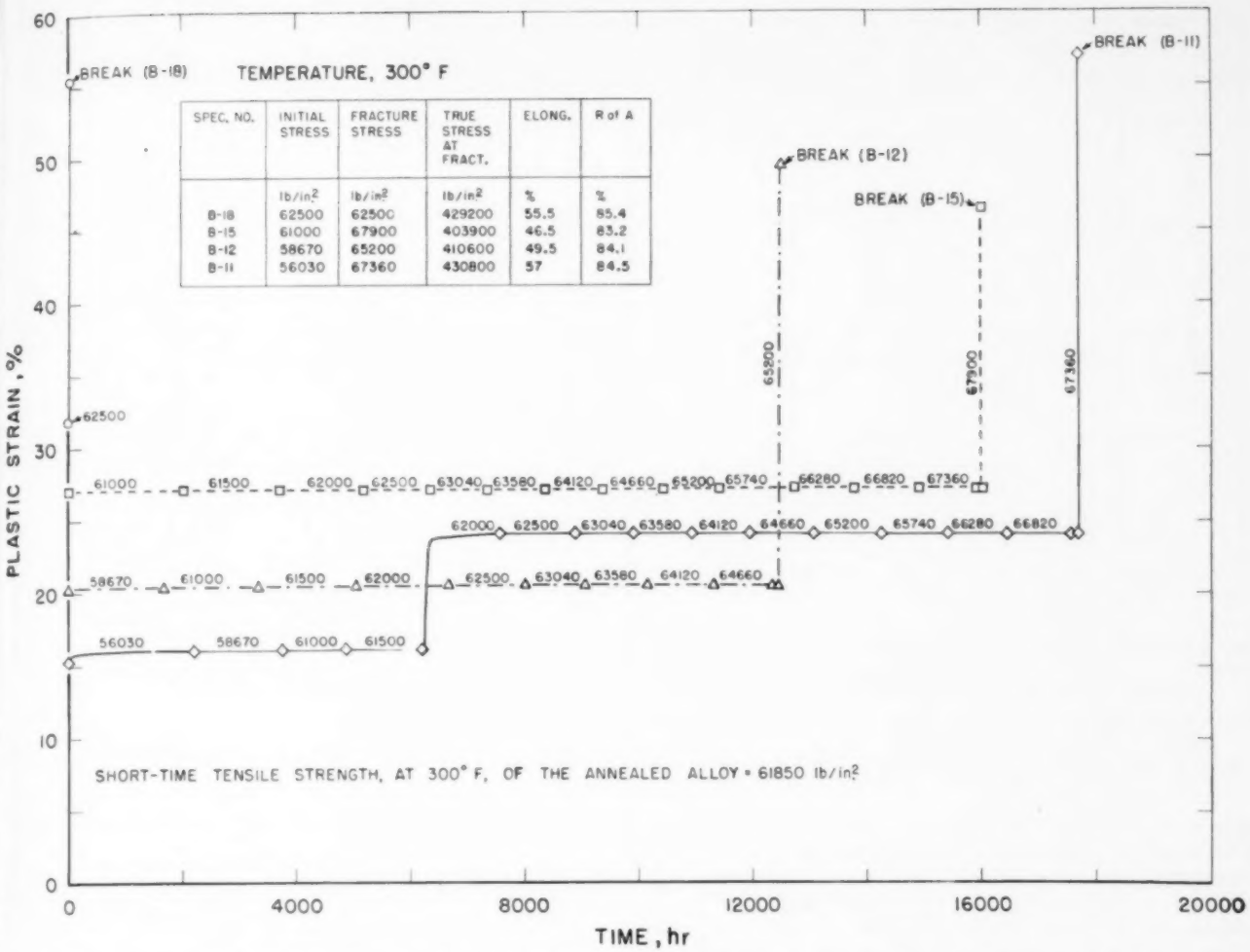

FIGURE 21. *Effect of rate of loading at 300° F on the strain-time characteristics of 70-percent-*Ni*–30-percent-*Cu *alloy.*

required to produce fracture in 1,000 hr. The 70-percent-Ni–30-percent-Cu alloy required a stress at least 3,350 lb/in.^{2} in excess of its short time tensile strength (fig. 21) whereas the nickel required only 1,600 lb/in.^{2} or less, in excess of its tensile strength to produce complete fracture in 1,000 hours in slowly loaded specimens [5]; the short-time tensile strengths at 300° F of the alloy and nickel were 61,850 and 46,400 lb/in.^{2}, respectively. This increase in creep strengths at 300° F of both the alloy and the nickel is primarily attributed to a combination of strain-aging and strain-hardening characteristics. The results show that the strain aging and hardening are much more prominent in the specimen loaded slowly than in the specimens loaded rapidly to the selected creep stresses.

The strain-aging characteristics at 300° F of the alloy are further illustrated, in figure 22, by a comparison of the relative positions of the stress-strain curves associated with the slowly loaded specimens (dashed curves) and the specimens loaded at 5,330 lb/in.^{2} hr (solid curve). In the absence of strain aging, the curves for the four specimens should coincide.

The effect of straining a 70-percent-Ni–30-percent-Cu specimen at a lower stress at 900° F on the subsequent creep behavior at a higher stress and at the same temperature, is shown in figure 23. Although the second stage creep rate was approximately the same for the specimen (B–14) prestrained 2.23 percent at 18,670 lb/in.^{2} as that for the specimen (B–4) not prestrained, the behavior of the two specimens in the first stage was somewhat different. The duration of the first stage of the former specimen was relatively short in comparison with that of the latter. These observations are consistent with Wood's theory describing the tendency of the subgrains to approach an equilibrium size. The fact that this behavior is not typical at 900 °F is shown by the results reproduced in figure 24. The specimens were prestrained different amounts at temperatures of 300°, 700°, 900°, or 1,200° F. The specimens prestrained at 300°, 700°, and 1,200° F showed a tendency toward an increase in second stage creep rate and a decrease in fracture time when compared to the specimen loaded at the standard rate and strained at 900° F. Straining slowly at 900° F (B–14) to a value of 5 percent tended to decrease the second stage creep

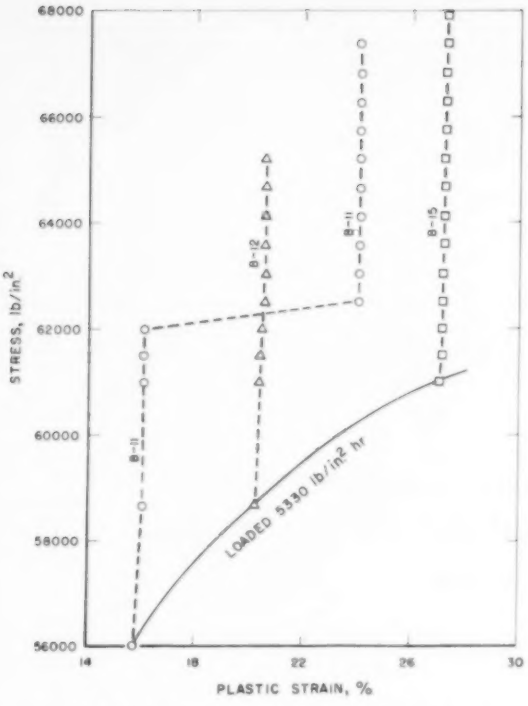

FIGURE 22. *Effect of rate of loading at 300° F on the stress-strain relations of 70-percent-Ni–30-percent-Cu alloy.*

For rate of loading schedule, see figure 21.

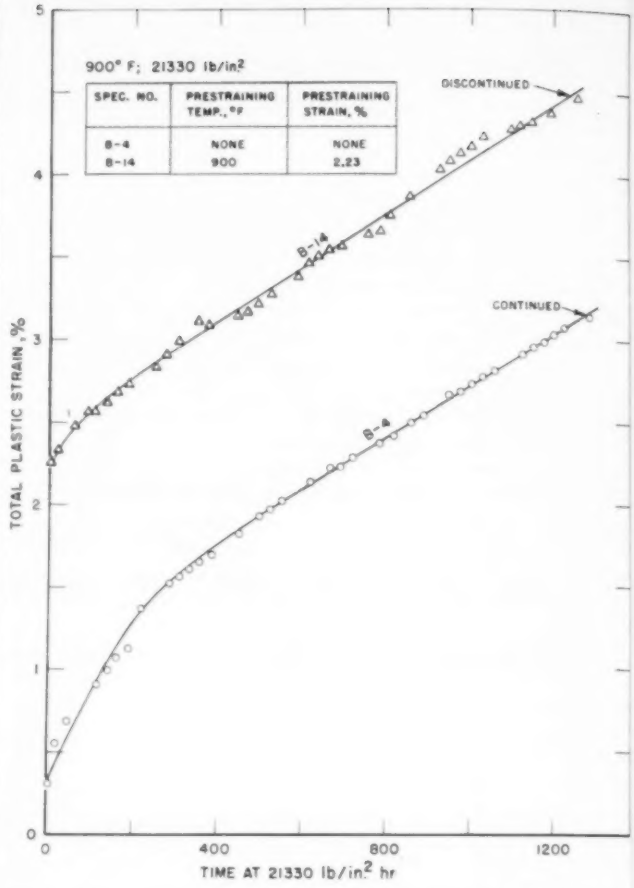

FIGURE 23. *Influence of prestraining at 900° F on the strain-time relations of specimens of 70-percent-Ni–30-percent-Cu alloy tested with a stress of 21,330 lb/in.².*

For rate of loading schedule of specimen B-14, see table 5.

rate and increase the fracture time and elongation. The strain associated with the first stage of creep increased as the prestraining temperature was increased. Moreover, the first stage was practically eliminated for the specimens prestrained relatively large amounts at 300° or 700° F (B–17 and B–9).

The effect of prestraining at 900° F on the creep characteristics at 1,200° F of the 70-percent-Ni–30-percent-Cu alloy is shown in figure 25. Prestraining caused a detectable first stage, a decrease in second-stage creep rate, elongation, and fracture time at 1,200° F.

The influence of prestraining temperature and the amount of prestrain on the creep characteristics of The 30-percent-Ni–70-percent-Cu alloy tested at 900° F with a stress of 18,670 lb/in.² is shown in figure 26. Compared to the reference specimen (C–8) the fracture time was decreased and the second-stage creep rate increased for all the prestrained specimens. The maximum increase in creep rate was observed for the specimen (C–13) prestrained at 1,200° F to 10.22 percent whereas the minimum increase was observed for the specimen (C–21) prestrained at 900° F to a small strain value. Apparently, the substructures developed in the latter specimen had only a slight effect on the second-stage rate, but caused a marked decrease in fracture time and elongation. Generally, for the specimens of 30-percent-Ni–70-percent-Cu an increase in the prestraining temperature (amount of prestrain constant) was accompanied by an increase in second-stage creep rate and a decrease in values of elongation or reduction of area. Increasing the amount of prestrain at 300° or 900° F tended to cause an increase in second-stage creep rate, elongation, and reduction of area for the specimens; whereas the increase in creep rate for the specimens prestrained at 1,200° F was accompanied by a decrease in elongation.

Although prior-strain history appeared to have a pronounced effect on the subsequent mechanical properties at 900° F of the 30-percent-Ni–70-percent-Cu alloy, the properties at 300° F were practically independent of the rate of loading (tables 3 and 6). The latter observation is not in agreement with the results obtained on the 70-percent-Ni–30-percent-Cu alloy and may be due, in part, to the differences in the degree of strain aging in the metals.

b. Specimen Contour and Post-Test Hardness

The effect of prior-strain history on the necking characteristics and the post-test hardness of specimens of the 30-percent-Ni–70-percent-Cu alloy, fractured at 900° F with a stress of 18,670 lb/in.²

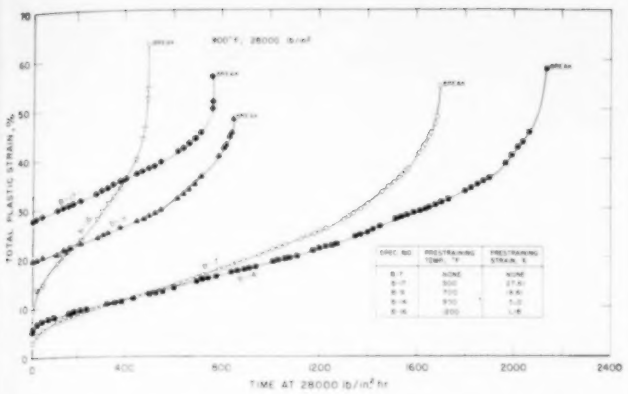

FIGURE 24. *Influence of prior-strain history on the strain-time relations at 900° F of specimens of 70-percent-Ni–30-percent-Cu alloy tested to complete fracture with a stress of 28,000 lb/in².*

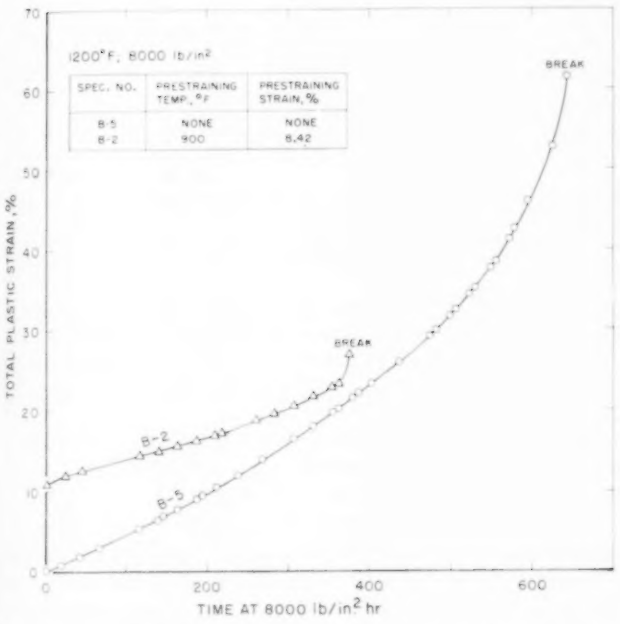

FIGURE 25. *Influence of prior strain history on the strain-time relations at 1,200° F of specimens of 70-percent-Ni–30-percent-Cu alloy tested to complete fracture with a stress of 8,000 lb/in².*

is shown in figure 27. No necking of the specimens was observed during the first or second stage of creep. Therefore, it was concluded that the specimen contours after fracture (figure 27a) were due, in part, to the different mechanisms existing in the third stage. A further examination of the data indicates that the specimen contour was affected more by prestraining temperature than by the subsequent second-stage creep rate. For example, the greatest tendency to neck was shown by specimen C–24 and the least tendency by specimen C–13. The prestraining temperature of the latter specimen was 1,200° F and the second stage creep rate exceeded that of the former specimen, which was prestrained at 300° F, by a factor of about 50. In general, prestraining at the lower temperatures increased the severity of the neck, the post-test hardness (fig. 27B), and the rate of strain hardening. It is evident that both the strain-hardening and necking characteristics of the specimens, tested under the same conditions, were strongly dependent on the initial structure, temperature, and chemical composition of the metal.

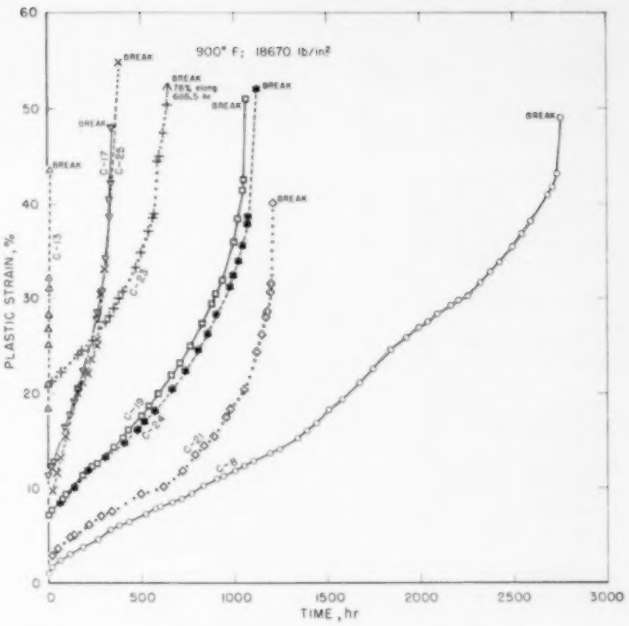

FIGURE 26. *Effect of prior strain history on the strain-time relations at 900° F of specimens of 30-percent-Ni–70-percent-Cu alloy tested to fracture with a stress of 18,670 lb/in².*

Specimen number	Prestrain temperature	Prestrain	Avg. creep rate, second stage
	° F	*Percent*	*%/1,000 hr*
C–8	None	None	9.5
C–23	300	20.7	19.2
C–24	300	7.74	18.0
C–19	700	7.33	21.5
C–17	900	10.12	57
C–21	900	0.865	11.6
C–13	1,200	10.22	905
C–25	1,200	2.374	60

4. Summary

Creep tests were made at 300°, 700°, 900° and 1,200° F on initially-annealed specimens of copper, nickel, and 70-percent-Ni–30-percent-Cu and 30-percent-Ni–70-percent-Cu alloys. The study was extended to include an evaluation of the rate of loading and prior-strain history on the creep characteristics, hardness, and contours of specimens of the two alloys.

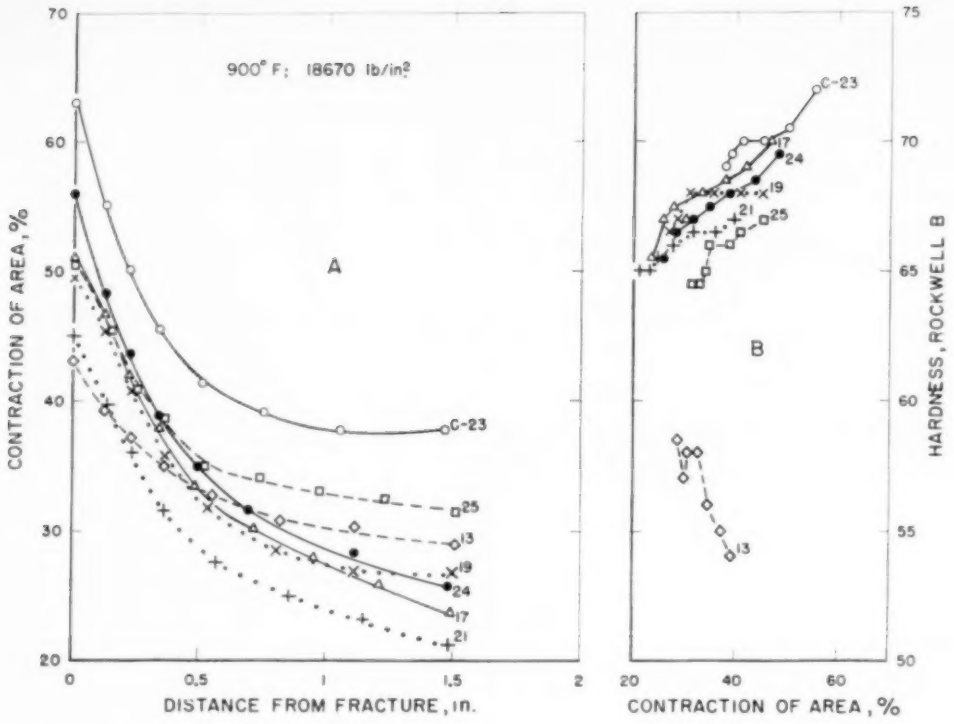

FIGURE 27. *Effect of prior-strain history on specimen contour and hardness distributions of specimens of 30-percent-Ni–70-percent-Cu alloy tested to fracture at 900° F with a stress of 18,670 lb/in².*

Refer to figure 26 for prior strain history and second-stage creep rates of the specimens.

The initial resistance to flow was increased by alloying the component metals. The maximum resistance was obtained in specimens of the 70-percent-Ni–30-percent-Cu alloy.

Conformance to both the theory of exhaustion and of generation of lattice defects during the first stage of creep was obtained over limited ranges of temperatures and stresses.

The shape of the stress-creep rate curves during the first and second stages was altered markedly as the test temperature was increased.

The stress dependence of second stage creep rate was interpreted on the basis of a hyperbolic sine law based on the chemical-rate theory. Strict conformance was limited by the relative balance between strain hardening and recovery of the specimens at the different temperatures. At the same temperature the resistance to creep in the second stage was highest for the 70-percent-Ni–30-percent-Cu alloy and lowest for the copper; however, the increase in creep resistance above that of the component metal was greater when 30 percent of nickel was added to the copper than when 30 percent of copper was added to the nickel.

The creep characteristics of the specimens conformed closely to a theory based on a Cottrell effect at low temperatures and to a theory based on recovery at high temperatures; for specimens tested at low stresses, the results were not easily explainable by either of these theories.

With the exception of the copper specimens tested at 900° F, the creep rates or fracture times of each metal were expressed in terms of single parameters which varied monotonically with values of the applied creep stress.

Elongation or reduction of area values of the alloys was intermediate between the high values for the nickel and low values for the copper.

Post-test hardness values and the rate of strain hardening of the alloys decreased and the tendency toward uniform contraction of specimens increased with increase in temperature or decrease in second-stage creep rate.

Strain aging induced by slowly loading specimens at 300° F, was more pronounced for the 70-percent-Ni–30-percent-Cu than for the 30-percent-Ni–70-percent-Cu alloy or for that previously obtained for the nickel.

In general, the shape of the creep curves, mechanical properties, and the fracture times were apparently affected by the substructure induced in the specimens by prestraining; however, all phases of Wood's theory of subgrain formation were not generally in agreement with present data.

Prestraining the specimens at the higher temperatures reduced the post-test hardness values, the rate of strain hardening, and the tendency toward a formation of an acute neck.

5. References

[1] W. D. Jenkins and T. G. Digges, Creep of high-purity copper, J. Research NBS **45,** 153 (1950) RP2121.

[2] W. D. Jenkins and T. G. Digges, Creep of annealed and cold-drawn high-purity copper, J. Research NBS **47,** 272 (1951) RP2254.

[3] W. D. Jenkins and T. G. Digges, Effect of temperature on the tensile properties of high-purity nickel, J. Research NBS **48,** 313 (1952) RP2317.

[4] W. D. Jenkins and T. G. Digges, Influence of prior strain history on the tensile properties and structures of high-purity copper, J. Research NBS **49,** 167 (1952) RP2354.

[5] W. D. Jenkins, T. G. Digges, and C. R. Johnson, Creep of high-purity nickel, J. Research NBS **53,** 329 (1954) RP2551.

[6] W. D. Jenkins, T. G. Digges, and C. R. Johnson, Effect of temperature on the tensile properties of a commercial and a high-purity 70-percent-nickel–30-percent-copper alloy, J. Research NBS **54,** 21 (1955) RP2561.

[7] W. D. Jenkins, T. G. Digges, and C. R. Johnson, Tensile properties of copper, nickel, and 70-percent-copper–30-percent-nickel and 30-percent-copper–70-percent-nickel alloys at high temperatures, J. Research NBS **58,** 201 (1957) RP2753.

[8] E. R. Parker and T. H. Hazlett, Principles of solution hardening, Seminar on Relation of Properties to Microstructure, Am. Soc. Metals, p. 30 (1953).

[9] T. H. Hazlett and R. D. Hansen, Influence of substructure on the shape of the creep curve, Trans. Am. Soc. Metals **47,** 508 (1955).

[10] R. S. French and W. R. Hibbard, Jr., Tensile deformation of copper, Trans. Am. Inst. Mining Met. Engrs., **188,** 53 (1950).

[11] C. S. Barrett, Structure of metals, 2d ed., p. 220 (McGraw-Hill Book Co., New York, N. Y., 1952).

[12] B. L. Averbach, The structure of solid solutions, Seminar on Theory of Alloy Phases, Am. Soc. Metals, p. 301 (1955).

[13] J. C. Fisher, On the strength of solid solution alloys, Acta Metallurgica **2,** 9 (1954).

[14] A. H. Cottrell, Interactions of dislocations and solute atoms, Seminar on Relation of Properties to Microstructure, Am. Soc. Metals, p. 131 (1953).

[15] E. N. da C. Andrade, The creep of metals, Report of a Conference on Strength of Solids, Phys. Soc. p. 20 (1948).

[16] M. Davis and N. Thompson, Creep in a precipitation-hardened alloy, Proc. Phys. Soc. [B] **63,** 847 (1950).

[17] A. Nadai and P. G. McVetty, Hyperbolic sine chart for estimating working stresses of alloys at elevated temperatures, Proc. Am. Soc. Testing Materials, **43,** 735 (1943).

[18] H. Eyring, The activated complex in chemical reactions, J. Chem. Phys. **3,** 107 (1935).

[19] F. R. Larson and J. Miller, A time-temperature relationship for rupture and creep stresses, Trans. Am. Soc. Mech. Engrs. **74,** 765 (1952).

[20] E. S. Machlin, Creep-rupture by vacancy condensation, J. of Metals, Trans. Am. Inst. Mining Met. Engrs. **8,** 106 (1956).

[21] B. R. Coles, The Lattice spacings of nickel-copper and palladium-silver alloys, J. Inst. Metals **84,** 346 (1956).

[22] J. Weertman and P. Shahinian, Creep of polycrystalline nickel, J. of Metals, Trans. Am. Inst. Mining Met. Engrs., **8,** 1223 (1956).

[23] M. J. Manjoine and W. L. Mudge, Jr., Creep properties of annealed unalloyed zirconium, Proc. Am. Soc. Testing Materials, **54,** 1050 (1954).

[24] P. Ludwik, Elemente der Technologischen Mechanik (Julius Springer, Berlin, 1909).

[25] W. A. Wood, Creep processes, Symposium on Creep and Fracture of Metals at High Temperatures, Natl. Phys. Lab. (1956).

Washington, August 1, 1957.

Journal of Research of the National Bureau of Standards Vol. 60, No. 3, March 1958 Research Paper 2837

Stress-Strain Relation of Pure-Gum Rubber Vulcanizates in Compression and Tension

Lawrence A. Wood

The stress-strain curve in tension for a typical pure-gum rubber vulcanizate after a given period of creep, according to Martin, Roth, and Stiehler, can be represented by an empirical equation

$$F=M(L^{-1}-L^{-2})\exp A(L-L^{-1})$$

where F is the stress based on the original-cross sectional area, and L is the ratio of stressed to unstressed length, M is the slope of the stress-strain curve at $L=1$ and A normally has a value close to 0.38. The present paper shows by an examination of data published by Sheppard and Clapson, Treloar, and Rivlin and Saunders that the equation is also valid in the region of compression for values of L as small as 0.5 (50 percent compression). The features of the empirical equation are discussed, and comparisons are made with the equation predicted by the statistical theory of rubber elasticity and the equation derived by assuming Hooke's law for the stressed cross section. The consequences of the validity of the empirical equation in terms of the Mooney-Rivlin presentation of the strain energy function are pointed out. The equation predicted by the statistical theory represents observed data very well in the compression region from $L=0.5$ to $L=1.0$. The Mooney equation is approximately valid from $L=1.5$ to $L=3.5$. Neither of these equations is satisfactory in the important intermediate region from $L=1.0$ to $L=1.5$. The empirical equation represents the observed data over all three of these regions. It is concluded that Young's modulus M can best be obtained from the intercept of a plot of log $F/(L^{-1}-L^{-2})$ against $(L-L^{-1})$. For $0.75<L<2.00$ it is thoroughly satisfactory to determine M as the intercept of a plot of $F/(L^{-1}-L^{-2})$ against $(L-1)$.

1. Introduction

The stress-elongation curve of a typical pure-gum rubber vulcanizate after a given period of creep, according to recent work of Martin, Roth, and Stiehler [1],[1] can be represented up to 200 percent elongation or more by an empirical equation

$$F=M(L^{-1}-L^{-2})\exp A(L-L^{-1}) \qquad (1)$$

where F is the stress based on the original cross-sectional area, L is the ratio of stressed length to unstressed length, and M and A are constants. M is Young's modulus, the slope of the stress-elongation curve at zero stress (where $L=1$). A normally has a value close to 0.38.

A graph of F/M against L as computed from eq (1) is given by the solid line of figure 1, reproduced from a recent review [2]. Although the range of conditions of applicability of eq (1) has not been thoroughly explored, Martin, Roth, and Stiehler [1] showed it to be valid for the first extension of pure-gum vulcanizates of natural rubber, GR–S, GR–I, and Neoprene over a 10-fold range of times of vulcanization and for constant times of creep from 1 to 10,000 min. It was found not applicable to vulcanizates containing carbon black or other fillers.

The investigations of Martin, Roth, and Stiehler were limited to specimens in simple tension. Consequently it was considered to be of interest to determine whether the same empirical equation can be applied to the compression region. The present paper shows from data already published by Sheppard and Clapson [3], Treloar [4], and Rivlin and Saunders [5], that, until the compression exceeds about 50 percent ($L=0.50$), the equation is valid with the same constants that apply in the extension region.

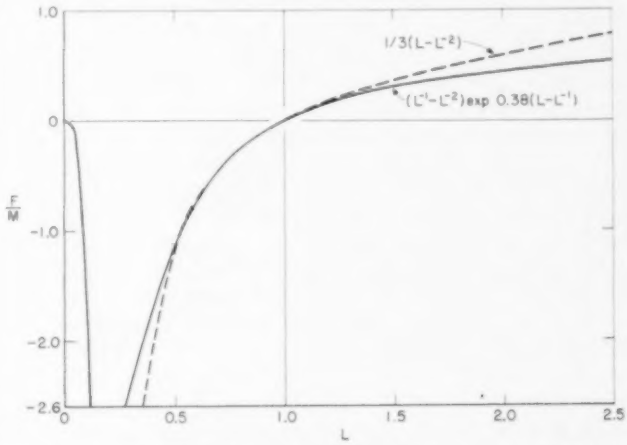

FIGURE 1. *Relation between stress-modulus ratio F/M and length ratio L.*

Solid line: empirical function $(L^{-1}-L^{-2})$ exp 0.38 $(L-L^{-1})$. Dashed line: statistical theory function (1/3) $(L-L^{-2})$.

2. Compression and Tension Data

The friction that arises when compressional forces are applied to a flat specimen is a major source of experimental difficulty. It was pointed out years ago by Sheppard and Clapson [3] that a system fully equivalent to friction-free compression with freedom of displacement normal to the compressive force is obtained by subjecting a sheet to two-dimensional stresses in the plane of the sheet while

[1] Figures in brackets indicate the literature references at the end of this paper.

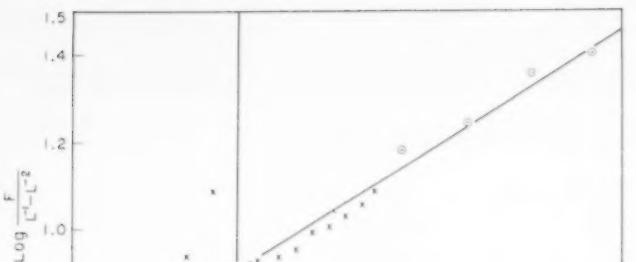

FIGURE 2. *Determination of constants in empirical equation from plot suggested by eq (1).*

×, Data from figure 10 of Sheppard and Clapson [3]; ⊙, data from figure 9 of Sheppard and Clapson [3].

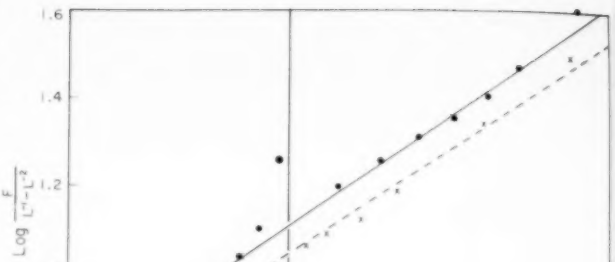

FIGURE 3. *Determination of constants in empirical equation from plot suggested by eq (1).*

●, Data of Treloar [4]. ×, Data of Rivlin and Saunders [5].

allowing freedom of displacement in the direction normal to the sheet. Data obtained by studying the relation between deformation and inflation pressure in balloons were presented by these authors. Values obtained on both compression and tension shown in figures 9 and 10 of the paper by Sheppard and Clapson [3] have been read from the figures to obtain log $F/L^{-1}-L^{-2}$) and ($L-L^{-1}$), the quantities necessary for checking the validity of eq (1). They have been plotted as co-ordinates in figure 2 of the present paper. It has already been pointed out [1] that such a plot in the tension region should yield a straight line with A as slope and log M as intercept. The linearity of the plot shown here covering both compression and tension seems quite satisfactory. Sheppard and Clapson themselves have called attention to the probable inaccuracy of the two points obtained at the smallest value of compression (where $L=0.8$ and 0.9). The values of A obtained from the plot in figure 2 is 0.36 in close agreement with values found by Martin, Roth, and Stiehler [1]. The value for log M of 0.91, corresponding to a Young's modulus of 8.1 kg/cm^2, is quite reasonable for a "cold-cured" balloon rubber. It is presumed that the vulcanizing agent was sulfur chloride.

The upper curve of figure 3 represents data from the work of Treloar [4], who made measurements similar to those already described but used a vulcanizate compounded with 8 parts of sulfur per hundred parts of rubber. The data in the compression region are taken from Treloar's table 1. For the points corresponding to compression ratios of 0.80, 0.77, and 0.69 the values of the equivalent compressive force were taken as 3.39, 3.89, and 5.82 kg/cm^2, respectively, after correcting an apparent typographical error in Treloar's table 1. Values in the tension region were read from figures 3 and 5 of Treloar's paper.

For values of L greater than 0.5 the experimental points lie quite close to the straight line drawn in figure 3, with the exception of the point for $L=0.95$. The value of A obtained from this plot is 0.394, in satisfactory agreement with previous work [1]. The value for log M of 1.1 corresponds to a Young's modulus of 12.7 kg/cm^2, nearly the same as the value, 12.0 kg/cm^2, taken by Treloar to represent the data in the compression region and up to about 30 percent elongation.

The lower curve of figure 3 represents data from the work of Rivlin and Saunders [5], whose measurements were similar to those of Treloar. The rubber was a conventional sulfur vulcanizate accelerated with benzothiazyl disulfide (MBTS). The data in the compression region were taken from table 8 of the paper by Rivlin and Saunders, while the data in the tension region were read from figure 14 of their paper. Values of $A=0.382$ and $M=11.1$ kg/cm^2 are obtained from figure 3.

It will be noted that in 2 of the 3 sets of data in figures 2 and 3, the values of the ordinate lie increasingly above the straight line as L approaches 1 in the compression region. It is possible that this represents a significant characteristic or it may be that it was due to residual stresses or other non-isotropic phenomena. Martin, Roth, and Stiehler [1] also reported instances of apparent high values near $L=1$ for certain vulcanizates in the tension region. However, in the present paper we shall neglect the possibility that the observation is significant since better data in the region near $L=1$ would be required to establish a definite conclusion of this sort.

It is concluded from figures 2 and 3 that eq (1) provides a satisfactory representation of the stress-strain relation for compressions less than 50 percent (i. e., for L greater than 0.5), and for elongations up to about 250 percent (i. e., $L=3.5$).

3. Features of the Empirical Equation

The solid line in figure 1, depicting the values of F/M computed from eq (1) with $A=0.38$, includes both compression and tension regions. The de-

scending portion, beginning at the origin, of course has no physical significance. A minimum value of $F/M=-3.3$ at $L=0.18$ is followed by the rising portion shown. A point of inflection (corresponding to a maximum slope) at $L=0.26$ is followed by a steady decrease of slope, passing through unit slope at $L=1$, until another point of inflection (corresponding to a minimum slope) is reached at $L=2.91$. As pointed out in the preceding sections, the equation represents the experimental data reasonably well over the interval from $L=0.5$ to about $L=3.5$.

One can find two approximations to eq (1) that are useful over limited regions. The exponential term in eq (1) can be expanded in a power series. If only the first two terms of the series are retained and a reciprocal term is approximated [1], the following equation is obtained:

$$F/M=[L^{-1}-L^{-2}][1+2A(L-1)] \qquad (2a)$$

or

$$F/M=2A-(4A-1)L^{-1}-(1-2A)L^{-2}. \qquad (2b)$$

For $A=0.38$ this becomes

$$F/M=0.76-0.52L^{-1}-0.24L^{-2}. \qquad (3)$$

This equation approximates eq (1) within about 0.5 percent over the range from $L=0.75$ to $L=2.0$. The compensating effect of some pairs of terms neglected in the expansions makes the approximation better than would be expected at first glance.

In the range above $L=2$ the empirical function is nearly linear over considerable region. A useful approximation here is

$$F/M=0.164L+0.125. \qquad (4)$$

Values computed from eq (4) differ from values given by eq (1) by less than 4 percent from $L=2$ to $L=4.5$. The upper limit given is above the normal range of validity of eq (1).

4. Equation Predicted by Statistical Theory

The dashed line in figure 1 shows the function

$$F/M=(1/3)(L-L^{-2}) \qquad (5)$$

predicted by the statistical theory of rubber elasticity [2, 6, 7] for the entropy component of the "equilibrium" stress of an ideal network. The agreement between the two functions in the region between $L=0.5$ and $L=1$ is quite striking. Calculation of numerical values shows that the difference is less than 4 percent throughout this interval. Since the precision of the available compression data is no better than this figure, no statement can be made as to which function conforms better to experimental observations in this region.

This agreement, together with the conclusion of Treloar [4] that eq (5) adequately represents his experimental data in this region, confirms the validity of eq (1) here, as already demonstrated directly by figures 2 and 3. Recent direct measurements of compression of specimens with lubricated surfaces by Forster [8] have also shown conformity to eq (5) or eq (1) from $L=0.67$ to $L=1$.

In the region of tension, however, the difference between the two functions becomes steadily greater as L increases. The value of (1/3) ($L-L^{-2}$) is about 4 percent greater than that of the empirical function at $L=1.15$, about 32 percent greater at $L=2.0$, and about 57 percent greater at $L=3.0$. These differences preclude the use of eq (5) for values of L above about 1.15. The slope of the graph of (1/3) ($L-L^{-2}$) against L approaches 0.333 as L is increased; the slope of a similar graph of the empirical function is 0.164 for a considerable region beyond $L=2$, as shown by eq (4).

Equation (5) is intended to apply to the entropy component of the stress of an ideal network of permanent cross links under "equilibrium" conditions. Equation (1), on the other hand, represents experimental values of stress obtained on conventional pure-gum vulcanizates after a fixed period of creep. Most, if not all, of the divergence between the two equations is to be ascribed to these differences. In the case of natural rubber at least, the divergence is associated with the entropy and can not be ascribed to changes of internal energy on stretching [2].

The observations are consistent with the representation of a conventional pure-gum vulcanizate as a network differing from the ideal network in having labile cross links that disappear during extension, the number disappearing increasing slightly with time at a fixed elongation and increasing considerably with increasing elongation at a fixed time. The cross links which have disappeared reform in time if the elongation is reduced. The data would indicate that the cross links are not affected by moderate compression. Such a network would be similar to an actual vulcanizate in showing creep in tension and a stress-modulus ratio increasingly less than the ideal as the elongation increases.

5. Equation Assuming Hooke's Law for Stress on Deformed Section

Another equation that has often been suggested for representing the stress-strain curve is obtained by assuming the constancy of Young's modulus M with the stress based on the stressed cross section. The result is

$$F/M=1-L^{-1}. \qquad (6)$$

Calculation shows that this function is not at all satisfactory in the compression region. This function yields values about 11.5 percent less in absolute magnitude than the empirical function at $L=0.5$ and the difference falls below 4 percent when L is greater than 0.85.

In the region of tension eq (6) gives a value about 4 percent greater than that given by eq (1) at $L=1.18$. The difference has a maximum of about 13.2 percent at $L=2.2$ and falls to 9 percent at $L=3$.

It is clearly inaccurate to assume the validity of eq (6) up to about $L=2$, as has been done by some previous workers. If one should attempt to represent observations in the tension region by assuming an apparent modulus 6.6 percent less than M, positive and negative differences of about 6.6 percent would be obtained between the values from eq (6) and those observed. In the compression region, however, the differences would be increased by about 6.6 percent to become as great as about 18 percent at $L=0.5$. This is not a satisfactory representation of the observed data, which are given by eq (1) within the experimental accuracy of the observations discussed.

6. Mooney-Rivlin Equation

The work of Mooney [9] and Rivlin [5, 6, 7, 10] leads to an equation which may be written in the case of simple compression or tension, as

$$F/2=S_1(L-L^{-2})+S_2(1-L^{-3}) \tag{7}$$

where S_1 and S_2 are, in general, functions of L. In a region where Mooney's assumptions are valid S_1 and S_2 have constant values C_1 and C_2, respectively.

If one wishes to put eq (7) into a form suitable for a convenient plot he has two choices, suggested by the following two modifications of the equation:

$$\frac{F}{2(L-L^{-2})}=S_1+S_2L^{-1} \tag{8}$$

$$\frac{F}{2(1-L^{-3})}=S_1L+S_2 \tag{9}$$

More general relations are obtained by dividing both sides of each equation by M, the slope of the stress-strain curve at $L=1$.

$$\frac{F}{2M(L-L^{-2})}=\frac{S_1}{M}+\frac{S_2}{M}L^{-1} \tag{10}$$

$$\frac{F}{2M(1-L^{-3})}=\frac{S_1}{M}L+\frac{S_2}{M}. \tag{11}$$

Figure 4 shows a plot of Φ defined as $F/[2M(L-L^{-2})]$ against L^{-1} when F is obtained from the empirical equation, eq (1), giving A the value of 0.38. Correspondingly figure 5 shows a plot of θ defined as $F/[2M(1-L^{-3})]$ against L also utilizing eq (1). It will be noted, of course, that the compression regions appear on opposite sides of the value corresponding to $L=1$ in the two plots. From the equations it is obvious that the slope of the curve in figure 4 at any point is the intercept of the tangent to the curve of figure 5 at the corresponding point and vice versa. Furthermore it can readily be shown from their definitions that at $L=1$ both Φ and θ have the same value, namely 1/6, and that this value is independent of the form of the stress-strain relation. Consequently from eq (10) or (11) it is clear that $M=6(S_1+S_2)_{L=1}$.

It will be noted from figures 4 and 5 that no portions of the curves are linear for any extended range. However, over the range from $L=0.5$ to $L=1$ the values of Φ and θ are in reasonable agreement with the prediction of the statistical theory of rubber elasticity which would set $S_1/M=0.1667$ and $S_2/M=0$. The actual value of S_1/M, as calculated from eq (1), falls from 0.223 to 0.1267 in the range mentioned, while the value of S_2/M rises from -0.03 to $+0.04$. The average values over the range may well be taken as those predicted by the statistical theory. It will be noted, as already mentioned, that both the statistical theory and the empirical function require that at $L=1$ $\Phi=\theta=S_1/M+S_2/M=0.1667$.

Figures 4 and 5 show that over a range from perhaps $L=1.5$ to about $L=3.5$ the values of Φ and θ fall

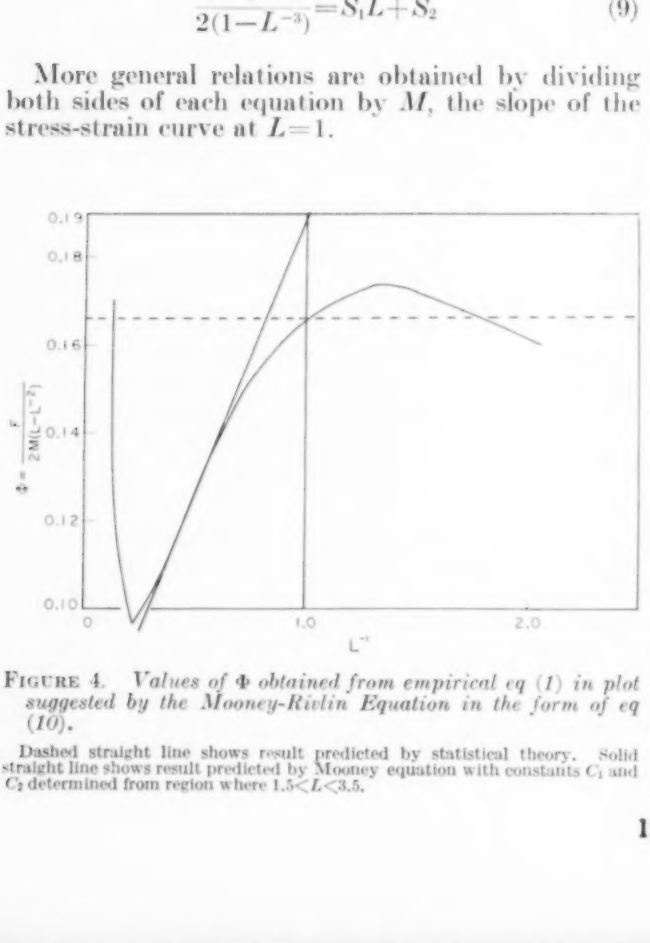

FIGURE 4. *Values of Φ obtained from empirical eq (1) in plot suggested by the Mooney-Rivlin Equation in the form of eq (10).*

Dashed straight line shows result predicted by statistical theory. Solid straight line shows result predicted by Mooney equation with constants C_1 and C_2 determined from region where $1.5<L<3.5$.

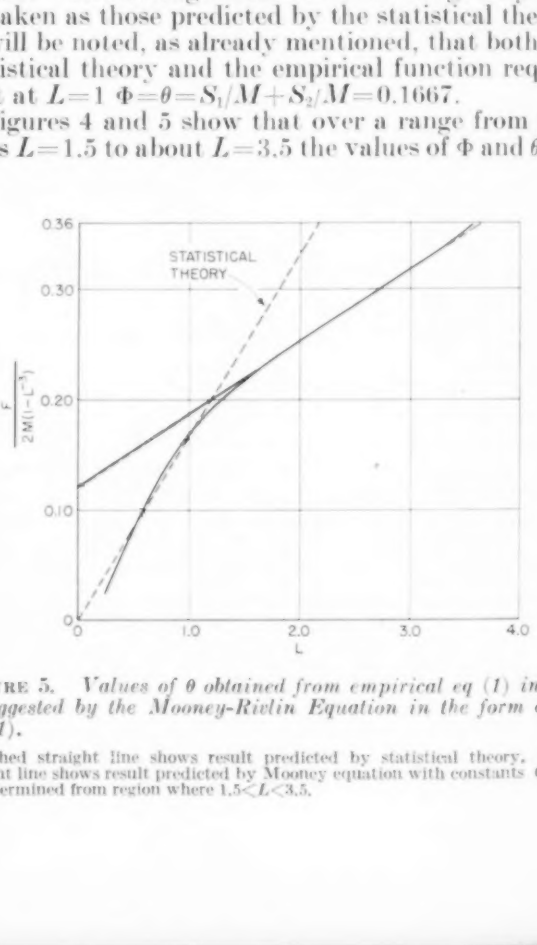

FIGURE 5. *Values of θ obtained from empirical eq (1) in plot suggested by the Mooney-Rivlin Equation in the form of eq (11).*

Dashed straight line shows result predicted by statistical theory. Solid straight line shows result predicted by Mooney equation with constants C_1 and C_2 determined from region where $1.5<L<3.5$.

approximately on a straight line in accordance with the prediction of the Mooney eq (9) calling for the constancy of S_1/M and S_2/M. It is clear that this is only an approximate constancy arising from the fact that the value of S_1/M passes through a minimum in this region, at a point of inflection of each curve, while the value of S_2/M is correspondingly passing through a maximum. Values of S_1/M and S_2/M at this point of inflection may be read from the solid lines of figures 4 and 5, but may be obtained more accurately by computation from eq (1). The values obtained by either procedure are $[S_1/M]_{min}=0.064$ and $[S_2/M]_{max}=0.124$. These values correspond to $L=2.3-2.4$. A straight line corresponding to a larger value of S_1/M and a smaller value of S_2/M would approximate the functions Φ and θ over a slightly larger range of values of L at the expense of accuracy of representation of the functions.

Over the important intermediate range for L between 1.0 and 1.5, however, neither statistical theory nor Mooney equation can satisfactorily represent Φ and θ, as shown in figures 4 and 5. Instead, S_1/M decreases continuously from 0.1267 to 0.08 in this transition interval while S_2/M increases continuously from 0.04 to 0.096.

A number of previous workers [11 to 16] have evaluated the Mooney constants C_1 and C_2 from stress-strain observations in tension, largely between $L=1.1$ and $L=2.0$. Almost all the specimens used differed considerably in degree of vulcanization from those for which eq (1) has been shown to be valid. Even more significantly, most of the measurements were apparently made after a prescribed procedure of prestretching and recovery, whereas the other observations mentioned up to this point were made with specimens stretched for the first time. From plots of the type suggested by eq (8) it was concluded [11 to 15] that C_2 had a value of approximately 1.03 kg/cm^2 for pure-gum vulcanizates containing sulfur and an accelerator. Under the same conditions C_1 had values ranging from about 1.0 to 3.0 kg/cm^2. Among more than 25 values given in these papers [11 to 15] there are only two instances where the same compound was investigated at different times of cure. In one case [11] covering 12, 15, and 17 min of cure C_1 increased ,C_2 decreased, and their sum increased slightly with increasing cure; in the other case [12] with cures of 10 and 30 min C_1 and the sum increased, but there was little change in C_2.

Blackwell [16] using plots of the type suggested by eq (9) obtained values for C_2 of about 0.8 kg/cm^2 and for C_1 of about 1.25 or 1.55 kg/cm^2 depending on the kind of rubber, but showing no variation with time of cure. It appears, from an examination of the conditions employed, that even at the shortest time of cure his vulcanizates had already reached a point where little change of modulus would be expected.

It is clear that under the experimental conditions employed by these workers, the value of C_2/C_1 is smaller than $0.124/0.064=1.94$ as given by the empirical function. As a result the size of the transition interval (in which S_2 increases from zero to a nearly constant value) is smaller than that given by the empirical function. The reason for the discrepancy is not clear but it is probably related to the very high degree of vulcanization and the previous mechanical history of the specimens employed by the British workers, as contrasted with those used by Martin, Roth, and Stiehler [1] and the observers whose results are given in figures 2 and 3.

In any case, unless Φ and θ show a sharp discontinuity in slope exactly at $L=1$, a transition interval must exist and must lie in the region of low elongations. Consequently linear extrapolation of tension data to $L=1$ is not justified in the region of low elongations in plots similar to figures 4 and 5. It may be concluded that the Mooney equation is not valid in the region of low elongations, since S_1 and S_2 show no approach to constancy in this region. Some of the implications of this conclusion in terms of the strain energy function have been pointed out in a recent review [2].

Thomas [17] has applied a correction term to the stress predicted by the statistical theory. Although this operation yields a graph of Φ qualitatively similar to figure 4 the stress-strain relationship predicted by Thomas's work departs so markedly from the solid line shown in figure 1 that the correction can not be regarded as satisfactory.

7. Young's Modulus from Experimental Observations

It is often a matter of considerable theoretical and practical importance to obtain a value of Young's modulus M from experimental observations of stress at one or more finite strains.

Since M is defined as the slope of the graph of F against L at $L=1$, the simplest method of determining its value would be to draw a tangent to the curve at this point and measure its slope. For values of L greater than 0.5 a plot of observed values of stress F against L will have the shape given by the solid curve of figure 1; the ordinates will simply be those shown, multiplied by the constant factor M. It can be seen from figure 1 that the curvature at $L=1$ is so great that the simplest method would not be very satisfactory. The tangent would be determined mainly by a few observations near $L=1$ where the experimental precision is not high.

Equations (1), (2a), (5), and (6) each represent satisfactorily the observed values of F in the region very near $L=1$, but differ in their ranges of applicability. Each equation can be put into such a form as to suggest coordinates that will give a linear plot near $L=1$, from which M may be obtained. Since eq (1) represents the data over a greater range than any of the others, a plot based on it can include a greater range of experimental observations than any of the others. The most satisfactory coordinates for a plot based on eq (1) are $\log F/(L^{-1}-L^{-2})$ and $(L-L^{-1})$, as illustrated by figures 2 and 3, where $\log M$ is obtained as the intercept. If only tension

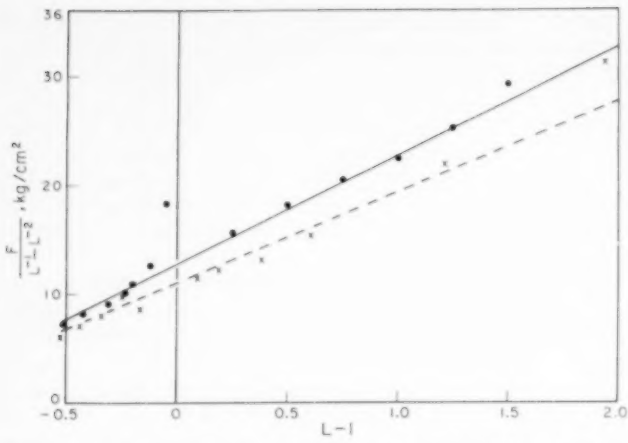

FIGURE 6. *Determination of constants in empirical eq (1) from plot suggested by approximation given as eq (2a).*

●, Data of Treloar [4]. ×, Data of Rivlin and Saunders [5].

data or only compression data are available this represents an extrapolation, but if data in both regions can be plotted, as in figures 2 and 3, the advantages of interpolation can be realized. A plot of this form shows by its linearity whether eq (1) is valid for the particular observations concerned and, if it is linear, its slope gives the value of A. Even if the plot should not be linear, the procedure of obtaining log M by interpolation should be satisfactory.

If the range of observations is not too great, a plot based on the approximation given by eq (2a) can be made. It can be seen that a plot of $F/(L^{-1}-L^{-2})$ against $(L-1)$ should yield a straight line with intercept M and with slope $2AM$. This is a thoroughly satisfactory procedure for observations between $L=0.75$ and $L=2.0$ since the approximation represents eq (1) within 0.5 percent over this region. Figure 6, showing this type of plot for the data of Treloar [4] and Rivlin and Saunders [5] may be compared with figure 3 showing the applicability of eq (1) to the same data.

Under conditions where the validity of eq (1) with $A=0.38$ may be reasonably presumed, M may be calculated from the equation, using a single observation of stress and the corresponding strain. If a repetition of the calculation with other observed values gives a constant value for M within experimental error, the validity of the equation is confirmed and the average obtained by such calculations may be taken as the desired Young's modulus.

The equation predicted by the statistical theory of rubber elasticity, eq (5), in spite of its disagreement with observed values in the tension region, has been frequently used to determine M. Since values of F/M predicted by this equation in this region are systematically too high as noted in figure 1, the calculated values of M are systemically too small by the amounts indicated in section 4, unless the results are extrapolated in some manner to $L=1$. The simplest graph based on eq (5) calls for a plot of F against $(L-L^{-2})$ for a determination of M from the slope. This procedure has been followed in recent work of Charlesby and von Arnim [18] on rubber cross linked by radiation. Unlike the conventional vulcanizates considered in the present paper, this material appears to conform to eq (5) up to high elongations. A similar method employed by Bueche [19] requires a plot of FL^2 against L^3 for a determination of M by extrapolating the observed slope to $L=1$.

A more sensitive method than either of these is to plot $F/(L-L^{-2})$ against L as in the work of Gee [20] or against L^{-1} as in other work [5, 11 to 15, 21]. These graphs should have the constant value $M/3$ where the statistical equation is applicable. This has indeed been found true [4, 8] in the compression region for L between 0.1 and 1. In the tension region, however, the value is not constant, and a linear extrapolation to $L=1$ is not justified, as already mentioned. Figure 4, differing from the latter plot only by two constant factors, shows the curvature to be expected near $L=1$.

The following modifications of eq (6)

$$F=M(1-L^{-1}) \tag{12}$$

and

$$FL=M(L-1) \tag{13}$$

show that straight lines of constant slope M would result from a plot of F against $(1-L^{-1})$ or of FL against $(L-1)$, if Hooke's law based on actual section were valid. It has been shown in section 5 that values of F/M obtained on this assumption are about 4 percent too high at $L=1.18$. If greater accuracy than this is desired, the slope must be obtained from lower values of L. The use of eqs (12) and (13) for L between 1.0 and 1.1 is a reasonably satisfactory approximation since the value of F/M obtained is less than 2.5 percent too great in this region. Baldwin, Ivory, and Anthony [22] have obtained linear plots of eq (13) for pure-gum vulcanizates of nitrile rubber and GR–I in this region.

Considerations outlined more fully in the section on the Mooney-Rivlin equation show that M can be obtained by determining the value of $F/2(L-L^{-2})$ or the value of $F/2(1-L^{-3})$ at $L=1$ since these quantities both are equal to $M/6$ at this point. If these operations are done graphically, curves similar to figures 4 and 5 are obtained, except that the ordinates are multiplied by a constant factor. It is clear that the curvature in the region of low elongations is so great as to make satisfactory extrapolation quite difficult.

In summary, Young's modulus M can best be determined from the intercept of a plot like figure 2 or 3, based on eq (1). This will permit the utilization of observations over the widest possible range of values of L in compression and tension. A plot like figure 6, based on the approximation given by eq (2a) is thoroughly satisfactory between $L=0.75$ and $L=2.0$. It is considerably superior to any of those based on eq (5), (6), or (7). The use of a plot based on eq (6) will give apparent values of M less than 2.5 percent too low if observations are confined to elongations of less than 10 percent. The use of a plot based on eq (5) will be satisfactory in the com-

pression region and also will give apparent values of M less than about 2.7 percent too low if observations are confined to elongations of less than 10 percent. The use of a plot based on eq (7), differing only in scale from figure 4 or 5, is not satisfactory for obtaining M by extrapolation because of its large curvature in the region from $L=1.0$ to $L=1.5$.

8. Conclusions

The empirical function of Martin, Roth, and Stiehler [1] represented by eq (1) where A has the value of 0.38 may be regarded as an adequate representation of the available experimental data covering both the compression and tension of pure-gum vulcanizates. The stress and strain are to be measured after a constant time of creep. The approximate validity extends over the range $0.5<L<3.5$. The success of the single empirical function in representing data obtained in both compression and tension over a range as great as this is regarded as very significant.

In the range of values of L from 0.5 to 1.0 (compression) the empirical function gives results in agreement with the predictions of the statistical theory of rubber elasticity. After representing the stress and strain in a transition region extending from $L=1.0$ to 1.5, the empirical function gives approximately constant coefficients C_1 and C_2 in the Mooney equation over the range from 1.5 to about 3.5.

The behavior of the empirical function in the transition region from $L=1.0$ to $L=1.5$ shows that the statistical theory of elasticity fails to represent the experimental data even at the lowest elongations while proving satisfactory in the compression region. The Mooney-Rivlin equation also fails to furnish adequate representation of the experimental data at low elongations.

The most satisfactory method of determining Young's modulus from experimental observations of stress and strain in pure-gum vulcanizates involves a plot of log $F/(L^{-1}-L^{-2})$ against $(L-L^{-1})$. For observations within the range of $L=0.75$ to 2.0 the simpler plot of $F/(L^{-1}-L^{-2})$ against $(L-1)$ is thoroughly satisfactory. In both cases M is obtained from the intercept, and the constant A in eq (1) is determined from the slope.

WASHINGTON, September 16, 1957.

9. References

[1] G. M. Martin, F. L. Roth, and R. D. Stiehler, Behavior of "pure-gum" rubber vulcanizates in tension, Trans. Inst. Rubber Ind. **32,** 189 (1956).

[2] L. A. Wood, The elasticity of rubber, J. Wash. Acad. Sci. **47,** 281 (1957).

[3] J. R. Sheppard and W. J. Clapson, Compression stress-strain of rubber, Ind. Eng. Chem. **24,** 782 (1932); Rubber Chem. and Technol. **6,** 126 (1933).

[4] L. R. G. Treloar, Stress-strain data for vulcanized rubber under various types of deformation, Trans. Faraday Soc. **40,** 59 (1944); Rubber Chem and Techol. **17,** 813 (1944).

[5] R. S. Rivlin and D. W. Saunders, Large elastic deformations of isotropic materials, VII, Phil. Trans. Roy. Soc. London [A] **243,** 251 (1951).

[6] L. R. G. Treloar, The physics of rubber elasticity (Oxford University Press, London, 1949).

[7] L. R. G. Treloar, Structure and mechanical properties of rubber-like materials, Chapter 5 in book "Die Physik der Hochpolymeren", Vol. IV. Edited by H. A. Stuart (Springer-Verlag, Berlin, 1956).

[8] M. J. Forster, Unilateral compression of rubber, J. Appl. Phys. **26,** 1104 (1955).

[9] M. Mooney, A theory of large elastic deformation, J. Appl. Phys. **11,** 582 (1940).

[10] R. S. Rivlin, Large elastic deformations of isotropic materials, Phil. Trans. Roy. Soc. London [A] **240,** 459 and 491 (1948).

[11] R. S. Rivlin and D. W. Saunders, Free energy of deformation for vulcanized rubber, Trans. Faraday Soc. **48,** 200 (1952).

[12] S. M. Gumbrell, L. Mullins, and R. S. Rivlin, Departure of the elastic behavior of rubber in simple extension from the kinetic theory, Trans. Faraday, Soc. **49,** 1495 (1953); Rubber Chem. and Technol. **28,** 24 (1955).

[13] R. S. Rivlin and A. G. Thomas, Rupture of rubber. I, Characteristic energy for tearing, J. Polymer Sci. **10,** 291 (1953).

[14] A. G. Thomas, Rupture of rubber. II, Strain concentration at an incision, J. Polymer Sci. **18,** 177 (1955).

[15] H. W. Greensmith and A. G. Thomas, Rupture of rubber. III, Determination of tear properties, J. Polymer Sci. **18,** 189 (1955).

[16] R. F. Blackwell, Quantitative characterization of cure, Trans. Inst. Rubber Ind. **28,** 75 (1952); Rubber Chem. and Technol. **25,** 430 (1952).

[17] A. G. Thomas, Departure from the statistical theory of rubber elasticity, Trans. Faraday Soc. **51,** 569 (1955).

[18] A. Charlesby and E. von Arnim, Cross-linking of oriented rubber, J. Polymer Sci. **25,** 151 (1957).

[19] A. M. Bueche, An investigation of the theory of rubber elasticity using irradiated polydimethylsiloxanes. J. Polymer Sci. **19,** 297 (1956).

[20] G. Gee, Elastic behavior of dry and swollen rubbers, Trans. Faraday Soc. **42,** 585 (1946); Rubber Chem. and Technol. **20,** 442 (1947).

[21] A. N. Gent and R. S. Rivlin, Experiments on the mechanics of rubber. I, Everson of a tube, Proc. Phys. Soc. (London) [B] **65,** 118 (1952).

[22] F. P. Baldwin, J. E. Ivory, and R. L. Anthony, Experimental examination of the statistical theory of rubber elasticity; Low extension studies, J. Appl. Phys. **26,** 750 (1955); Rubber Chem. and Technol. **29,** 227 (1956).

Journal of Research of the National Bureau of Standards Vol. 60, No. 3, March 1958 Research Paper 2838

Tables for Diagonalizing Second-Order Matrices

R. E. Trees and C. DeW. Coleman

Sets of tables are given to facilitate the evaluation of the eigenvalues and eigenvectors of second-order matrices.

The tables were prepared to facilitate hand computation of the eigenvalues and eigenvectors of a second-order matrix. A straightforward calculation with a desk computer requires about 5 min, whereas with the tables the time is about 1 min. The times involved are sma l in either case, so that the tables are useful only because the calculation must be made frequently in some branches of physics.

It is common in theoretical atomic and nuclear spectroscopy to estimate the eigenvalues of large matrices by eliminating large off-diagonal elements and then by applying perturbation theory. The elimination of each off-diagonal element in the large matrix requires the calculation of eigenvalues and eigenvectors for a second-order matrix. The number of large elements that must be eliminated before perturbation theory can be applied is about the same as the order of the matrix in many of these applications.

The first part of the procedure just described is that of the Jacobi method, which is often used to find eigenvalues and eigenvectors of a large matrix with a digital computer. By using a computer, it is practical to reduce all nondiagonal elements to very small values, so that the subsequent application of perturbation theory is unnecessary. This machine procedure has not been used very much for hand computations, but it is hoped that with the help of these tables a reasonably fast hand calculation can be patterned along the lines of the Jacobi method.

Without any loss of generality, the second-order matrix can be assumed to have the form

$$U=\begin{pmatrix} A & C \\ C & B \end{pmatrix} \tag{1}$$

$$A\geq B \qquad C>0.$$

Ordinarily, the eigenvalues of the matrix would be computed with the formula

$$E^{\pm}=\tfrac{1}{2}(A+B)\pm\tfrac{1}{2}\sqrt{(A-B)^2+(2C)^2}. \tag{2}$$

The eigenvectors are defined as the columns of a matrix S that diagonalizes U.

$$S^{-1}U\,S=\begin{pmatrix} E^+ & 0 \\ 0 & E^- \end{pmatrix} \qquad S=\begin{pmatrix} a & -b \\ b & a \end{pmatrix}. \tag{3}$$

The matrix S would be calculated by use of the relations

$$\frac{b}{a}=\frac{E^+-A}{C}=\frac{B-E^-}{C} \tag{4a}$$

and

$$a^2+b^2=1. \tag{4b}$$

The procedure used with these tables is easily shown equivalent to the above method. The tables are in two parts, the first (tables 1 to 6) being applicable when C is less than $(A-B)$, and the second (tables 7 to 12) when it is greater. The ratio of C to $(A-B)$ is evaluated in the first case, and the ratio of $(A-B)$ to C in the second. The values of a and b are given directly by entering the tables with the value of this ratio, and each of the eigenvalues is obtained with an additional multiplication and addition. More explicitly, the angle θ is defined by the equation

$$\theta=\text{arc tan}\,\frac{2C}{(A-B)}. \tag{5}$$

It is then easy to show that

$$E^+=A+C\tan\frac{\theta}{2} \qquad E^-=B-C\tan\frac{\theta}{2} \tag{6a}$$

and

$$a=\cos\frac{\theta}{2} \qquad b=\sin\frac{\theta}{2}. \tag{6b}$$

The tables list $\tan\theta/2$, $\sin\theta/2$, and $\cos\theta/2$ as functions of the ratio $C/(A-B)$ when C is less than $(A-B)$, and as functions of $(A-B)/C$ when C is greater than $(A-B)$. The method could, of course, be applied by using tables of trigonometric functions that have already been published. An additional step of evaluating θ explicitly with relation (5) is required, preferably with tables of the arc tan function. It is then necessary to refer to one or more other sets of tables to determine the functions of the half angle.

An example is given to illustrate the use of the tables with a symmetric third-order matrix. Successive lines of the matrix correspond to the transformed form of the original matrix at successive stages, the given matrix having the element on the top line in each square (only the upper-right half of the matrix is given).

39097	1795	−1130
39478	0	−871
39478	−450	−745
	31021	1130
(25)	30640	1340
	31450	0
		29233
(50)	(0)	29233
		29423
39553	31425	28373
(39555)	(31418)	(28378) (exact values).

To get the second line, a rotation is carried out, which reduces the element 1795 to zero;

$$\begin{matrix} 39097 & 1795 & -1130 \\ 31021 & (0.222) & 1130 \end{matrix} \quad \begin{pmatrix} 0.21202 & 0.97825 \\ 0.20741 & \end{pmatrix} \quad \begin{matrix} 39478 & 0 & -871 \\ 30640 & & 1340. \end{matrix}$$

The ratio of C (i. e., 1795) to $A-B$ (i. e., 8076) was taken to three significant figures, $(C/(A-B)=0.222)$ and the values of the corresponding trigonometric functions (given in parentheses) were taken direct from the tables without interpolation. The new values of the matrix elements are given on the right-hand side;

$$\begin{aligned} 39478&=39097+1795\times 0.21202 \\ 30640&=31021-1795\times 0.21202 \\ -871&=(-1130)\times 0.97825+1130\times 0.20741 \\ 1340&=1130\times 0.97825+(-1130)\times(-0.20741). \end{aligned}$$

The largest nondiagonal element in the matrix is now 1340, and to get the third line of the matrix a similar rotation is carried out to reduce this to zero;

$$\begin{matrix} 30640 & 1340 & 0 \\ 29233 & (.952) & -871 \end{matrix} \quad \begin{pmatrix} 0.60432 & 0.85586 \\ 0.51721 & \end{pmatrix} \quad \begin{matrix} 31450 & 0 & -450 \\ 28423 & & -745. \end{matrix}$$

The nondiagonal elements are reduced to less than a tenth the difference between the diagonal elements they connect at this stage. The perturbations—i. e., the ratio of the square of the nondiagonal element to the difference between the elements it connects—are inserted on the lower-left half of of the matrix and combined with the diagonal elements to give the estimated eigenvalues 39553, 31425, and 28373. These agree with the exact values to 0.07 percent of the spread of eigenvalues or better. With practice, successive rows of the matrix can be written down without recopying the previous pair of rows. After several rotations are carried out, the matrix must be recopied, and the previous stages of the calculation checked by verifying the constancy of the trace and the norm. The eigenvectors can be obtained at the same time, but the time and effort required is approximately doubled.

C/ A−B		0.000	0.001	0.002	0.003	0.004	0.005	0.006	0.007	0.008	0.009
0.000	TAN	0.00000	0.00100	0.00200	0.00300	0.00400	0.00500	0.00600	0.00700	0.00800	0.00900
	SIN	0.00000	0.00100	0.00200	0.00300	0.00400	0.00500	0.00600	0.00700	0.00800	0.00900
	COS	1.00000	1.00000	1.00000	1.00000	0.99999	0.99999	0.99998	0.99998	0.99997	0.99996
0.010	TAN	0.01000	0.01100	0.01200	0.01300	0.01400	0.01500	0.01600	0.01700	0.01799	0.01899
	SIN	0.01000	0.01100	0.01200	0.01300	0.01400	0.01499	0.01599	0.01699	0.01799	0.01899
	COS	0.99995	0.99994	0.99993	0.99992	0.99990	0.99989	0.99987	0.99986	0.99984	0.99982
0.020	TAN	0.01999	0.02099	0.02199	0.02299	0.02399	0.02498	0.02598	0.02698	0.02798	0.02898
	SIN	0.01999	0.02099	0.02198	0.02298	0.02398	0.02498	0.02597	0.02697	0.02797	0.02896
	COS	0.99980	0.99978	0.99976	0.99974	0.99971	0.99969	0.99966	0.99964	0.99961	0.99958
0.030	TAN	0.02997	0.03097	0.03197	0.03296	0.03396	0.03496	0.03595	0.03695	0.03795	0.03894
	SIN	0.02996	0.03096	0.03195	0.03295	0.03394	0.03494	0.03593	0.03692	0.03792	0.03891
	COS	0.99955	0.99952	0.99949	0.99946	0.99942	0.99939	0.99935	0.99932	0.99928	0.99924
0.040	TAN	0.03994	0.04093	0.04193	0.04292	0.04392	0.04491	0.04590	0.04690	0.04789	0.04888
	SIN	0.03990	0.04090	0.04189	0.04288	0.04387	0.04486	0.04585	0.04685	0.04784	0.04882
	COS	0.99920	0.99916	0.99912	0.99908	0.99904	0.99899	0.99895	0.99890	0.99886	0.99881
0.050	TAN	0.04988	0.05087	0.05186	0.05285	0.05384	0.05483	0.05583	0.05682	0.05781	0.05880
	SIN	0.04981	0.05080	0.05179	0.05278	0.05377	0.05475	0.05574	0.05672	0.05771	0.05869
	COS	0.99876	0.99871	0.99866	0.99861	0.99855	0.99850	0.99845	0.99839	0.99833	0.99828
0.060	TAN	0.05979	0.06077	0.06176	0.06275	0.06374	0.06473	0.06571	0.06670	0.06769	0.06867
	SIN	0.05968	0.06066	0.06165	0.06263	0.06361	0.06459	0.06557	0.06655	0.06753	0.06851
	COS	0.99822	0.99816	0.99810	0.99804	0.99797	0.99791	0.99785	0.99778	0.99772	0.99765
0.070	TAN	0.06966	0.07065	0.07163	0.07262	0.07360	0.07458	0.07557	0.07655	0.07753	0.07851
	SIN	0.06949	0.07047	0.07145	0.07242	0.07340	0.07438	0.07535	0.07633	0.07730	0.07827
	COS	0.99758	0.99751	0.99744	0.99737	0.99730	0.99723	0.99716	0.99708	0.99701	0.99693
0.080	TAN	0.07949	0.08048	0.08146	0.08244	0.08342	0.08439	0.08537	0.08635	0.08733	0.08831
	SIN	0.07924	0.08022	0.08119	0.08216	0.08313	0.08410	0.08506	0.08603	0.08700	0.08796
	COS	0.99686	0.99678	0.99670	0.99662	0.99654	0.99646	0.99638	0.99629	0.99621	0.99612
0.090	TAN	0.08928	0.09026	0.09123	0.09221	0.09318	0.09416	0.09513	0.09610	0.09708	0.09805
	SIN	0.08893	0.08989	0.09086	0.09182	0.09278	0.09374	0.09470	0.09566	0.09662	0.09758
	COS	0.99604	0.99595	0.99586	0.99578	0.99569	0.99560	0.99551	0.99541	0.99532	0.99523
0.100	TAN	0.09902	0.09999	0.10096	0.10193	0.10290	0.10387	0.10483	0.10580	0.10677	0.10773
	SIN	0.09854	0.09949	0.10045	0.10140	0.10236	0.10331	0.10426	0.10521	0.10617	0.10711
	COS	0.99513	0.99504	0.99494	0.99485	0.99475	0.99465	0.99455	0.99445	0.99435	0.99425
0.110	TAN	0.10870	0.10967	0.11063	0.11159	0.11256	0.11352	0.11448	0.11544	0.11640	0.11736
	SIN	0.10806	0.10901	0.10996	0.11090	0.11185	0.11279	0.11374	0.11468	0.11562	0.11656
	COS	0.99414	0.99404	0.99394	0.99383	0.99373	0.99362	0.99351	0.99340	0.99329	0.99318
0.120	TAN	0.11832	0.11928	0.12024	0.12119	0.12215	0.12311	0.12406	0.12502	0.12597	0.12692
	SIN	0.11750	0.11844	0.11938	0.12031	0.12125	0.12218	0.12312	0.12405	0.12498	0.12591
	COS	0.99307	0.99296	0.99285	0.99274	0.99262	0.99251	0.99239	0.99228	0.99216	0.99204
0.130	TAN	0.12787	0.12883	0.12978	0.13073	0.13168	0.13263	0.13357	0.13452	0.13547	0.13641
	SIN	0.12684	0.12777	0.12870	0.12962	0.13055	0.13147	0.13240	0.13332	0.13424	0.13516
	COS	0.99192	0.99180	0.99168	0.99156	0.99144	0.99132	0.99120	0.99107	0.99095	0.99082
0.140	TAN	0.13736	0.13830	0.13925	0.14019	0.14113	0.14207	0.14301	0.14395	0.14489	0.14583
	SIN	0.13608	0.13700	0.13792	0.13883	0.13975	0.14066	0.14157	0.14248	0.14340	0.14430
	COS	0.99070	0.99057	0.99044	0.99032	0.99019	0.99006	0.98993	0.98980	0.98967	0.98953
0.150	TAN	0.14677	0.14771	0.14864	0.14958	0.15051	0.15144	0.15238	0.15331	0.15424	0.15517
	SIN	0.14521	0.14612	0.14703	0.14793	0.14883	0.14974	0.15064	0.15154	0.15244	0.15334
	COS	0.98940	0.98927	0.98913	0.98900	0.98886	0.98873	0.98859	0.98845	0.98831	0.98817
0.160	TAN	0.15610	0.15703	0.15796	0.15889	0.15981	0.16074	0.16166	0.16259	0.16351	0.16443
	SIN	0.15423	0.15513	0.15602	0.15692	0.15781	0.15870	0.15959	0.16048	0.16137	0.16225
	COS	0.98803	0.98789	0.98775	0.98761	0.98747	0.98733	0.98718	0.98704	0.98689	0.98675
0.170	TAN	0.16535	0.16627	0.16719	0.16811	0.16903	0.16995	0.17086	0.17178	0.17269	0.17361
	SIN	0.16314	0.16402	0.16490	0.16578	0.16666	0.16754	0.16842	0.16930	0.17017	0.17105
	COS	0.98660	0.98646	0.98631	0.98616	0.98601	0.98586	0.98572	0.98557	0.98541	0.98526
0.180	TAN	0.17452	0.17543	0.17634	0.17725	0.17816	0.17907	0.17998	0.18088	0.18179	0.18269
	SIN	0.17192	0.17279	0.17366	0.17453	0.17540	0.17626	0.17713	0.17799	0.17886	0.17972
	COS	0.98511	0.98496	0.98481	0.98465	0.98450	0.98434	0.98419	0.98403	0.98388	0.98372
0.190	TAN	0.18360	0.18450	0.18540	0.18630	0.18720	0.18810	0.18900	0.18990	0.19079	0.19169
	SIN	0.18058	0.18144	0.18229	0.18315	0.18400	0.18486	0.18571	0.18656	0.18741	0.18826
	COS	0.98356	0.98340	0.98324	0.98309	0.98293	0.98277	0.98260	0.98244	0.98228	0.98212

TABLE 2.

C/ A-B		0.000	0.001	0.002	0.003	0.004	0.005	0.006	0.007	0.008	0.009
0.200	TAN	0.19258	0.19348	0.19437	0.19526	0.19615	0.19704	0.19793	0.19882	0.19970	0.20059
	SIN	0.18911	0.18995	0.19080	0.19164	0.19248	0.19332	0.19416	0.19500	0.19584	0.19667
	COS	0.98196	0.98179	0.98163	0.98147	0.98130	0.98114	0.98097	0.98080	0.98064	0.98047
0.210	TAN	0.20148	0.20236	0.20324	0.20412	0.20501	0.20589	0.20677	0.20764	0.20852	0.20940
	SIN	0.19751	0.19834	0.19917	0.20000	0.20083	0.20166	0.20248	0.20331	0.20413	0.20495
	COS	0.98030	0.98013	0.97996	0.97980	0.97963	0.97946	0.97929	0.97912	0.97894	0.97877
0.220	TAN	0.21027	0.21115	0.21202	0.21289	0.21376	0.21463	0.21550	0.21637	0.21724	0.21811
	SIN	0.20577	0.20659	0.20741	0.20823	0.20904	0.20986	0.21067	0.21148	0.21229	0.21310
	COS	0.97860	0.97843	0.97825	0.97808	0.97791	0.97773	0.97756	0.97738	0.97721	0.97703
0.230	TAN	0.21897	0.21984	0.22070	0.22156	0.22242	0.22328	0.22414	0.22500	0.22586	0.22672
	SIN	0.21390	0.21471	0.21551	0.21632	0.21712	0.21792	0.21872	0.21951	0.22031	0.22110
	COS	0.97685	0.97668	0.97650	0.97632	0.97615	0.97597	0.97579	0.97561	0.97543	0.97525
0.240	TAN	0.22757	0.22842	0.22928	0.23013	0.23098	0.23183	0.23268	0.23353	0.23438	0.23522
	SIN	0.22190	0.22269	0.22348	0.22427	0.22506	0.22584	0.22663	0.22741	0.22819	0.22897
	COS	0.97507	0.97489	0.97471	0.97453	0.97435	0.97416	0.97398	0.97380	0.97362	0.97343
0.250	TAN	0.23607	0.23691	0.23775	0.23860	0.23944	0.24028	0.24112	0.24195	0.24279	0.24363
	SIN	0.22975	0.23053	0.23131	0.23208	0.23286	0.23363	0.23440	0.23517	0.23594	0.23670
	COS	0.97325	0.97307	0.97288	0.97270	0.97251	0.97233	0.97214	0.97195	0.97177	0.97158
0.260	TAN	0.24446	0.24530	0.24613	0.24696	0.24779	0.24862	0.24945	0.25028	0.25110	0.25193
	SIN	0.23747	0.23823	0.23900	0.23976	0.24052	0.24127	0.24203	0.24279	0.24354	0.24429
	COS	0.97140	0.97121	0.97102	0.97083	0.97065	0.97046	0.97027	0.97008	0.96989	0.96970
0.270	TAN	0.25275	0.25357	0.25440	0.25522	0.25604	0.25686	0.25767	0.25849	0.25931	0.26012
	SIN	0.24505	0.24580	0.24654	0.24729	0.24804	0.24878	0.24952	0.25027	0.25101	0.25174
	COS	0.96951	0.96932	0.96913	0.96894	0.96875	0.96856	0.96837	0.96818	0.96799	0.96779
0.280	TAN	0.26094	0.26175	0.26256	0.26337	0.26418	0.26499	0.26579	0.26660	0.26741	0.26821
	SIN	0.25248	0.25322	0.25395	0.25468	0.25542	0.25615	0.25688	0.25760	0.25833	0.25905
	COS	0.96760	0.96741	0.96722	0.96702	0.96683	0.96664	0.96644	0.96625	0.96606	0.96586
0.290	TAN	0.26901	0.26981	0.27062	0.27142	0.27221	0.27301	0.27381	0.27460	0.27540	0.27619
	SIN	0.25978	0.26050	0.26122	0.26194	0.26266	0.26337	0.26409	0.26480	0.26551	0.26622
	COS	0.96567	0.96547	0.96528	0.96508	0.96489	0.96469	0.96450	0.96430	0.96411	0.96391
0.300	TAN	0.27698	0.27777	0.27856	0.27935	0.28014	0.28093	0.28171	0.28250	0.28328	0.28407
	SIN	0.26693	0.26764	0.26835	0.26905	0.26976	0.27046	0.27116	0.27186	0.27256	0.27325
	COS	0.96372	0.96352	0.96332	0.96313	0.96293	0.96273	0.96253	0.96234	0.96214	0.96194
0.310	TAN	0.28485	0.28563	0.28641	0.28718	0.28796	0.28874	0.28951	0.29029	0.29106	0.29183
	SIN	0.27395	0.27464	0.27534	0.27603	0.27672	0.27741	0.27809	0.27878	0.27946	0.28015
	COS	0.96174	0.96155	0.96135	0.96115	0.96095	0.96075	0.96055	0.96036	0.96016	0.95996
0.320	TAN	0.29260	0.29337	0.29414	0.29491	0.29567	0.29644	0.29720	0.29797	0.29873	0.29949
	SIN	0.28083	0.28151	0.28219	0.28286	0.28354	0.28421	0.28489	0.28556	0.28623	0.28690
	COS	0.95976	0.95956	0.95936	0.95916	0.95896	0.95876	0.95856	0.95836	0.95816	0.95796
0.330	TAN	0.30025	0.30101	0.30177	0.30252	0.30328	0.30403	0.30479	0.30554	0.30629	0.30704
	SIN	0.28757	0.28823	0.28890	0.28956	0.29023	0.29089	0.29155	0.29220	0.29286	0.29352
	COS	0.95776	0.95756	0.95736	0.95716	0.95696	0.95676	0.95656	0.95636	0.95615	0.95595
0.340	TAN	0.30779	0.30854	0.30928	0.31003	0.31078	0.31152	0.31226	0.31300	0.31374	0.31448
	SIN	0.29417	0.29482	0.29548	0.29613	0.29677	0.29742	0.29807	0.29871	0.29936	0.30000
	COS	0.95575	0.95555	0.95535	0.95515	0.95495	0.95475	0.95454	0.95434	0.95414	0.95394
0.350	TAN	0.31522	0.31596	0.31670	0.31743	0.31816	0.31890	0.31963	0.32036	0.32109	0.32182
	SIN	0.30064	0.30128	0.30192	0.30255	0.30319	0.30382	0.30446	0.30509	0.30572	0.30635
	COS	0.95374	0.95354	0.95333	0.95313	0.95293	0.95273	0.95253	0.95232	0.95212	0.95192
0.360	TAN	0.32255	0.32327	0.32400	0.32472	0.32545	0.32617	0.32689	0.32761	0.32833	0.32905
	SIN	0.30697	0.30760	0.30822	0.30885	0.30947	0.31009	0.31071	0.31133	0.31195	0.31256
	COS	0.95172	0.95152	0.95131	0.95111	0.95091	0.95071	0.95050	0.95030	0.95010	0.94990
0.370	TAN	0.32976	0.33048	0.33119	0.33191	0.33262	0.33333	0.33404	0.33475	0.33546	0.33617
	SIN	0.31318	0.31379	0.31440	0.31501	0.31562	0.31623	0.31683	0.31744	0.31804	0.31865
	COS	0.94970	0.94949	0.94929	0.94909	0.94889	0.94868	0.94848	0.94828	0.94808	0.94787
0.380	TAN	0.33688	0.33758	0.33828	0.33899	0.33969	0.34039	0.34109	0.34179	0.34249	0.34318
	SIN	0.31925	0.31985	0.32045	0.32104	0.32164	0.32223	0.32283	0.32342	0.32401	0.32460
	COS	0.94767	0.94747	0.94727	0.94706	0.94686	0.94666	0.94646	0.94626	0.94605	0.94585
0.390	TAN	0.34388	0.34458	0.34527	0.34596	0.34665	0.34734	0.34803	0.34872	0.34941	0.35010
	SIN	0.32519	0.32578	0.32636	0.32695	0.32753	0.32811	0.32870	0.32927	0.32985	0.33043
	COS	0.94565	0.94545	0.94524	0.94504	0.94484	0.94464	0.94444	0.94423	0.94403	0.94383

TABLE 3.

C/	A-B	0.000	0.001	0.002	0.003	0.004	0.005	0.006	0.007	0.008	0.009
0.400	TAN	0.35078	0.35146	0.35215	0.35283	0.35351	0.35419	0.35487	0.35555	0.35623	0.35690
	SIN	0.33101	0.33158	0.33215	0.33273	0.33330	0.33387	0.33444	0.33500	0.33557	0.33613
	COS	0.94363	0.94343	0.94322	0.94302	0.94282	0.94262	0.94242	0.94222	0.94202	0.94181
0.410	TAN	0.35758	0.35825	0.35892	0.35960	0.36027	0.36094	0.36160	0.36227	0.36294	0.36360
	SIN	0.33670	0.33726	0.33782	0.33838	0.33894	0.33950	0.34005	0.34061	0.34116	0.34172
	COS	0.94161	0.94141	0.94121	0.94101	0.94081	0.94061	0.94041	0.94020	0.94000	0.93980
0.420	TAN	0.36427	0.36493	0.36560	0.36626	0.36692	0.36758	0.36824	0.36889	0.36955	0.37020
	SIN	0.34227	0.34282	0.34337	0.34392	0.34446	0.34501	0.34555	0.34609	0.34664	0.34718
	COS	0.93960	0.93940	0.93920	0.93900	0.93880	0.93860	0.93840	0.93820	0.93800	0.93780
0.430	TAN	0.37086	0.37151	0.37216	0.37282	0.37347	0.37412	0.37476	0.37541	0.37606	0.37670
	SIN	0.34772	0.34826	0.34879	0.34933	0.34986	0.35040	0.35093	0.35146	0.35199	0.35252
	COS	0.93760	0.93740	0.93720	0.93700	0.93680	0.93660	0.93640	0.93620	0.93600	0.93580
0.440	TAN	0.37735	0.37799	0.37863	0.37927	0.37991	0.38055	0.38119	0.38183	0.38247	0.38310
	SIN	0.35305	0.35357	0.35410	0.35462	0.35515	0.35567	0.35619	0.35671	0.35723	0.35775
	COS	0.93561	0.93541	0.93521	0.93501	0.93481	0.93461	0.93441	0.93421	0.93402	0.93382
0.450	TAN	0.38374	0.38437	0.38500	0.38563	0.38626	0.38689	0.38752	0.38815	0.38877	0.38940
	SIN	0.35826	0.35878	0.35929	0.35981	0.36032	0.36083	0.36134	0.36185	0.36235	0.36286
	COS	0.93362	0.93342	0.93322	0.93303	0.93283	0.93263	0.93243	0.93224	0.93204	0.93184
0.460	TAN	0.39002	0.39065	0.39127	0.39189	0.39251	0.39313	0.39375	0.39437	0.39499	0.39560
	SIN	0.36337	0.36387	0.36437	0.36487	0.36537	0.36587	0.36637	0.36687	0.36737	0.36786
	COS	0.93165	0.93145	0.93125	0.93106	0.93086	0.93066	0.93047	0.93027	0.93008	0.92988
0.470	TAN	0.39622	0.39683	0.39744	0.39805	0.39866	0.39927	0.39988	0.40049	0.40110	0.40170
	SIN	0.36836	0.36885	0.36934	0.36983	0.37032	0.37081	0.37130	0.37178	0.37227	0.37275
	COS	0.92968	0.92949	0.92929	0.92910	0.92890	0.92871	0.92851	0.92832	0.92812	0.92793
0.480	TAN	0.40231	0.40291	0.40352	0.40412	0.40472	0.40532	0.40592	0.40652	0.40712	0.40771
	SIN	0.37324	0.37372	0.37420	0.37468	0.37516	0.37564	0.37611	0.37659	0.37707	0.37754
	COS	0.92774	0.92754	0.92735	0.92715	0.92696	0.92677	0.92657	0.92638	0.92619	0.92599
0.490	TAN	0.40831	0.40890	0.40950	0.41009	0.41068	0.41127	0.41186	0.41245	0.41304	0.41363
	SIN	0.37801	0.37848	0.37895	0.37942	0.37989	0.38036	0.38083	0.38129	0.38176	0.38222
	COS	0.92580	0.92561	0.92542	0.92522	0.92503	0.92484	0.92465	0.92445	0.92426	0.92407
0.500	TAN	0.41421	0.41480	0.41538	0.41597	0.41655	0.41713	0.41771	0.41829	0.41887	0.41945
	SIN	0.38268	0.38314	0.38360	0.38406	0.38452	0.38498	0.38544	0.38589	0.38635	0.38680
	COS	0.92388	0.92369	0.92350	0.92331	0.92312	0.92292	0.92273	0.92254	0.92235	0.92216
0.510	TAN	0.42002	0.42060	0.42118	0.42175	0.42232	0.42290	0.42347	0.42404	0.42461	0.42518
	SIN	0.38725	0.38770	0.38815	0.38860	0.38905	0.38950	0.38995	0.39039	0.39084	0.39128
	COS	0.92197	0.92178	0.92159	0.92141	0.92122	0.92103	0.92084	0.92065	0.92046	0.92027
0.520	TAN	0.42574	0.42631	0.42688	0.42744	0.42801	0.42857	0.42913	0.42970	0.43026	0.43082
	SIN	0.39172	0.39216	0.39260	0.39304	0.39348	0.39392	0.39436	0.39479	0.39523	0.39566
	COS	0.92008	0.91990	0.91971	0.91952	0.91933	0.91915	0.91896	0.91877	0.91858	0.91840
0.530	TAN	0.43137	0.43193	0.43249	0.43305	0.43360	0.43416	0.43471	0.43526	0.43581	0.43637
	SIN	0.39609	0.39652	0.39696	0.39739	0.39781	0.39824	0.39867	0.39910	0.39952	0.39995
	COS	0.91821	0.91802	0.91784	0.91765	0.91747	0.91728	0.91709	0.91691	0.91672	0.91654
0.540	TAN	0.43692	0.43747	0.43801	0.43856	0.43911	0.43965	0.44020	0.44074	0.44129	0.44183
	SIN	0.40037	0.40079	0.40121	0.40163	0.40205	0.40247	0.40289	0.40331	0.40372	0.40414
	COS	0.91635	0.91617	0.91598	0.91580	0.91562	0.91543	0.91525	0.91506	0.91488	0.91470
0.550	TAN	0.44237	0.44291	0.44345	0.44399	0.44453	0.44506	0.44560	0.44614	0.44667	0.44720
	SIN	0.40455	0.40497	0.40538	0.40579	0.40620	0.40661	0.40702	0.40743	0.40783	0.40824
	COS	0.91451	0.91433	0.91415	0.91397	0.91378	0.91360	0.91342	0.91324	0.91306	0.91287
0.560	TAN	0.44774	0.44827	0.44880	0.44933	0.44986	0.45039	0.45092	0.45144	0.45197	0.45250
	SIN	0.40865	0.40905	0.40945	0.40986	0.41026	0.41066	0.41106	0.41146	0.41186	0.41225
	COS	0.91269	0.91251	0.91233	0.91215	0.91197	0.91179	0.91161	0.91143	0.91125	0.91107
0.570	TAN	0.45302	0.45354	0.45407	0.45459	0.45511	0.45563	0.45615	0.45667	0.45719	0.45770
	SIN	0.41265	0.41305	0.41344	0.41384	0.41423	0.41462	0.41501	0.41540	0.41579	0.41618
	COS	0.91089	0.91071	0.91053	0.91035	0.91017	0.90999	0.90982	0.90964	0.90946	0.90928
0.580	TAN	0.45822	0.45873	0.45925	0.45976	0.46028	0.46079	0.46130	0.46181	0.46232	0.46283
	SIN	0.41657	0.41696	0.41734	0.41773	0.41811	0.41850	0.41888	0.41926	0.41964	0.42002
	COS	0.90910	0.90893	0.90875	0.90857	0.90840	0.90822	0.90804	0.90787	0.90769	0.90751
0.590	TAN	0.46334	0.46384	0.46435	0.46486	0.46536	0.46587	0.46637	0.46687	0.46737	0.46787
	SIN	0.42040	0.42078	0.42116	0.42154	0.42191	0.42229	0.42266	0.42304	0.42341	0.42378
	COS	0.90734	0.90716	0.90699	0.90681	0.90664	0.90646	0.90629	0.90611	0.90594	0.90576

TABLE 4.

C/ A-B		0.000	0.001	0.002	0.003	0.004	0.005	0.006	0.007	0.008	0.009
0.600	TAN	0.46837	0.46887	0.46937	0.46987	0.47037	0.47086	0.47136	0.47185	0.47235	0.47284
	SIN	0.42415	0.42453	0.42490	0.42526	0.42563	0.42600	0.42637	0.42673	0.42710	0.42746
	COS	0.90559	0.90542	0.90524	0.90507	0.90490	0.90472	0.90455	0.90438	0.90421	0.90403
0.610	TAN	0.47333	0.47382	0.47431	0.47480	0.47529	0.47578	0.47627	0.47676	0.47724	0.47773
	SIN	0.42783	0.42819	0.42855	0.42891	0.42927	0.42963	0.42999	0.43035	0.43071	0.43106
	COS	0.90386	0.90369	0.90352	0.90335	0.90317	0.90300	0.90283	0.90266	0.90249	0.90232
0.620	TAN	0.47821	0.47870	0.47918	0.47966	0.48014	0.48062	0.48110	0.48158	0.48206	0.48254
	SIN	0.43142	0.43178	0.43213	0.43248	0.43284	0.43319	0.43354	0.43389	0.43424	0.43459
	COS	0.90215	0.90198	0.90181	0.90164	0.90147	0.90130	0.90113	0.90097	0.90080	0.90063
0.630	TAN	0.48302	0.48349	0.48397	0.48444	0.48492	0.48539	0.48586	0.48633	0.48681	0.48728
	SIN	0.43494	0.43529	0.43563	0.43598	0.43632	0.43667	0.43701	0.43736	0.43770	0.43804
	COS	0.90046	0.90029	0.90012	0.89996	0.89979	0.89962	0.89946	0.89929	0.89912	0.89896
0.640	TAN	0.48775	0.48821	0.48868	0.48915	0.48962	0.49008	0.49055	0.49101	0.49148	0.49194
	SIN	0.43838	0.43872	0.43906	0.43940	0.43974	0.44007	0.44041	0.44075	0.44108	0.44142
	COS	0.89879	0.89862	0.89846	0.89829	0.89813	0.89796	0.89780	0.89763	0.89747	0.89730
0.650	TAN	0.49240	0.49286	0.49332	0.49378	0.49424	0.49470	0.49516	0.49562	0.49607	0.49653
	SIN	0.44175	0.44208	0.44242	0.44275	0.44308	0.44341	0.44374	0.44407	0.44440	0.44472
	COS	0.89714	0.89697	0.89681	0.89665	0.89648	0.89632	0.89616	0.89599	0.89583	0.89567
0.660	TAN	0.49698	0.49744	0.49789	0.49834	0.49880	0.49925	0.49970	0.50015	0.50060	0.50105
	SIN	0.44505	0.44538	0.44570	0.44603	0.44635	0.44668	0.44700	0.44732	0.44764	0.44796
	COS	0.89551	0.89534	0.89518	0.89502	0.89486	0.89470	0.89453	0.89437	0.89421	0.89405
0.670	TAN	0.50150	0.50194	0.50239	0.50284	0.50328	0.50372	0.50417	0.50461	0.50505	0.50550
	SIN	0.44828	0.44860	0.44892	0.44924	0.44956	0.44987	0.45019	0.45050	0.45082	0.45113
	COS	0.89389	0.89373	0.89357	0.89341	0.89325	0.89309	0.89293	0.89277	0.89262	0.89246
0.680	TAN	0.50594	0.50638	0.50682	0.50726	0.50769	0.50813	0.50857	0.50901	0.50944	0.50988
	SIN	0.45145	0.45176	0.45207	0.45238	0.45269	0.45300	0.45331	0.45362	0.45393	0.45424
	COS	0.89230	0.89214	0.89198	0.89182	0.89167	0.89151	0.89135	0.89119	0.89104	0.89088
0.690	TAN	0.51031	0.51074	0.51118	0.51161	0.51204	0.51247	0.51290	0.51333	0.51376	0.51419
	SIN	0.45455	0.45485	0.45516	0.45546	0.45577	0.45607	0.45637	0.45668	0.45698	0.45728
	COS	0.89072	0.89057	0.89041	0.89025	0.89010	0.88994	0.88979	0.88963	0.88948	0.88932
0.700	TAN	0.51462	0.51504	0.51547	0.51590	0.51632	0.51675	0.51717	0.51759	0.51801	0.51844
	SIN	0.45758	0.45788	0.45818	0.45848	0.45878	0.45908	0.45937	0.45967	0.45996	0.46026
	COS	0.88917	0.88901	0.88886	0.88871	0.88855	0.88840	0.88824	0.88809	0.88794	0.88778
0.710	TAN	0.51886	0.51928	0.51970	0.52012	0.52054	0.52095	0.52137	0.52179	0.52220	0.52262
	SIN	0.46055	0.46085	0.46114	0.46143	0.46173	0.46202	0.46231	0.46260	0.46289	0.46318
	COS	0.88763	0.88748	0.88733	0.88717	0.88702	0.88687	0.88672	0.88657	0.88642	0.88627
0.720	TAN	0.52303	0.52345	0.52386	0.52427	0.52469	0.52510	0.52551	0.52592	0.52633	0.52674
	SIN	0.46347	0.46375	0.46404	0.46433	0.46462	0.46490	0.46519	0.46547	0.46575	0.46604
	COS	0.88611	0.88596	0.88581	0.88566	0.88551	0.88536	0.88521	0.88506	0.88491	0.88476
0.730	TAN	0.52714	0.52755	0.52796	0.52837	0.52877	0.52918	0.52958	0.52999	0.53039	0.53079
	SIN	0.46632	0.46660	0.46688	0.46717	0.46745	0.46773	0.46801	0.46828	0.46856	0.46884
	COS	0.88462	0.88447	0.88432	0.88417	0.88402	0.88387	0.88373	0.88358	0.88343	0.88328
0.740	TAN	0.53119	0.53160	0.53200	0.53240	0.53280	0.53320	0.53359	0.53399	0.53439	0.53479
	SIN	0.46912	0.46939	0.46967	0.46994	0.47022	0.47049	0.47077	0.47104	0.47131	0.47159
	COS	0.88314	0.88299	0.88284	0.88270	0.88255	0.88240	0.88226	0.88211	0.88197	0.88182
0.750	TAN	0.53518	0.53558	0.53597	0.53637	0.53676	0.53715	0.53755	0.53794	0.53833	0.53872
	SIN	0.47186	0.47213	0.47240	0.47267	0.47294	0.47321	0.47348	0.47374	0.47401	0.47428
	COS	0.88167	0.88153	0.88138	0.88124	0.88110	0.88095	0.88081	0.88066	0.88052	0.88038
0.760	TAN	0.53911	0.53950	0.53989	0.54028	0.54067	0.54105	0.54144	0.54183	0.54221	0.54260
	SIN	0.47454	0.47481	0.47507	0.47534	0.47560	0.47587	0.47613	0.47639	0.47665	0.47691
	COS	0.88023	0.88009	0.87995	0.87980	0.87966	0.87952	0.87938	0.87923	0.87909	0.87895
0.770	TAN	0.54298	0.54336	0.54375	0.54413	0.54451	0.54489	0.54527	0.54565	0.54603	0.54641
	SIN	0.47718	0.47744	0.47770	0.47796	0.47821	0.47847	0.47873	0.47899	0.47924	0.47950
	COS	0.87881	0.87867	0.87853	0.87838	0.87824	0.87810	0.87796	0.87782	0.87768	0.87754
0.780	TAN	0.54679	0.54717	0.54755	0.54792	0.54830	0.54868	0.54905	0.54943	0.54980	0.55017
	SIN	0.47976	0.48001	0.48027	0.48052	0.48077	0.48103	0.48128	0.48153	0.48178	0.48204
	COS	0.87740	0.87726	0.87712	0.87698	0.87684	0.87671	0.87657	0.87643	0.87629	0.87615
0.790	TAN	0.55055	0.55092	0.55129	0.55166	0.55203	0.55240	0.55277	0.55314	0.55351	0.55388
	SIN	0.48229	0.48254	0.48279	0.48304	0.48329	0.48353	0.48378	0.48403	0.48428	0.48452
	COS	0.87601	0.87588	0.87574	0.87560	0.87546	0.87533	0.87519	0.87505	0.87492	0.87478

C/ A-B		0.000	0.001	0.002	0.003	0.004	0.005	0.006	0.007	0.008	0.009
0.800	TAN	0.55425	0.55461	0.55498	0.55535	0.55571	0.55608	0.55644	0.55680	0.55717	0.55753
	SIN	0.48477	0.48501	0.48526	0.48550	0.48575	0.48599	0.48623	0.48648	0.48672	0.48696
	COS	0.87464	0.87451	0.87437	0.87424	0.87410	0.87396	0.87383	0.87369	0.87356	0.87342
0.810	TAN	0.55789	0.55825	0.55861	0.55897	0.55933	0.55969	0.56005	0.56041	0.56077	0.56113
	SIN	0.48720	0.48744	0.48768	0.48792	0.48816	0.48840	0.48864	0.48888	0.48911	0.48935
	COS	0.87329	0.87316	0.87302	0.87289	0.87275	0.87262	0.87249	0.87235	0.87222	0.87209
0.820	TAN	0.56148	0.56184	0.56219	0.56255	0.56290	0.56326	0.56361	0.56397	0.56432	0.56467
	SIN	0.48959	0.48982	0.49006	0.49029	0.49053	0.49076	0.49100	0.49123	0.49146	0.49170
	COS	0.87195	0.87182	0.87169	0.87156	0.87142	0.87129	0.87116	0.87103	0.87090	0.87077
0.830	TAN	0.56502	0.56537	0.56572	0.56607	0.56642	0.56677	0.56712	0.56747	0.56782	0.56816
	SIN	0.49193	0.49216	0.49239	0.49262	0.49285	0.49308	0.49331	0.49354	0.49377	0.49400
	COS	0.87064	0.87051	0.87037	0.87024	0.87011	0.86998	0.86985	0.86972	0.86959	0.86946
0.840	TAN	0.56851	0.56885	0.56920	0.56954	0.56989	0.57023	0.57058	0.57092	0.57126	0.57160
	SIN	0.49422	0.49445	0.49468	0.49490	0.49513	0.49536	0.49558	0.49581	0.49603	0.49625
	COS	0.86933	0.86921	0.86908	0.86895	0.86882	0.86869	0.86856	0.86843	0.86831	0.86818
0.850	TAN	0.57195	0.57229	0.57263	0.57297	0.57331	0.57364	0.57398	0.57432	0.57466	0.57500
	SIN	0.49648	0.49670	0.49692	0.49714	0.49737	0.49759	0.49781	0.49803	0.49825	0.49847
	COS	0.86805	0.86792	0.86780	0.86767	0.86754	0.86741	0.86729	0.86716	0.86703	0.86691
0.860	TAN	0.57533	0.57567	0.57600	0.57634	0.57667	0.57701	0.57734	0.57767	0.57801	0.57834
	SIN	0.49869	0.49891	0.49912	0.49934	0.49956	0.49978	0.49999	0.50021	0.50043	0.50064
	COS	0.86678	0.86666	0.86653	0.86640	0.86628	0.86615	0.86603	0.86590	0.86578	0.86565
0.870	TAN	0.57867	0.57900	0.57933	0.57966	0.57999	0.58032	0.58065	0.58098	0.58131	0.58163
	SIN	0.50086	0.50107	0.50129	0.50150	0.50171	0.50193	0.50214	0.50235	0.50256	0.50277
	COS	0.86553	0.86541	0.86528	0.86516	0.86503	0.86491	0.86479	0.86466	0.86454	0.86442
0.880	TAN	0.58196	0.58229	0.58261	0.58294	0.58326	0.58359	0.58391	0.58424	0.58456	0.58488
	SIN	0.50299	0.50320	0.50341	0.50362	0.50383	0.50404	0.50424	0.50445	0.50466	0.50487
	COS	0.86429	0.86417	0.86405	0.86393	0.86380	0.86368	0.86356	0.86344	0.86332	0.86320
0.890	TAN	0.58520	0.58553	0.58585	0.58617	0.58649	0.58681	0.58713	0.58745	0.58777	0.58808
	SIN	0.50508	0.50528	0.50549	0.50570	0.50590	0.50611	0.50631	0.50652	0.50672	0.50692
	COS	0.86308	0.86295	0.86283	0.86271	0.86259	0.86247	0.86235	0.86223	0.86211	0.86199
0.900	TAN	0.58840	0.58872	0.58904	0.58935	0.58967	0.58998	0.59030	0.59061	0.59093	0.59124
	SIN	0.50713	0.50733	0.50753	0.50774	0.50794	0.50814	0.50834	0.50854	0.50874	0.50894
	COS	0.86187	0.86175	0.86163	0.86151	0.86139	0.86128	0.86116	0.86104	0.86092	0.86080
0.910	TAN	0.59156	0.59187	0.59218	0.59249	0.59280	0.59311	0.59343	0.59374	0.59405	0.59435
	SIN	0.50914	0.50934	0.50954	0.50974	0.50994	0.51013	0.51033	0.51053	0.51073	0.51092
	COS	0.86068	0.86056	0.86045	0.86033	0.86021	0.86009	0.85998	0.85986	0.85974	0.85963
0.920	TAN	0.59466	0.59497	0.59528	0.59559	0.59589	0.59620	0.59651	0.59681	0.59712	0.59742
	SIN	0.51112	0.51131	0.51151	0.51171	0.51190	0.51209	0.51229	0.51248	0.51268	0.51287
	COS	0.85951	0.85939	0.85928	0.85916	0.85904	0.85893	0.85881	0.85870	0.85858	0.85847
0.930	TAN	0.59773	0.59803	0.59834	0.59864	0.59894	0.59924	0.59955	0.59985	0.60015	0.60045
	SIN	0.51306	0.51325	0.51345	0.51364	0.51383	0.51402	0.51421	0.51440	0.51459	0.51478
	COS	0.85835	0.85824	0.85812	0.85801	0.85789	0.85778	0.85766	0.85755	0.85744	0.85732
0.940	TAN	0.60075	0.60105	0.60135	0.60165	0.60195	0.60225	0.60254	0.60284	0.60314	0.60344
	SIN	0.51497	0.51516	0.51535	0.51553	0.51572	0.51591	0.51610	0.51628	0.51647	0.51666
	COS	0.85721	0.85710	0.85698	0.85687	0.85676	0.85664	0.85653	0.85642	0.85631	0.85619
0.950	TAN	0.60373	0.60403	0.60432	0.60462	0.60491	0.60521	0.60550	0.60579	0.60609	0.60638
	SIN	0.51684	0.51703	0.51721	0.51740	0.51758	0.51777	0.51795	0.51813	0.51832	0.51850
	COS	0.85608	0.85597	0.85586	0.85574	0.85563	0.85552	0.85541	0.85530	0.85519	0.85508
0.960	TAN	0.60667	0.60696	0.60725	0.60754	0.60784	0.60813	0.60841	0.60870	0.60899	0.60928
	SIN	0.51868	0.51887	0.51905	0.51923	0.51941	0.51959	0.51977	0.51995	0.52013	0.52031
	COS	0.85497	0.85486	0.85475	0.85464	0.85453	0.85441	0.85431	0.85420	0.85409	0.85398
0.970	TAN	0.60957	0.60986	0.61014	0.61043	0.61072	0.61100	0.61129	0.61158	0.61186	0.61215
	SIN	0.52049	0.52067	0.52085	0.52103	0.52121	0.52138	0.52156	0.52174	0.52192	0.52209
	COS	0.85387	0.85376	0.85365	0.85354	0.85343	0.85332	0.85321	0.85311	0.85300	0.85289
0.980	TAN	0.61243	0.61271	0.61300	0.61328	0.61356	0.61384	0.61413	0.61441	0.61469	0.61497
	SIN	0.52227	0.52244	0.52262	0.52280	0.52297	0.52315	0.52332	0.52349	0.52367	0.52384
	COS	0.85278	0.85267	0.85257	0.85246	0.85235	0.85224	0.85214	0.85203	0.85192	0.85182
0.990	TAN	0.61525	0.61553	0.61581	0.61609	0.61637	0.61665	0.61692	0.61720	0.61748	0.61776
	SIN	0.52401	0.52419	0.52436	0.52453	0.52470	0.52488	0.52505	0.52522	0.52539	0.52556
	COS	0.85171	0.85160	0.85150	0.85139	0.85128	0.85118	0.85107	0.85097	0.85086	0.85076

TABLE 6.

C/	A-B	0.000	0.001	0.002	0.003	0.004	0.005	0.006	0.007	0.008	0.009
1.000	TAN	0.61803	0.61831	0.61859	0.61886	0.61914	0.61941	0.61968	0.61996	0.62023	0.62051
	SIN	0.52573	0.52590	0.52607	0.52624	0.52641	0.52658	0.52675	0.52691	0.52708	0.52725
	COS	0.85065	0.85055	0.85044	0.85034	0.85023	0.85013	0.85002	0.84992	0.84981	0.84971
1.010	TAN	0.62078	0.62105	0.62132	0.62159	0.62187	0.62214	0.62241	0.62268	0.62295	0.62322
	SIN	0.52742	0.52758	0.52775	0.52792	0.52808	0.52825	0.52842	0.52858	0.52875	0.52891
	COS	0.84961	0.84950	0.84940	0.84930	0.84919	0.84909	0.84899	0.84888	0.84878	0.84868
1.020	TAN	0.62349	0.62376	0.62402	0.62429	0.62456	0.62483	0.62509	0.62536	0.62563	0.62589
	SIN	0.52908	0.52924	0.52940	0.52957	0.52973	0.52989	0.53006	0.53022	0.53038	0.53054
	COS	0.84857	0.84847	0.84837	0.84827	0.84817	0.84806	0.84796	0.84786	0.84776	0.84766
1.030	TAN	0.62616	0.62642	0.62669	0.62695	0.62722	0.62748	0.62775	0.62801	0.62827	0.62853
	SIN	0.53071	0.53087	0.53103	0.53119	0.53135	0.53151	0.53167	0.53183	0.53199	0.53215
	COS	0.84756	0.84746	0.84735	0.84725	0.84715	0.84705	0.84695	0.84685	0.84675	0.84665
1.040	TAN	0.62880	0.62906	0.62932	0.62958	0.62984	0.63010	0.63036	0.63062	0.63088	0.63114
	SIN	0.53231	0.53247	0.53263	0.53278	0.53294	0.53310	0.53326	0.53341	0.53357	0.53373
	COS	0.84655	0.84645	0.84635	0.84625	0.84615	0.84605	0.84595	0.84585	0.84576	0.84566
1.050	TAN	0.63140	0.63166	0.63192	0.63217	0.63243	0.63269	0.63294	0.63320	0.63346	0.63371
	SIN	0.53388	0.53404	0.53420	0.53435	0.53451	0.53466	0.53482	0.53497	0.53513	0.53528
	COS	0.84556	0.84546	0.84536	0.84526	0.84516	0.84507	0.84497	0.84487	0.84477	0.84467
1.060	TAN	0.63397	0.63422	0.63448	0.63473	0.63499	0.63524	0.63549	0.63575	0.63600	0.63625
	SIN	0.53543	0.53559	0.53574	0.53589	0.53605	0.53620	0.53635	0.53650	0.53666	0.53681
	COS	0.84458	0.84448	0.84438	0.84429	0.84419	0.84409	0.84399	0.84390	0.84380	0.84370
1.070	TAN	0.63650	0.63675	0.63701	0.63726	0.63751	0.63776	0.63801	0.63826	0.63851	0.63876
	SIN	0.53696	0.53711	0.53726	0.53741	0.53756	0.53771	0.53786	0.53801	0.53816	0.53831
	COS	0.84361	0.84351	0.84342	0.84332	0.84322	0.84313	0.84303	0.84294	0.84284	0.84275
1.080	TAN	0.63900	0.63925	0.63950	0.63975	0.64000	0.64024	0.64049	0.64074	0.64098	0.64123
	SIN	0.53846	0.53861	0.53876	0.53890	0.53905	0.53920	0.53935	0.53949	0.53964	0.53979
	COS	0.84265	0.84256	0.84246	0.84237	0.84227	0.84218	0.84208	0.84199	0.84190	0.84180
1.090	TAN	0.64147	0.64172	0.64196	0.64221	0.64245	0.64270	0.64294	0.64318	0.64343	0.64367
	SIN	0.53993	0.54008	0.54023	0.54037	0.54052	0.54066	0.54081	0.54095	0.54110	0.54124
	COS	0.84171	0.84161	0.84152	0.84143	0.84133	0.84124	0.84115	0.84105	0.84096	0.84087
1.100	TAN	0.64391	0.64415	0.64440	0.64464	0.64488	0.64512	0.64536	0.64560	0.64584	0.64608
	SIN	0.54139	0.54153	0.54167	0.54182	0.54196	0.54210	0.54224	0.54239	0.54253	0.54267
	COS	0.84077	0.84068	0.84059	0.84050	0.84040	0.84031	0.84022	0.84013	0.84004	0.83995
1.110	TAN	0.64632	0.64656	0.64680	0.64703	0.64727	0.64751	0.64775	0.64799	0.64822	0.64846
	SIN	0.54281	0.54295	0.54310	0.54324	0.54338	0.54352	0.54366	0.54380	0.54394	0.54408
	COS	0.83985	0.83976	0.83967	0.83958	0.83949	0.83940	0.83931	0.83922	0.83912	0.83903
1.120	TAN	0.64870	0.64893	0.64917	0.64940	0.64964	0.64987	0.65011	0.65034	0.65057	0.65081
	SIN	0.54422	0.54436	0.54450	0.54464	0.54477	0.54491	0.54505	0.54519	0.54533	0.54546
	COS	0.83894	0.83885	0.83876	0.83867	0.83858	0.83849	0.83840	0.83831	0.83822	0.83813
1.130	TAN	0.65104	0.65127	0.65151	0.65174	0.65197	0.65220	0.65243	0.65267	0.65290	0.65313
	SIN	0.54560	0.54574	0.54588	0.54601	0.54615	0.54628	0.54642	0.54656	0.54669	0.54683
	COS	0.83804	0.83796	0.83787	0.83778	0.83769	0.83760	0.83751	0.83742	0.83733	0.83725
1.140	TAN	0.65336	0.65359	0.65382	0.65405	0.65428	0.65451	0.65473	0.65496	0.65519	0.65542
	SIN	0.54696	0.54710	0.54723	0.54737	0.54750	0.54764	0.54777	0.54790	0.54804	0.54817
	COS	0.83716	0.83707	0.83698	0.83689	0.83680	0.83672	0.83663	0.83654	0.83645	0.83637
1.150	TAN	0.65565	0.65587	0.65610	0.65633	0.65655	0.65678	0.65700	0.65723	0.65745	0.65768
	SIN	0.54830	0.54844	0.54857	0.54870	0.54883	0.54897	0.54910	0.54923	0.54936	0.54949
	COS	0.83628	0.83619	0.83611	0.83602	0.83593	0.83585	0.83576	0.83567	0.83559	0.83550
1.160	TAN	0.65790	0.65813	0.65835	0.65858	0.65880	0.65902	0.65925	0.65947	0.65969	0.65991
	SIN	0.54962	0.54975	0.54988	0.55001	0.55014	0.55027	0.55040	0.55053	0.55066	0.55079
	COS	0.83541	0.83533	0.83524	0.83516	0.83507	0.83498	0.83490	0.83481	0.83473	0.83464
1.170	TAN	0.66014	0.66036	0.66058	0.66080	0.66102	0.66124	0.66146	0.66168	0.66190	0.66212
	SIN	0.55092	0.55105	0.55118	0.55131	0.55143	0.55156	0.55169	0.55182	0.55195	0.55207
	COS	0.83456	0.83447	0.83439	0.83430	0.83422	0.83413	0.83405	0.83396	0.83388	0.83380
1.180	TAN	0.66234	0.66256	0.66278	0.66299	0.66321	0.66343	0.66365	0.66387	0.66408	0.66430
	SIN	0.55220	0.55233	0.55245	0.55258	0.55271	0.55283	0.55296	0.55308	0.55321	0.55333
	COS	0.83371	0.83363	0.83354	0.83346	0.83338	0.83329	0.83321	0.83313	0.83304	0.83296
1.190	TAN	0.66452	0.66473	0.66495	0.66516	0.66538	0.66559	0.66581	0.66602	0.66624	0.66645
	SIN	0.55346	0.55358	0.55371	0.55383	0.55396	0.55408	0.55421	0.55433	0.55445	0.55458
	COS	0.83288	0.83279	0.83271	0.83263	0.83254	0.83246	0.83238	0.83230	0.83222	0.83213

A–B /C		0.000	0.001	0.002	0.003	0.004	0.005	0.006	0.007	0.008	0.009
0.000	TAN	1.00000	0.99950	0.99900	0.99850	0.99800	0.99750	0.99700	0.99651	0.99601	0.99551
	SIN	0.70711	0.70693	0.70675	0.70658	0.70640	0.70622	0.70605	0.70587	0.70569	0.70551
	COS	0.70711	0.70728	0.70746	0.70764	0.70781	0.70799	0.70817	0.70834	0.70852	0.70870
0.010	TAN	0.99501	0.99452	0.99402	0.99352	0.99302	0.99253	0.99203	0.99154	0.99104	0.99055
	SIN	0.70534	0.70516	0.70498	0.70480	0.70463	0.70445	0.70427	0.70410	0.70392	0.70374
	COS	0.70887	0.70905	0.70922	0.70940	0.70958	0.70975	0.70993	0.71011	0.71028	0.71046
0.020	TAN	0.99005	0.98956	0.98906	0.98857	0.98807	0.98758	0.98708	0.98659	0.98610	0.98561
	SIN	0.70356	0.70338	0.70321	0.70303	0.70285	0.70267	0.70250	0.70232	0.70214	0.70196
	COS	0.71063	0.71081	0.71099	0.71116	0.71134	0.71151	0.71169	0.71186	0.71204	0.71221
0.030	TAN	0.98511	0.98462	0.98413	0.98364	0.98314	0.98265	0.98216	0.98167	0.98118	0.98069
	SIN	0.70178	0.70161	0.70143	0.70125	0.70107	0.70089	0.70071	0.70054	0.70036	0.70018
	COS	0.71239	0.71257	0.71274	0.71292	0.71309	0.71327	0.71344	0.71362	0.71379	0.71397
0.040	TAN	0.98020	0.97971	0.97922	0.97873	0.97824	0.97775	0.97726	0.97678	0.97629	0.97580
	SIN	0.70000	0.69982	0.69964	0.69947	0.69929	0.69911	0.69893	0.69875	0.69857	0.69839
	COS	0.71414	0.71432	0.71449	0.71467	0.71484	0.71502	0.71519	0.71536	0.71554	0.71571
0.050	TAN	0.97531	0.97483	0.97434	0.97385	0.97336	0.97288	0.97239	0.97191	0.97142	0.97093
	SIN	0.69821	0.69804	0.69786	0.69768	0.69750	0.69732	0.69714	0.69696	0.69678	0.69660
	COS	0.71589	0.71606	0.71624	0.71641	0.71659	0.71676	0.71693	0.71711	0.71728	0.71746
0.060	TAN	0.97045	0.96996	0.96948	0.96900	0.96851	0.96803	0.96754	0.96706	0.96658	0.96609
	SIN	0.69642	0.69624	0.69607	0.69589	0.69571	0.69553	0.69535	0.69517	0.69499	0.69481
	COS	0.71763	0.71780	0.71798	0.71815	0.71833	0.71850	0.71867	0.71885	0.71902	0.71919
0.070	TAN	0.96561	0.96513	0.96465	0.96417	0.96368	0.96320	0.96272	0.96224	0.96176	0.96128
	SIN	0.69463	0.69445	0.69427	0.69409	0.69391	0.69373	0.69355	0.69337	0.69319	0.69301
	COS	0.71937	0.71954	0.71971	0.71989	0.72006	0.72023	0.72041	0.72058	0.72075	0.72093
0.080	TAN	0.96080	0.96032	0.95984	0.95936	0.95888	0.95840	0.95792	0.95745	0.95697	0.95649
	SIN	0.69283	0.69265	0.69247	0.69229	0.69211	0.69193	0.69175	0.69157	0.69139	0.69121
	COS	0.72110	0.72127	0.72144	0.72162	0.72179	0.72196	0.72214	0.72231	0.72248	0.72265
0.090	TAN	0.95601	0.95553	0.95506	0.95458	0.95410	0.95363	0.95315	0.95268	0.95220	0.95172
	SIN	0.69103	0.69085	0.69067	0.69049	0.69031	0.69013	0.68995	0.68977	0.68959	0.68941
	COS	0.72283	0.72300	0.72317	0.72334	0.72352	0.72369	0.72386	0.72403	0.72420	0.72438
0.100	TAN	0.95125	0.95077	0.95030	0.94983	0.94935	0.94888	0.94840	0.94793	0.94746	0.94698
	SIN	0.68923	0.68904	0.68886	0.68868	0.68850	0.68832	0.68814	0.68796	0.68778	0.68760
	COS	0.72455	0.72472	0.72489	0.72506	0.72523	0.72541	0.72558	0.72575	0.72592	0.72609
0.110	TAN	0.94651	0.94604	0.94557	0.94509	0.94462	0.94415	0.94368	0.94321	0.94274	0.94227
	SIN	0.68742	0.68724	0.68705	0.68687	0.68669	0.68651	0.68633	0.68615	0.68597	0.68579
	COS	0.72626	0.72643	0.72661	0.72678	0.72695	0.72712	0.72729	0.72746	0.72763	0.72780
0.120	TAN	0.94180	0.94133	0.94086	0.94039	0.93992	0.93945	0.93898	0.93851	0.93805	0.93758
	SIN	0.68560	0.68542	0.68524	0.68506	0.68488	0.68470	0.68452	0.68433	0.68415	0.68397
	COS	0.72797	0.72814	0.72832	0.72849	0.72866	0.72883	0.72900	0.72917	0.72934	0.72951
0.130	TAN	0.93711	0.93664	0.93618	0.93571	0.93524	0.93478	0.93431	0.93384	0.93338	0.93291
	SIN	0.68379	0.68361	0.68343	0.68324	0.68306	0.68288	0.68270	0.68252	0.68234	0.68215
	COS	0.72968	0.72985	0.73002	0.73019	0.73036	0.73053	0.73070	0.73087	0.73104	0.73121
0.140	TAN	0.93245	0.93198	0.93152	0.93105	0.93059	0.93012	0.92966	0.92920	0.92873	0.92827
	SIN	0.68197	0.68179	0.68161	0.68143	0.68124	0.68106	0.68088	0.68070	0.68052	0.68033
	COS	0.73138	0.73155	0.73172	0.73189	0.73206	0.73223	0.73240	0.73256	0.73273	0.73290
0.150	TAN	0.92781	0.92735	0.92688	0.92642	0.92596	0.92550	0.92504	0.92458	0.92412	0.92366
	SIN	0.68015	0.67997	0.67979	0.67960	0.67942	0.67924	0.67906	0.67887	0.67869	0.67851
	COS	0.73307	0.73324	0.73341	0.73358	0.73375	0.73392	0.73409	0.73425	0.73442	0.73459
0.160	TAN	0.92319	0.92273	0.92228	0.92182	0.92136	0.92090	0.92044	0.91998	0.91952	0.91906
	SIN	0.67833	0.67814	0.67796	0.67778	0.67760	0.67741	0.67723	0.67705	0.67687	0.67668
	COS	0.73476	0.73493	0.73510	0.73527	0.73543	0.73560	0.73577	0.73594	0.73611	0.73627
0.170	TAN	0.91861	0.91815	0.91769	0.91723	0.91678	0.91632	0.91586	0.91541	0.91495	0.91450
	SIN	0.67650	0.67632	0.67613	0.67595	0.67577	0.67559	0.67540	0.67522	0.67504	0.67485
	COS	0.73644	0.73661	0.73678	0.73695	0.73711	0.73728	0.73745	0.73762	0.73778	0.73795
0.180	TAN	0.91404	0.91359	0.91313	0.91268	0.91222	0.91177	0.91132	0.91086	0.91041	0.90996
	SIN	0.67467	0.67449	0.67431	0.67412	0.67394	0.67376	0.67357	0.67339	0.67321	0.67302
	COS	0.73812	0.73829	0.73845	0.73862	0.73879	0.73895	0.73912	0.73929	0.73946	0.73962
0.190	TAN	0.90950	0.90905	0.90860	0.90815	0.90769	0.90724	0.90679	0.90634	0.90589	0.90544
	SIN	0.67284	0.67266	0.67247	0.67229	0.67211	0.67192	0.67174	0.67156	0.67137	0.67119
	COS	0.73979	0.73996	0.74012	0.74029	0.74045	0.74062	0.74079	0.74095	0.74112	0.74129

TABLE 8.

A-B /C		0.000	0.001	0.002	0.003	0.004	0.005	0.006	0.007	0.008	0.009
0.200	TAN	0.90499	0.90454	0.90409	0.90364	0.90319	0.90274	0.90229	0.90184	0.90139	0.90095
	SIN	0.67101	0.67082	0.67064	0.67045	0.67027	0.67009	0.66990	0.66972	0.66954	0.66935
	COS	0.74145	0.74162	0.74178	0.74195	0.74212	0.74228	0.74245	0.74261	0.74278	0.74294
0.210	TAN	0.90050	0.90005	0.89960	0.89916	0.89871	0.89826	0.89782	0.89737	0.89692	0.89648
	SIN	0.66917	0.66899	0.66880	0.66862	0.66843	0.66825	0.66807	0.66788	0.66770	0.66751
	COS	0.74311	0.74328	0.74344	0.74361	0.74377	0.74394	0.74410	0.74427	0.74443	0.74460
0.220	TAN	0.89603	0.89559	0.89514	0.89470	0.89425	0.89381	0.89336	0.89292	0.89248	0.89203
	SIN	0.66733	0.66715	0.66696	0.66678	0.66659	0.66641	0.66623	0.66604	0.66586	0.66567
	COS	0.74476	0.74493	0.74509	0.74526	0.74542	0.74559	0.74575	0.74591	0.74608	0.74624
0.230	TAN	0.89159	0.89115	0.89071	0.89026	0.88982	0.88938	0.88894	0.88850	0.88806	0.88761
	SIN	0.66549	0.66531	0.66512	0.66494	0.66475	0.66457	0.66438	0.66420	0.66402	0.66383
	COS	0.74641	0.74657	0.74674	0.74690	0.74706	0.74723	0.74739	0.74755	0.74772	0.74788
0.240	TAN	0.88717	0.88673	0.88629	0.88585	0.88541	0.88498	0.88454	0.88410	0.88366	0.88322
	SIN	0.66365	0.66346	0.66328	0.66309	0.66291	0.66273	0.66254	0.66236	0.66217	0.66199
	COS	0.74805	0.74821	0.74837	0.74854	0.74870	0.74886	0.74903	0.74919	0.74935	0.74952
0.250	TAN	0.88278	0.88234	0.88191	0.88147	0.88103	0.88060	0.88016	0.87972	0.87929	0.87885
	SIN	0.66180	0.66162	0.66143	0.66125	0.66106	0.66088	0.66070	0.66051	0.66033	0.66014
	COS	0.74968	0.74984	0.75000	0.75017	0.75033	0.75049	0.75065	0.75082	0.75098	0.75114
0.260	TAN	0.87841	0.87798	0.87754	0.87711	0.87667	0.87624	0.87581	0.87537	0.87494	0.87450
	SIN	0.65996	0.65977	0.65959	0.65940	0.65922	0.65903	0.65885	0.65866	0.65848	0.65829
	COS	0.75130	0.75147	0.75163	0.75179	0.75195	0.75211	0.75228	0.75244	0.75260	0.75276
0.270	TAN	0.87407	0.87364	0.87321	0.87277	0.87234	0.87191	0.87148	0.87105	0.87061	0.87018
	SIN	0.65811	0.65792	0.65774	0.65755	0.65737	0.65718	0.65700	0.65681	0.65663	0.65644
	COS	0.75292	0.75308	0.75325	0.75341	0.75357	0.75373	0.75389	0.75405	0.75421	0.75437
0.280	TAN	0.86975	0.86932	0.86889	0.86846	0.86803	0.86760	0.86717	0.86674	0.86631	0.86589
	SIN	0.65626	0.65607	0.65589	0.65570	0.65552	0.65533	0.65515	0.65496	0.65478	0.65459
	COS	0.75454	0.75470	0.75486	0.75502	0.75518	0.75534	0.75550	0.75566	0.75582	0.75598
0.290	TAN	0.86546	0.86503	0.86460	0.86417	0.86375	0.86332	0.86289	0.86247	0.86204	0.86161
	SIN	0.65441	0.65422	0.65404	0.65385	0.65367	0.65348	0.65330	0.65311	0.65293	0.65274
	COS	0.75614	0.75630	0.75646	0.75662	0.75678	0.75694	0.75710	0.75726	0.75742	0.75758
0.300	TAN	0.86119	0.86076	0.86034	0.85991	0.85949	0.85906	0.85864	0.85821	0.85779	0.85736
	SIN	0.65256	0.65237	0.65219	0.65200	0.65182	0.65163	0.65144	0.65126	0.65107	0.65089
	COS	0.75774	0.75790	0.75806	0.75822	0.75838	0.75854	0.75870	0.75886	0.75901	0.75917
0.310	TAN	0.85694	0.85652	0.85609	0.85567	0.85525	0.85483	0.85441	0.85398	0.85356	0.85314
	SIN	0.65070	0.65052	0.65033	0.65015	0.64996	0.64978	0.64959	0.64941	0.64922	0.64903
	COS	0.75933	0.75949	0.75965	0.75981	0.75997	0.76013	0.76028	0.76044	0.76060	0.76076
0.320	TAN	0.85272	0.85230	0.85188	0.85146	0.85104	0.85062	0.85020	0.84978	0.84936	0.84894
	SIN	0.64885	0.64866	0.64848	0.64829	0.64811	0.64792	0.64774	0.64755	0.64736	0.64718
	COS	0.76092	0.76108	0.76123	0.76139	0.76155	0.76171	0.76187	0.76202	0.76218	0.76234
0.330	TAN	0.84852	0.84810	0.84768	0.84727	0.84685	0.84643	0.84601	0.84560	0.84518	0.84476
	SIN	0.64699	0.64681	0.64662	0.64644	0.64625	0.64607	0.64588	0.64569	0.64551	0.64532
	COS	0.76250	0.76265	0.76281	0.76297	0.76312	0.76328	0.76344	0.76360	0.76375	0.76391
0.340	TAN	0.84435	0.84393	0.84352	0.84310	0.84268	0.84227	0.84185	0.84144	0.84103	0.84061
	SIN	0.64514	0.64495	0.64477	0.64458	0.64439	0.64421	0.64402	0.64384	0.64365	0.64347
	COS	0.76407	0.76422	0.76438	0.76454	0.76469	0.76485	0.76501	0.76516	0.76532	0.76547
0.350	TAN	0.84020	0.83978	0.83937	0.83896	0.83854	0.83813	0.83772	0.83731	0.83689	0.83648
	SIN	0.64328	0.64309	0.64291	0.64272	0.64254	0.64235	0.64217	0.64198	0.64179	0.64161
	COS	0.76563	0.76579	0.76594	0.76610	0.76625	0.76641	0.76657	0.76672	0.76688	0.76703
0.360	TAN	0.83607	0.83566	0.83525	0.83484	0.83443	0.83402	0.83361	0.83320	0.83279	0.83238
	SIN	0.64142	0.64124	0.64105	0.64087	0.64068	0.64049	0.64031	0.64012	0.63994	0.63975
	COS	0.76719	0.76734	0.76750	0.76765	0.76781	0.76796	0.76812	0.76827	0.76843	0.76858
0.370	TAN	0.83197	0.83156	0.83115	0.83074	0.83033	0.82993	0.82952	0.82911	0.82870	0.82830
	SIN	0.63957	0.63938	0.63919	0.63901	0.63882	0.63864	0.63845	0.63826	0.63808	0.63789
	COS	0.76874	0.76889	0.76905	0.76920	0.76935	0.76951	0.76966	0.76982	0.76997	0.77013
0.380	TAN	0.82789	0.82748	0.82708	0.82667	0.82627	0.82586	0.82545	0.82505	0.82464	0.82424
	SIN	0.63771	0.63752	0.63733	0.63715	0.63696	0.63678	0.63659	0.63641	0.63622	0.63603
	COS	0.77028	0.77043	0.77059	0.77074	0.77089	0.77105	0.77120	0.77135	0.77151	0.77166
0.390	TAN	0.82384	0.82343	0.82303	0.82262	0.82222	0.82182	0.82141	0.82101	0.82061	0.82021
	SIN	0.63585	0.63566	0.63548	0.63529	0.63510	0.63492	0.63473	0.63455	0.63436	0.63417
	COS	0.77181	0.77197	0.77212	0.77227	0.77243	0.77258	0.77273	0.77288	0.77304	0.77319

TABLE 9.

A-B /C		0.000	0.001	0.002	0.003	0.004	0.005	0.006	0.007	0.008	0.009
0.400	TAN	0.81980	0.81940	0.81900	0.81860	0.81820	0.81780	0.81740	0.81700	0.81660	0.81620
	SIN	0.63399	0.63380	0.63362	0.63343	0.63325	0.63306	0.63287	0.63269	0.63250	0.63232
	COS	0.77334	0.77349	0.77365	0.77380	0.77395	0.77410	0.77426	0.77441	0.77456	0.77471
0.410	TAN	0.81580	0.81540	0.81500	0.81460	0.81420	0.81380	0.81340	0.81301	0.81261	0.81221
	SIN	0.63213	0.63194	0.63176	0.63157	0.63139	0.63120	0.63101	0.63083	0.63064	0.63046
	COS	0.77486	0.77501	0.77517	0.77532	0.77547	0.77562	0.77577	0.77592	0.77607	0.77622
0.420	TAN	0.81181	0.81142	0.81102	0.81062	0.81023	0.80983	0.80943	0.80904	0.80864	0.80825
	SIN	0.63027	0.63009	0.62990	0.62971	0.62953	0.62934	0.62916	0.62897	0.62878	0.62860
	COS	0.77638	0.77653	0.77668	0.77683	0.77698	0.77713	0.77728	0.77743	0.77758	0.77773
0.430	TAN	0.80785	0.80746	0.80706	0.80667	0.80627	0.80588	0.80549	0.80509	0.80470	0.80431
	SIN	0.62841	0.62823	0.62804	0.62785	0.62767	0.62748	0.62730	0.62711	0.62693	0.62674
	COS	0.77788	0.77803	0.77818	0.77833	0.77848	0.77863	0.77878	0.77893	0.77908	0.77923
0.440	TAN	0.80391	0.80352	0.80313	0.80274	0.80235	0.80195	0.80156	0.80117	0.80078	0.80039
	SIN	0.62655	0.62637	0.62618	0.62600	0.62581	0.62562	0.62544	0.62525	0.62507	0.62488
	COS	0.77938	0.77953	0.77968	0.77983	0.77998	0.78012	0.78027	0.78042	0.78057	0.78072
0.450	TAN	0.80000	0.79961	0.79922	0.79883	0.79844	0.79805	0.79766	0.79727	0.79689	0.79650
	SIN	0.62470	0.62451	0.62432	0.62414	0.62395	0.62377	0.62358	0.62339	0.62321	0.62302
	COS	0.78087	0.78102	0.78117	0.78131	0.78146	0.78161	0.78176	0.78191	0.78206	0.78220
0.460	TAN	0.79611	0.79572	0.79533	0.79495	0.79456	0.79417	0.79379	0.79340	0.79301	0.79263
	SIN	0.62284	0.62265	0.62247	0.62228	0.62209	0.62191	0.62172	0.62154	0.62135	0.62117
	COS	0.78235	0.78250	0.78265	0.78279	0.78294	0.78309	0.78324	0.78338	0.78353	0.78368
0.470	TAN	0.79224	0.79186	0.79147	0.79109	0.79070	0.79032	0.78993	0.78955	0.78916	0.78878
	SIN	0.62098	0.62079	0.62061	0.62042	0.62024	0.62005	0.61987	0.61968	0.61949	0.61931
	COS	0.78383	0.78397	0.78412	0.78427	0.78441	0.78456	0.78471	0.78485	0.78500	0.78515
0.480	TAN	0.78840	0.78801	0.78763	0.78725	0.78687	0.78648	0.78610	0.78572	0.78534	0.78496
	SIN	0.61912	0.61894	0.61875	0.61857	0.61838	0.61820	0.61801	0.61782	0.61764	0.61745
	COS	0.78529	0.78544	0.78559	0.78573	0.78588	0.78602	0.78617	0.78632	0.78646	0.78661
0.490	TAN	0.78458	0.78419	0.78381	0.78343	0.78305	0.78267	0.78229	0.78191	0.78153	0.78116
	SIN	0.61727	0.61708	0.61690	0.61671	0.61653	0.61634	0.61615	0.61597	0.61578	0.61560
	COS	0.78675	0.78690	0.78704	0.78719	0.78734	0.78748	0.78763	0.78777	0.78792	0.78806
0.500	TAN	0.78078	0.78040	0.78002	0.77964	0.77926	0.77889	0.77851	0.77813	0.77775	0.77738
	SIN	0.61541	0.61523	0.61504	0.61486	0.61467	0.61449	0.61430	0.61411	0.61393	0.61374
	COS	0.78821	0.78835	0.78849	0.78864	0.78878	0.78893	0.78907	0.78922	0.78936	0.78951
0.510	TAN	0.77700	0.77662	0.77625	0.77587	0.77550	0.77512	0.77475	0.77437	0.77400	0.77362
	SIN	0.61356	0.61337	0.61319	0.61300	0.61282	0.61263	0.61245	0.61226	0.61208	0.61189
	COS	0.78965	0.78979	0.78994	0.79008	0.79022	0.79037	0.79051	0.79066	0.79080	0.79094
0.520	TAN	0.77325	0.77287	0.77250	0.77213	0.77175	0.77138	0.77101	0.77063	0.77026	0.76989
	SIN	0.61171	0.61152	0.61133	0.61115	0.61096	0.61078	0.61059	0.61041	0.61022	0.61004
	COS	0.79109	0.79123	0.79137	0.79152	0.79166	0.79180	0.79194	0.79209	0.79223	0.79237
0.530	TAN	0.76952	0.76915	0.76877	0.76840	0.76803	0.76766	0.76729	0.76692	0.76655	0.76618
	SIN	0.60985	0.60967	0.60948	0.60930	0.60911	0.60893	0.60874	0.60856	0.60837	0.60819
	COS	0.79251	0.79266	0.79280	0.79294	0.79308	0.79323	0.79337	0.79351	0.79365	0.79379
0.540	TAN	0.76581	0.76544	0.76507	0.76470	0.76433	0.76396	0.76360	0.76323	0.76286	0.76249
	SIN	0.60800	0.60782	0.60763	0.60745	0.60726	0.60708	0.60689	0.60671	0.60652	0.60634
	COS	0.79393	0.79408	0.79422	0.79436	0.79450	0.79464	0.79478	0.79492	0.79507	0.79521
0.550	TAN	0.76212	0.76176	0.76139	0.76102	0.76066	0.76029	0.75992	0.75956	0.75919	0.75883
	SIN	0.60615	0.60597	0.60578	0.60560	0.60541	0.60523	0.60504	0.60486	0.60468	0.60449
	COS	0.79535	0.79549	0.79563	0.79577	0.79591	0.79605	0.79619	0.79633	0.79647	0.79661
0.560	TAN	0.75846	0.75810	0.75773	0.75737	0.75700	0.75664	0.75627	0.75591	0.75555	0.75518
	SIN	0.60431	0.60412	0.60394	0.60375	0.60357	0.60338	0.60320	0.60301	0.60283	0.60264
	COS	0.79675	0.79689	0.79703	0.79717	0.79731	0.79745	0.79759	0.79773	0.79787	0.79801
0.570	TAN	0.75482	0.75446	0.75409	0.75373	0.75337	0.75301	0.75265	0.75228	0.75192	0.75156
	SIN	0.60246	0.60227	0.60209	0.60191	0.60172	0.60154	0.60135	0.60117	0.60098	0.60080
	COS	0.79815	0.79829	0.79843	0.79857	0.79871	0.79885	0.79898	0.79912	0.79926	0.79940
0.580	TAN	0.75120	0.75084	0.75048	0.75012	0.74976	0.74940	0.74904	0.74868	0.74832	0.74796
	SIN	0.60061	0.60043	0.60025	0.60006	0.59988	0.59969	0.59951	0.59932	0.59914	0.59896
	COS	0.79954	0.79968	0.79982	0.79995	0.80009	0.80023	0.80037	0.80051	0.80064	0.80078
0.590	TAN	0.74761	0.74725	0.74689	0.74653	0.74617	0.74582	0.74546	0.74510	0.74474	0.74439
	SIN	0.59877	0.59859	0.59840	0.59822	0.59804	0.59785	0.59767	0.59748	0.59730	0.59711
	COS	0.80092	0.80106	0.80119	0.80133	0.80147	0.80161	0.80174	0.80188	0.80202	0.80216

TABLE 10.

A-B /C		0.000	0.001	0.002	0.003	0.004	0.005	0.006	0.007	0.008	0.009
0.600	TAN	0.74403	0.74367	0.74332	0.74296	0.74261	0.74225	0.74190	0.74154	0.74119	0.74083
	SIN	0.59693	0.59675	0.59656	0.59638	0.59619	0.59601	0.59583	0.59564	0.59546	0.59528
	COS	0.80229	0.80243	0.80257	0.80270	0.80284	0.80298	0.80311	0.80325	0.80339	0.80352
0.610	TAN	0.74048	0.74012	0.73977	0.73942	0.73906	0.73871	0.73836	0.73801	0.73765	0.73730
	SIN	0.59509	0.59491	0.59472	0.59454	0.59436	0.59417	0.59399	0.59381	0.59362	0.59344
	COS	0.80366	0.80379	0.80393	0.80407	0.80420	0.80434	0.80447	0.80461	0.80474	0.80488
0.620	TAN	0.73695	0.73660	0.73624	0.73589	0.73554	0.73519	0.73484	0.73449	0.73414	0.73379
	SIN	0.59325	0.59307	0.59289	0.59270	0.59252	0.59234	0.59215	0.59197	0.59179	0.59160
	COS	0.80501	0.80515	0.80529	0.80542	0.80556	0.80569	0.80583	0.80596	0.80609	0.80623
0.630	TAN	0.73344	0.73309	0.73274	0.73239	0.73204	0.73169	0.73135	0.73100	0.73065	0.73030
	SIN	0.59142	0.59124	0.59105	0.59087	0.59069	0.59050	0.59032	0.59014	0.58995	0.58977
	COS	0.80636	0.80650	0.80663	0.80677	0.80690	0.80704	0.80717	0.80730	0.80744	0.80757
0.640	TAN	0.72995	0.72961	0.72926	0.72891	0.72856	0.72822	0.72787	0.72752	0.72718	0.72683
	SIN	0.58959	0.58940	0.58922	0.58904	0.58885	0.58867	0.58849	0.58831	0.58812	0.58794
	COS	0.80771	0.80784	0.80797	0.80811	0.80824	0.80837	0.80851	0.80864	0.80877	0.80891
0.650	TAN	0.72649	0.72614	0.72580	0.72545	0.72511	0.72476	0.72442	0.72407	0.72373	0.72339
	SIN	0.58776	0.58757	0.58739	0.58721	0.58702	0.58684	0.58666	0.58648	0.58629	0.58611
	COS	0.80904	0.80917	0.80930	0.80944	0.80957	0.80970	0.80983	0.80997	0.81010	0.81023
0.660	TAN	0.72304	0.72270	0.72236	0.72201	0.72167	0.72133	0.72099	0.72065	0.72030	0.71996
	SIN	0.58593	0.58575	0.58556	0.58538	0.58520	0.58501	0.58483	0.58465	0.58447	0.58428
	COS	0.81036	0.81050	0.81063	0.81076	0.81089	0.81102	0.81115	0.81129	0.81142	0.81155
0.670	TAN	0.71962	0.71928	0.71894	0.71860	0.71826	0.71792	0.71758	0.71724	0.71690	0.71656
	SIN	0.58410	0.58392	0.58374	0.58356	0.58337	0.58319	0.58301	0.58283	0.58264	0.58246
	COS	0.81168	0.81181	0.81194	0.81207	0.81220	0.81234	0.81247	0.81260	0.81273	0.81286
0.680	TAN	0.71622	0.71588	0.71554	0.71520	0.71487	0.71453	0.71419	0.71385	0.71351	0.71318
	SIN	0.58228	0.58210	0.58191	0.58173	0.58155	0.58137	0.58119	0.58100	0.58082	0.58064
	COS	0.81299	0.81312	0.81325	0.81338	0.81351	0.81364	0.81377	0.81390	0.81403	0.81416
0.690	TAN	0.71284	0.71250	0.71217	0.71183	0.71149	0.71116	0.71082	0.71049	0.71015	0.70982
	SIN	0.58046	0.58028	0.58009	0.57991	0.57973	0.57955	0.57937	0.57919	0.57900	0.57882
	COS	0.81429	0.81442	0.81455	0.81468	0.81481	0.81494	0.81507	0.81520	0.81532	0.81545
0.700	TAN	0.70948	0.70915	0.70881	0.70848	0.70814	0.70781	0.70748	0.70714	0.70681	0.70648
	SIN	0.57864	0.57846	0.57828	0.57810	0.57791	0.57773	0.57755	0.57737	0.57719	0.57701
	COS	0.81558	0.81571	0.81584	0.81597	0.81610	0.81623	0.81635	0.81648	0.81661	0.81674
0.710	TAN	0.70614	0.70581	0.70548	0.70515	0.70481	0.70448	0.70415	0.70382	0.70349	0.70316
	SIN	0.57683	0.57664	0.57646	0.57628	0.57610	0.57592	0.57574	0.57556	0.57538	0.57519
	COS	0.81687	0.81700	0.81712	0.81725	0.81738	0.81751	0.81763	0.81776	0.81789	0.81802
0.720	TAN	0.70283	0.70250	0.70217	0.70184	0.70151	0.70118	0.70085	0.70052	0.70019	0.69986
	SIN	0.57501	0.57483	0.57465	0.57447	0.57429	0.57411	0.57393	0.57375	0.57357	0.57339
	COS	0.81814	0.81827	0.81840	0.81853	0.81865	0.81878	0.81891	0.81903	0.81916	0.81929
0.730	TAN	0.69953	0.69920	0.69887	0.69855	0.69822	0.69789	0.69756	0.69724	0.69691	0.69658
	SIN	0.57320	0.57302	0.57284	0.57266	0.57248	0.57230	0.57212	0.57194	0.57176	0.57158
	COS	0.81941	0.81954	0.81967	0.81979	0.81992	0.82004	0.82017	0.82030	0.82042	0.82055
0.740	TAN	0.69626	0.69593	0.69560	0.69528	0.69495	0.69463	0.69430	0.69398	0.69365	0.69333
	SIN	0.57140	0.57122	0.57104	0.57086	0.57068	0.57050	0.57032	0.57014	0.56996	0.56978
	COS	0.82067	0.82080	0.82092	0.82105	0.82117	0.82130	0.82143	0.82155	0.82168	0.82180
0.750	TAN	0.69300	0.69268	0.69235	0.69203	0.69170	0.69138	0.69106	0.69074	0.69041	0.69009
	SIN	0.56960	0.56942	0.56923	0.56905	0.56887	0.56869	0.56851	0.56833	0.56816	0.56798
	COS	0.82193	0.82205	0.82217	0.82230	0.82242	0.82255	0.82267	0.82280	0.82292	0.82305
0.760	TAN	0.68977	0.68944	0.68912	0.68880	0.68848	0.68816	0.68784	0.68752	0.68719	0.68687
	SIN	0.56780	0.56762	0.56744	0.56726	0.56708	0.56690	0.56672	0.56654	0.56636	0.56618
	COS	0.82317	0.82329	0.82342	0.82354	0.82367	0.82379	0.82391	0.82404	0.82416	0.82428
0.770	TAN	0.68655	0.68623	0.68591	0.68559	0.68527	0.68495	0.68463	0.68432	0.68400	0.68368
	SIN	0.56600	0.56582	0.56564	0.56546	0.56528	0.56510	0.56492	0.56474	0.56456	0.56438
	COS	0.82441	0.82453	0.82465	0.82478	0.82490	0.82502	0.82514	0.82527	0.82539	0.82551
0.780	TAN	0.68336	0.68304	0.68272	0.68241	0.68209	0.68177	0.68145	0.68114	0.68082	0.68050
	SIN	0.56421	0.56403	0.56385	0.56367	0.56349	0.56331	0.56313	0.56295	0.56277	0.56259
	COS	0.82563	0.82576	0.82588	0.82600	0.82612	0.82625	0.82637	0.82649	0.82661	0.82673
0.790	TAN	0.68019	0.67987	0.67955	0.67924	0.67892	0.67861	0.67829	0.67798	0.67766	0.67735
	SIN	0.56242	0.56224	0.56206	0.56188	0.56170	0.56152	0.56134	0.56116	0.56099	0.56081
	COS	0.82685	0.82698	0.82710	0.82722	0.82734	0.82746	0.82758	0.82770	0.82783	0.82795

TABLE 11.

° A-B	/C	0.000	0.001	0.002	0.003	0.004	0.005	0.006	0.007	0.008	0.009
0.800	TAN	0.67703	0.67672	0.67641	0.67609	0.67578	0.67546	0.67515	0.67484	0.67453	0.67421
	SIN	0.56063	0.56045	0.56027	0.56009	0.55992	0.55974	0.55956	0.55938	0.55920	0.55902
	COS	0.82807	0.82819	0.82831	0.82843	0.82855	0.82867	0.82879	0.82891	0.82903	0.82915
0.810	TAN	0.67390	0.67359	0.67328	0.67296	0.67265	0.67234	0.67203	0.67172	0.67141	0.67110
	SIN	0.55885	0.55867	0.55849	0.55831	0.55813	0.55796	0.55778	0.55760	0.55742	0.55724
	COS	0.82927	0.82939	0.82951	0.82963	0.82975	0.82987	0.82999	0.83011	0.83023	0.83035
0.820	TAN	0.67079	0.67048	0.67017	0.66986	0.66955	0.66924	0.66893	0.66862	0.66831	0.66800
	SIN	0.55707	0.55689	0.55671	0.55653	0.55636	0.55618	0.55600	0.55582	0.55565	0.55547
	COS	0.83047	0.83059	0.83071	0.83082	0.83094	0.83106	0.83118	0.83130	0.83142	0.83154
0.830	TAN	0.66769	0.66739	0.66708	0.66677	0.66646	0.66615	0.66585	0.66554	0.66523	0.66493
	SIN	0.55529	0.55511	0.55494	0.55476	0.55458	0.55441	0.55423	0.55405	0.55387	0.55370
	COS	0.83166	0.83177	0.83189	0.83201	0.83213	0.83225	0.83236	0.83248	0.83260	0.83272
0.840	TAN	0.66462	0.66431	0.66401	0.66370	0.66340	0.66309	0.66279	0.66248	0.66218	0.66187
	SIN	0.55352	0.55334	0.55317	0.55299	0.55281	0.55264	0.55246	0.55228	0.55211	0.55193
	COS	0.83284	0.83295	0.83307	0.83319	0.83331	0.83342	0.83354	0.83366	0.83377	0.83389
0.850	TAN	0.66157	0.66126	0.66096	0.66065	0.66035	0.66005	0.65974	0.65944	0.65914	0.65883
	SIN	0.55175	0.55158	0.55140	0.55122	0.55105	0.55087	0.55069	0.55052	0.55034	0.55016
	COS	0.83401	0.83413	0.83424	0.83436	0.83448	0.83459	0.83471	0.83482	0.83494	0.83506
0.860	TAN	0.65853	0.65823	0.65793	0.65763	0.65732	0.65702	0.65672	0.65642	0.65612	0.65582
	SIN	0.54999	0.54981	0.54964	0.54946	0.54928	0.54911	0.54893	0.54876	0.54858	0.54840
	COS	0.83517	0.83529	0.83540	0.83552	0.83564	0.83575	0.83587	0.83598	0.83610	0.83621
0.870	TAN	0.65552	0.65522	0.65492	0.65462	0.65432	0.65402	0.65372	0.65342	0.65312	0.65282
	SIN	0.54823	0.54805	0.54788	0.54770	0.54752	0.54735	0.54717	0.54700	0.54682	0.54665
	COS	0.83633	0.83644	0.83656	0.83667	0.83679	0.83690	0.83702	0.83713	0.83725	0.83736
0.880	TAN	0.65252	0.65222	0.65192	0.65163	0.65133	0.65103	0.65073	0.65044	0.65014	0.64984
	SIN	0.54647	0.54630	0.54612	0.54595	0.54577	0.54560	0.54542	0.54524	0.54507	0.54489
	COS	0.83748	0.83759	0.83771	0.83782	0.83793	0.83805	0.83816	0.83828	0.83839	0.83850
0.890	TAN	0.64954	0.64925	0.64895	0.64865	0.64836	0.64806	0.64777	0.64747	0.64718	0.64688
	SIN	0.54472	0.54454	0.54437	0.54419	0.54402	0.54385	0.54367	0.54350	0.54332	0.54315
	COS	0.83862	0.83873	0.83885	0.83896	0.83907	0.83919	0.83930	0.83941	0.83953	0.83964
0.900	TAN	0.64659	0.64629	0.64600	0.64570	0.64541	0.64511	0.64482	0.64453	0.64423	0.64394
	SIN	0.54297	0.54280	0.54262	0.54245	0.54227	0.54210	0.54192	0.54175	0.54158	0.54140
	COS	0.83975	0.83986	0.83998	0.84009	0.84020	0.84031	0.84043	0.84054	0.84065	0.84076
0.910	TAN	0.64365	0.64335	0.64306	0.64277	0.64248	0.64219	0.64189	0.64160	0.64131	0.64102
	SIN	0.54123	0.54105	0.54088	0.54071	0.54053	0.54036	0.54018	0.54001	0.53984	0.53966
	COS	0.84088	0.84099	0.84110	0.84121	0.84132	0.84144	0.84155	0.84166	0.84177	0.84188
0.920	TAN	0.64073	0.64044	0.64015	0.63986	0.63957	0.63927	0.63898	0.63870	0.63841	0.63812
	SIN	0.53949	0.53931	0.53914	0.53897	0.53879	0.53862	0.53845	0.53827	0.53810	0.53793
	COS	0.84199	0.84210	0.84222	0.84233	0.84244	0.84255	0.84266	0.84277	0.84288	0.84299
0.930	TAN	0.63783	0.63754	0.63725	0.63696	0.63667	0.63638	0.63610	0.63581	0.63552	0.63523
	SIN	0.53775	0.53758	0.53741	0.53723	0.53706	0.53689	0.53671	0.53654	0.53637	0.53620
	COS	0.84310	0.84321	0.84332	0.84343	0.84354	0.84365	0.84376	0.84387	0.84398	0.84409
0.940	TAN	0.63494	0.63466	0.63437	0.63408	0.63380	0.63351	0.63322	0.63294	0.63265	0.63237
	SIN	0.53602	0.53585	0.53568	0.53550	0.53533	0.53516	0.53499	0.53481	0.53464	0.53447
	COS	0.84420	0.84431	0.84442	0.84453	0.84464	0.84475	0.84486	0.84497	0.84508	0.84519
0.950	TAN	0.63208	0.63179	0.63151	0.63122	0.63094	0.63066	0.63037	0.63009	0.62980	0.62952
	SIN	0.53430	0.53412	0.53395	0.53378	0.53361	0.53343	0.53326	0.53309	0.53292	0.53275
	COS	0.84530	0.84541	0.84552	0.84562	0.84573	0.84584	0.84595	0.84606	0.84617	0.84628
0.960	TAN	0.62923	0.62895	0.62867	0.62838	0.62810	0.62782	0.62754	0.62725	0.62697	0.62669
	SIN	0.53257	0.53240	0.53223	0.53206	0.53189	0.53171	0.53154	0.53137	0.53120	0.53103
	COS	0.84638	0.84649	0.84660	0.84671	0.84682	0.84692	0.84703	0.84714	0.84725	0.84735
0.970	TAN	0.62641	0.62613	0.62584	0.62556	0.62528	0.62500	0.62472	0.62444	0.62416	0.62388
	SIN	0.53086	0.53068	0.53051	0.53034	0.53017	0.53000	0.52983	0.52966	0.52949	0.52931
	COS	0.84746	0.84757	0.84768	0.84778	0.84789	0.84800	0.84811	0.84821	0.84832	0.84843
0.980	TAN	0.62360	0.62332	0.62304	0.62276	0.62248	0.62220	0.62192	0.62164	0.62136	0.62109
	SIN	0.52914	0.52897	0.52880	0.52863	0.52846	0.52829	0.52812	0.52795	0.52778	0.52761
	COS	0.84853	0.84864	0.84875	0.84885	0.84896	0.84906	0.84917	0.84928	0.84938	0.84949
0.990	TAN	0.62081	0.62053	0.62025	0.61997	0.61970	0.61942	0.61914	0.61886	0.61859	0.61831
	SIN	0.52744	0.52726	0.52709	0.52692	0.52675	0.52658	0.52641	0.52624	0.52607	0.52590
	COS	0.84960	0.84970	0.84981	0.84991	0.85002	0.85012	0.85023	0.85033	0.85044	0.85055

TABLE 12.

A-B /C		0.000	0.001	0.002	0.003	0.004	0.005	0.006	0.007	0.008	0.009
1.000	TAN	0.61803	0.61776	0.61748	0.61721	0.61693	0.61666	0.61638	0.61610	0.61583	0.61555
	SIN	0.52573	0.52556	0.52539	0.52522	0.52505	0.52488	0.52471	0.52454	0.52437	0.52420
	COS	0.85065	0.85076	0.85086	0.85097	0.85107	0.85118	0.85128	0.85138	0.85149	0.85159
1.010	TAN	0.61528	0.61501	0.61473	0.61446	0.61418	0.61391	0.61364	0.61336	0.61309	0.61282
	SIN	0.52403	0.52386	0.52369	0.52352	0.52335	0.52319	0.52302	0.52285	0.52268	0.52251
	COS	0.85170	0.85180	0.85191	0.85201	0.85212	0.85222	0.85232	0.85243	0.85253	0.85263
1.020	TAN	0.61254	0.61227	0.61200	0.61173	0.61145	0.61118	0.61091	0.61064	0.61037	0.61009
	SIN	0.52234	0.52217	0.52200	0.52183	0.52166	0.52149	0.52132	0.52116	0.52099	0.52082
	COS	0.85274	0.85284	0.85295	0.85305	0.85315	0.85326	0.85336	0.85346	0.85356	0.85367
1.030	TAN	0.60982	0.60955	0.60928	0.60901	0.60874	0.60847	0.60820	0.60793	0.60766	0.60739
	SIN	0.52065	0.52048	0.52031	0.52014	0.51997	0.51981	0.51964	0.51947	0.51930	0.51913
	COS	0.85377	0.85387	0.85398	0.85408	0.85418	0.85428	0.85439	0.85449	0.85459	0.85469
1.040	TAN	0.60712	0.60685	0.60658	0.60631	0.60605	0.60578	0.60551	0.60524	0.60497	0.60470
	SIN	0.51896	0.51880	0.51863	0.51846	0.51829	0.51812	0.51796	0.51779	0.51762	0.51745
	COS	0.85480	0.85490	0.85500	0.85510	0.85520	0.85531	0.85541	0.85551	0.85561	0.85571
1.050	TAN	0.60444	0.60417	0.60390	0.60363	0.60337	0.60310	0.60283	0.60257	0.60230	0.60204
	SIN	0.51728	0.51712	0.51695	0.51678	0.51661	0.51645	0.51628	0.51611	0.51594	0.51578
	COS	0.85581	0.85591	0.85602	0.85612	0.85622	0.85632	0.85642	0.85652	0.85662	0.85672
1.060	TAN	0.60177	0.60150	0.60124	0.60097	0.60071	0.60044	0.60018	0.59991	0.59965	0.59938
	SIN	0.51561	0.51544	0.51528	0.51511	0.51494	0.51477	0.51461	0.51444	0.51427	0.51411
	COS	0.85682	0.85692	0.85702	0.85712	0.85723	0.85733	0.85743	0.85753	0.85763	0.85773
1.070	TAN	0.59912	0.59886	0.59859	0.59833	0.59806	0.59780	0.59754	0.59728	0.59701	0.59675
	SIN	0.51394	0.51377	0.51361	0.51344	0.51327	0.51311	0.51294	0.51277	0.51261	0.51244
	COS	0.85783	0.85793	0.85803	0.85813	0.85822	0.85832	0.85842	0.85852	0.85862	0.85872
1.080	TAN	0.59649	0.59622	0.59596	0.59570	0.59544	0.59518	0.59492	0.59465	0.59439	0.59413
	SIN	0.51228	0.51211	0.51194	0.51178	0.51161	0.51145	0.51128	0.51111	0.51095	0.51078
	COS	0.85882	0.85892	0.85902	0.85912	0.85922	0.85932	0.85941	0.85951	0.85961	0.85971
1.090	TAN	0.59387	0.59361	0.59335	0.59309	0.59283	0.59257	0.59231	0.59205	0.59179	0.59153
	SIN	0.51062	0.51045	0.51028	0.51012	0.50995	0.50979	0.50962	0.50946	0.50929	0.50913
	COS	0.85981	0.85991	0.86001	0.86010	0.86020	0.86030	0.86040	0.86050	0.86059	0.86069
1.100	TAN	0.59127	0.59101	0.59075	0.59050	0.59024	0.58998	0.58972	0.58946	0.58921	0.58895
	SIN	0.50896	0.50880	0.50863	0.50847	0.50830	0.50814	0.50797	0.50781	0.50764	0.50748
	COS	0.86079	0.86089	0.86098	0.86108	0.86118	0.86128	0.86137	0.86147	0.86157	0.86167
1.110	TAN	0.58869	0.58843	0.58818	0.58792	0.58766	0.58741	0.58715	0.58689	0.58664	0.58638
	SIN	0.50731	0.50715	0.50698	0.50682	0.50665	0.50649	0.50632	0.50616	0.50600	0.50583
	COS	0.86176	0.86186	0.86196	0.86205	0.86215	0.86225	0.86234	0.86244	0.86254	0.86263
1.120	TAN	0.58613	0.58587	0.58561	0.58536	0.58510	0.58485	0.58459	0.58434	0.58408	0.58383
	SIN	0.50567	0.50550	0.50534	0.50517	0.50501	0.50485	0.50468	0.50452	0.50436	0.50419
	COS	0.86273	0.86282	0.86292	0.86302	0.86311	0.86321	0.86330	0.86340	0.86350	0.86359
1.130	TAN	0.58358	0.58332	0.58307	0.58282	0.58256	0.58231	0.58206	0.58180	0.58155	0.58130
	SIN	0.50403	0.50386	0.50370	0.50354	0.50337	0.50321	0.50305	0.50288	0.50272	0.50256
	COS	0.86369	0.86378	0.86388	0.86397	0.86407	0.86416	0.86426	0.86435	0.86445	0.86454
1.140	TAN	0.58104	0.58079	0.58054	0.58029	0.58004	0.57978	0.57953	0.57928	0.57903	0.57878
	SIN	0.50239	0.50223	0.50207	0.50190	0.50174	0.50158	0.50142	0.50125	0.50109	0.50093
	COS	0.86464	0.86473	0.86483	0.86492	0.86502	0.86511	0.86521	0.86530	0.86540	0.86549
1.150	TAN	0.57853	0.57828	0.57803	0.57778	0.57753	0.57728	0.57703	0.57678	0.57653	0.57628
	SIN	0.50076	0.50060	0.50044	0.50028	0.50011	0.49995	0.49979	0.49963	0.49947	0.49930
	COS	0.86558	0.86568	0.86577	0.86587	0.86596	0.86605	0.86615	0.86624	0.86633	0.86643
1.160	TAN	0.57603	0.57578	0.57553	0.57528	0.57503	0.57479	0.57454	0.57429	0.57404	0.57379
	SIN	0.49914	0.49898	0.49882	0.49866	0.49849	0.49833	0.49817	0.49801	0.49785	0.49768
	COS	0.86652	0.86661	0.86671	0.86680	0.86689	0.86699	0.86708	0.86717	0.86727	0.86736
1.170	TAN	0.57355	0.57330	0.57305	0.57280	0.57256	0.57231	0.57206	0.57182	0.57157	0.57132
	SIN	0.49752	0.49736	0.49720	0.49704	0.49688	0.49672	0.49655	0.49639	0.49623	0.49607
	COS	0.86745	0.86754	0.86764	0.86773	0.86782	0.86791	0.86801	0.86810	0.86819	0.86828
1.180	TAN	0.57108	0.57083	0.57059	0.57034	0.57010	0.56985	0.56961	0.56936	0.56912	0.56887
	SIN	0.49591	0.49575	0.49559	0.49543	0.49527	0.49511	0.49494	0.49478	0.49462	0.49446
	COS	0.86837	0.86847	0.86856	0.86865	0.86874	0.86883	0.86892	0.86902	0.86911	0.86920
1.190	TAN	0.56863	0.56838	0.56814	0.56789	0.56765	0.56741	0.56716	0.56692	0.56668	0.56643
	SIN	0.49430	0.49414	0.49398	0.49382	0.49366	0.49350	0.49334	0.49318	0.49302	0.49286
	COS	0.86929	0.86938	0.86947	0.86956	0.86965	0.86975	0.86984	0.86993	0.87002	0.87011

WASHINGTON, October 3, 1957.

Journal of Research of the National Bureau of Standards Vol. 60, No. 3, March 1958 Research Paper 2839

Effects of Capillary Shape on Flow Characteristics and Degradation of Polymer Solutions

Hobart S. White and Harriet V. Belcher

Flow data were obtained using a tapered capillary, a chamfered capillary, and a uniform-bore capillary in a McKee worker consistometer. With polyisobutene-cetane solutions, degradation occurred at lower rates of flow and persisted for a greater number of passes with flow entering the smaller end compared to flow entering the larger end of the tapered capillary. When degradation occurred in both directions at high rates of flow the pressure was larger for flow entering the larger end though after degradation ceased the pressure (used to overcome viscous resistance) was less for flow in this direction, compared to flow entering the smaller end in each case. Errors which might arise in the use of single pass instruments with nonuniform capillaries are pointed out.

1. Introduction

The development of the McKee worker-consistometer for investigating the effect of mechanical working on the rheological properties of lubricating greases, polymer solutions, and similar materials has been described in earlier publications [1, 2].[1] With this apparatus the sample may be worked and its flow characteristics measured in the same series of operations. It has been used to degrade polymers in solution mechanically [3, 4].

The worker-consistometer consists essentially of two coaxial steel cylinders and mating pistons with a capillary shearing element in a disk between them. By means of the closely fitting pistons the material being tested is forced repeatedly through the shearing element, back and forth from one cylinder to the other. In recent work when measuring the force in both directions with capillary disks having drilled holes, it was observed that the higher force associated with shear degradation in the worker-consistometer persisted for more passes through the capillary in one direction than in the opposite direction. It was believed that this effect might be due to the geometry of the drilled holes of the capillary disks.

To investigate this effect three new capillary disks were constructed. One disk was made with as uniform a bore as could be constructed, another was made with a uniform bore chamfered at one end, and the third was made with a taper of the bore. This paper reports the results of this study.

2. Apparatus

With the worker-consistometer as formerly used, the measured force acting on the pistons included piston friction. From calibration data, corrections for piston friction could be applied for Newtonian fluids, but proper corrections could not be made for non-Newtonian samples. Samples containing volatile solvents could not be investigated because of the abnormally high piston friction resulting from evaporation of the solvent from the cylinder walls, and consequent formation of a polymer film on the cylinder walls. Therefore, a new worker-consistometer unit was designed to permit measuring the pressure within the cylinders, thus avoiding errors resulting from piston friction, and to provide for minimizing evaporation of volatile solvents.

The cylinders and pistons of the new unit were made of hardened 440C stainless steel. Figure 1 shows the essential parts of the modified cam-operated instrument. The cam-operated driving mechanism [2] previously used was modified to operate the new unit in a horizontal position, to prevent spillage from the pressure ports during assembly. One cylinder has been set in the housing with the strain gage pressure pickup in place. The other cylinder, A, with accessories and strain gage pressure pickup, B, are left unassembled in front of the housing to show detail of design. The cylinders and push rods, C, were made longer than in the original units, and the push rods were fitted with Teflon seals, D, to provide a closed vapor space at the outer end of each cylinder to minimize evaporation of volatile solvents from the cylinder walls. To further reduce evaporation, in using the new unit with volatile solvents, a drop of the solvent was placed in the outer end of each cylinder before the push rods were inserted.

Provision was made for connecting a small port, E, near the inner end of each cylinder to fittings, F, provided with unbonded strain gage pressure pickups. A jelly made of glycerol, water, and gelatin was found to be preferable to liquid as a pressure-transmitting medium since it stayed in place in the pressure fitting and did not mix with benzene and similar solvents.

An indicating potentiometer for each strain gage was used so that readings from both gages could be observed at practically the same time to obtain the pressure difference in the cylinders. The strain gage pressure pickups were calibrated frequently with a dead weight gage tester.

Both the cam- and screw-operated instruments were used in obtaining measurements in this investigation. When working with solvents having relatively low volatility the pressures determined from the forces on the pistons were as accurate as the pressures measured directly on the modified cam-operated instrument. Accordingly, much of the

[1] Figures in brackets indicate the literature references at the end of this paper.

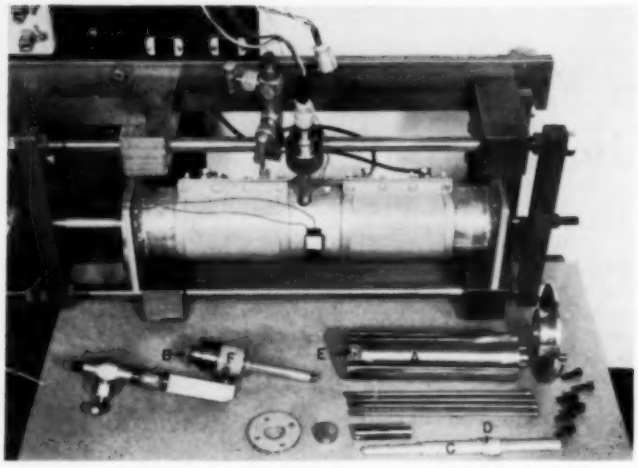

FIGURE 1. *Modified parts of cam-operated McKee worker-consistometer.*

data for the cetane-polyisobutene solution were obtained on the screw-operated instrument.

The new capillary disks were made with holes somewhat smaller than those used for most of the previous work, in order to extend the investigation to higher rates of shear. Disk No. 1044 (hole diameter=0.01044 in.) was made by soldering a piece of stainless steel capillary tubing in a stainless steel disk, grinding the ends to the desired length (L=0.250 in.), and carefully removing the grinding burrs with a jeweler's reamer. This avoided the slight taper and roughness normally found in the drilled holes of previous capillary disks. Another disk, No. 1048 (hole diameter=0.01048 in.), was made in the same manner and then a 45° chamfer was made at one end of the capillary, giving an entrance diameter of 0.0196 in. at the chamfered end. A third disk, No. 10–15, was made in the same way and was then reamed with a jeweler's tapered reamer so as to form a tapered hole, the hole being somewhat bell-mouthed instead of having a straight taper because of the flexibility of the very small reamer. The diameters of the ends of the tapered capillary (measured with a microscope) were 0.0101 in. and 0.0148 in., and the effective diameter was 0.01100 in. The effective diameters of the capillaries were determined by computation from flow measurements with NBS standard viscosity samples. These capillaries are shown diagrammatically (drawn to scale) in figures 2, 3, and 4.

In Poiseuille's equation,

$$Q=\frac{\pi a^4 P}{8\eta L},$$

a correction [5] for conicality may be made by substituting

$$\frac{3a_1^3a_2^3}{a_1^2+a_1a_2+a_2^2}$$

for a^4 (where a_1 and a_2 are the radii of the two ends of the capillary and a is the radius of a uniform bore capillary). For disk No. 10–15 the mean diameter

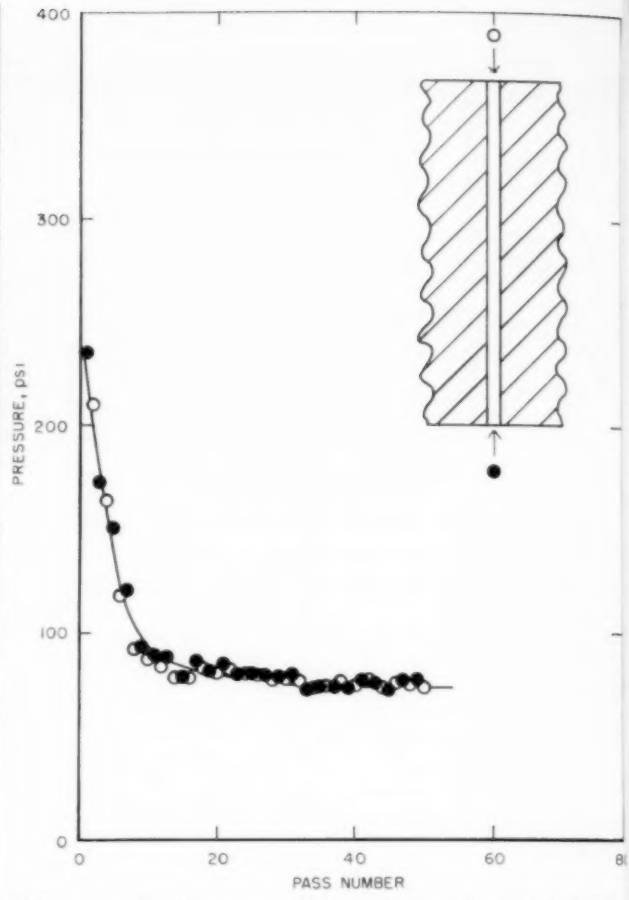

FIGURE 2. *Pressure curve for 10 percent of polyisobutene in benzene worked through a uniform bore capillary at 56,000 reciprocal seconds rate of shear, at 30° C.*

See sketch of capillary hole for directions of flow; bore, 0.01044 in.; length, 0.250 in.

computed from this expression is 0.0121 in. Since the hole in this disk is not truly conical because of the bell-mouth at the large end, this computed diameter is somewhat larger than the 0.011 in. effective diameter found by calibration. The effective diameter corresponds approximately to a straight-tapered hole 0.250 in. long with diameters of 0.010 in. and 0.0125 in. at the ends (1 percent taper).

An Ubbelohde suspended-level viscometer [6], in which the reservoir had been enlarged to serve as a mixing chamber, was used to determine reduced viscosities.

3. Materials and Methods

Most of the measurements were made on a 10-percent (weight) solution of polyisobutene in cetane (*n*-hexadecane). This polyisobutene is the unfractionated commercial Vistanex B–100 supplied by the Enjay Company. The solution was prepared by placing weighed quantities of polymer and solvent in glass jars and rolling the jars at about 6 rpm until the solution appeared homogeneous on inspection. Previous experience [4] indicated that 2 weeks of rolling

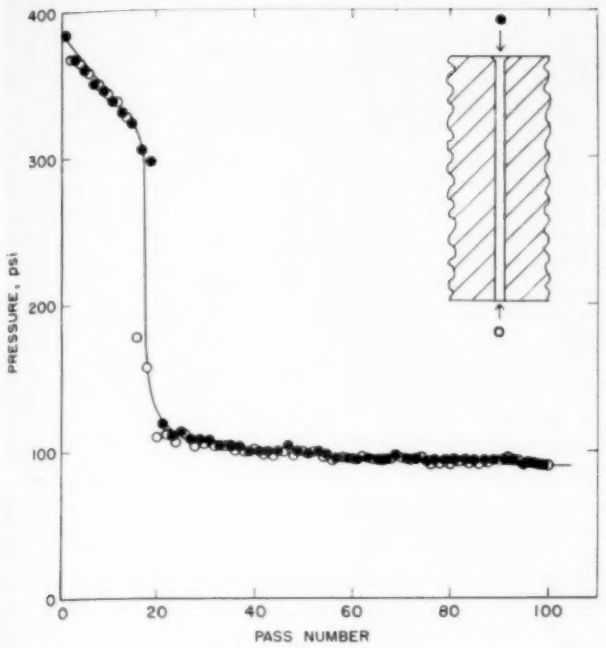

FIGURE 3. *Pressure curve for 10 percent of polyisobutene in cetane worked through a chamfered capillary at 65,000 reciprocal seconds rate of shear, at 40° C.*

See sketch of chamfered capillary hole for directions of flow; bore, 0.01048 in.; length, 0.250 in.; chamfer, to scale in sketch.

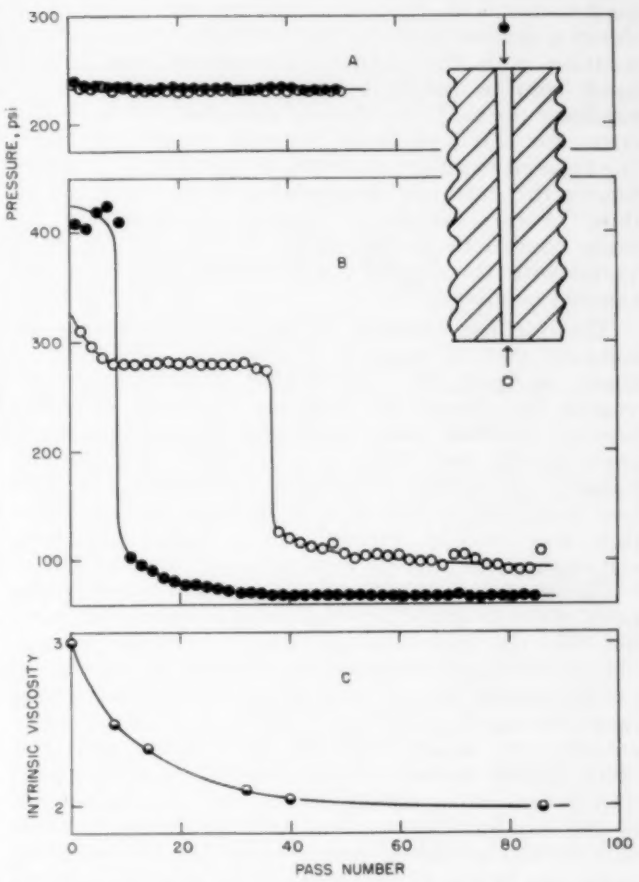

FIGURE 4A *and* 4B. *Pressure curves for NBS standard viscosity sample oil N–24 (A) and 10 percent of polyisobutene in cetane (B), worked through the tapered capillary at 56,000 reciprocal seconds rate of shear, at 40° C.*

See sketch of tapered capillary hole for directions of flow; effective diameter 0.0110 in.; length, 0.250 in.; taper, to scale in sketch.

FIGURE 4C. *Relation of intrinsic viscosity to number of passes worked through the tapered capillary at 56,000 reciprocal seconds rate of shear for 10 percent of polyisobutene in cetane.*

was ample for achieving complete solution. A 10-percent solution of the same polyisobutene in benzene was also prepared.

For purposes of comparison a material which is Newtonian over the range of rates of shear investigated, and a non-Newtonian solution which does not degrade under the conditions of the investigation were included. The Newtonian material used was an NBS standard viscosity sample, No. N–24. The non-Newtonian solution was a 10-percent solution of polystyrene in toluene. The polystyrene was a high molecular weight sample (average molecular weight $\approx 2.0 \times 10^6$) supplied by the Dow Chemical Company. The solution was prepared in the same manner as the polyisobutene-cetane solution.

Measurements were made in the worker-consistometer on the polyisobutene-cetane system with each of the three capillary disks, the force or pressure required to move the sample through the capillary at a fixed rate being the measured variable. The number of passes for each run made with the tapered capillary varied from 8 to 100 in order to obtain samples at various stages of degradation for intrinsic viscosity determinations. One run of 530 passes was made to see if the difference in pressure in the two directions persisted after the main drop in pressure had occurred for both directions. Some runs were made with the sample entering the larger end of the tapered capillary on the initial pass, others were made with the sample entering the smaller end first. Similar measurements, but considerably fewer of them, were made with polyisobutene in benzene, the polystyrene system, and with the N–24 oil.

Dilute solutions were prepared from each of the worked samples from the worker-consistometer and from the unworked solutions. The intrinsic viscosities were determined for the dilute solutions (½, ¼, ⅛, and $\frac{1}{16}$%) by measuring flow time in the Ubbelohde viscometer, computing the reduced viscosities from the flow time and the viscometer constants, and extrapolating the reduced viscosities to zero concentration.

4. Results

Figure 2 shows a curve for a degradation run for polyisobutene in benzene using the uniform bore capillary. It was impossible to get such data with benzene or other highly volatile solvents prior to the

modification of the cam instrument. Figure 3 shows a similar curve for the polyisobutene in cetane solution with the chamfered capillary disk. This same solution worked through the uniform bore capillary formed an almost identical curve. The curve for the Newtonian material worked through the tapered capillary is shown in figure 4A. In these figures the data are independent of the direction of flow. Figure 4B shows the curves for nearly the same conditions as for figure 3 (the rate of shear varies with the capillary dimensions) but using the tapered capillary.

The intrinsic viscosity of the polyisobutene-cetane solution plotted against the number of passes is shown in figure 4C. No further degradation as revealed by change in intrinsic viscosity occurred beyond the 86th pass, but some difference in pressures in the two directions persisted through 530 passes. A similar difference in pressures in the two directions occurred when the polystyrene solution was worked through the tapered capillary, although there was no indication of degradation.

Figure 5 shows a family of curves at different rates of shear (based on the mean diameter of 0.011 in.) for the polyisobutene-cetane system worked through the tapered capillary. At low rates of shear no observable degradation occurs. With increasing rate of shear, degradation occurs first with the sample entering the smaller end of the tapered capillary. With further increase in the rate of shear, degradation occurs when the sample enters the larger end of the capillary also. During degradation a large part of the observed pressure is used in breaking molecular bonds of the larger molecules [4]. When degradation occurs in both directions at relatively high rates of shear (above 24,000 sec^{-1} in fig. 5) the pressure is larger for flow entering the larger end, though after degradation has ceased the pressure (used to overcome viscous resistance) is less for flow in this direction, compared to flow entering the smaller end of the capillary in each case. This indicates that the energy per pass used in degradation is larger for flow entering the larger end.

Special tests were made with 10-percent polyisobutene in cetane to ascertain if more degradation occurred for flow entering the larger end of the capillary compared to flow entering the smaller end. In these tests the driving gear train was changed for each pass so as to provide a rate of shear of 85,000 reciprocal seconds for flow in the direction being investigated and 3,400 reciprocal seconds for each return pass (no degradation occurs at 3,400 reciprocal seconds). Intrinsic viscosities were obtained with samples after 5 passes and after 10 passes entering the larger end at the high rate of shear and likewise after 5 and after 10 passes entering the smaller end. In each case the intrinsic viscosity for the sample entering the larger end was lower than for the sample entering the smaller end the same number of passes, which indicates more degradation per pass for flow entering the larger end under these conditions.

The apparent viscosity versus rate of shear

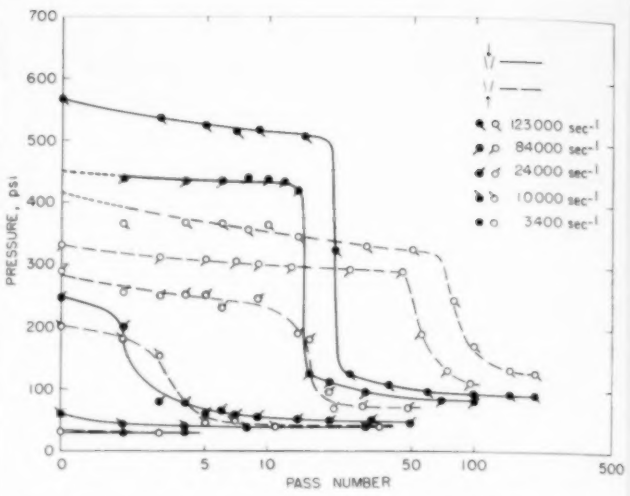

FIGURE 5. *Family of typical pressure curves for 10 percent of polyisobutene in cetane, worked through the tapered capillary at 40° C, at several rates of shear.*

Plotted on semilogarithmic graph to accentuate plateaus before sudden drops in pressure.

(based on the 0.011 in. mean diameter) has been plotted in figure 6 for first pass values and for values after 530 passes at 56,000 reciprocal seconds. These data have been taken from the runs plotted in figure 5 and from additional similar runs. The difference in values in the two directions after 530 passes is not significant except at the higher rates of shear. The difference in first pass values in the two directions results from the fact that the pressures being measured are those of viscous flow combined with those necessary to bring about degradation. For this particular material (10 percent polyisobutene in cetane) the difference in values in the two directions at 3,000 reciprocal seconds is slight, but at 10,000 reciprocal seconds the value for the direction in which the sample enters the smaller end of the capillary is about 225-percent higher than for the direction in which the sample enters the larger end. Then at about 27,000 reciprocal seconds there is no difference in values in the two directions, but at 100,000 reciprocal seconds there is again a difference in values of about 34 percent with the directions reversed. Where viscosity measurements are made on this kind of material in single-pass capillary viscometers, a slight taper in the capillary may make great differences in the values obtained in comparison with capillaries having no taper or having taper in the opposite direction.

5. Discussion

The objective of this work with special capillaries was to investigate the effects encountered with flow of non-Newtonian materials which undergo shear degradation through capillaries having slight tapers or slight defects (unrecognized) at one edge, by using capillaries with somewhat exaggerated cases of these departures from uniform bore. The results indicate that a slight taper may have a large effect on the flow

characteristics, but that a slight chamfer at the edge of the hole has no significant effect.

The equation for flow of a Newtonian material through a tapered capillary can be solved, ignoring end effects, and predicts the relation between pressure drop and quantity of flow as given by Barr [5]. This equation indicates that the pressure drop is independent of the direction of flow, and this was confirmed with tests with Newtonian oils. The analysis of the flow of a non-Newtonian fluid in a tapered capillary has not been made, nor have the end effects been analyzed mathematically.

For a non-Newtonian fluid, when no degradation is occurring it appears that the orientation and alinement of the polymer molecules require less pressure at a given rate of flow when entering the larger end of the tapered capillary than when entering the smaller end.

For given rates of flow the rate of shear at the smaller end is greater than at the larger end of the capillary. At high rates of flow a large proportion of the pressure drop probably occurs in the capillary near each entrance end. This could explain why degradation occurs at lower rates of flow and persists for a greater number of passes with flow entering the smaller end compared to flow entering the larger end of the capillary. When the rate of flow (and rate of shear at the larger end) is large enough to cause degradation with flow entering the larger end the pressure associated with the degradation is abnormally high compared to the pressure for flow in the opposite direction; this and the fact that the degradation per pass is larger for flow entering the larger end may be associated with the larger cross-sectional area of the larger end.

In figure 6, the effective capillary diameter (0.011 in.) obtained with Newtonian oils was used for computing the rate of shear and the apparent viscosity values. If we assume diameters of 0.01055 in. and 0.0129 in. (averages of 0.011 in. and the respective end dimaters) and compute the values of rate of shear and apparent viscosity for the first pass data in figure 6 accordingly, the curves nearly coincide in the range of rates of shear from 2,000 to 15,000 reciprocal seconds; but at higher rates of shear the apparent viscosity for flow entering the larger end becomes increasingly higher than for flow entering the smaller end at given rates of shear (although in both cases the apparent viscosity is decreasing with increase in rate of shear).

In these flow experiments the Reynolds numbers were far below the value of 2,000 frequently considered as a criterion for the onset of perceptible turbulence with Newtonian fluids in capillaries. For the data presented in figure 6, if we consider the apparent viscosity as ranging from 5 down to 1 poise for rates of shear ranging from 7,000 to 121,000 reciprocal seconds, respectively (not counting the energy used in degradation) then the Reynolds numbers range from 0.5 to 45, computed from the mean diameter of 0.011 in. With polyisobutene

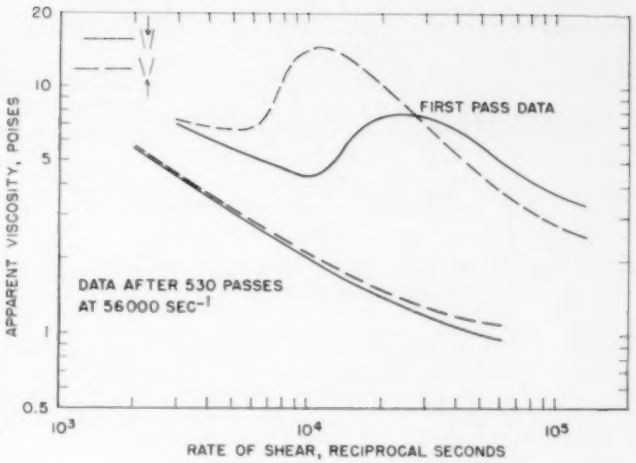

FIGURE 6. *Apparent viscosity versus rate of shear for 10 percent of polyisobutene in cetane, with the tapered capillary, at 40° C, for new (unworked) samples and for a worked sample.*

solutions Schnurman [7] has obtained data which he believes indicate turbulence beginning at a Reynolds number of about 10. In figure 6 the curve for the sample which had been degraded by working 530 passes indicates that there is no turbulence under these conditions. The abnormally high values of apparent viscosity for the first pass data are the result of including the forces used in degradation; and, although rupturing of large molecules may disturb the flow pattern, it is not believed that the flow is turbulent in the sense that this term is applied to flow with Newtonian fluids.

The authors are grateful for consultations with A. B. Bestul, R. S. Marvin, E. A. Kearsley, J. F. Swindells, C. M. Tchen, and L. A. Wall.

6. References

[1] S. A. McKee and H. S. White, A worker-consistometer for lubricating greases, ASTM Bul. **153,** 90 (August 1948).
[2] S. A. McKee and H. S. White, The McKee worker-consistometer with constant speed drives, J. Research NBS **46,** 18 (1951) RP2170.
[3] A. B. Bestul and H. V. Belcher, Degradation of polyisobutenes on shearing in solution, J. Appl. Phys. **24,** 1069 (1953).
[4] A. B. Bestul, Composition of apparent shearing forces during shear degradation of polymers, J. Appl. Phys. **25,** 1011 (1954).
[5] G. Barr, A monograph of viscosity, p. 64 (Oxford University Press, London, 1931).
[6] J. Ubbelohde, J. Inst. Petrol. Tech. **19,** 376 (1933).
[7] Quoted by Frisch and Simha in: F. R. Eirich, Rheology, theory and applications, **1,** 607 (Academic Press, Inc., New York, N. Y., 1956).

Washington, August 19, 1957.

Journal of Research of the National Bureau of Standards Vol. 60, No. 3, March, 1958 Research Paper 2840

Ortho-Para Catalysis in Liquid-Hydrogen Production[1]

D. H. Weitzel, W. V. Loebenstein, J. W. Draper, and O. E. Park

A series of selected or specially prepared catalysts were studied for their ability to accelerate the ortho to para conversion of hydrogen. The results of this study are presented, and the performance of various catalysts are compared with that of chromic oxide on alumina pellets. An outstanding catalyst, unsupported hydrous ferric oxide granules, was selected for further study and used in the liquefiers of the National Bureau of Standards Cryogenic Engineering Laboratory. One and one-half liters of this catalyst has now been used to convert more than 100,000 liters of liquid hydrogen to 90 to 95 percent para at an average rate of about 235 liters of liquid per hour. There is to date no evidence of decrease in efficiency with continued use.

1. Introduction

Freshly liquefied hydrogen that has not been catalyzed consists of a 3-to-1 ortho-para mixture. There is a slow but definite change in the mixture on standing, which complicates the problem of keeping the liquid for any great length of time. The exothermic heat of conversion of ortho- to parahydrogen at 20° K is about 254 calories per mole, whereas the endothermic heat of vaporization of liquid hydrogen is 216 calories per mole [1].[2] As a result of this slow change, a thermally isolated tank of liquid hydrogen prepared without conversion to the para form will lose about 18 percent of its volume during the first day of storage. In the absence of this internal evolution of heat, the heat transfer to a well-insulated Dewar may result in a loss of less than 1 percent per day.

The obvious solution of the above difficulty is the conversion to the para form either in the gas phase before liquefaction or in the liquid phase immediately after liquefaction, but in any case before delivery to the storage Dewar.

1.1. Background

Farkas and Sachsse [2] observed the catalytic effect of the paramagnetic molecule of oxygen in the gas phase on the conversion of parahydrogen to normal hydrogen. They also showed that the diamagnetic gases nitrogen, nitrous oxide, carbon dioxide, ammonia, hydriodic acid, sulfur dioxide, and iron pentacarbonyl caused no conversion, whereas the effects of the paramagnetic gases, nitric oxide and nitrogen dioxide, were similar to that of oxygen. The associated molecule N_2O_4 was ineffective.

Bonhoeffer and Harteck [3] were the first to make use of heterogeneous catalysis to establish ortho-para equilibrium. They used charcoal at liquid-air temperatures and were able to establish equilibrium quickly when normal hydrogen was passed over the catalyst. However, when parahydrogen was passed over charcoal at room temperature, no conversion took place [4].

Taylor and collaborators [5, 6] studied the catalytic activity of the metallic oxides and found that the paramagnetic substances chromic oxide, cerium oxide, and neodymium oxide brought about rapid conversion, whereas zinc oxide, lanthanum oxide, and vanadium pentoxide, having low or negligible paramagnetism, showed low or negligible conversion efficiencies. They conclude that the magnetic character of the surface of the catalyst is a controlling factor and may account for their earlier success with metallic nickel, as well as for the results of Emmett and Harkness [7] with Van der Waal's adsorption on iron synthetic ammonia catalysts.

1.2 Chromic Oxide Catalyst

Grilly [8] made use of commercially available chromic oxide on alumina for both gas and liquid phase conversion, his object being improvement in the keeping quality of the liquid produced. He successfully modified a liquefier so as to operate at 25 liters per hour for regular production of 85-percent para liquid.

Essentially pure (95 to 97 percent) parahydrogen was first produced in quantity at the National Bureau of Standards Cryogenic Engineering Laboratory in 1953 [9]. The catalyst was placed in the bottom of the liquefier reservoir. Liquid hydrogen from the expansion valve filtered through the catalyst before reaching the transfer siphon for delivery to the storage Dewar. Due to the urgency of the project, the chromic oxide catalyst, which had proved effective in Grilly's work, was used. It consisted of ⅛-in. by ⅛-in. pellets of approximately 20-percent chromic oxide on alumina.

About 65 liters of this catalyst resulted in conversion to 95 to 97 percent parahydrogen when the production was about 240 liters of liquid hydrogen per hour. Many thousands of liters of liquid parahydrogen were produced with the aid of this catalyst bed. So long as the catalyst was reactivated by heating and pumping (104° C, 25 mm Hg, for 24 hr or more) whenever exposure to atmospheric air had

[1] This work was supported by the U. S. Atomic Energy Commission.
[2] Figures in brackets indicate the literature references at the end of this paper.

occurred, there appeared to be no reduction in its effectiveness for bringing about the conversion to near equilibrium concentrations.

The results obtained with chromic oxide were gratifying, but a search for a more effective catalyst was continued in the hope of finding one that would occupy less space in the liquid reservoir. The large volume of chromic oxide catalyst required resulted in the formation of considerable quantities of dust or fines that could be carried through the system. To prevent this, filters and baffle plates had to be installed to prevent any shifting or motion of the catalyst pellets. This was probably the most serious difficulty overcome in the adaptation of chromic oxide on alumina to the NBS Cryogenic Engineering Laboratory liquefiers. Another disadvantage was the delay in initial cool-down resulting from the heat capacity of the large catalyst mass.

Since it was evident that the design of more compact parahydrogen liquefiers of various capacities would be simplified if a more efficient catalyst were available, a systematic study of materials that might catalyze the ortho-parahydrogen conversion was undertaken.

2. Catalyst Survey

The choice of materials to be tested was limited by such practical considerations as resistance to abrasion, availability, and economic feasibility. Beyond these considerations the selection of samples was based on the reports of previous investigators and on experience with the chromic oxide on alumina. Taylor and Diamond [10] found definite correlation between catalytic effectiveness and both magnetic susceptibility and adsorptive capacity. Of interest also was the theory advanced by Wigner [11], which states that the velocity constant of the reaction is proportional to the square of the effective magnetic moment in Bohr magnetons.

The effective moment μ_{eff} is given by the relation

$$\mu_{eff}=2\sqrt{S(S+1)},$$

where S represents total spin of the ion.

If n is the number of unpaired electrons in the ion, then $S=n/2$. Therefore, $\mu_{eff}=\sqrt{n(n+2)}$.

For chromic ion (Cr^{+3}) having three unpaired electrons ($n=3$), $\mu_{eff}=3.87$ magnetons, and for ferric ion (Fe^{+3}) having five unpaired electrons ($n=5$), $\mu_{eff}=5.92$ magnetons.

Therefore, the ratio of the velocity constants according to Wigner's theory, should be

$$\frac{(5.92)^2}{(3.87)^2}=2.34.$$

Accordingly, the ferric ion should be two and one-third times as effective for ortho-parahydrogen conversion as chromic ion, other things being equal.

2.1. Catalyst Preparations

With the above considerations in mind, 15 catalysts were obtained either commercially or prepared in the laboratory. A brief description of each material follows:

Paramagnetic ferric oxide (15%) on Florex:

Fuller's earth granules obtained from the Floridin Co. were impregnated with a concentrated solution of ferrous ammonium nitrate. This was followed by heating the granules in a vacuum at 200° C for 48 hours. This technique for the preparation of supported ferric oxide free from ferromagnetism has been described by Selwood [12].

Paramagnetic ferric oxide (2%) on porous glass:

Porous glass granules, obtained from the Corning Glass Works, were impregnated and oxidized as described above.

Magnetite (Fe_3O_4) unsupported:

Granules of a synthetic magnetite were obtained from the U. S. Bureau of Mines. The granules were reduced in hydrogen at 450° C, then oxidized in air at 490° C.

Paramagnetic ferric oxide (15%) and chromia (9.3%) on alumina:

This mixed catalyst was prepared by impregnating pellets of Cr_2O_3 on Davison alumina with paramagnetic Fe_2O_3.

Ferric ammonium sulfate, unsupported:

This material was chosen because of its unusually high magnetic susceptibility at low temperatures.

Hydrous ferric oxide, unsupported:

The preparation of this material consisted of precipitation of the gel by addition of sodium hydroxide to a solution of ferric chloride, followed by washing the gel with distilled water. The gel was then filtered, extruded, dried, and activated in air at 140° C.

Hydrous manganese oxide, unsupported:

The preparation here was the same as that for the hydrous ferric oxide, except that manganese chloride was substituted for the ferric chloride.

Manganese dioxide (18%) on silica gel:

This material was prepared by addition of a solution of $Mn(NO_3)_2$ to a deactivated sample of Davison "Intermediate Density" silica gel. The granules were then dried and heated in a stream of air at 400° C. This caused the nitrate to decompose, forming MnO_2.

Ferrous chloride on silica gel:

Deactivated silica gel was impregnated with a water solution of ferrous chloride.

Nickel (0.5%) on alumina:

This catalyst was obtained from Baker & Co., Inc.

Nickel (5.3%) and thoria (0.24%) on Davison alumina:

Since thoria is known to be a good promoter of nickel catalysts at high temperatures, this material was made by using a solution of 0.10 mole nickelous nitrate and 0.001 mole thorium nitrate in water. Alumina pellets were wetted with this solution,

then dried and the nitrates decomposed to oxides in a stream of air at 400° C. Finally, the nickel oxide distributed throughout the pellets was reduced to metallic nickel by treatment with hydrogen at 400° C.

Gadolinium oxide.

Neodymium oxide.

Crude cerium oxide:

These rare-earth oxides were tested because their successful use as ortho-parahydrogen conversion catalysts had been reported by Taylor and others. The oxides were tested in the form of unsupported powder.

Chromia (20%) on alumina:

This was the Harshaw catalyst that had been used in the Cryogenic Engineering Laboratory liquefiers. It was used as a comparison in the evaluation of the other catalysts.

2.2. Activities of Catalysts

a. Apparatus

The apparatus constructed for the ortho-para-hydrogen studies is shown schematically in figure 1, and the analyzer is represented in figure 2.

The analyzer was built around a thermal-conductivity cell and is described in a previous paper [13]. A reversing valve was, however, installed in the flow lines leading to the cell. This valve makes it possible to alternate the reference and analyzed gas streams from one side of the bridge to the other, thus obtaining an average reading from which a number of errors due to imperfect zero balance and filament matching have been eliminated. A four-way selector valve was also added to the analyzer as shown.

The central part of the apparatus shown in figure 1 is a stainless-steel Dewar enclosed in a sealed and vented metal container, which in turn is surrounded by a large liquid-nitrogen bath. The chamber that contained the catalyst being tested was a copper cylinder, ¾-in. diameter by 4 in. long, suspended vertically from the top plate of the apparatus by

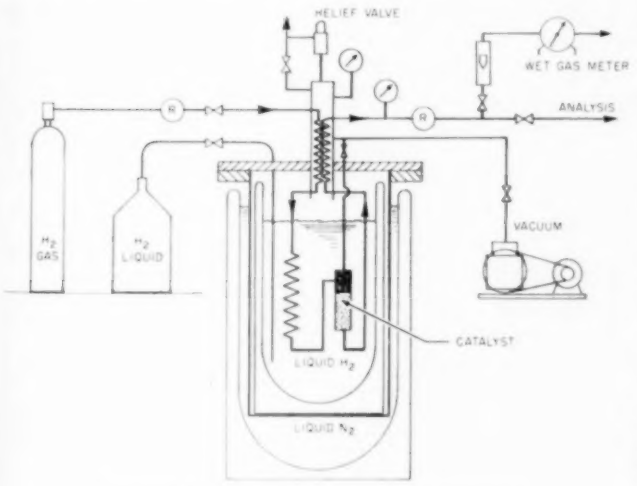

FIGURE 1. *Catalyst evaluation apparatus.*

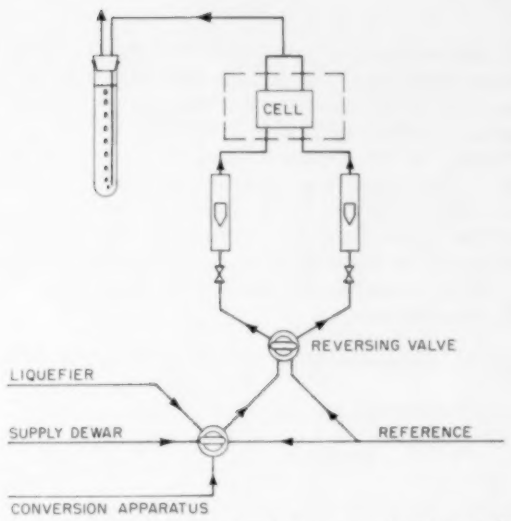

FIGURE 2. *Flow sheet of ortho-para conductivity cell.*

means of a stainless-steel tube, which also served as the pumping tap during catalyst cleanup. Hydrogen gas entering the chamber was first led through a heat exchanger, counter-current to the exhaust flow, then through a coil of copper tubing (⅛ in.) in the bath liquid, and finally through the catalyst. The flow through the chamber was downward. The top inch of the chamber was packed with copper sponge to provide a volume of good heat exchange for recondensation of vapor formed by heat of conversion during liquid-phase studies. After passing through the catalyst, the hydrogen was warmed to room temperature, partly through heat exchange with the incoming gas and partly by passing through additional copper tubing after emerging from the Dewars. About 50 ml per minute of the exhaust flow was deflected through the analyzer system, and the balance went through a rotameter and wet-gas meter before being vented to the atmosphere.

The catalyst temperature was assumed to be the same as that of the bath, and this could be varied by choice of bath liquid and by adjustment of the pressure under which the bath was maintained. For studying the catalyzed reconversion of para to normal hydrogen, the Dewars could be removed and a wire-wound sleeve heater controlled by a variable transformer placed around the catalyst chamber. This heater, together with the combined suspension tube and pumping tap mentioned above, served to reactivate the catalyst prior to a space-velocity measurement.

The same cylinder of purified normal hydrogen was used to provide reference gas for the analysis cell and gas to be converted in the catalyst chamber. Calibration of the analysis system at 99.8 percent parahydrogen was conveniently obtained at the beginning of a run simply by using the exhaust gas from the catalyst chamber at two different (low) flow rates, both of which gave the same analysis signal. Calibration at 25 percent parahydrogen resulted from passing the normal reference hydrogen simultaneously through both sides of the analysis cell.

b. Results

To determine the comparative effectiveness of the various catalysts, the space velocity was measured for each in STP volumes per minute per unit volume of catalyst when converting normal 25 percent parahydrogen to 90 percent para with the catalyst at 20°K. The results of this initial series of measurements are shown in table 1, where the catalysts are arranged according to increasing space velocities. Also shown is the relative effectiveness of each catalyst when compared with the Harshaw chromic oxide on alumina.

TABLE 1. *Conversion of 25-percent para to 90-percent para at 20° K, 15 psig*

Catalyst	Space velocity	Relative space velocity (Cr_2O_3=1)
	STP/min	
Gadolinium oxide, unsupported	10	0.2
Crude ceric oxide, unsupported	20	.4
Neodymium oxide, unsupported	20	.4
$FeCl_2$ on silica gel	20	.4
2% paramagnetic Fe_2O_3 on porous glass	20	.4
15% paramagnetic Fe_2O_3 on Florex	24	.5
Ferric ammonium sulfate, unsupported	30	.6
Magnetite, Fe_3O_4, unsupported	40	.8
20% Cr_2O_3 on alumina (Harshaw)	50	1.0
15% paramagnetic Fe_2O_3 and 9.3% Cr_2O_3 on alumina	50	1.0
5.3% Ni and 0.24% thoria on alumina	60	1.2
18% MnO_2 on silica gel	80	1.6
0.5% Ni on alumina	100	2.0
Hydrous manganese dioxide, unsupported	190	3.8
Hydrous ferric oxide, unsupported	330	6.6

The rare-earth oxides did not show up very well, being less than half as active as chromic oxide on alumina. (It is difficult to compare these results with the work of Taylor and Diamond [6] because no actual space velocities are reported in their article.) In the present investigation, the laboratory preparations of iron oxide free from ferromagnetism were hardly as good as the reference chromic oxide on alumina. The high magnetic susceptibility of ferric ammonium sulfate at the temperature of the conversion did not result in an outstanding catalyst, but gave an activity between those of paramagnetic iron oxide on Florex and unsupported synthetic magnetite. The nickel and manganese compounds resulted in good catalysts, with ½ percent nickel on alumina twice as good and manganese dioxide on silica gel 1.6 times as good as the reference chromic oxide on alumina.

Although attempts to reduce ferromagnetism of supported iron oxide catalysts did not help the catalytic effectiveness, there was a marked improvement in both manganese and iron when the supported oxide was replaced by the unsupported hydrous form. Thus hydrous manganese oxide was about four times and hydrous iron oxide almost seven times as good as chromic oxide on alumina.

3. Hydrous Iron Oxide Catalyst

3.1. Laboratory Studies

Additional measurements with the hydrous iron oxide disclosed at once that the space velocity for liquid-phase conversion could be further increased by a very significant factor simply by using a smaller particle size. The original measurements had been made with approximately ⅛-in. pellets. Cutting each of these into about four pieces increased the space velocity from 330 to 750, and grinding the material into a fine powder resulted in a STP space velocity of almost 2,000 per minute.

Since there are obvious disadvantages to the use of fine powders in liquefiers, it was desirable to prepare more of the material in order to experiment with various mesh sizes and particle modifications. Difficulties were encountered, some of which are referred to by Weiser [14], i. e., properties of the hydrous oxides may show marked variations with small variations in treatment of the sample. Although reasonable care was taken to use the same procedure in the preparation of several samples, the space velocities of the resultant products would vary, sometimes by a factor of 2 or 3. It was necessary to prepare a number of batches before sufficient high-activity material was collected to support the research and charge one of the large Cryogenic Engineering Laboratory liquefiers.

The reasons for the increased activity of the better preparations were not entirely clear. No correlation was found, for example, between catalytic activity and the concentration of various metallic impurities as determined by spectrographic analysis. Increased bulk density was identified with increased catalytic activity, but the procedure for obtaining a high-density product was not apparent. Of course, some increased activity of the unsupported oxide should be anticipated because of the higher percentage of iron in the sample. This is certainly an over simplification and would not explain the range in catalytic activities of the other iron preparations.

An excellent correlation was found between catalytic activity and surface area as determined from low-temperature nitrogen adsorption by application of the Brunauer, Emmett, and Teller theory [15]. The surface areas of three laboratory preparations of 30 to 100 mesh hydrous iron oxide are shown in figure 3 plotted against their corresponding catalytic ac-

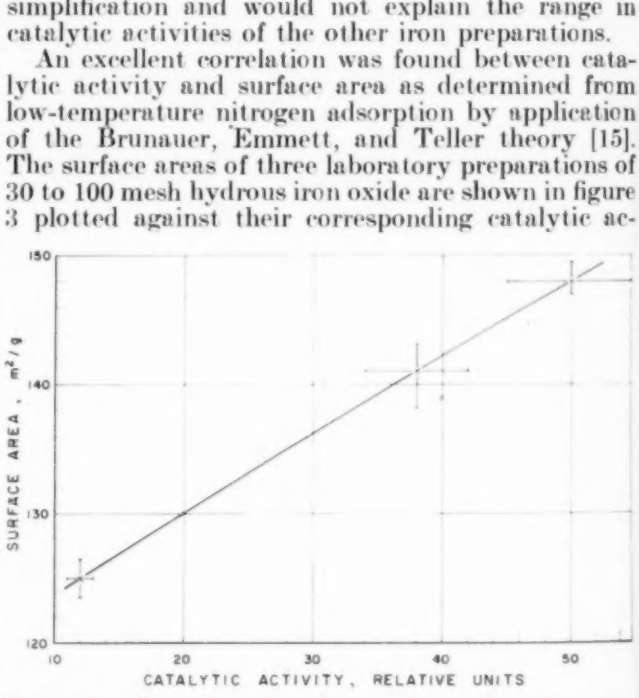

FIGURE 3. *Correlation of catalytic activity with surface area.*

tivities relative to the reference chromia catalyst. The crosses passing through each point correspond to the confidence limits of the measurements. It is apparent that the degree of correlation is striking within the range studied. The factors that affect the surface area of the ultimate catalyst have not been thoroughly investigated, but it is felt that variations in the degree and extent of heating during formation and/or activation are of prime importance in this regard.

Selwood [12] described in considerable detail the preparation of iron oxide free from ferromagnetism. When Selwood's directions were not followed, as in the preparation of unsupported hydrous ferric oxide, appreciable ferromagnetism was introduced.[3] Yet, these were the very samples that exhibited the highest catalytic activity. Admittedly, very little is known regarding the effect of ferromagnetism on catalytic activity. In discussing the applicability of ferromagnetic studies to catalyst structure problems, Selwood [12] states, "Ferromagnetism, in contrast to paramagnetism, is a cooperative phenomenon. A substance does not become ferromagnetic until the grain size exceeds a certain critical size, sometimes referred to as the ferromagnetic domain. This is a situation which somewhat weakens the applicability of ferromagnetic studies to catalyst structure problems. Those particles which are too finely divided to show ferromagnetism are precisely those which are likely to exhibit the most catalytic activity. This is true by virtue of their large surface area, if for no other reason." From the results of the present work, the influence of ferromagnetism might, indeed, have enhanced the activity of the catalyst. As stated previously, only 2⅓-fold increase in activity of iron over chromium was to be expected, based on paramagnetic considerations. The actual improvement realized was many fold greater than this.

The results of the particle-size investigation are interesting. For liquid-phase conversion granules of 20 to 30 mesh proved almost twice as effective as 10 to 20 mesh, but 40 to 50 mesh was very little better than 20 to 30 mesh. Tests of particles smaller than 50 mesh showed very little further improvement. For vapor-phase conversion at 76° K the situation was somewhat different. Here the gain in going from 10 to 20 mesh to 40 to 50 mesh was only about 15 percent, and again beyond 50 mesh there was little or no further improvement.

The space velocities for ortho-para conversion in the presence of these hydrous iron oxide granules are so high that very small samples of catalyst, usually 7 ml, were used for making the measurements. This was necessary to avoid having complete conversion at all but excessively high flow rates. The smaller samples also made possible a considerable simplification of the apparatus, as shown in figure 4. The catalyst was merely placed in a slim capsule with ⅛-in.-diameter inlet and outlet lines and dropped through the neck of a standard 50-liter

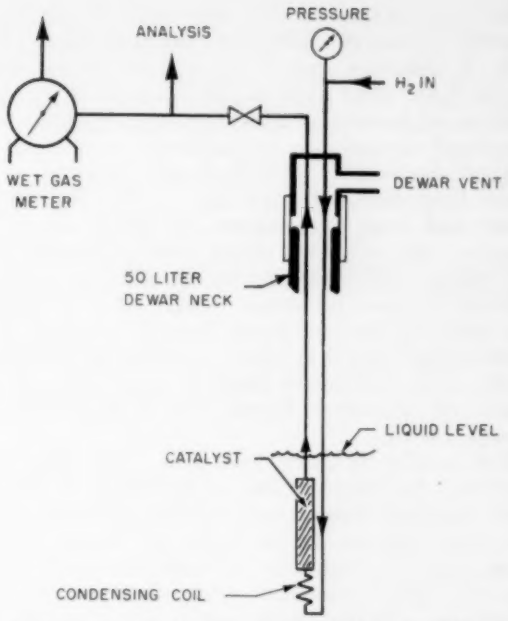

FIGURE 4. *Ortho-para catalyst testing capsule.*

liquid-hydrogen Dewar. Space velocities for conversion of 25 to 90 percent para, measured in this way, had STP values between 2,000 and 2,500 per minute for liquid-phase conversion when using granules of 20 mesh or smaller. In terms of liquid-hydrogen production, this means 1 liter of catalyst placed in the liquid receiver will convert 150 to 190 liters of liquid per hour from 25 to 90 percent para.

3.2. Hydrous Iron Oxide in CEL Liquefiers

The hydrous iron oxide catalyst has been used for liquid-phase conversion in two small and one large liquefier at the NBS Cryogenic Engineering Laboratory and has performed at least as well as predicted by the laboratory-scale space-velocity measurements. In the small liquefiers the catalyst was placed between screens in such a way that liquid head building up outside the catalyst container provided sufficient force to push liquid up through the bed from bottom to top. This was found to be more satisfactory than simply discharging the unconverted liquid on top of the catalyst and attempting to withdraw it from the bottom of the bed. The difficulty in the latter approach arises because returning vapor, caused by heat of conversion, forms a barrier that effectively prevents downward flow of liquid. The liquid therefore builds up on the catalyst until it spills over the top of the container. With the former arrangement, however, one liquefier, using 370 ml of 30- to 40-mesh catalyst, produced 40 liters per hour of 90 percent para, and another using 1,200 ml of 10- to 20-mesh produced 80 liters per hour of 95 percent para. The realized space velocity is, in the first instance, a little less than was predicted on the basis of laboratory measurements, whereas in the second case the catalyst performed somewhat better than predicted

[3] It was possible to pick up particles of this catalyst preparation by means of a small permanent magnet.

For installation of the new catalyst in the large liquefier a novel split-flow arrangement designed by V. J. Johnson and P. C. Vander Arend was employed [16]. The system, as illustrated in figure 5, involves a second Joule-Thomson expansion valve connected directly to an assembly made up of the catalyst container, preceded and followed by adequate heat-exchanger surface. The catalyst container and heat exchangers are immersed in liquid supplied through the usual Joule-Thomson expansion valve. After passing through this condensation-conversion-recondensation train, the entire steam goes directly to the liquid-transfer siphon. Thus, unconverted liquid is used as refrigerant to condense totally and to remove heat of conversion from the stream of converted liquid that is delivered to the storage vessel.

The results of three trial runs with this arrangement and 1.5 liters of 30- to 100-mesh hydrous iron oxide catalyst were reported by Johnson [16]. At that time about 4,500 liters of liquid had been made, and the quantity of catalyst, as well as the area of heat-exchanger surface, appeared to be borderline. Since these initial runs, however, the catalyst has received more consistent cleanup treatment, and experience has been gained in operation of the split-flow double-valve arrangement. Although no changes in catalyst or heat exchangers have been made, there has been a significant improvement in performance. An additional 100,000 liters of liquid has since been produced. Most of this has passed through the catalyst at 230 to 240 liters of liquid per hour. This represents a liquid space velocity of about 2.6 per minute, or an STP space velocity of a little more than 2,000 per minute. Space velocity measured in the laboratory for a small sample of this batch of catalyst gave 2,200 STP per minute for conversion from 25 to 90 percent para.

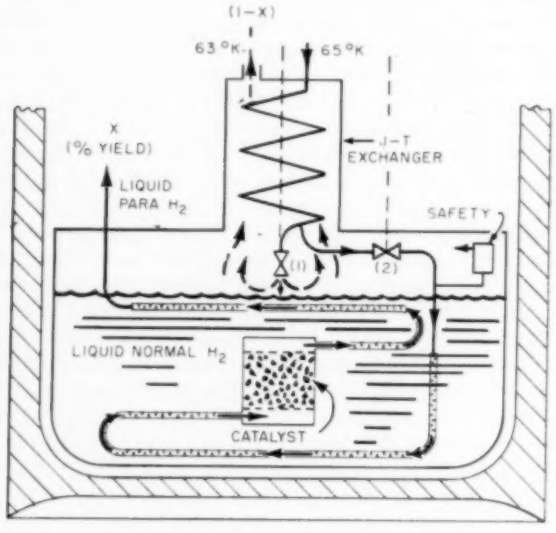

FIGURE 5. *Installationof hydrous iron oxide catalyst in large Cryogenic Engineering Laboratory liquefier.*

3.3. Catalyst Activation and Lifetime

After initial drying and activation of the catalyst in air at temperatures up to 140° C, the normal activation procedure has been to maintain the hydrous iron oxide granules at reduced pressure and moderate temperature for at least 16 hr. In the laboratory, evacuation has been to the order of 1 mm Hg or less at 110° to 120° C. These conditions are maintained immediately prior to an activity test, and the vacuum is broken with pure hydrogen gas. The catalyst changes its structure and is completely ruined if heated much beyond 140° C.

In one test it was found that a few days of exposure to atmospheric air reduced the effectiveness to one-third of its normal value. In another test a cleanup of 6 hr resulted in a space velocity of 1,800 per minute, whereas a 3-day cleanup raised this to 2,600 per minute. The behavior indicated by these laboratory tests is also borne out in the large liquefier. For example, power failure prior to one liquefaction run resulted in a cleanup of only 3 hr at the specified temperature. This run produced 80 to 85 percent parahydrogen. Subsequent runs with the same catalyst and a 16-hr cleanup resulted in 90 to 95 percent parahydrogen at equal or higher production rates.

In an effort to obtain data on the probable lifetime of the catalyst, a sample was cycled in the laboratory between use at 20° K and activation at 110° C. The sample was subjected to a total of 31 cycles over a period of 6 weeks. The total time in use for conversion was 137 hr, and the total time on activation was 821 hr. The conversion activity remained essentially constant throughout, being actually a little higher at the end than at the beginning of the tests. Plant-scale data on catalyst lifetime consists at present of production of about 100,000 liters of converted liquid over a period of about 5 months. The hydrous ferric oxide catalyst (1.5 liters of 30 to 100 mesh) being used shows no sign of decreasing activity.

The authors express appreciation to Frank E. E. Germann for literature survey and for writing the introduction to this paper. K. D. Timmerhaus has followed the course of much of the work and offered valuable suggestions. C. C. Van Valin has contributed by making many of the more recent space-velocity measurements. L. E. White[4] was in charge of the group when the catalyst survey program was initiated. Also, we acknowledge and appreciate the contribution of the gas liquefaction group of CEL, particularly V. J. Johnson, W. A. Wilson, and J. E. Jensen, who installed and tested the iron catalyst in various liquefiers. Finally, thanks are due P. C. Vander Arend[5] for guidance and encouragement over a period of several years, during which the ortho-parahydrogen program experienced a number of changes of fortune.

[4] Presently associated with Aerojet General Corporation.
[5] Presently associated with Air Products, Inc.

4. References

[1] H. W. Wooley, R. B. Scott, and F. G. Brickwedde, J. Research NBS **41,** 379 (1948) RP1932.

[2] L. Farkas and H. Sachsse, Z. Physik. Chem. **B23,** 1 and 19 (1933).

[3] K. F. Bonhoeffer and P. Harteck, Naturwiss. **17,** 182 (1929).

[4] A. Farkas, Orthohydrogen, parahydrogen, and heavy hydrogen (Cambridge University Press, p. 89, 1935).

[5] H. S. Taylor and A. Sherman, J. Am. Chem. Soc. **53,** 1614 (1931).

[6] H. S. Taylor and H. Diamond, J. Am. Chem. Soc. **55,** 2613 (1933).

[7] P. H. Emmett and R. W. Harkness, J. Am. Chem. Soc. **57,** 1624 and 1631 (1935).

[8] E. R. Grilly, Rev. Sci. Instr. **24,** 1 (1953); **24,** 899 (1953).

[9] L. E. White, P. C. Vander Arend, and P. L. Barrick (unpublished report).

[10] H. S. Taylor and H. Diamond, J. Am. Chem. Soc. **57,** 1251 (1935).

[11] E. Wigner, Z. Physik. Chem. **B19,** 203 (1932); **B23,** 28 (1933).

[12] P. W. Selwood, Advances in catalysis, III, p. 80–85 (Academic Press, Inc., New York, N. Y., 1951).

[13] D. H. Weitzel and L. E. White, Rev. Sci. Instr. **26,** 290 (1955).

[14] H. B. Weiser, Inorganic colloid chemistry, VII. The hydrous oxides and hydroxides, p. 27, 31 ff, (John Wiley & Sons, Inc., New York, N. Y., 1935).

[15] S. Brunauer, P. H. Emmett, and E. Teller, J. Am. Chem. Soc. **60,** 309 (1938).

[16] Proceedings of 1956 Cryogenic Engineering Conference held at NBS in Boulder, Colo., Paper A–4 (September 1956).

BOULDER, COLO., OCTOBER 7, 1957.

Journal of Research of the National Bureau of Standards Vol. 60, No. 3, March 1958 Research Paper 2841

Degradation of Cellulose in a Vacuum with Ultraviolet Light

Joseph H. Flynn, William K. Wilson, and William L. Morrow

Dried, purified, cotton cellulose sheets were irradiated in a vacuum at 40° C with light of 2537 A wavelength. Hydrogen, carbon monoxide, and carbon dioxide were evolved, the degree of polymerization (D. P.) decreased, and CHO and COOH groups were produced. The evolution of hydrogen has not been reported previously. The rate of hydrogen evolution followed a parabolic rate law indicating inhibition by a product. The rate of evolution of carbon monoxide plus carbon dioxide increased slightly during irradiation. The initial quantum yield was 10^{-2} for hydrogen and 10^{-3} for carbon monoxide and carbon dioxide. A mechanism is proposed in which alcohol groups are photolyzed to carbonyl with the liberation of hydrogen.

1. Introduction

The study of the irradiation in a vacuum of polymeric materials that contain specific functional groups holds several advantages over the gas-phase photochemical studies of smaller organic compounds containing such groups. In the former, the gaseous dissociation products of the primary process may be allowed to diffuse from the system to a collection point. The reactions of labile dissociation products attached to the solid are minimized due to their immobility, and these products may be characterized to some extent after exposure to various gaseous atmospheres. Thus, complicating kinetic chains can be eliminated and the interaction of reactants, intermediates, and products can be kept at a minimum.

Cellulose is a substrate that is particularly adaptable to this type of study. Celluloses containing various amounts of carboxyl, aldehyde, and other groups are easily prepared, and quantitative procedures are available for determining concentrations of these groups before and after irradiation.

The photochemical degradation of cellulose has been extensively investigated as it is an important cause of deterioration of textiles and paper. Past investigators have found that the irradiation of cellulose with 2537 A light results in considerable degradation both in the presence and absence of oxygen. Increase in carboxyl and reducing groups upon exposure to air after irradiation has been noted, carbon monoxide and carbon dioxide have been observed as gaseous products, and decrease in glucosidic linkages has been evidenced by loss in strength, decrease in percent alpha-cellulose, and decrease in degree of polymerization (D. P.) [1].[1]

The amount of degradation was independent of the presence of oxygen during irradiation and was inhibited by water vapor [2]. A post-irradiation decomposition took place at a very low rate in the presence of oxygen [2, 3], suggesting the presence of labile dissociation products in the irradiated polymer.

This paper describes the irradiation of purified, dried, cotton cellulose in an evacuated system with 2537 A light. The composition and rate of evolution of gaseous products were measured and changes in functional group content and degree of polymerization of the irradiated cellulose were determined.

[1] Figure in brackets indicate the literature references at the end of this paper.

2. Experimental Procedure

2.1. Preparation of Cellulose

Clean cotton sliver was purified by a modification of the method of Warner and Mease [4]. The purified cotton was cut into quarter-inch lengths, beaten with the minimum amount of distilled water in an agate mortar, and made into sheets on a British Handsheet Machine. These sheets were cut to form rectangles of 92 cm^2, 0.0018-cm thick and weighing 0.86 g. These were dried by occasional heating at 100° C in the irradiation apparatus for over a week until the system would maintain a pressure of less than 10^{-6} mm of Hg.

2.2. Irradiation of Cellulose

The reaction vessel and irradiation apparatus are shown in figure 1. The cellulose sheet was placed around a cold finger through which water from a constant-temperature bath was circulated. The cold finger was sealed into a large quartz tube which was

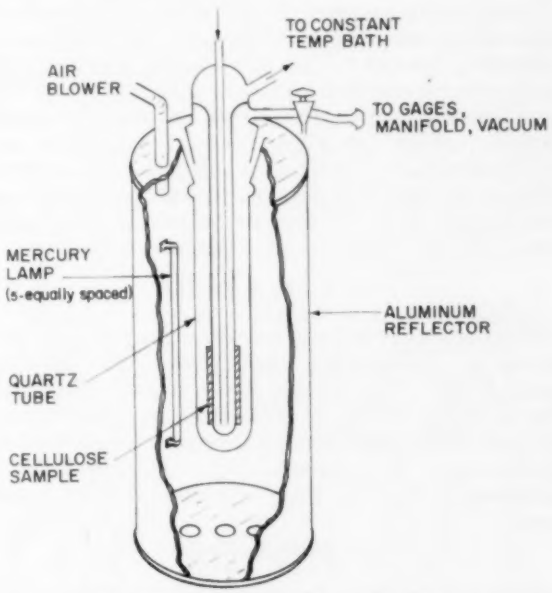

FIGURE 1. *Irradiation apparatus.*

inserted axially into the irradiation apparatus and connected by a stopcock to the vacuum manifold.

The cellulose was irradiated by five Hanovia quartz low-pressure mercury lamps spaced evenly about the interior of an etched cylindrical aluminum reflector. The lamps were controlled by separate Variacs and transformers, and their operating temperature was maintained at 50° ±1° C by an air blower, as their output is quite dependent on temperature [5]. Under these conditions, the energy in the ultraviolet region results almost entirely from the 2537 A Hg line. The intensity of the irradiating light was calculated from periodic calibration of the lamps in place in the reflector by a selenium photovoltaic cell with a Willemite converter. This sensing device was calibrated against a standard 2537 A source by the Radiometry Section of the Bureau and used in its most sensitive range.

The pressure of evolved gas was measured by a thermocouple gage and a discharge gage of the RCA Vacuum Gage Unit, Type EMG–1, and by a McLeod mercury manometer.

2.3. Analysis of Gaseous Products

The composition of gaseous products was determined with a mass spectrometer. Also, the percent hydrogen of the gases in the system was estimated by comparison of the thermocouple and McLeod gage readings.

2.4. Analysis of the Irradiated Cellulose

The irradiated cellulose was stored for several months in air and was analyzed to determine changes in the degree of polymerization, carboxyl content, and aldehyde content.

a. Degree of Polymerization (D. P.)

The weight-average D. P. was calculated from cuprammonium viscosity data using a relation developed by Battista [6]. The cuprammonium solvent was prepared by the method of Launer and Wilson [7]. The cellulose was dissolved in the cuprammonium solvent in glass vessels containing copper and filled with solvent to exclude air. The viscosities of the 0.50 percent by weight cellulose solutions were determined with Ostwald-Cannon-Fenske viscometers calibrated with NBS standard oils.

b. Carboxyl Content

The carboxyl content was determined by a modification of Davidson's methylene blue adsorption method [8]. Automatic 1-ml pipets coated with Dow Corning 200 fluid were used to deliver the centrifuged methylene blue solutions to volumetric flasks for dilution. A Beckman Model DU Quartz Spectrophotometer was used for the absorbance measurements.

c. Aldehyde Content

Aldehyde was determined by oxidation of the irradiated cellulose with a solution of sodium chlorite in HOAc–NaOAc buffer (pH=3.5, ionic strength=0.11) at 40°C followed by determination of the amount of chlorite consumed [9]. In calculating the aldehyde content, an equation developed from the kinetics of the oxidation of glucose with this reagent was used [10].

2.5. Reflectance

The reflectance of the cellulose sheets was measured by comparison with a fresh surface of magnesium carbonate. The latter reflects 72 percent of the 2537 A radiation [11]. The cellulose sheets initially reflected 55 percent and transmitted 1.8 percent of the 2537 A light.

3. Results

3.1. Gaseous Products

Hydrogen, carbon monoxide, and carbon dioxide were evolved during the irradiation. The mole percent of hydrogen decreased with increasing dosage and could be extrapolated to an initial value of 92 percent. Table 1 gives the results of the mass spectrometric analysis of gases evolved during an irradiation of 2.84×10^{-4} $Nh\nu$/cm^2 at 40° C where N is Avogadro's number, h is Planck's constant, and ν is the frequency of the irradiating light.

TABLE 1. *Gaseous products from irradiation of cellulose in a vacuum*

	Component		
	H_2	CO	CO_2
Mole percent	87.5	8.2	4.3

The rate of hydrogen evolution fell off with increasing dosage but behaved erratically at higher total gas pressure. In order to minimize the reaction between gaseous products and the irradiated cellulose, the system was alternately isolated and evacuated for 5-min periods during the irradiation for many of the runs. Thus, the total gas pressure was kept below 0.03 mm. A plot of the square of the reciprocal of the rate of hydrogen evolution versus dosage (time) in figure 2 gave a linear relationship, indicating conformance to the parabolic rate law [12] given in eq (1):

$$\frac{dx}{dt}=\frac{k}{1+ax} \tag{1}$$

where t=time, x=moles of hydrogen formed, and both k, the initial rate, and a are constants. A plot of log k for a particular cellulose sheet versus log intensity resulted in a straight line of unit slope for intensities of

13.4×10^{-9}, 9.62×10^{-9}, and 6.49×10^{-9} $Nh\nu$/cm^2 sec.

The intensities recorded in this paper and used in

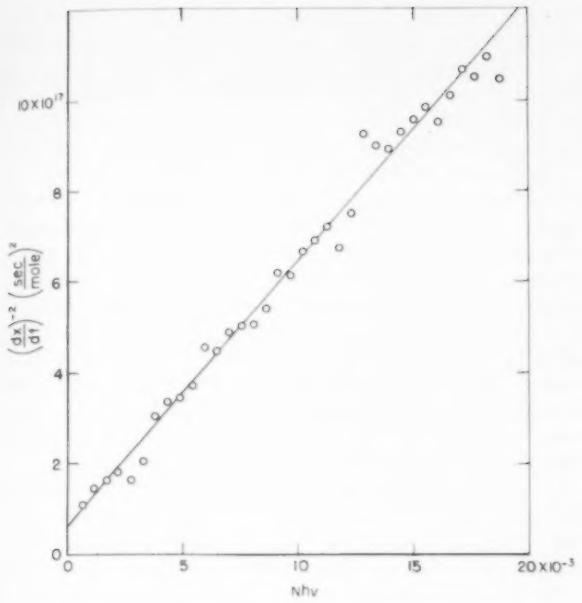

FIGURE 2. *(Rate of* H_2 *evolution)*$^{-2}$ *versus dosage.*

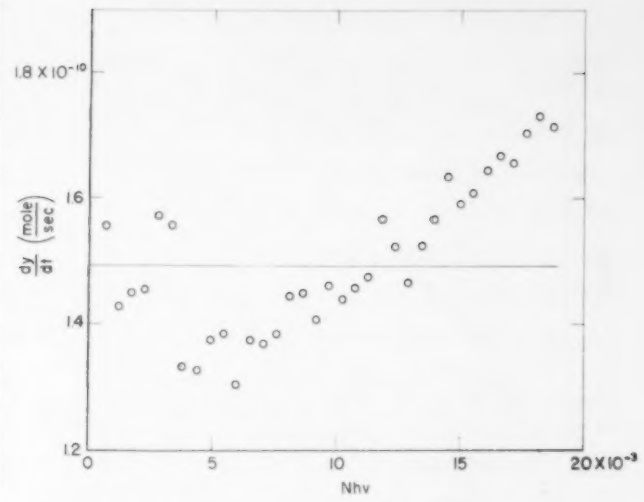

FIGURE 3. *Rate of* CO *plus* CO_2 *evolution versus dosage.*

the calculation of quantum yields are probably accurate to within ±2 percent. Therefore $k = I_a\Phi_H$ where Φ_H is the initial quantum yield of hydrogen and I_a is the intensity of absorbed light. It was assumed in the calculation of quantum yields that 43 percent of the light was absorbed. For a series of cellulose sheets of D. P. 1,710 containing initially 3.7×10^{-6} equivalents of aldehyde per gram and 6.3×10^{-6} equivalents of carboxyl per gram, $\Phi_H = 0.0130$ mole/*Nhν* for the above intensities. A second series of sheets of D. P. 1,910, containing 6.4×10^{-6} aldehyde and 8.3×10^{-6} carboxyl gave $\Phi_H = 0.0097$. The intersheet variation in Φ_H was less than ±10 percent. Values of the constant, a, for the two series varied erratically between 6.0×10^6 and 10.0×10^6 moles^{-1}, and could not be correlated with intensity.

The rate of evolution of carbon monoxide plus carbon dioxide remained relatively constant. However, as can be seen from values obtained from a run at 9.62×10^{-9} *Nhν*/cm^2 sec at 40° C in figure 3, the rate of evolution of these gases decreases at first, passes through a minimum, and then steadily increases. The rate was proportional to the first power of the intensity, and the zero-order rate equation showed a combined quantum yield of carbon monoxide and carbon dioxide of 10.9×10^{-4} moles/*Nhν* for the first series of cellulose sheets and 8.0×10^{-4} for the second series.

3.2. Functional Groups

Table 2 contains degree of polymerization (D. P.) and equivalents per gram of aldehyde and carboxyl groups for a series of cellulose sheets that received various dosages of 2537 A light at 40° C.

The D. P. in table 2 was calculated from an equation relating cuprammonium viscosity with weight-average D. P. obtained from sedimentation data [13].

If the gradient in dosage follows Lambert's law, the number of chain scissions can be calculated from initial and final weight-average D. P.'s, the absorption coefficient, and the thickness of the sheet by assuming random fractures of an initially random distribution [14].

The absorption coefficient for unit thickness is 3.22 for the sheets described in table 2.

Figure 4 contains the moles formed of aldehyde, carboxyl, hydrogen, carbon monoxide, and carbon dioxide, and chain fractures versus dosage of 2537 A light at 40° C for the 0.86-g cellulose sheets described in table 2.

Interruption of the irradiation by an evacuation for several days at 100° C had no effect on the kinetics of gaseous evolution. A period of treatment with hydrogen followed by evacuation also had no effect. Treatment of the irradiated sample with oxygen followed by evacuation at 100° C, however, caused a temporary inhibition of evolution of gas upon resumption of the irradiation, as shown in figure 5.

TABLE 2. *Results of analyses of irradiated cellulose*

Dose	D. P.	RCHO	RCOOH
Nhν/g		*Moles/g*	*Moles/g*
0.00×10^{-3}	1,710	0.37×10^{-6}	0.63×10^{-6}
1.09	1,270	1.43	1.23
2.18	1,200	2.27	1.51
4.35	1,070	2.70	1.60
6.52	940	3.27	1.58
9.57	870	4.46	2.11
13.05	790	6.51	2.64
19.58	690	8.47	2.65

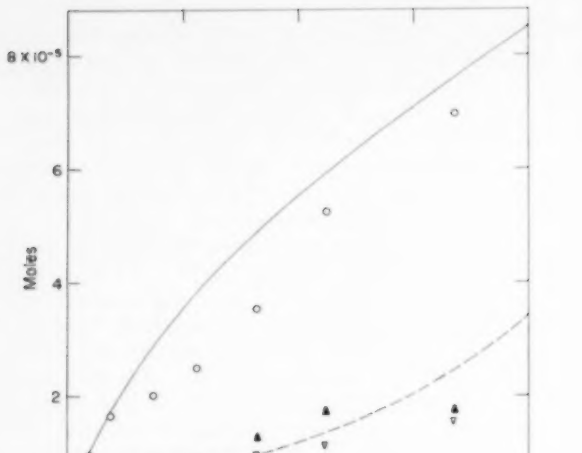

FIGURE 4. *Moles of product versus dosage.*

○, Aldehyde; ▲, carboxyl; ▽, chain fracture; ——, hydrogen; . . . . , CO and CO_2.

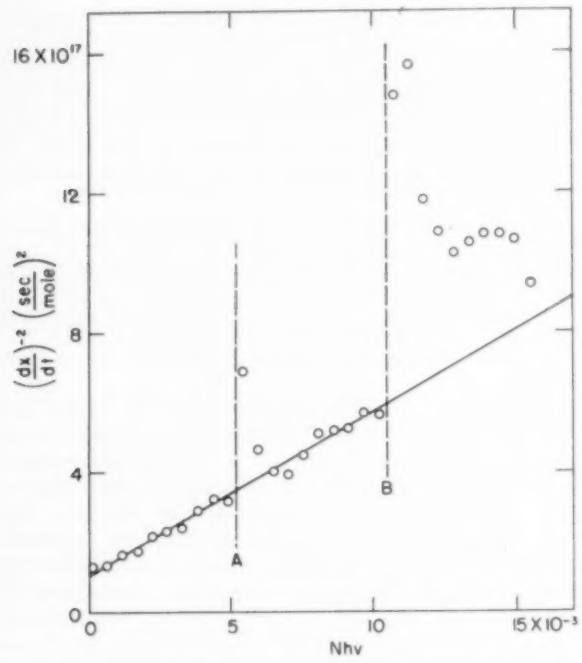

FIGURE 5. *Effect of treatment with* H_2 *and* O_2 *on (rate of* H_2 *evolution)*$^{-2}$ *versus dosage.*

A, At this point the run was interrupted, H_2 added, the sample heated at 100° C for 6 hr, and evacuated at 100° C for 1 week before resumption of the run; B, as in A, except O_2 added instead of H_2.

4. Discussion

The only direct measurement of the primary process in these experiments is the measurement of the rate of evolution of the gaseous products.

Before the measurement of change in carboxyl, aldehyde, and D. P., the irradiated specimens which contained oxygen-labile groups had been stored in air for several months until presumably all photosensitized oxidation was complete. The specimens may have been further modified by the fracture of alkali-sensitive linkages during the viscosity determinations and by the acidic reagents used in the carboxyl and aldehyde determinations. Since the more crystalline regions of the cellulose are not completely accessible to the latter two reagents, the carboxyl and aldehyde values may be low. However, a dosage of 0.02 *Nhν* produced 8.5×10^{-5} mole of hydrogen from a sample that contained initially 0.32×10^{-5} equivalents of aldehyde and 0.54×10^{-5} equivalents of carboxyl groups. Thus, even if the values for aldehyde and carboxyl are somewhat low, the amounts of aldehyde and carboxyl initially present are quite insufficient to account for the amount of hydrogen formed during the irradiation.

The evolution of hydrogen upon irradiation of cellulose with 2537 A light has not been noted by other investigators [2]. The prolonged degassing of the cellulose and the maintenance of a high vacuum during the irradiation apparently removed traces of water, adsorbed oxygen, or some other substance that either inhibited hydrogen formation directly or reacted with any hydrogen atoms produced before they could combine to form molecular hydrogen.

If hydrogen were formed by reactions involving the glucoside linkages, it would be necessary to postulate that these reactions do not involve chain scission because the ratio of chain scissions to molecules of hydrogen formed is 0.18.

A plausible explanation of the source of hydrogen is the photolysis of alcohol groups by the over-all reaction in eq (2)

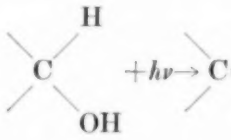

(2)

known to take place when simple alcohols are irradiated in the gas and liquid phases at below 2000 A [15, 16]. Simple alcohols are transparent to 2537 A radiation.

Simple aldehydes and ketones fluoresce in the ultraviolet and are decomposed photochemically in the gas phase to produce carbon monoxide, various hydrocarbons, a little hydrogen, and, in the case of ketones, RCOCOR [17].

Although the reducing groups in cellulose may not be present as free aldehyde, these groups and any aldehyde groups formed from the irradiation of primary alcohol groups in the cellulose might be expected to react analogously to gas-phase photodecompositions as in eq (3). Likewise, keto groups from the photolysis of the secondary alcohol groups might react as in eq (4).

$$XCHO+h\nu\rightarrow X\cdot+\cdot CHO\rightarrow CO+\tfrac{1}{2}H_2+X\cdot \qquad (3)$$

$$XCO+h\nu\rightarrow \dot{X}—\dot{C}O\rightarrow CO+X: \qquad (4)$$

where X represents the remaining cellulose chain which may contain free radicals or other labile groups.

The increasing carbonyl concentration from reaction (2) at the surface of the cellulose sheet would act as a nonvolatile filtering layer that would decrease the rate of photolysis of the alcohol groups. This effect can explain the product-inhibited rate equation for hydrogen evolution and the decreasing apparent quantum yields of hydrogen and functional groups as well as the increasing yield of carbon monoxide. Cellulose is known to fluoresce in the ultraviolet and the fluorescence increases upon irradiation [18].

Oxygen-labile linkages are formed during the irradiation of cellulose [2, 3]; therefore, the close stoichiometric parallel to be seen in figure 4 between the calculated number of chain scissions and the amount of carboxyl formed indicates that the reactions involving chain fracture and oxidation to carboxyl in air may be closely related.

WASHINGTON, April 8, 1957.

5. References

[1] L. F. McBurney, Cellulose and Cellulose Derivatives, Part I, Eds. E. Ott and H. M. Spurlin, p. 168 (Interscience Publishers, New York, N. Y., 1954).
[2] H. F. Launer and W. K. Wilson, J. Am. Chem. Soc. **71,** 958 (1949).
[3] R. A. Stillings and R. J. Van Nostrand, J. Am. Chem. Soc. **66,** 753 (1944).
[4] R. K. Warner and R. T. Mease, J. Research NBS **21,** 609 (1938) RP1146.
[5] L. J. Heidt and H. B. Boyles, J. Am. Chem. Soc. **73,** 5728 (1951).
[6] O. A. Battista, Ind. Eng. Chem., Anal. Ed. **16,** 351 (1944).
[7] H. F. Launer and W. K. Wilson, Anal. Chem. **22,** 455 (1950).
[8] G. F. Davidson, J. Text. Inst. **39,** T65 (1948).
[9] W. K. Wilson and A. A. Padgett, Tappi **38,** 292 (1955).
[10] H. F. Launer, W. K. Wilson, and J. H. Flynn, J. Research NBS **51,** 237 (1953) RP2456.
[11] F. Benford, S. Schwartz, and G. Lloyd, J. Opt. Soc. Am. **38,** 964 (1948).
[12] J. H. Flynn, J. Phys. Chem. **60,** 1332 (1956).
[13] E. O. Kraemer, Ind. Eng. Chem. **30,** 1200 (1938).
[14] J. H. Flynn, J. Polymer Sci. **27, 83** (1958).
[15] E. Patat, Z. Elektrochem **40,** 425 (1934).
[16] L. Farkas and Y. Hirshberg, J. Am. Chem. Soc. **59,** 2450 (1937).
[17] W. A. Noyes and P. A. Leighton, The Photochemistry of Gases, p. 336 (Reinhold Publishing Co., New York, N. Y., 1941).
[18] S. J. Lewis, J. Soc. Dyers Colourists **15,** 29 (1924).

Journal of Research of the National Bureau of Standards Vol. 60, No. 3, March 1958 Research Paper 2842

Cavity Ionization as a Function of Wall Material

Frank H. Attix,[1] LeRoy DeLa Vergne, and Victor H. Ritz

A study has been made of the ionization within a flat cavity chamber under irradiation by X- and gamma rays in the energy region 38 to 1,250 kilovolts effective (kev). Chamber walls were made of carbon, aluminum, copper, tin, and lead, and the wall separation was varied from 0.5 to 10 millimeters. Results are compared with cavity theory.

1. Introduction

In 1953 an experimental study of cavity ionization [2] was carried out at the Bureau by means of a chamber of the parallel-plate type, having walls of C, Al, Cu, Sn, or Pb, which could be varied in separation from about 0.5 to 10 mm. The gas between the plates was air at room pressure and temperature. Relative ionizations were compared when the chamber was irradiated by heavily filtered X-rays of 50 to 250 kv, and by γ-rays from Au^{198} (411 kev), Cs^{137} (670 kev), and Co^{60} (1,250 kev). For the X-rays, measurements of ionization were also made with a free-air chamber.

The results were presented in informal communications which were intended for limited distribution and were not, therefore, generally available. The work has not been published heretofore because, in retrospect, it was regarded as preliminary in nature and because the chamber design was not ideally suited to the problem.

The principal objections to the design of the experimental ionization chamber are that: (a) It should have side walls to eliminate the escape of electrons from between the plates; and (b) varying the gas-pressure instead of the separation of the plates would give the experiment greater accuracy and simplicity. Several experiments have since been done here and elsewhere [1 to 4] [3] employing pressure-variation in closed cavities, and there can be no doubt as to the inherent advantages of the method.

In spite of its shortcomings, however, the present experiment does yield some information about cavity ionization, particularly for small wall separations where the electron losses are negligible. Furthermore, the apparatus and results have recently been referred to in several published papers [2, 4, 5, 6, 7], indicating a general interest which makes the present publication of the work worthwhile.

Measurements with the γ-rays from Co^{60} have recently been repeated to determine the degree of the electron losses at that energy, and to eliminate, by increasing the filtration of the γ-ray beam, the effect of low-energy scattered radiation originating in the source and its housing.

2. Experimental Apparatus

2.1. Ionization Chamber

Figure 1 shows a section through the chamber, indicating its design. The collecting volume was 5 cm in diameter, and the irradiated area about twice this size, providing some compensation for electron losses by irradiation of the guard-ring area. Connection with the collecting electrode was made through a fine wire embedded in the rear supporting wall. This wall was constructed of two sheets of polyethylene, bonded together (with the wire between) by heating, to give a total thickness of 1.8 mm.

Thin foils were cemented to the polyethylene and the groove cut afterward with a lathe tool. Thicker metal walls were precut into collector and guard ring, then attached to the polyethylene by means of double adhesive tape,[4] which gave a very strong bond. It

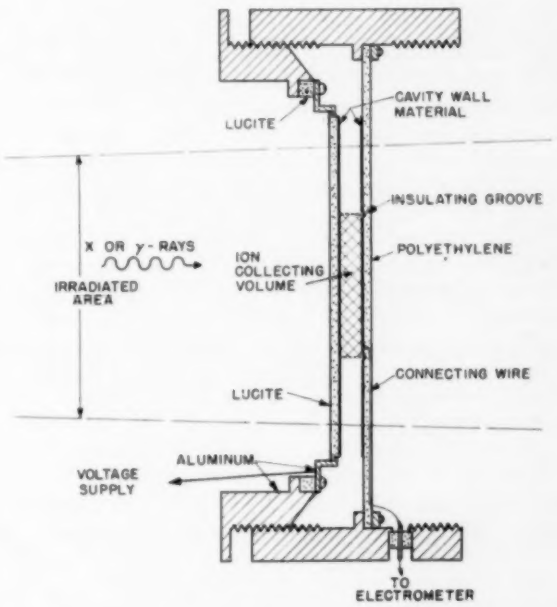

FIGURE 1. *Cross section of experimental ionization chamber.*

[1] A portion of this work was submitted by F. H. Attix in partial fulfillment of the requirements for the master of science degree at the University of Maryland.

[2] This work was supported by the U. S. Army Signal Corps, Fort Monmouth, N. J.

[3] Figures in brackets indicate the literature references at the end of this paper.

[4] "Scotch" Tape No. 400, manufactured by Minnesota Mining and Mfg. Co.

was found necessary to fill the 0.25-mm-wide gap between the guard ring and collecting electrode with a strip of polyethylene to avoid ion collection from that volume.

The front [5] chamber wall was supported on a screw of 1-mm pitch, to allow variation of the wall separation. The collecting voltage was applied to this wall; ± 22 v/mm was found to be an adequate gradient for saturation.

The effective position of the chamber for a given separation was taken to be midway between the front and back walls.

2.2. Wall Materials

Table 1 gives the thicknesses of the walls used for the various energies. In each case the thickness is greater than that necessary for electronic equilibrium. Thicknesses of supporting materials, if present, are also shown. Attenuation and scattering from both the front and back walls were corrected for in the usual manner by varying the thicknesses (always maintaining at least equilibrium thickness) and extrapolating the observed ionization to zero wall thickness. In most cases this correction was only a few percent, but for low X-ray energies the attenuation in the front walls of high-atomic number became larger, reaching about 60 percent for the lead wall with 38-kev X-rays.

Spectroscopic analysis of the wall materials indicated that the impurities present would alter the ionization by less than 1 percent for any of the radiations used in the experiment.

[5] The chamber was ordinarily placed with this wall toward the source. No difference in response was observed whether the front or back of the chamber faced the source, if appropriate wall-attenuation corrections were applied.

2.3. Measurement of Ionization Current and Wall Separation

Ionization currents were measured by means of a vibrating-reed electrometer employed in a null method. Currents larger than 10^{-12} amp were passed through high megohm resistors and the IR drop balanced by a calibrated potentiometer. Smaller currents were measured by observing the rate of charge of a 10^{-11}-f calibrated capacitor.

Each current measurement was made with both polarities and averaged to eliminate the effects of: (a) Extracameral ionization; (b) radiation-induced leakage of current through the polyethylene rear supporting wall; and (c) current of energetic electrons crossing the chamber from one wall to the other. Positive and negative currents were found to agree closely except for separations less than 1 mm, where they diverged by as much as a few percent.

The plate separation was measured electrically (in the absence of radiation), employing the circuit shown in figure 2. The two potentiometers were

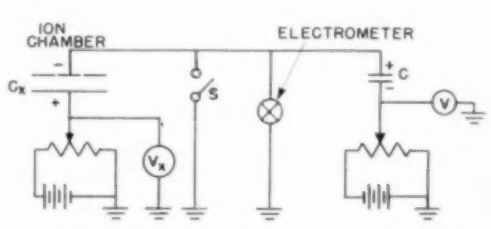

FIGURE 2. *Circuit used in determining the separation of the chamber walls by measurement of the capacitance between them.*

TABLE 1. *Thicknesses of wall materials*

Gamma or X-ray effective;[1] photon energy	Graphite		Al		Cu		Sn		Pb	
	Front wall	Rear wall	Front wall	Rear wall	Front wall	Rear wall	Front wall	Rear wall	Front wall	Rear wall
kev										
38	307 mg/cm²	307 mg/cm² +0.072 in. polyethylene.	109 mg/cm² +0.062 in. lucite.	109 mg/cm² +0.072 in. polyethylene.	23.5 mg/cm² +0.062 in. lucite.	68 mg/cm² +0.072 in. polyethylene.	10 mg/cm² +0.062 in. lucite.	57 mg/cm² +0.135 in. polyethylene.	60 mg/cm² +0.062 in. lucite.	50 mg/cm² 0.072 in. polyethylene.
70	do	do	do	do	do	do	do	do	do	Do.
118	do	do	do	do	65.5 mg/cm² +0.062 in. lucite.	do	57 mg/cm² +0.135 in. polyethylene.	do	do	Do.
169	do	do	do	do	do	do	do	do	do	Do.
206	do	do	do	do	do	do	do	do	124 mg/cm² +0.062 in. lucite.	124 mg/cm² +0.072 in. polyethylene.
411	do	do	do	do	925 mg/cm²	925 mg/cm² +0.072 in.	770 mg/cm²	770 mg/cm² +0.072 in. polyethylene.	872 mg/cm² +0.062 in. lucite.	872 mg/cm² +0.072 in. polyethylene.
670	do	do	do	do	do	do	do	do	do	Do.
1,250	do	do	437 mg/cm²	437 mg/cm² +0.072 in. polyethylene.	do	do	do	do	do	Do.

[1] Determined by attenuation in copper.

varied to balance a charge on C by an equal charge on C_x (the chamber capacitance), the balance being indicated by the vibrating-reed electrometer. This procedure was repeated at each of several settings of the chamber screw, using the same setting of potential V each time (i. e., constant charge). If V_x is plotted versus the indicated settings of the screw, a linear relationship results, intersecting the $V_x=0$ axis at the screw setting where the wall separation is zero. This can be shown as follows:

$$q=\text{constant}=VC=V_xC_x$$

and

$$C_x=\frac{KA}{d}$$

where:

V=voltage on known capacitor,
C=capacitance of known capacitor,
V_x=voltage applied to chamber wall,
C_x=capacitance between walls of chamber,
K=constant,
A=effective area of collecting electrode, and
d=wall separation.

Combining the two equations, we have

$$d=\left[\frac{KA}{q}\right]V_x$$

where the bracket term is the slope of the observed plot of V_x versus screw setting. Thus the separation is obtained for any measured value of V_x by multiplying it by the previously determined slope, which need be measured only once for each rear-wall assembly.

Note that the actual value of C is not needed in finding the separation. However, if it is known, one can solve for A and thence the diameter of the collecting electrode. This was found to agree with the directly measured diameters to within 1 percent.

3. X-ray Measurements

3.1. Source of X-rays

A Westinghouse 250-kv tube was operated with a well-stabilized constant potential generator to provide the X-ray source. The beam was collimated to give a diameter about twice that of the collector at 1-m distance, where the chamber was located. The kilovoltages and filtrations used are given in table 2, and are similar to those of Ehrlich and Fitch [8].[6] The effective energies were obtained from attenuation data in copper, referring to the attenuation coefficients of White [9]. These X-ray spectra are, of course, not monochromatic, but consist of a spread of photon energies [8]. Further narrowing of the spectra by increased filtration would have made the beam intensities too low for accurate measurements.

[6] Note that the filtration data given for 150 kv in this reference are in error, according to private communication with the authors.

TABLE 2. *X-ray potentials and filtrations*

Constant potential applied to X-ray tube	Added filtration [1]	Effective X-ray energy [2]
kev	*mm*	
50	0.125 Pb	38
100	.52 Pb	70
150	1.53 Sn+4.00 Cu	118
200	0.70 Pb+4.00 Sn+0.59 Cu	169
250	2.70 Pb+1.00 Sn+.59 Cu	206

[1] The inherent filtration of the X-ray tube was equivalent to 3-mm Al.
[2] As determined from attenuation measurements in copper.

Uniformity of the beam over the area of the chamber was ascertained by photographic densitometer measurements.

3.2. Free-Air Chamber

The exposure-dose rate (in roentgens per unit time) of the X-rays in the plane of the experimental chamber was measured by replacing that chamber with a free-air chamber having a defining diaphragm 8 mm in aperture diameter. The 12-cm plate separation of this chamber [10] was inadequate for the heavily filtered X-rays used, and it was, therefore, calibrated against the NBS 250-kv standard free-air chamber [11].

3.3. Results with X-rays

Figures 3 to 7 show the curves obtained for the ratio of ionization density in the experimental chamber to that in the calibrated free-air chamber, as a function of the wall separation in the former. Corrections for wall attenuation and scattering in the experimental chamber walls have been included.

The shapes of the curves are influenced by two effects: (a) The transition from wall-dependent ionization at small separations to air-dependent ionization at large separations, and (b) the loss of electrons out the edges of the chamber, an effect that becomes more pronounced at large separations and high X-ray energies. For walls of atomic number higher than air, the flux of electrons generated within the wall material will be greater than that in air because of the greater coefficient for absorbing energy from X-rays, (due to photoelectric effect), and because of the lower electron stopping-power (in cm^2/electron) of the wall material. Furthermore, the increased reflection of electrons from walls of high-atomic number results in larger electron losses from the edge of the chamber. Thus one expects the ionization to rise as the wall separation is decreased in such a chamber, as indicated in figures 4 to 7. It is interesting to note the somewhat steeper descent of the 38-kev curve for Sn (fig. 6), as compared with that for Pb (fig. 7). (At this energy the edge losses are negligible because of the short ranges of the electrons present.) The K-edge for photoelectric absorption in Sn is located at 29 kev, giving a large component of photoelectrons with energies of the order of 9 kev (see table 5). The range of

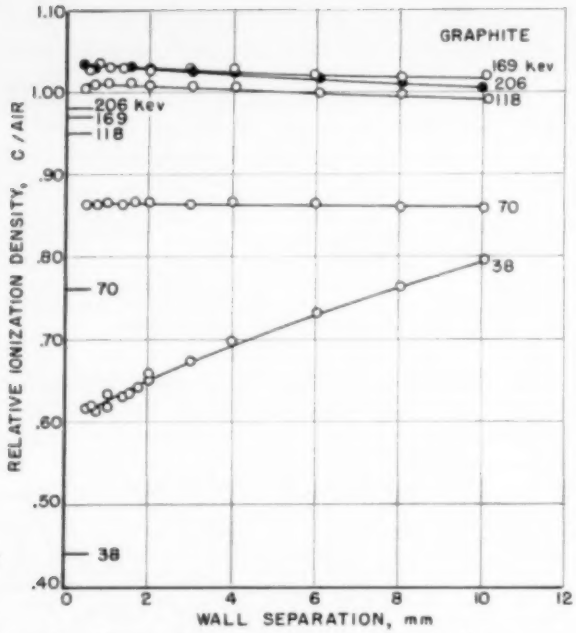

FIGURE 3. *Curves showing the ratio of ionization per unit volume in the experimental chamber to that in the free-air chamber, as a function of the separation of the walls in the experimental chamber.*

The marks at the vertical axis, labeled with the appropriate values of X-ray energy in kilovolts effective, indicate the corresponding theoretical ratios from the Bragg-Gray relation.

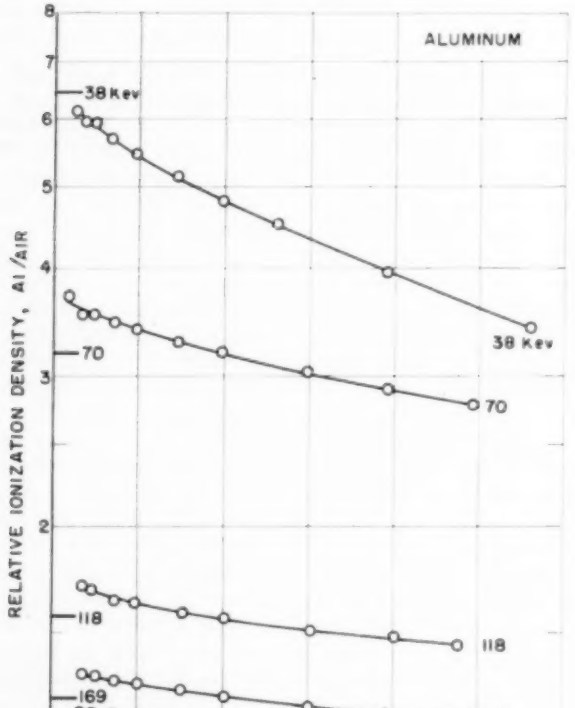

FIGURE 4.

(See caption for fig. 3)

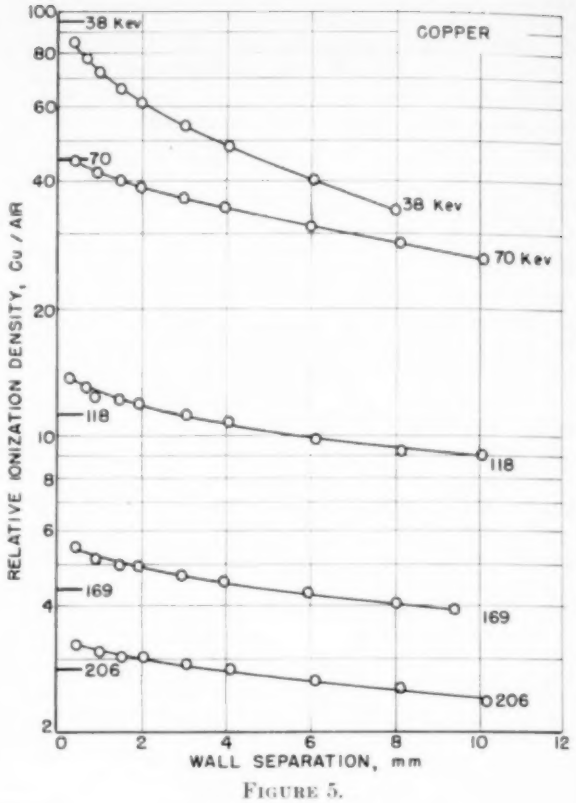

FIGURE 5.

(See caption for fig. 3)

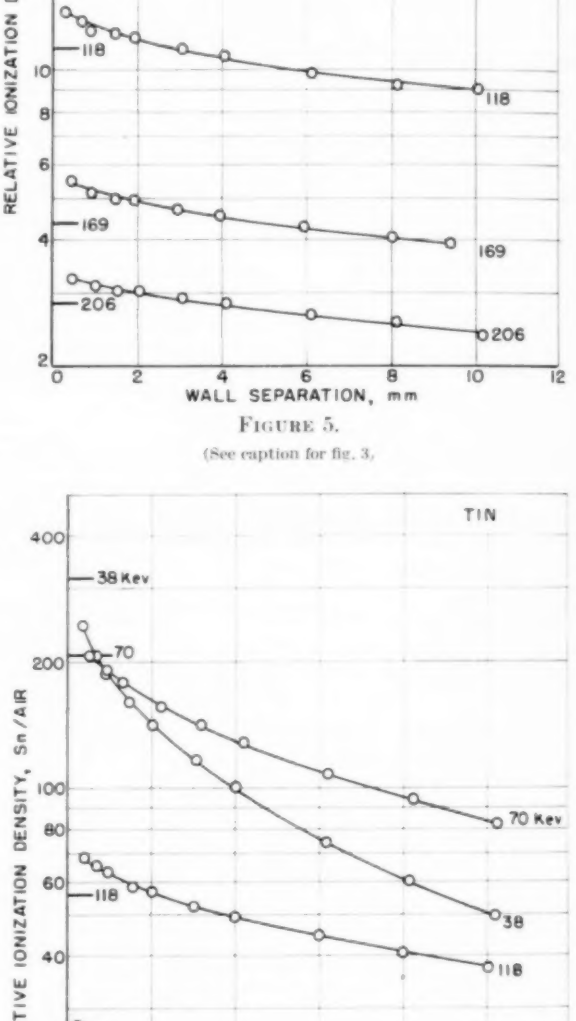

FIGURE 6.

(See caption for fig. 3)

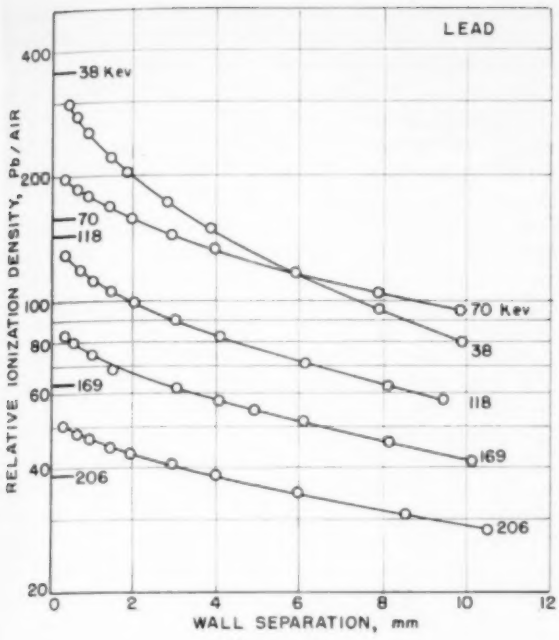

FIGURE 7.

(See caption for fig. 3)

such electrons in air is about 2 mm. On the other hand, in lead the K-orbit electrons do not interact with 38-kev X-rays, and the L-shell photoelectrons predominate. These have energies in the vicinity of 22 kev, and ranges of about 1 cm. Thus this curve is less steep than the corresponding one for Sn. Similar arguments can be applied to explain the trends of the other curves at 38 and 70 kev, referring to table 5 for dominant electron energies. At higher X-ray energies the edge losses of electrons begin to predominate. Here the slopes are not strongly dependent on X-ray energy, because the electron ranges are large compared with the lateral chamber dimensions.

3.4 Comparison with Cavity Theory

The Bragg-Gray theory of cavity ionization [12,-13,6] gives for the ratio of ionizations per gram of air in two cavity chambers, A and B:

$$\frac{J_A}{J_B}=\frac{(\mu_{en})_A}{(\mu_{en})_B}\frac{s_B}{s_A}$$

where s is the ratio of electronic stopping powers (per electron/cm^2) of the wall material to air, evaluated for the electron spectrum present. If cavity B is a free-air chamber, $s_B=1$ and the above formula is further simplified.

μ_{en} is defined as the sum of those fractions of the photoelectric-, Compton-, and pair-production attenuation coefficients for γ-rays, representing energy converted from electromagnetic energy into electron-kinetic energy. The units of μ_{en} are cm^2/electron throughout this paper [14].

For valid application of this theory, the cavity must be small in comparison with the ranges of the electrons present, and the ionization contributed by electrons generated in the gas directly by X-rays must be negligible. These requirements are difficult to fulfill with low-energy X-rays, because of the short ranges of the electrons present. Moreover, the theory itself is only an approximation, as it neglects the production (through collision) of energetic secondary electrons by the Compton-recoil electrons and photoelectrons in traversing the wall material and the air.[7]

Table 3 lists the values of the ratio $(\mu_{en})_Z/(\mu_{en})_{air}$, calculated from the X-ray attenuation coefficients of White [9], assuming the X-ray spectra to be monochromatic at the effective energy. (μ_{en}) is the sum of the photoelectric coefficient (less fluorescence losses) and the "true" Compton coefficient σ_a.[8]

TABLE 3. *Ratios of energy-absorption coefficients μ_{en} (in cm^2/electron) relative to air*

Effective photon energy	$(\mu_{en})_Z/(\mu_{en})_{air}$				
	C	Al	Cu	Sn	Pb
Kev					
38	0.45	5.62	70.6	176	176
70	.77	2.79	34.6	136	90.2
118	.96	1.37	8.78	38.8	78.5
169	.98	1.11	3.41	14.2	38.5
206	.99	1.05	2.24	8.29	24.4
411	1.00	1.00	1.15	2.00	5.37
670	1.00	1.00	1.04	1.29	2.55
1,250	1.00	1.00	1.00	1.10	1.56

The stopping-power calculations were done by means of Bethe's formula,[9] using the mean-excitation potentials of Bakker and Segre [16] as modified for the binding correction by Bethe and Ashkin [15]. The values used were $I_{air}=80.5$ ev, $I_C=76.4$ ev, $I_{Al}=150$ ev, $I_{Cu}=276$ ev, $I_{Sn}=463$ ev, and $I_{Pb}=705$ ev. The correction for density effect according to Sternheimer [17] was included.

The stopping-power ratio of air to wall material $(1/s)$, evaluated over the electron spectrum present, is obtained [6] from the integration

$$\frac{1}{s}=\frac{1}{T_0}\int_0^{T_0}\frac{S_{air}}{S_{wall}}\,dT$$

where T_0 is the intial energy of the electrons generated in the wall material by X- or γ-rays, and s is the stopping power (per electron/cm^2) of the air or wall for an electron of energy T. Values of $(1/s)$ are tabulated as a function of T_0 in table 4.

---

[7] A recently proposed modification to the theory [6] takes the "knock-on" secondary electrons into account and relates ionization to cavity size. This has not been applied here to the X-ray results because the necessary electron spectra have not been calculated for low-electron starting energies. This modified theory is, however, compared with the results of the γ-ray measurements, for which the calculated electron spectra are available.

[8] A small fraction of μ_{en} for Pb and Sn at 1,250 kev is attributable to pair production, see table 5.

[9] See eq (52), p. 254 in reference [15].

TABLE 4. *Stopping power ratio, $(1/s)$,[1] air to wall material*

Initial electron energy T_0	$1/s$				
	C	Al	Cu	Sn	Pb
Mev					
0.001	0.981	1.304	1.856	2.90	5.33
.003	.983	1.258	1.691	2.42	3.88
.007	.986	1.209	1.531	2.01	2.84
.01	.987	1.191	1.476	1.882	2.54
.03	.989	1.148	1.348	1.600	1.939
.07	.991	1.124	1.283	1.468	1.690
.1	.991	1.116	1.262	1.427	1.617
.3	.993	1.096	1.213	1.335	1.463
.7	.999	1.085	1.189	1.286	1.386
1.0	1.004	1.081	1.182	1.270	1.360
1.4	1.011	1.079	1.179	1.257	1.339
2.0	1.020	1.080	1.178	1.246	1.320

[1] $(1/s) = \frac{1}{T_0}\int_0^{T_0} \frac{S_{air}}{S_{wall}}\,dT.$

The Compton process, of course, produces a continuous spread of initial electron energies T_0. For present purposes, this distribution was approximated by a monoenergetic-starting energy given by $(\sigma_a/\sigma)h\bar{\nu}$ where σ_a is the Compton "true" absorption coefficient, σ is the total Compton coefficient, and $h\bar{\nu}$ is the γ-ray energy or the effective energy of the X-ray spectrum. Photoelectrons are taken to have initial energy equal to that of the incident photon less the binding energy of the electron in its orbit. Table 5 lists the values of T_0 which apply to air and the wall materials studied, together with the relative importance of each energy-absorbing process present in the materials.

Mean values $(\overline{1/s})$, of the stopping-power ratios $(1/s)$, evaluated for the γ-ray and effective X-ray energies, are given in table 6. These data were obtained from tables 4 and 5 as described in the footnote following table 6.

The theoretical ionization ratios J_Z/J_{air} are then obtained by taking the product of corresponding terms in tables 3 and 6. The resulting values are plotted as short lines at the y-axes in figures 3 to 7 for X-rays.

It will be seen that, while the agreement between theory and experiment at small separations is not particularly close, neither is it unsatisfactory in view of the approximations used in applying the theory, and the approximate nature of the theory itself.

In the case of the graphite wall, it is particularly difficult to satisfy the requirement that the cavity be small enough to make negligible the ionization produced by electrons originating in the air itself. This is because, as can be seen from table 5, the air has considerably more photoelectric effect than does the graphite for X-rays below 100 kev. This may account for the large discrepancies between theory and experiment in figure 3 at 38 and 70 kev.

At 169 and 206 kev, the graphite chamber apparently reads higher than the free-air chamber by about 4 percent. Probably the major factor con-

TABLE 5. *Initial electron-energy distribution*

Effective photon energy	Type of electron	Air		C		Al		Cu		Sn		Pb	
		1	2	1	2	1	2	1	2	1	2	1	2
38	Compton	2	0.15	2	0.33	2	0.03	2	0	2	0	2	0
	K-photo	38	.85	38	.67	37	.97	29	0.91	9	0.66		0
	L-photo							38	.09	38	.34	22	0.76
	M-photo											34	.24
70	Compton	7	.66	7	.85	7	.24	7	.02	7	.01	7	.01
	K-photo	70	.34	70	.15	69	.76	61	.90	41	.82		0
	L-photo							70	.08	70	.17	54	.79
	M-photo											66	.20
118	Compton	19	.94	19	.97	19	.68	19	.11	19	.03	19	.02
	K-photo	118	.06	118	.03	117	.32	109	.82	89	.84	30	.66
	L-photo							118	.07	118	.13	102	.27
	M-photo											114	.05
169	Compton	34	.98	34	1.00	31	.88	34	.29	34	.07	34	.03
	K-photo	169	.02	169	0	168	.12	160	.66	140	.81	81	.76
	L-photo							169	.05	169	.12	153	.18
	M-photo											165	.03
206	Compton	46	.99	46	1.00	46	.94	46	.45	46	.12	46	.04
	K-photo	206	.01	206	0	205	.06	197	.51	177	.77	118	.78
	L-photo							206	.04	206	.11	190	.15
	M-photo											202	.03
411	Compton	129	1.00	129	1.00	129	1.00	129	.87	129	.50	129	.19
	K-photo	411	0	411	0	410	0	402	.12	382	.44	323	.69
	L-photo							411	.01	411	.06	395	.10
	M-photo											407	.02
670	Compton	257	1.00	257	1.00	257	1.00	257	.96	257	.78	257	.40
	K-photo	670	0	670	0	669	0	661	.04	641	.20	582	.52
	L-photo							670	0	670	.20	654	.07
	M-photo											666	.01
1,250	Compton	588	1.00	588	1.00	588	1.00	588	1.00	588	.00	588	.65
	K-photo	.....	.....	.....	.....	.....	.....	.....	.....	1,220	.08	1,160	.30
	L-photo	.....	.....	.....	.....	.....	.....	.....	.....	1,250	.01	1,230	.04
	M-photo	.....	.....	.....	.....	.....	.....	.....	.....	1,250		1,250	.005
	Pair	.....	.....	.....	.....	.....	.....	.....	.....	114	.01	114	.005

Columns 1 ..... Average initial energy T_0 (in kev) of electrons produced by the indicated processes.
Columns 2 ..... Fraction of total flux of electron energy carried by electrons resulting from the indicated processes.

tributing to this effect is that the experimental chamber receives more scattered radiation from the X-ray beam than does the free-air chamber. The diaphragms in the latter chamber admit only the primary rays and those scattered in a nearly forward direction. This probably also contributes to the discrepancies between theory and experiment for the other wall materials in figures 4 to 7 as well.

TABLE 6. *Mean stopping-power ratios* $(\overline{1/s})$,[1] *air relative to wall material*

Effective photon energy	$\overline{(1/s)}$				
	C	Al	Cu	Sn	Pb
kev					
38	0.99	1.14	1.35	1.80	2.03
70	.99	1.14	1.29	1.54	1.75
118	.99	1.15	1.27	1.44	1.84
169	.99	1.14	1.27	1.40	1.64
206	.99	1.13	1.27	1.39	1.58
411	.99	1.11	1.24	1.36	1.48
670	.99	1.10	1.22	1.33	1.43
1,250	1.00	1.09	1.19	1.29	1.38

[1] These data were obtained by graphical interpolation of the data given in table 4, at the electron energies (T_0) given in columns 1 of table 5. The stopping-power ratios (1/s) so obtained were then weighted by the appropriate factors given in columns 2 of table 5 to obtain $\overline{(1/s)}$.

4. γ-Ray Measurements

4.1. γ-Ray Sources

Sources consisting of several curies of Au^{198}, Cs^{137}, and Co^{60} were enclosed in lead housings to provide collimated beams as for the X-ray work already described. The Au^{198} and Cs^{137} source-housings were constructed to allow the rays going in a rearward direction to escape through a hole, thus avoiding the production of 180° backscattered γ-rays of low energy. The forward beam was filtered by 2.4-mm Sn+0.5-mm Cu+0.8-mm Al to suppress any fluorescense emitted by the lead housing.

The Co^{60} source first used was a 10-curie source in a large lead housing, closed in the rearward direction and lined with brass on the inside. The first results were taken with the same filter used for the other sources, but it was found later that the scattered radiation originating in the housing and source was not adequately removed by this filter, and as a result the ionization in the chamber with high-atomic-number walls was spuriously high because of excess photoelectric effect. The final data described here were taken with a 1-curie Co^{60} source 3 mm in diameter, enclosed in a lead housing relatively free of backscattering, and with a filter of 12-mm Pb in addition to the previously described filter of Sn, Cu, and Al. Additional thicknesses of lead were found not to change the observed ionization ratio of Pb/C.

The spectra of gamma rays from Au^{198} and Cs^{137} are nearly monochromatic, and located at 411 kev and 670 kev, respectively. Co^{60} emits two lines of equal intensity at 1.17 Mev and 1.33 Mev, but for present purposes it has been assumed to be monochromatic at 1.25 Mev.

4.2. Results with γ-Rays

For the γ-ray measurements no free-air chamber was employed. Only the experimental ionization chamber was used and the relative ionization densities observed with the various wall materials. These results are given in figures 8 to 10.

As a test of the influence of the electron losses out the edge of the chamber, side walls were constructed of the various wall materials. These consisted of rings about 9 cm in diameter, thick enough for electronic equilibrium and having various depths so that

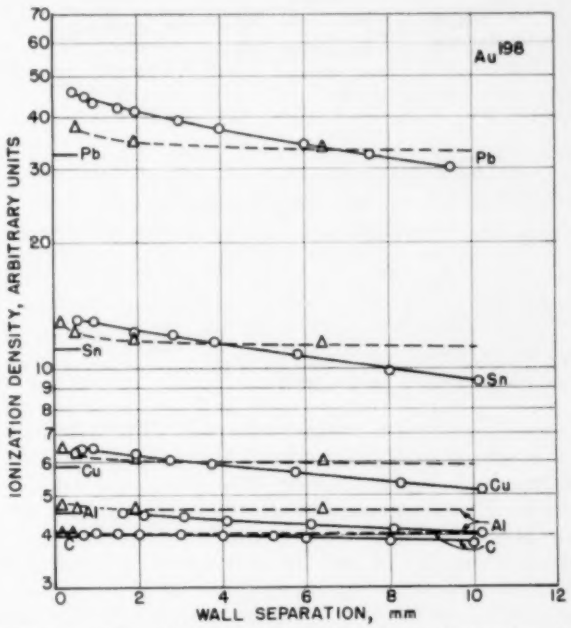

FIGURE 8. *The solid curves show the relative ionization densities measured in the experimental chamber with γ-rays from* Au^{198} *or* Cs^{137}.

The marks at the vertical axis are the ionization ratios, relative to graphite, predicted by the Bragg-Gray theory. The dashed curves are the corresponding ratios predicted by the modified cavity theory. Both sets of theoretical data have been normalized to the experimental graphite curve at small separations.

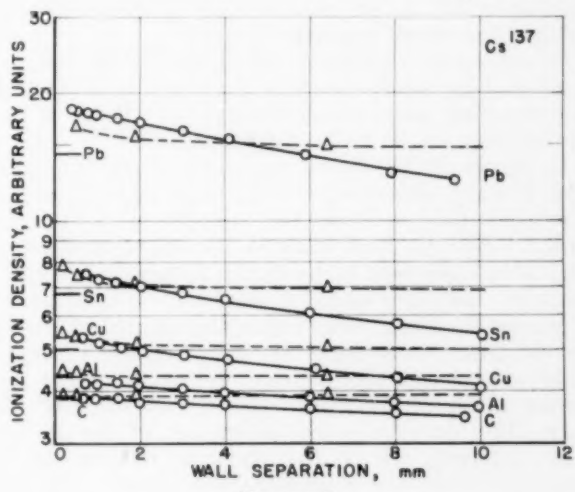

FIGURE 9.

(See caption for fig. 8)

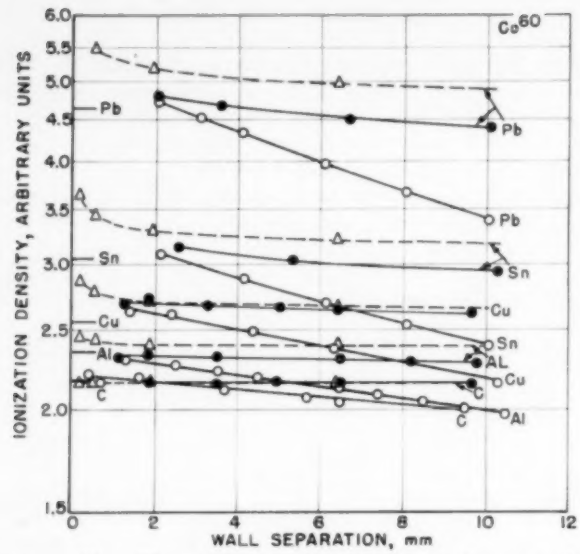

FIGURES 10. *The solid curves drawn through the open circles show the relative ionization densities measured in the experimental chamber with γ-rays from* Co^{60}, *without side walls.*

The solid curves drawn through the filled circles show the corresponding results when side walls were added. The marks at the vertical axis, are the ionization ratios, relative to graphite, predicted by the Bragg-Gray theory. The dashed curves are the corresponding ratios predicted by the modified cavity theory. Both sets of theoretical data have been normalized to the experimental graphite curve (with side walls) at small separations.

the wall separation could be varied. The γ-ray beam was large enough to irradiate these rings, producing electrons to replace those lost from the collecting region. The rings were insulated both from the guard ring and the high-voltage wall of the chamber by polyethylene 0.025 mm in thickness. It was found that, for wall separations as great as 1 cm, there was a negligible difference in ionization collected whether the rings were operated at the potential of the high-voltage wall or at ground potential, indicating no field-distorting effect. Glancing angle attenuation (1) of the γ-rays striking the rings was checked by also constructing rings of 1-cm depth but with a cone shape to allow the rays to strike the inner-ring surface at a 45° angle rather than a glancing angle, resulting in much less attenuation.

Gamma-ray scattering from the rings was also measured by doubling their thickness and observing the resulting increase in ionization. Both of these effects were found to be negligible.

In figure 10 the open points indicate the ionization density observed without the edge rings, and the solid points show the results with the rings added. For the lead walls at 10-mm separation, the edge losses are seen to be about 23 percent, while for graphite they are about 9 percent. This difference is caused by the greater reflecting ability of the lead for electrons, increasing the effective solid angle for their escape out the edges. While the edge losses shown in figure 10 apply strictly to the Co^{60} data only, they do give some indication of the losses at other energies where the electron ranges are long compared with the chamber dimensions. They also supply an upper limit for the magnitude of the losses at lower energies.

4.3. Comparison with Bragg-Gray Cavity Theory

Bragg-Gray theory calculations have already been described in the comparison with X-ray ionization data. Tables 3 and 6 also contain data applicable to the γ-ray results in the same fashion. However, because there are, for γ-rays, no free-air chamber results available for comparison with cavity-chamber results, the theoretical ionization ratios J_e/J_{air} have been divided by J_c/J_{air} to give J_e/J_c. These ratios are then normalized to the experimental graphite-chamber ionization density at small separations, and plotted as short lines adjacent to the y-axis in figures 7 to 10. Although they generally tend to be too low, these theoretical ratios do roughly predict the experimental-ionization ratios relative to graphite, particularly for Co^{60} γ-rays.

4.4. Comparison with Modified Cavity Theory

A modified cavity theory (see footnote 7) which takes into account the production of secondary electrons and which relates the ionization to the cavity size, has also been compared with the experimental γ-ray results. The difference from the conventional Bragg-Gray treatment comes in the calculation of the stopping-power ratio $(1/s)$, the details of which are given in reference [6]. In the modified theory $(1/s)$ is a function not only of T_0, but also of a parameter Δ, which is taken to be the energy needed by an electron to cross the cavity.

In table 7 are listed the values of $\overline{(1/s)}$ obtained from this theory, based upon the same mean-excitation potentials (I) and density-effect data as were used before. Table 5 has again been used to weight $(1/s)$ by the electron-energy flux at each (mean) energy, T_0 present in a material. The approximate electron linear ranges corresponding to the values are also given, assuming the linear range to be about 0.8 times the actual electron-track length [18].

T_0 compare these data with the experimental results, one must assign an effective size to the experimental-chamber cavity. This has been taken to be simply the plate separation, because the accurate choice of Δ is not critical.

The product of the terms in table 7 with the corresponding terms in table 3 yields the theoretical ionization ratios relative to air, according to the modified theory. Having renormalized the data to be relative to graphite, as was done before for the Bragg-Gray results, they are plotted as dashed curves in figures 8 to 10.

It is interesting to note how closely the theory predicts the variation of ionization with chamber size for Co^{60}, where the edge losses of electrons are eliminated. The agreement between this theory and the experimental results otherwise is not very exact, although it generally seems to be an improvement upon the other theory, particularly at small separations. Recent ionization measurements by Greening [2], by Whyte [3], and by Attix and Ritz [1], also confirm that the modified cavity theory gives improved agreement and predicts closely the

TABLE 7. *Mean stopping-power ratios $\overline{(l/s)}$ air relative to wall material, from modified cavity theory*

Wall material	γ-ray energy	Electron range (mm air)				
		0.15	0.51	1.9	6.4	22
		Δ(kev)				
		2.5	5.1	10.2	20.4	40.9
	Mev					
C	0.411	0.99	0.99	0.99	0.99	0.99
	.670	.99	.99	.99	.99	.99
	1.25	.99	.99$_5$	1.00	1.00	1.00
Al	0.411	1.14	1.13	1.12	1.11	1.10
	.670	1.14	1.12	1.11	1.10$_5$	1.10
	1.25	1.13	1.12	1.11	1.10	1.09
Cu	0.411	1.35	1.31	1.27$_5$	1.25	1.23
	.670	1.33$_5$	1.29	1.26	1.24	1.22
	1.25	1.32	1.28	1.25	1.23	1.21
Sn	0.411	1.50$_5$	1.48	1.42	1.38	1.35
	.670	1.55	1.46	1.41	1.37	1.34
	1.25	1.52	1.44	1.38$_5$	1.35	1.32
Pb	0.411	.....	1.68	1.58	1.52	1.47
	.670	.....	1.65	1.56	1.50	1.45
	1.25	.....	1.62	1.53	1.47	1.43

variation of ionization with cavity size. In particular, reference [1] shows very close agreement between theory and experiment with Co^{60} γ-rays and chamber walls of C, Al, and Cu. Other recent work in this laboratory [19] has also confirmed the agreement between a graphite cavity chamber and a pressurized free-air chamber in measuring exposure dose (in roentgens) of γ-rays from Co^{60} and Cs^{137}, after cavity-theory corrections are applied to the graphite chamber results.

The authors express their appreciation to H. O. Wyckoff and L. V. Spencer for many helpful discussions of the work, and to J. Hopfield and P. R. Fry for assisting in the early phases of the experiment. F. H. Attix would especially like to thank F. G. Brickwedde for serving as his advisor for that part of the work constituting a master's degree thesis at the University of Maryland.

5. References

[1] F. H. Attix and V. H. Ritz, A determination of the γ-ray emission of radium, J. Research NBS **59,** 293 (1957) RP2801.
[2] J. R. Greening, An experimental examination of theories of cavity ionization, Brit. J. Radiol. **30,** 254 (1957).
[3] G. N. Whyte, An attempt to measure the Bragg-Gray stopping power correction, Radiation Research (in press).
[4] H. V. Larson, Radiation Research **5,** 558 (1956).
[5] G. J. Hine and G. L. Brownell, Radiation dosimetry (Academic Press, New York, N. Y., 1956).
[6] L. V. Spencer and F. H. Attix, Radiation Research **3,** 239 (1955).
[7] J. McElhinney, B. Zendle, and S. R. Domen, Radiation Research **6,** 40 (1957).
[8] M. Ehrlich and S. H. Fitch, Nucleonics **9,** No. 3, 5 (1951).
[9] G. R. White (private communication); also tables by R. H. Morgan and H. E. Corrigan, Handbook of Radiology (The Year Book Publishers, Inc., Chicago, 1955).
[10] L. S. Taylor and G. Singer, Radiology **15,** 637 (1930).
[11] G. H. Aston and F. H. Attix, Acta Radiol. **46,** 747 (1956).
[12] W. H. Bragg, Studies in radioactivity, p. 94 (MacMillan and Co., New York, N. Y., 1912).
[13] L. H. Gray, Proc. Roy, Soc. (London) [A] **156,** 578 (1936).
[14] U. Fano, Nucleonics **11,** No. 8, 8 (1953).
[15] H. A. Bethe and J. Ashkin, Experimental nuclear physics, E. Segre, Ed., (John Wiley & Sons, Inc., New York, N. Y., 1953).
[16] C. J. Bakker and E. Segre, Phys. Rev. **81,** 489 (1951).
[17] R. M. Sternheimer, Phys. Rev. **88,** 851 (1952).
[18] L. V. Spencer, Phys. Rev. **98,** 1597 (1955).
[19] H. O. Wyckoff (private communication).

WASHINGTON, August 30, 1957.

Journal of Research of the National Bureau of Standards Vol. 60, No. 3, March 1958 Research Paper 2843

Fragmentation of Waterdrops in the Zone Behind an Air Shock*

Olive G. Engel

Observations made on the fragmentation of two waterdrop sizes, after collision with air shocks that were moving at three different supersonic velocities, are reported. The possible mechanisms of various aspects of the fragmentation process are discussed. The experimental observations indicate that high-speed-rain-erosion damage should not be observed on spheres having a diameter as large as 4 feet and moving with a Mach number in the range of 1.3 to 1.7 in rain that has a drop diameter of 1.4 millimeter. Waterdrops of this size should be reduced to mist in the zone of separation between the detached shock and the surface of the sphere according to the results that are reported. A means to extend this protection to spheres of smaller diameter or to rain of larger size is pointed out. The need for further experimental observation of the time required for the fragmentation of waterdrops using shocks moving at higher Mach numbers is indicated to verify and extend the information.

1. Introduction

A blunt object moving through air at supersonic velocity is preceded by a detached shock wave that is separated from the leading surface of the object by a zone in which air is moving forward at high velocity in front of the object. It has been shown [1] that if a waterdrop were subjected to the conditions that prevail in the zone of detachment between such a shock wave and the object (Mach number 1.7) that is producing it, the waterdrop would be reduced to droplets having diameters of the order of millionths of a foot. Droplets of this size are probably incapable of causing erosion of the surface of the object when they are intercepted by it, even though the object is moving at supersonic velocity. This follows because small drops are so much less effective than large drops in producing waterdrop impingement damage. If, therefore, the waterdrop has time to fragment into droplets before the surface of the object that is producing the shock intercepts it, the problem of erosion as a result of high-speed-rain impingement may be less serious at supersonic velocities than at subsonic velocities. A study of the breakup of waterdrops in high velocity airflows produced by a blast gun has been made at Porton in England. However, published reports of this work do not contain the quantitative information that is needed. To obtain this information, the photographic observation of the fragmentation of waterdrops in a shock tube was undertaken.

It was conjectured that the time required for the fragmentation of liquid drops under the conditions that exist behind an air shock would be found to be a function of several variables. For drops of distilled water these variables should reduce to the velocity of the air shock and the mass of the drop. Therefore, data were collected over a range of three air-shock velocities (Mach number of the shock was 1.3, 1.5, and 1.7) for both a large (2.7-mm diam) and a small (1.4-mm diam) drop size, respectively.

Results of this investigation indicate that high-speed-rain-erosion damage should not be observed on spheres having a diameter as large as 4 ft and moving with a Mach number in the range of 1.3 to 1.7 in rain that has a drop diameter of 1.4 mm. See section 5. Drops of this size should be reduced to mist in the zone of separation between the detached shock and the surface of the sphere according to the observations that have been made. It may be possible by means of design to extend this protection to spheres of smaller diameter or to rain of larger drop size. See section 5.

2. Details of the Observation Arrangement

Observations of the type required can be made best in a shock tube in which the velocity of the air shock can be controlled within a small range of variation and through which permanent photographic recording is possible. In order to take spark pictures of the waterdrop at known time intervals after it is struck by an air shock, a shock tube containing large planar glass windows is required.

2.1. Description of the Shock Tube and Waterdrop Source

The shock tube used was located at the Naval Ordnance Laboratory at White Oak, Maryland. It has been described previously [1].[2] The 4-ft pressure chamber of this tube was separated from the 14-ft expansion chamber by a plastic film. See figure 1. The pressure chamber was filled with helium gas to a gage pressure that was found sufficient to produce the required air-shock velocity. Sudden release of this gas by puncturing the plastic film with a needle plunger resulted in the formation of an air shock in the column of air that occupied the expansion chamber.

The exit end of the expansion chamber contained 3- by 8-in. glass windows of interferometric quality. To admit waterdrops, a set of ½-in.-diam holes was bored through the top and bottom walls of the shock tube at the left-hand side of the window. A fiducial marker was used to indicate the centers of these holes. An additional set of holes existed at the center of the window.

Drops of distilled water were formed at the tip of a hypodermic needle that was mounted above the

[1] Unpublished data of the author.

*The work described in this paper was sponsored by the Wright Air Development Center whose assistance and interest are gratefully acknowledged.

[2] Figures in brackets indicate the literature references at the end of this paper.

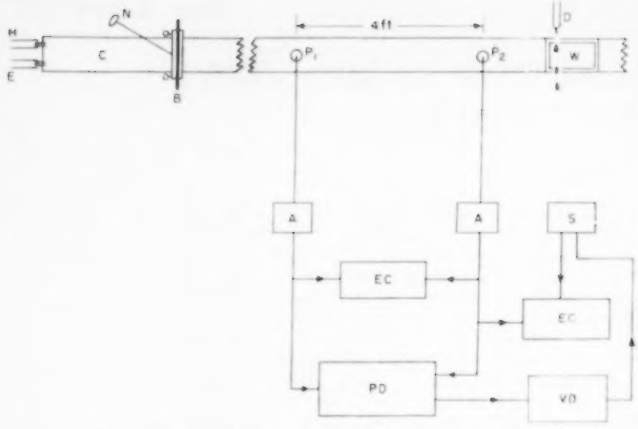

FIGURE 1. *Shock tube and electronic circuits.*

A, amplifier; B, plastic film barrier; C, high pressure chamber; D, waterdrop source; E, exhaust; EC, electronic counter; H, helium intake; N, needle plunger to puncture barrier; P_1, P_2, pressure pickups; PD, proportional delay; S, spark; VD, variable delay unit; W, glass window.

shock tube. The drops were allowed to fall through the holes in the tube into a reservoir located below the underside of it. The freely falling waterdrops were photographed at various time intervals after they were intercepted by an air shock. With use of this arrangement, every spark picture that was taken was of a different waterdrop. Due to the way in which the waterdrop fell from the needle and to adjustments of the needle itself, the waterdrops did not always fall on exactly the same path through the holes in the shock tube. This resulted in a certain amount of horizontal scatter in the location of the waterdrop at the time that the air shock collided with it. This horizontal scatter in the fall trajectories of the drops proved to be a disadvantage both in calculating the time that elapsed from the air-shock-waterdrop collision to the taking of the picture and in determining the drift of the waterdrop in the airstream behind the shock during the time interval from the collision instant to the instant that the picture was made. The scatter was greater in the case of small waterdrops, which were formed at the tip of a hypodermic needle of small bore, than in the case of large waterdrops, which were formed at the tip of a hypodermic needle of large bore.

The sizes of the drops that were produced varied with the rate at which the drops were formed at the tip of the hypodermic needle. When the dropping rate was such as to place only one drop in the picture with use of the small-bore needle, the drop was nearly as large as those formed at the same rate by the large-bore needle. It was, therefore, necessary to have more than one drop in the picture in the case of the small drops in order to have a notable difference in drop size to observe the effect of water mass on the time required for waterdrop fragmentation.

2.2. Photographic Recording

The shock tube extended from the NOL Ballistics Range Laboratory into a small adjoining room which served as the camera box as well as for a photographic dark room. The pressure chamber and the major part of the expansion chamber of the shock tube were in the main laboratory; the exit end, which contained the glass windows through which the photographic observations were made, was housed in the auxiliary room.

The light source for the pictures was a 1-μsec spark. See figure 2. Light from the spark was collimated and the collimated beam was passed through the windows of the shock tube. It was then concentrated by the field lens and focused by the camera lens on film that was exposed in darkness in the auxiliary room just before a picture was made. The spark appears as a dim circle of light in the pictures.

Pictures taken in this optical system were all originally about 1.4 ×. Figures 7 and 9 are enlargements of original photographs.

2.3. Time Measurement

The velocity at which the air shock was moving down the shock tube was calculated from the time that was required for it to traverse a known distance between two points. Two barium titanate pressure pickups were inserted 4 ft apart in the wall of the shock tube. See figure 1. Signals received by these pressure pickups, when the air shock passed them in its progress down the tube, were used to start and to stop a Potter electronic counter. The reading on this counter was the time in microseconds required for the air shock to move the 4-ft distance between the pressure pickups.

The time that elapsed between the instant that the air shock intercepted the waterdrop and the instant that the picture was made was found by measuring the distance between the air shock and the center of the waterdrop as seen in the picture itself. Eventually, a time was reached at which the air shock had progressed beyond the right-hand boundary of the picture. For the time range in which no shock was visible in the picture, a second Potter electronic counter was used to determine the time that had elapsed between the air-shock-

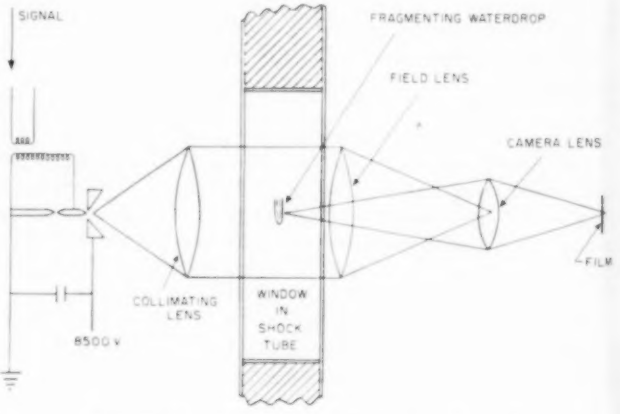

FIGURE 2. *Optical arrangement and spark.*

waterdrop collision and the instant that the picture was taken. This counter was started by the signal from the second pressure pickup and was stopped at the instant that the spark for the picture was set off. The time that elapsed from the instant that the shock passed the fiducial marker to the instant that the spark for the picture went off was found by subtracting the observed time required for the shock to advance from the second pressure pickup to the fiducial marker from the second counter reading.

2.4. Conditions in the Airflow Behind a Shock That Moves Into Still Air

The conditions that exist in the air through which the shock has moved constitute the environment in which the waterdrop finds itself after the air-shock-waterdrop collision.

a. Velocity of the Airstream That Exists Behind a Moving Shock

The velocity of the airstream in which the waterdrop finds itself after the air shock has intercepted it and passed by is an important factor in the fragmentation of the waterdrop. For the case of a stationary shock formed in a shock tube, the continuity equation is

$$\rho_1 u_1 = \rho_2 u_2 \tag{1}$$

so that

$$u_2 = \frac{\rho_1}{\rho_2} u_1 \tag{2}$$

where u_1 is the velocity of the airstream entering the shock and ρ_1 is the density of this air, u_2 is the velocity of the airstream after passing through the shock, and ρ_2 is the density of this air.

For the case of a moving shock, the airstream velocities on either side of the shock are those seen by an observer who is moving toward the shock at the velocity u_1. For this observer the velocity of air approaching the shock is U_1 and

$$U_1 = 0. \tag{3}$$

The shock appears to be approaching this observer at a velocity U_s, and

$$U_s = -u_1. \tag{4}$$

The velocity of air on the opposite side of the shock as seen by this observer is U_2 and

$$U_2 = u_2 - u_1 \tag{5}$$

or, by use of eq (2),

$$U_2 = \left[\frac{\rho_1}{\rho_2} - 1\right] u_1. \tag{6}$$

In terms of the velocity of the shock, by use of eq (4),

$$U_2 = U_s\left[1 - \frac{\rho_1}{\rho_2}\right] \tag{7}$$

from which it can be seen that U_2 is constant for any given shock velocity. For the moving air shock, the sub-1 notation applies to the undisturbed air ahead of the shock and the sub-2 notation applies to the air through which the shock has passed. In terms of the Mach number of the shock, M_s, the inverse of the air density ratio is [2]

$$\rho_2/\rho_1 = (\gamma+1)M_s^2/[(\gamma-1)M_s^2+2]. \tag{8}$$

The constant velocity of the air behind a shock moving down a shock tube can be calculated, therefore, if only the velocity of the shock itself is known. The velocity of the airstream behind the shock can also be calculated from the expression given in reference [3]

$$U_2 = (U_s^2 - c_1^2)/2U_s[(\gamma+1)/4] \tag{9}$$

where c_1 is the speed of sound in the undisturbed air ahead of the moving shock and γ is the ratio of the specific heat at constant pressure to the specific heat at constant volume, which for air is 1.4.

The calculated values of the velocity of the airflow behind shocks that have Mach numbers of 1.3, 1.5, and 1.7 are given in table 1.

b. Temperature of the Air Behind the Moving Shock

A knowledge of the temperature of the air in which the fragmentation of a waterdrop occurs is of interest in establishing the mechanism of the fragmentation process. The ratio of the temperature of the airstream behind the moving shock, T_2, to the temperature of the undisturbed air into which the shock is advancing, T_1, is given by the expression [2]

$$T_2/T_1 = [2\gamma M_s^2 - (\gamma-1)][(\gamma-1)M_s^2+2]/(\gamma+1)^2 M_s^2. \tag{10}$$

TABLE 1. *Conditions in the constant-velocity airstream flowing behind the air shock*

Shock, Mach number, M_s	Conditions in the constant-velocity airstream flowing behind the air shock (assuming that ρ_1=0.0011766 g/cm³; T_1=300° K; μ_1=184.2 micropoise)										
	Velocity, U_2	Sound speed, c_2	Mach number, M_2	Density, ρ_2	Temperature, T_2		Pressure, p_2	Stagnation pressure, p_t	Viscosity, μ_2	Kinematic viscosity, μ_2	Reynolds number for the 2.7-mm-diameter waterdrop
	cm/sec	*cm/sec*		*g/cm³*	*° K*	*° C*	*Dynes/cm²*	*Dynes/cm²*	*Poise*	*cm²/sec*	
1.3	1.52×10^5	3.75×10^4	0.4	0.00178	357	84	1.79×10^6	1.99×10^6	2.10×10^{-4}	0.118	35,000
1.5	2.37	3.96	.6	.00218	396	123	2.43	3.10	2.27	.104	61,000
1.7	3.16	4.16	.76	.00256	438	165	3.17	4.65	2.46	.096	89,000

The calculated values of the temperature of the air that is flowing behind shocks that have Mach numbers of 1.3, 1.5, and 1.7, taking the temperature of the undisturbed air ahead of the advancing shock to be 300° K, are given in table 1.

c. Viscosity of the Air Behind the Moving Shock

It is necessary to know the viscosity of the air that is flowing behind the moving shock to evaluate the Reynolds number of the airflow around the waterdrop. The viscosity coefficient of the air flowing behind the shock, μ_2, can be approximated from the expression [2]

$$\mu_2/\mu_1=(T_2/T_1)^{0.76}. \tag{11}$$

The calculated values of the viscosity coefficient of the air flowing behind shocks having Mach numbers of 1.3, 1.5, and 1.7, found by use of eq (10) and by taking the viscosity of the undisturbed air ahead of the advancing shock to be 184.2 μpoise, are given in table 1. The calculated values of the density, ρ_2, and of the kinematic viscosity, ν_2, of the air flowing behind shocks having these Mach numbers, found by use of eq (8) and by taking the density of the undisturbed air ahead of the advancing shock to be 0.0011766 g/cm^3, are also given in table 1.

d. Reynolds Number for the Flow Around the 2.7-mm Diameter Waterdrop

Knowing the velocity, U_2, the viscosity coefficient, μ_2, and the density, ρ_2, of the airstream that is flowing behind the shock, the Reynolds number of the flow around the waterdrop, $\rho_2 U_2 l/\mu_2$, where l is a characteristic length, can be calculated. The drift velocity has been neglected. The values of the Reynolds number of the flow around the 2.7-mm-diam waterdrop, taking l to be the diameter of the drop, are given in table 1 for the case that the Mach number of the shock was 1.3, 1.5, and 1.7.

e. Mach Number of the Airstream Flowing Behind the Moving Shock

To determine the Mach number of the airflow behind the moving shock, M_2, it is necessary to know the speed of sound in this air, c_2. The sound speed can be calculated from the expression given in [3]

$$c_2^2=c_1^2+\frac{2(\gamma-1)}{(\gamma+1)^2}\left[\gamma U_s^2-(\gamma-1)c_1^2-\frac{c_1^4}{U_s^2}\right] \tag{12}$$

where c_1 is the speed of sound in the undisturbed air ahead of the shock. The values of the sound speed and of the Mach number of the airflow behind the shock, U_2/c_2, found by use of eq (7) and (12) are given in table 1 for the condition that the Mach number of the shock is 1.3, 1.5, and 1.7.

f. Pressure in the Airstream Flowing Behind the Moving Shock

A knowledge of the free-stream pressure in the airflow behind the moving shock is needed to determine the pressure that exists on the windward and leeward faces of the waterdrop. The free-stream pressure, p_2, is given by [3]

$$p_2=p_1+\rho_1 U_s U_2, \tag{13}$$

and because

$$p_1=c_1^2\rho_1/\gamma, \tag{14}$$

$$p_2=\rho_1\left[\frac{c_1^2}{\gamma}+U_2 U_s\right]. \tag{15}$$

Taking ρ_1 to be 0.0011766 g/cm^3, c_1 to be 3.44x10 cm/sec, and using the values of U_2 found from eq (7), the values of p_2 were found for the condition that the Mach number of the shock was 1.3, 1.5, and 1.7. They are listed in table 1.

2.5. Pressure on the Windward and Leeward Faces of a Waterdrop in an Airstream

As soon as an air shock intercepts a waterdrop, the waterdrop exists in the airstream behind the shock, and pressure differences are established around it. Potential flow, in which there are no vortices, exists at first. There is a high pressure at the stagnation point in the center of both the windward and leeward face of the waterdrop, and these pressures are equivalent as long as potential flow persists. Low pressure exists at the equatorial belt between the two stagnation points. Eventually vortices appear at the leeward face of the drop. The pressure at the leeward face of the drop then falls to a value that is only slightly higher than that at the equatorial belt.

Fage [4] measured the pressure that developed on a 6-in.-diam sphere in an airflow. For Reynolds numbers up to 424,500, the results of Fage indicate that the pressure distribution on the windward face is essentially unchanged as the Reynolds number is increased but that at high Reynolds numbers the pressure drop around the equatorial belt becomes more intense and the pressure on the leeward face rises. Comparison of the values obtained for Reynolds number of 110,000 and 157,200 shows that there is little difference in them except that the pressure drop around the equatorial belt is less for the lower Reynolds number. In view of the value of the Reynolds number for the flow around the 2.7-mm-diam waterdrop when it exists in the airstream behind shocks having Mach numbers of 1.3, 1.5, and 1.7 (see table 1), it can be expected that the pressure distribution around it is closely the same as that found by Fage for a Reynolds number of 110,000 except that the minimum in the curve at an angle of about 75° is probably less pronounced. See section 4.7.

a. Stagnation Pressure on the Windward Face of the Waterdrop

The highest pressure that is developed on a waterdrop, which exists in the airflow behind an air shock, occurs at the center of the windward face. This is the stagnation point where the airstream velocity is zero. If the air is brought to rest isentropically, the

stagnation pressure is given by the expression [2]

$$p_2/p_t=\left[1+\frac{(\gamma-1)}{2}M_2^2\right]^{-\gamma/(\gamma-1)} \quad (16)$$

where p_t is the total pressure at the stagnation point. Values of p_t, which were calculated with use of values of p_2 obtained from eq(15) and with use of values of M_2 obtained from eq (7) and (12) for the condition that the Mach number of the shock is 1.3, 1.5, and 1.7, are given in table 1.

b. Pressure on the Leeward Face of the Waterdrop

After vortices form at the leeward face of the waterdrop, the pressure there drops to a value below the stagnation-point pressure on the windward face of the drop. From the data of Fage [4],

$$p_L-p_2=-0.4(\tfrac{1}{2}\rho_2 U_2^2) \quad (17)$$

where p_L is the leeward face pressure. Because

$$\rho_2=\gamma p_2/c_2^2, \quad (18)$$

$$p_L=p_2[1-(0.2\gamma U_2^2/c_2^2)]. \quad (19)$$

Using eq (9), (12), and (15), the value of p_L for a waterdrop that exists in the airflow behind a shock having a Mach number of 1.3 is 1.71×10^6 d/cm^2 (1.69 atm).

2.6. Temperature on the Windward and on the Leeward Face of a Waterdrop in an Airstream

If the airstream is brought to rest isentropically, the stagnation-point temperature, T_t, at the center of the windward face is given by the expression [2]

$$T_2/T_t=\left[1+\frac{(\gamma-1)}{2}M_2^2\right]^{-1}. \quad (20)$$

When the Mach number of the air shock is 1.3, T_t is found to be 368°K (95°C) by use of eq (7), (10), and (12).

It is necessary to know the air density at the leeward face of the drop to evaluate the leeward-face temperature. From the adiabatic equations

$$p_2=(\text{constant})\rho_2^\gamma, \quad (21)$$

$$p_L=(\text{constant})\rho_L^\gamma, \quad (22)$$

it follows that

$$\rho_L=\rho_2\sqrt[\gamma]{\frac{p_L}{p_2}}. \quad (23)$$

When the Mach number of the air shock is 1.3, ρ_2 is 0.00178 g/cm^3 (see section 2.4.c). From eq (23), ρ_L is then 0.00172 g/cm^3. Because

$$p_L=\rho_L R T_L$$
$$T_L=p_L/R\rho_L. \quad (24)$$

Using the value of p_L found in section 2.5.b, the value of the gas constant, R, in ergs per degree per gram, and the value of ρ_L found just above, T_L is 353° K (80° C) when the Mach number of the shock is 1.3.

3. Observed Stages in the Fragmentation of Two Waterdrop Sizes After Collision with Air Shocks that Were Moving at Three Different Velocities

The dropping rates used were such that waterdrops formed with use of the large hypodermic needle had an approximate average diameter of 2.7 mm and waterdrops formed with use of the small hypodermic needle had an approximate average diameter of 1.4 mm.

3.1. Mach Number of the Shock Is 1.3

The observed stages in the fragmentation of the large and of the small waterdrop in the airflow behind the shock when the Mach number of the shock was 1.3 are given in the following two sections. The velocity of the airflow behind the shock, which is the environment in which the fragmentation is accomplished, is 1.52×10^4 cm/sec for this air-shock velocity.

a. Stages in the Fragmentation of the Large Waterdrop

Casual inspection of a spark picture taken of a 2.7-mm-diam waterdrop 76 μsec after it was struck by an air shock leaves the impression that it is undisturbed. Actually, this is not the case. The high light in the shadowgraph of the drop, which appears as a dim pinpoint of light to the unaided eye, has a distinct structure at low magnification. It consists of a starlike cluster of sharp prongs of light. This is quite different from the appearance of the high light in a waterdrop that has not been struck by an air shock. In the undisturbed drop the high light is more or less circular and has little structure. More is said about this observation in section 3.2.a, and the possible significance of it is discussed in section 4.2. In a picture taken 84 μsec after the air-shock-waterdrop collision, the high light in the drop was so dim that the exact structure of it could not be determined. In addition to the change in the appearance of the high light, there is a slight corrugation on the windward face of the drop. The corrugation of the windward face is also evidence that the drop is not quiescent.

The first response of a waterdrop of this size that can be detected with the unaided eye is apparent in a spark picture taken at the end of 93 μsec after the air-shock-waterdrop collision. See figure 3, picture 1. The leeward face of the waterdrop appears to be flattened in this picture, and there is some evidence of the start of a radial flow of water from the drop in a plane through the center of it that is also perpendicular to the wind direction. This is manifested by a slightly pointed appearance of the top and bottom of the drop as it is viewed in the picture. The points are somewhat more apparent on the waterdrop

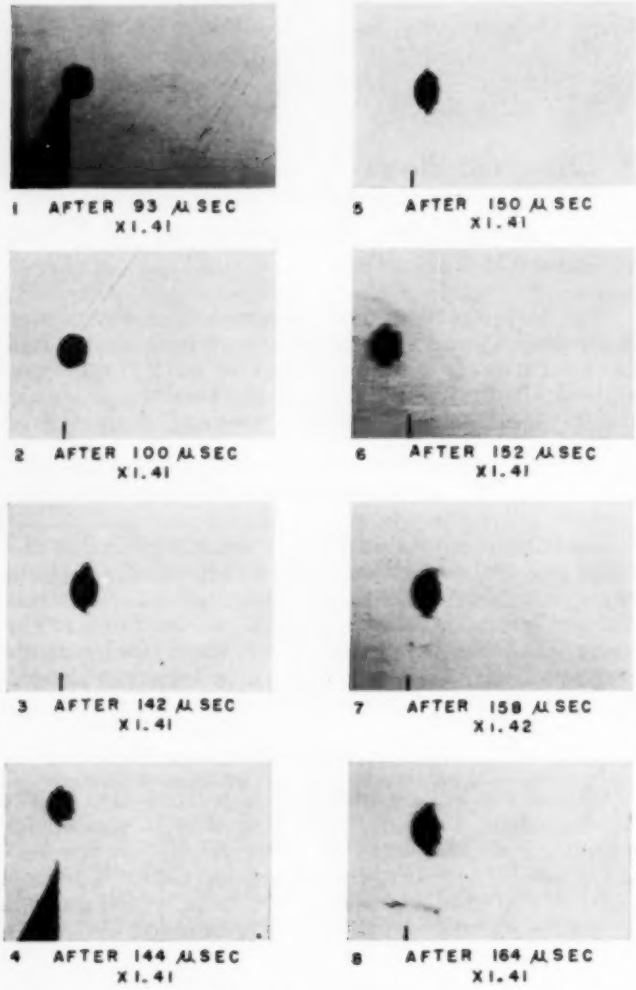

FIGURE 3. *Views of the 2.7-mm-diam waterdrop showing the flattening of the leeward face (right-hand side) of the drop, the development of the radial flow, the beginning of the formation of water mist, and the flattening of the drop perpendicular to the wind direction.*

Mach number of the air shock was 1.3.

shown in figure 3, picture 2, which was taken 100 μsec after the air-shock-waterdrop collision. The flattening of the leeward face of the waterdrop is discussed in section 4.3. The radial flow of the drop becomes more marked with the passage of time after the air-shock-waterdrop collision; the length of the protrusions increases with the time elapsed since the collision incident. The flow is, of course, not two spouts of water from the top and bottom of the drop as it is observed in the pictures; it is a ring of water moving radially out of the drop and appears as the rings of Saturn do when they are viewed on edge. From the pictures of figure 3 it can be seen that after this ring of water has moved out far enough from the drop, it is bent in the wind direction (toward the right) by the force of the rapid airflow. Possible causes of this radial flow of water from the drop are discussed in section 4.5.

The radial flow is accompanied by another process that is more important as far as the fragmentation of the waterdrop is concerned. This is the formation of water mist. Evidence of the formation of mist from the radially flowing water and from the leeward face of the waterdrop can be seen in figure 3, pictures 3 through 8. The limiting stage to which the mist formation goes can be seen in figure 4. In figure 4, picture 6, the streamers of mist extend to the right-hand boundary of the picture. Mechanisms that may be responsible for the formation of this mist are discussed in section 4.4.

The formation of water mist and of the beginning of radial water flow are accompanied by a gradual flattening of the drop, that is, by an increase in its diameter in all directions perpendicular to that of the rapid airflow. A graph of the measured values of the maximum diameter of 2.7-mm-diam waterdrops, after various intervals of time up to 420 μsec after they were struck by an air shock, is shown in figure 5. There are four distinct regions in the curve. The first region is a plateau from zero time after the air-shock-waterdrop collision to about 90 μsec after the collision incident. This corresponds with the time during which the waterdrop appears to be quiescent. Inspection of the experimental curves for the flattening with time after 2.7-mm-diam waterdrops collided with shocks when the Mach number of the shock was 1.5 and 1.7 (see fig. 5) leads to the conclusion that a very slight flattening probably does occur during at least part of the period of apparent quiescence and/or that the length of the period of quiescence is a function of the Mach number of the shock.

The second region in the curve of waterdrop flattening, as a result of collision with air shocks when the Mach number of the shock was 1.3, is an almost linear increase of the drop diameter perpendicular to the direction of the airflow. That the flattening is not a linear function of the time but that instead there is a very slight increase in the degree of flattening with time, can best be seen by inspection of the flattening curves when the Mach number of the air shock was 1.5 and 1.7. For the case of air-shock-waterdrop collisions when the Mach number of the shock was 1.3, the flattening appears to terminate at the end of 220 μsec after the collision incident.

The third region in the curve extends from 220 μsec to about 300 μsec. It is a plateau and the existence of it appears to indicate that at the end of 220 μsec the water of the drop has given a maximum response to the pressure difference that is set up by the airflow between the poles and the equator of it. Further flattening appears to be checked. Because a similar plateau appears to exist in the flattening curve at about this same time interval for the case that the Mach number of the shock was 1.5, it seems likely that it is the force of surface tension that acts as a check against further flattening of the drop. See section 4.6 and, for a further discussion of this point, section 4.8.

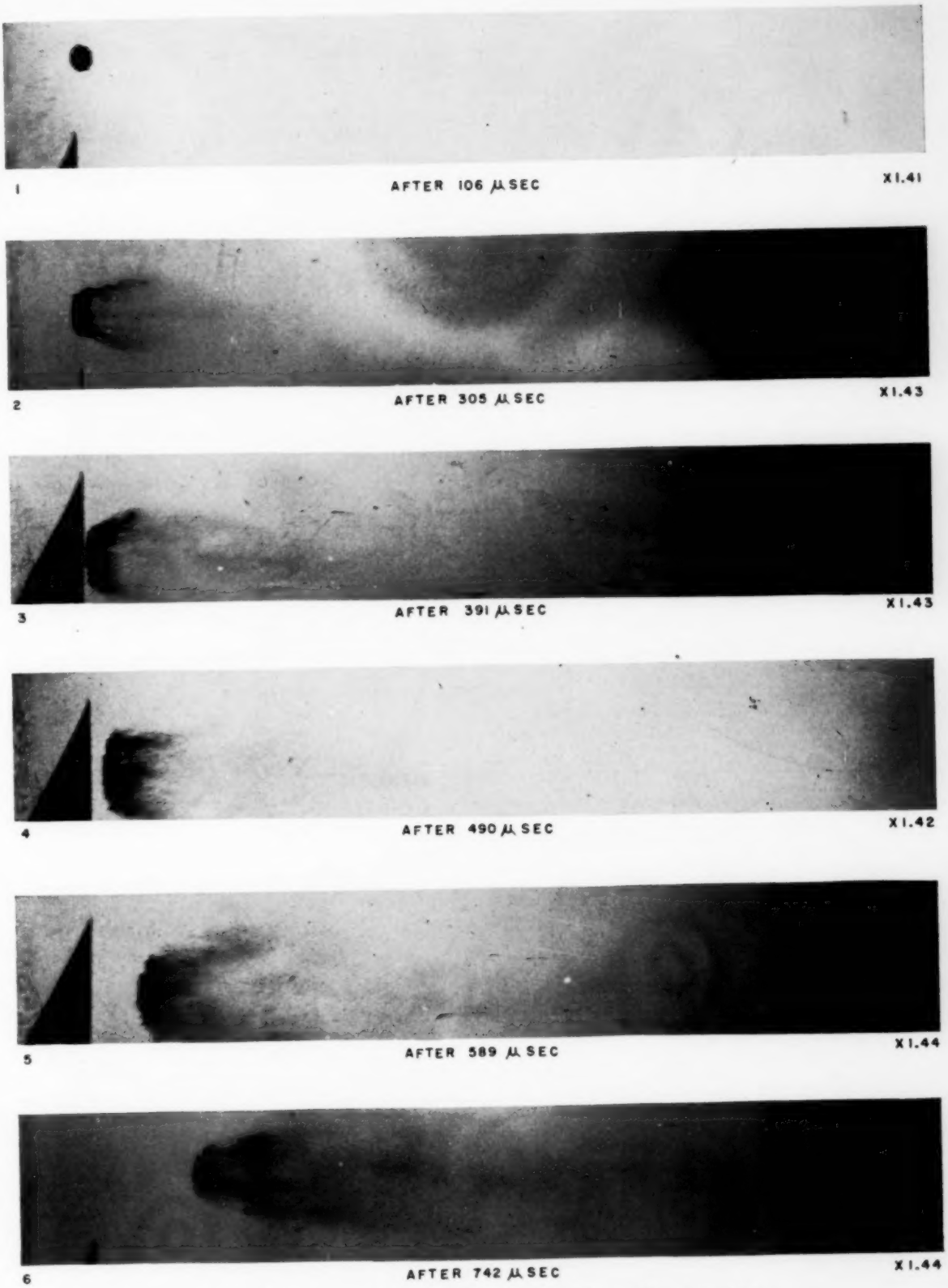

FIGURE 4. *Stages in the fragmentation of a 2.7-mm-diam waterdrop.*

Mach number of the air shock was 1.3.

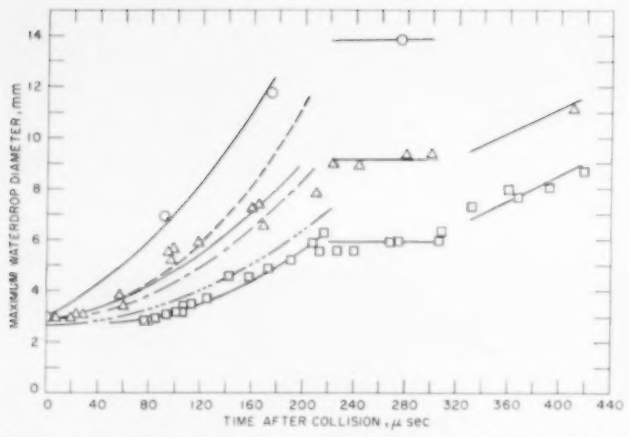

FIGURE 5. *Flattening of waterdrops after collision with air shocks having Mach numbers of 1.3, 1.5, and 1.7.*

Mach number of shock	
Empirical curve	Calculated curve
○, 1.7	— — —, 1.7
△, 1.5	— — —, 1.5
□, 1.3	— — — —, 1.3

In the fourth region, the diameter of the drop perpendicular to the direction of the airflow down the shock tube again increases, but the increase is at a slower rate. The intact portion of the waterdrop eventually segments. The fourth region of the flattening curve of figure 5 may mark the drifting apart of the separate segments of the waterdrop after segmentation has occurred.

It might be supposed that the waterdrop would start to move down the shock tube with the airstream as soon as the air shock had struck it and passed by. This, however, does not seem to be the case. Measurements of the distance from the edge of the fiducial marker to the leading edge of the waterdrop at various time intervals after a 2.7-mm-diam waterdrop collided with an air shock when the Mach number of the shock was 1.3 indicate that there was essentially no drift under 100 μsec after the collision incident. These data are not presented, but the condition of essentially no drift in the initial 100 μsec after the air-shock-waterdrop collision can be seen in graphs of similar data for collision of 2.7-mm-diam waterdrops with air shocks when the Mach number of the shock was 1.5 and 1.7. See figure 6, A and 6, B. The drift velocity of the waterdrop is discussed in section 4.7.

The final stages of the disintegration of the waterdrop are a distinct corrugation of its windward face followed by breakup of the remaining portion of the waterdrop into separate sections. From a comparison of calculated with observed values of the acceleration of the waterdrop in the airflow behind a shock, it appears likely that a hole forms in the disk of water to which the waterdrop flattens. See section 4.7. If, indeed, a hole is forced through the water disk in the early stages of the fragmentation process, the final stage is a segmentation of the resulting water ring into a chain of water beads.

b. Stages in the Fragmentation of the Small Waterdrop

The large waterdrop shows essentially no response 76 μsec after the passage of the air shock. The small waterdrops are streaming water mist and are in an advanced stage of radial flow 75 μsec after the passage of the shock. At the end of 93 μsec after

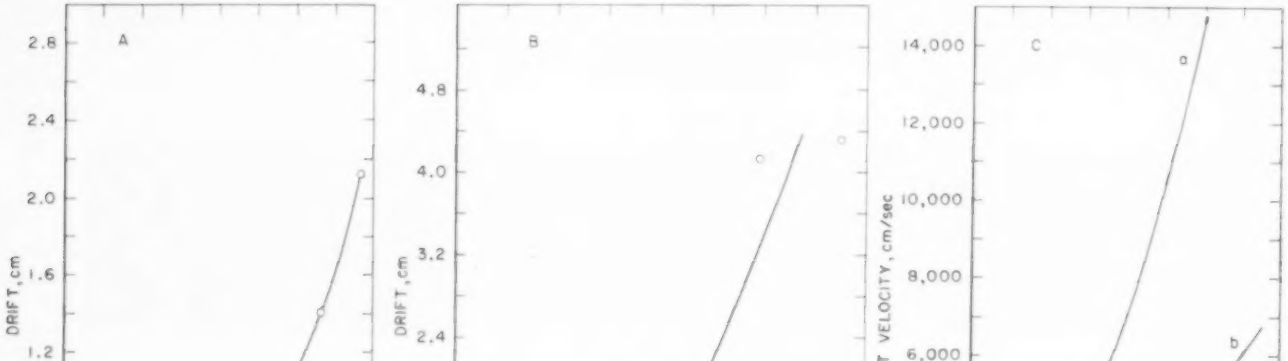

FIGURE 6. *A, Drift of 2.7-mm-diam waterdrops after collision with air shocks that had a Mach number of 1.5; B, drift of 2.7-mm-diam waterdrops after collision with air shocks that had a Mach number of 1.7; C, plot of drift velocity versus time for 2.7-mm-diam waterdrops.*

a) Mach number of the air shock was 1.7, and (b) Mach number of the air shock was 1.5.

the collision, the large waterdrop has only responded to the extent of developing a square appearance of the leeward face. By the end of less time than this, that is, after 82 and after 88 μsec, the small drops have flowed radially and have flattened in a plane perpendicular to the direction of motion of the shock and are emitting water mist both from the leeward face and from the periphery of the radial flow. A comparable stage of fragmentation is reached for the large waterdrop only at the end of about 200 μsec after the air-shock-waterdrop collision. From these observations, the large waterdrop is lagging the small waterdrop by better than 100 μsec in developing an initial stage of fragmentation.

Evidence of the corrugation of the windward face of the small waterdrop can be seen at the end of 75 μsec after the air-shock-waterdrop collision, and strong corrugation of the windward face can be seen 160 and 170 μsec after the collision incident. The stage of fragmentation reached by the small waterdrops 230 μsec after the air-shock-waterdrop collision about compares with that reached by the large waterdrop at the end of 331 μsec. In the development of this stage of fragmentation, the large waterdrop has again lagged behind the small waterdrop by about 100 μsec.

At the end of 593 μsec after the air shock collided with the waterdrop, the remaining portion of the small waterdrop is seriously corrugated; 698 μsec after the collision incident, the remaining portion of the small waterdrop is broken up. The remaining segments of the drop continue to emit water mist. The breakup of the intact portion of the large waterdrop when the Mach number of the shock was 1.3 was not observed; it occurs at a time longer than 742 μsec after the air-shock-waterdrop collision.

3.2. Mach Number of the Shock Is 1.5

In the following sections, the observed stages in the fragmentation of the large and of the small waterdrop in the airflow behind air shocks that have a Mach number of 1.5 are given. The velocity of the airflow behind the shock is 2.37×10^4 cm/sec for this air-shock velocity.

a. Stages in the Fragmentation of the Large Waterdrop

At the end of 7 μsec after the waterdrop has been struck by the air shock, the high light in it is very bright and seems to contain three points or prongs. See figure 7, picture 1. The pictures with primed numbers in figure 7 are of the high lights in waterdrops before they were struck by an air shock. The waterdrops, the high lights of which are shown in pictures 1′ and 2′, were both contained in the same spark picture. The waterdrop, the high light of which is shown in picture 1′, had just detached from the tip of the hypodermic needle and emerged through the hole in the top of the shock tube. Hence there is a strong probability that this waterdrop was disturbed. The high light of it has some structure. The waterdrop, the high light of which is shown in picture 2′, was close to the bottom of the shock tube and therefore had had some time in free fall in which

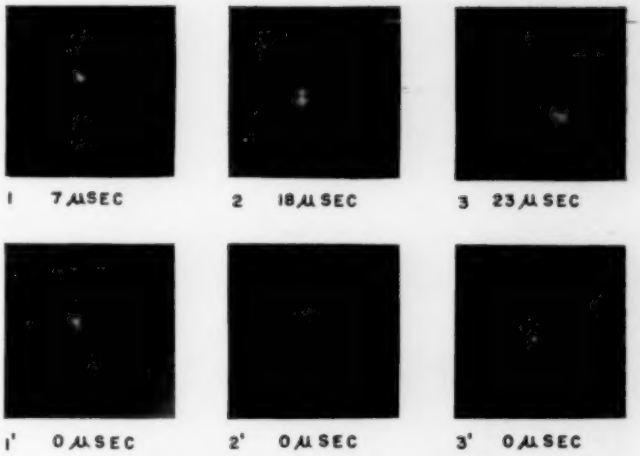

FIGURE 7. *Magnified views of the high light in waterdrops at various time intervals after they were struck by an air shock.*

Mach number of the air shock was 1.5. Pictures with primed numbers are of drops that were not yet struck by an air shock.

to recover from disturbances. The high light in it has no structure. The bright high light of a waterdrop shown in picture 3′ also has no structure. In view of these observations, the structure that appears on the waterdrop high light shown in picture 1 may indicate that the waterdrop in which it existed was disturbed as a result of collision with the air shock, although there is no other apparent indication of it.

The waterdrop high light shown in picture 2, which was taken 18 μsec after the air-shock-waterdrop collision, consists of two hazy pinpoints of light that are close together but that are entirely distinct. Each of these pinpoints of light consists of prongs and gives the appearance of a star. The waterdrop high light shown in picture 3, which was taken 23 μsec after the air-shock-waterdrop collision, is very large and diffuse and may consist of two high lights that are merged or partially superimposed. The diffuse high light is surrounded with spikes or prongs.

In a picture taken 27 μsec after the collision of the air shock with the waterdrop the high light in the drop was so dim that on first examination it was missed entirely. No picture was made in the time interval between 27 μsec and 57 μsec. The picture taken 27 μsec after the collision is the last picture in which any evidence of a high light can be seen in the waterdrop; it is the last picture in which the waterdrop shows no visible sign of distortion, or of reaction to its environment in the airstream behind the shock, or of reaction to having been struck by the air shock itself. In section 3.1.a, it was noted that in the case of large waterdrops that were struck by air shocks having a Mach number of 1.3, a high light could be detected in the drop up to 84 μsec after the air-shock-waterdrop collision. These times after the collision at which the high light may be said to have vanished determine curve A in figure 8 in which the time required to produce comparable stages of fragmentation is plotted against the Mach number of the shock.

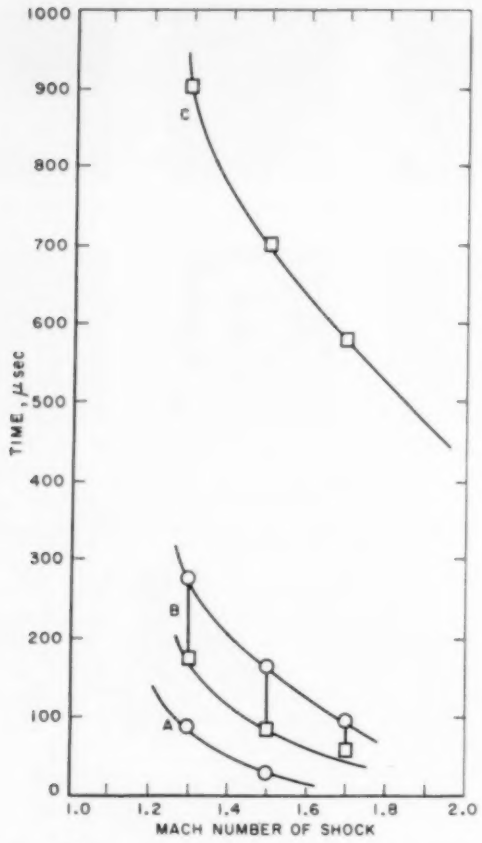

FIGURE 8. *Time to produce comparable stages of fragmentation.*

○ large waterdrop; □ small waterdrop. A, Time at which high light vanishes; B, time to produce a mist cone having a width-to-length ratio of 1 to 3; C, time to produce a trace of mist only.

In a picture taken 57 μsec after the air-shock-waterdrop collision, the waterdrop has no high light at all, and there is no high light in any of the pictures of waterdrops that were taken at longer intervals of time after the collision. The windward face of the waterdrop shows slight evidence of corrugation; mist is emanating from points on the leeward face and from the ends of the major axis of the ellipsoid. A second drop that appears in the picture taken at this interval of time after the collision has two point protrusions at the upper end of the major axis of the ellipsoid and one point protrusion at the lower end of it. These pointed protrusions are bent in the direction of the airflow, and a trail of mist extends into the airflow at the leeward side of the drop from each of them. The production of water mist must, therefore, have started sometime in the 30-μsec interval between 27 and 57 μsec after the collision of the waterdrop with the air shock. The disappearance of the high light may accompany a radial flow of the drop in all directions perpendicular to that of the airflow behind the shock. Such a radial flow of the drop, which was observed in the case of waterdrops struck by air shocks having a Mach number of 1.3 (see section 3.1.a), would destroy its ability to act as a lens for the collimated light in which the radial flow is viewed edge-on.

Because radial flow and production of mist occurred at slightly under 100 μsec for large waterdrops that were struck by air shocks having a Mach number of 1.3, and occur sometime between 27 and 57 μsec after the collision for the same size waterdrop that is struck by an air shock having a Mach number of 1.5, it would appear that an increase of 0.2 in the Mach number of the shock in this velocity range may have caused these phenomena to occur about 50 μsec sooner.

A view of the waterdrop at the end of 59 μsec after collision with the air shock is shown in figure 9. Very small irregularities or bumps can be detected on the windward face, and brushlike structures of mist extend out of the leeward face. The mist has been swept into a stubby, somewhat conical, structure in the airflow downstream beyond the leeward face of the waterdrop. Pictures 2, 3, and 4 of figure 9 show how the corrugation of the windward face of the drop increases with time elapsed since the air-shock-waterdrop collision. They will be referred to in chronological order.

At the end of 94 μsec after the collision of the air shock with the waterdrop, the drop is distinctly flattened against the airflow. See figure 9, picture 2, and figure 10, picture 1. The windward face is strongly corrugated. Brushes of mist extend from points all over the profile of the leeward face, but the largest and most dense are at the top and bottom of the drop as it appears in the pictures.

The mist has been blown into a conelike structure downstream beyond the leeward face of the drop. Pictures of waterdrops taken 97, 98, and 118 μsec after the air-shock-waterdrop collision are very similar in appearance to that shown in figure 10, picture 1, except that the mist cone becomes denser and longer with time elapsed since the collision. At the end of these time intervals after the collision, the leeward face of the drop appears essentially straight, while the windward face is curved and strongly corrugated.

At the end of 159 μsec after the air-shock-waterdrop collision, the contour of the remaining portion of the drop has taken on a distinct quarter-moon shape in which the horns of the quarter moon are on the leeward face and are pointed downstream. See figure 10, picture 2. Mist seems to be spraying from the leeward face in distinct streams, and the mist-cone extending downstream from the leeward face has grown in size and has a width-to-length ratio of about 1 to 3. The closest approximation to this degree of fragmentation for the case that the Mach number of the shock was 1.3 is that which is observed 273 μsec after the air-shock-waterdrop collision. Hence the lag of the lower over the higher velocity shock for producing this degree of fragmentation is 114 μsec. See curve B of figure 8. Pictures of waterdrops taken at the end of 168, 209, 222, and 242 μsec after collision of the air shock with waterdrops are similar in appearance to that shown in figure 10, picture 2, except that the mist-cone is longer and denser. The windward face continues to appear highly corrugated. See figure 9, picture 3.

At the end of 280 μsec after the air-shock-

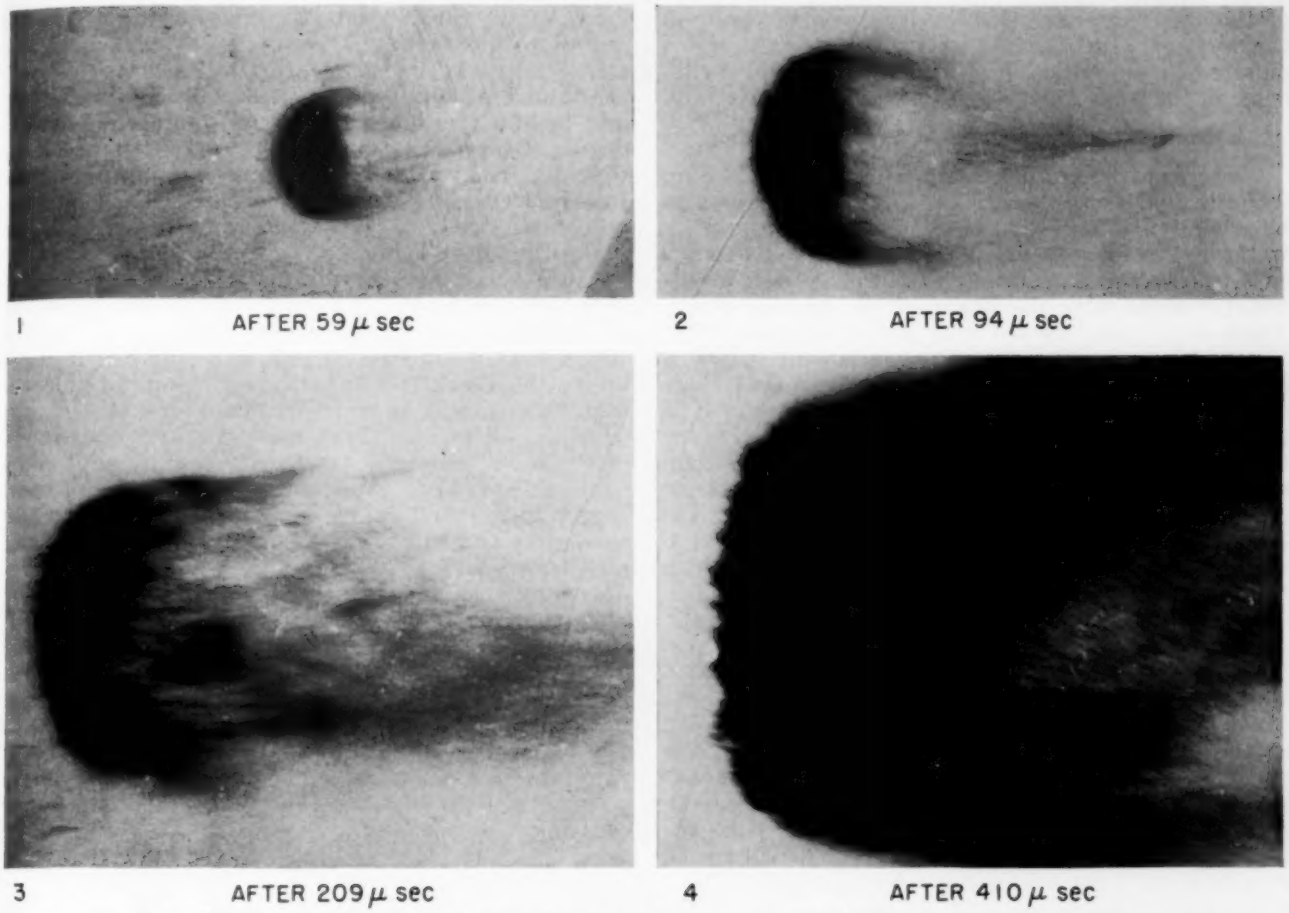

FIGURE 9. *Increase in corrugation of the windward face with time elapsed since the air-shock-waterdrop collision.* Mach number of the shock was 1.5.

waterdrop collision the windward face appears very fringy and the mist extending from the leeward face is hairlike and curled by the turbulence in the wake downstream. See figure 10, picture 3. The remaining portion of the drop is mushroom shaped and is bent at an angle to the airflow. In a picture taken 299 μsec after the collision, the corrugations on the windward face appear to be sharply pointed. In a picture taken 336 μsec after the collision, distinct sections of the remaining part of the drop appear in the mist cone extending downstream from the leeward face.

At the end of 410 μsec after collision of the waterdrop with the air shock, the corrugations of the windward face of the drop are distinctly pointed and appear to be tufted with mist. See figure 9, picture 4, and figure 10, picture 4. However, here, as in all similar appearances at shorter times since the collision, there does not seem to be an orientation of the pointed protrusions on the windward face with the radial flow about the stagnation point. If these pointed protrusions are the crests of waves, or centers of any kind for mist production, the mist emanating from the separate points must be of such low density that it does not show in the photographs. The crests or pointed protrusions also do not appear to be bent in the direction of the airflow from the stagnation point in the center of the windward face. In figure 10, picture 4, a dense hood of mist appears to extend downstream from the leeward face.

In a picture taken 501 μsec after the air-shock-waterdrop collision, the hood of mist that extends downstream from the leeward face is longer. In this picture, the pointed protrusions from the windward face are also longer and there is some sag of the windward face itself which may indicate that the remaining part of the drop is no longer a coherent structure and may possibly consist of mist. In a picture that was taken 589 μsec after the collision, the windward face of the drop has definitely slumped in the wind direction, and in picture 5 of figure 10, which was taken 667 μsec after the collision, this state of affairs is even more marked. A photograph taken 764 μsec after the collision is shown in figure 10, picture 6. Dense spots of mist with corrugated windward faces remain. The trail of mist has spread into a diamond-shaped structure.

In summary, the effect of an increase in the Mach number of the shock from 1.3 to 1.5 appears to be not only a shortening of the time required to bring about the various stages of fragmentation, which was to be expected from the graphs of the flattening

of the waterdrop and of the drift velocity of it in the airstream behind the shock, but also a much more copious production of water mist and of turbulence in the wake downstream behind the waterdrop.

b. Stages in the Fragmentation of the Small Waterdrop

The stage of fragmentation of the 1.4-mm-diam waterdrop shown in figure 11, picture 1, appears to be about the same as that of the 2.7-mm-diam waterdrop shown in figure 10, picture 2. In each case, the remaining part of the drop is bent into a quarter moon with the horns of the quarter moon, which are on the leeward face, pointing downstream. The width-to-length ratio of the mist cone, which is about 1 to 3 in each case, also indicates that these are about comparable stages of fragmentation. The time-after-collision that was required to produce this stage of fragmentation for the 2.7-mm-diam waterdrop is 80 μsec longer than that required to produce the similar stage of fragmentation for the 1.4-mm-diam waterdrop. This may be compared with the time interval of about 100 μsec by which the large waterdrop lagged behind the small waterdrop in reaching a somewhat similar stage of fragmentation when the Mach number of the shock was 1.3. See section 3.1.b and curve B of figure 8. The fact that the lag becomes smaller when the Mach number of the shock is increased may point to the existence of a shock velocity at which the effect of a size difference in the waterdrop is unimportant. Comparison of the pictures of figure 10 with those of figure 11 shows that at the time the 1.4-mm-diam drop is reduced to mist, the windward face of the 2.7-mm-diam waterdrop has just begun to sag in the wind direction.

3.3. Mach Number of the Shock is 1.7

To produce air shocks that had a Mach number of 1.7, a high-helium pressure was required. For safety, the pressure chamber of the shock tube, which was already reinforced with armor plate, was laced with cord. Even with this precaution, however, it was considered inadvisable to take a large number of pictures at this air-shock velocity with the shock tube that was used, and only a sampling was taken over the range of time-after-collision that was explored at the lower shock velocities. The velocity of the airflow behind a shock that has a Mach number of 1.7 is 3.16×10^4 cm/sec.

a. Stages in the Fragmentation of the Large Waterdrop

The state of fragmentation of the 2.7-mm-diam waterdrop 55 μsec after it was struck by the air shock is shown in figure 12, picture 1. Although the head of water of the drop is obscured by the fiducial marker, it is evident that the drop is already copiously emitting water mist. The state of fragmentation of the 2.7-mm-diam waterdrop 91 μsec after it was struck by the air shock is shown in figure 12, picture 2. The stage of fragmentation shown here is almost the same as that which resulted 159 μsec after a waterdrop of the same size was struck by an air shock that had a Mach number of 1.5. See figure 10, picture 2. The difference in the times required to produce this comparable stage of fragmentation is 68 μsec. Because the lag for the shock that had a Mach number of 1.3 over the shock that had a Mach number of 1.5 to produce a similar degree of fragmentation was 114 μsec, it can be seen that the reduction of the time required becomes smaller as the velocity is increased. The time required to produce this stage of fragmentation is plotted in curve B of figure 8.

From a comparison of the pictures of figure 12 with those of figure 10 it can be seen that the stage of fragmentation of the 2.7-mm-diam waterdrop was always much more severe when the Mach number of the shock was 1.7 than for comparable times after the air-shock-waterdrop collision when the Mach number of the shock was 1.5. The appearance of the waterdrop in figure 12, picture 5, about compares with its appearance in figure 10, picture 5, and it can be concluded that at the end of about 430 μsec after collision with a shock that had a Mach number of 1.7, a 2.7-mm-diam waterdrop was reduced to a cloud of mist. The difference in time after the collision for the two pictures is about 200 μsec. Figure 12, picture 6, at the end of 594 μsec after collision of the 2.7-mm-diam waterdrop with a shock that had a Mach number of 1.7, shows a far greater degree of dissipation of the mist that is left of the drop than does figure 10, picture 6, at the end of 764 μsec after collision of the 2.7-mm-diam waterdrop with a shock that had a Mach number of 1.5.

b. Stages in the Fragmentation of the Small Waterdrop

The stage of fragmentation acquired by the 1.4-mm-diam waterdrop 53 μsec after collision with a shock that had a Mach number of 1.7 about compares with its stage of fragmentation 79 μsec after collision with a shock that had a Mach number of 1.5. See figure 11, picture 1. The difference in the time required to attain this stage of fragmentation in the two cases is about 25 μsec. The points are plotted in curve B of figure 8. The 1.4-mm-diam waterdrop is found to be in more advanced stages of fragmentation than at comparable times after the air-shock-waterdrop collision when the Mach number of the shock was 1.5. In a picture taken 574 μsec after collision of the 1.4-mm-diam waterdrop with an air shock that had a Mach number of 1.7, the state of fragmentation is about the same as that in a picture taken 696 μsec after collision of the 1.4-mm-diam waterdrop with an air shock that had a Mach number of 1.5.

3.4. Observed Dependence of the Fragmentation Time on the Diameter of the Drop and the Velocity of the Shock

Because the fragmentation of waterdrops has been observed in this study at only three air-shock velocities for two waterdrop sizes, the amount of generalization as to the effect of the diameter of the drop and the velocity of the shock on the fragmentation time which it is possible to make is limited. In

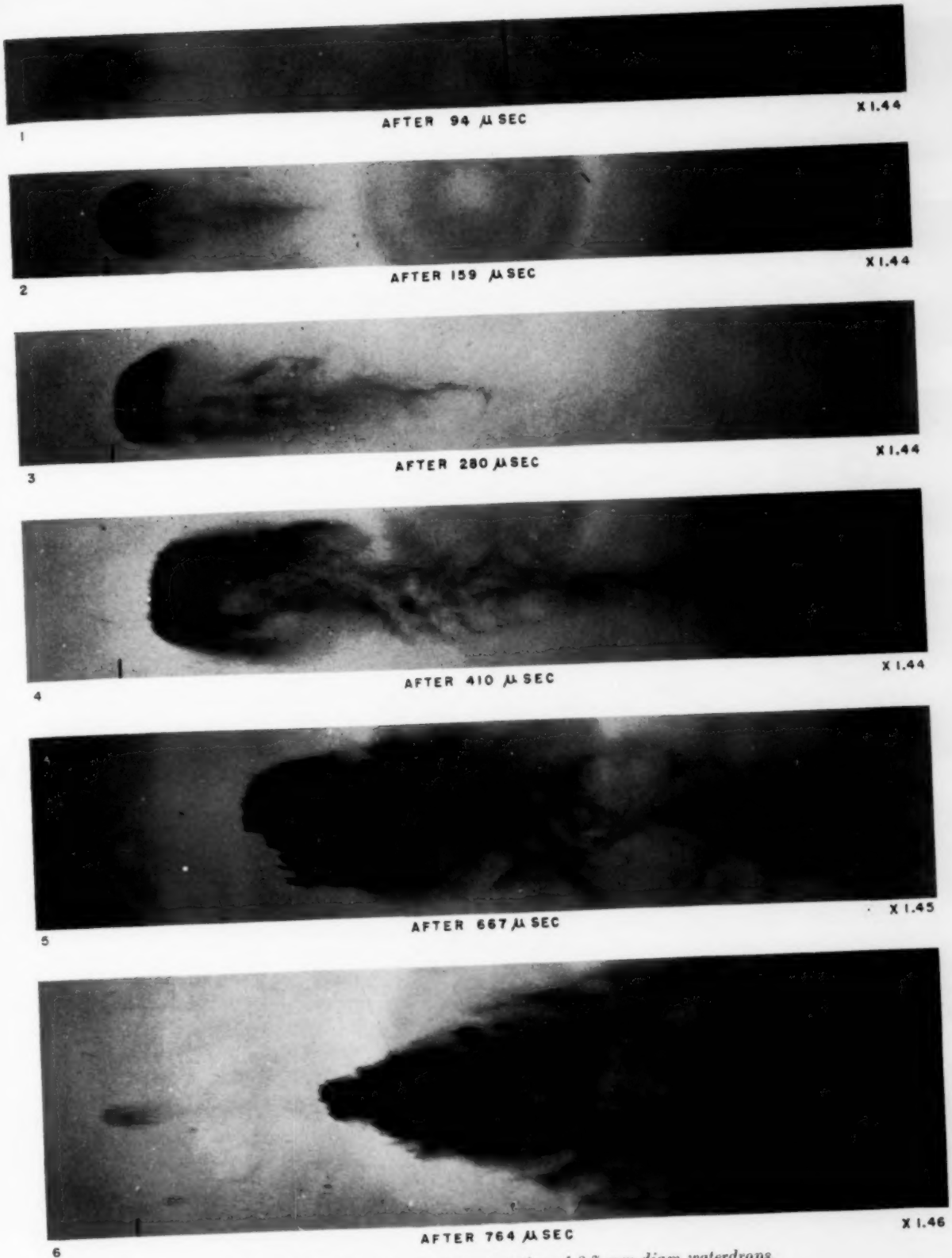

FIGURE 10. *Stages in the fragmentation of 2.7-mm-diam waterdrops.*

Mach number of the air shock was 1.5.

455334—58——8

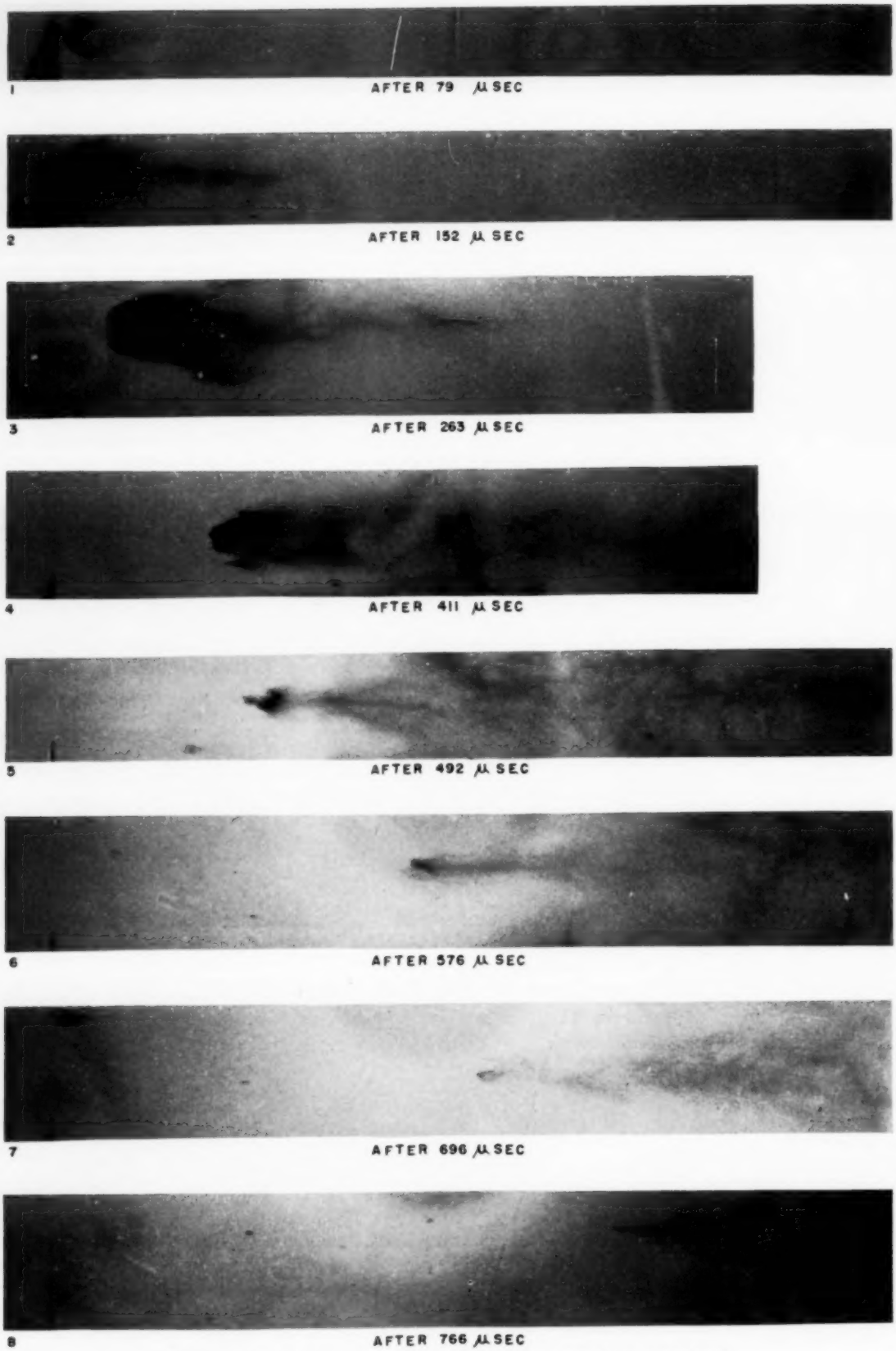

FIGURE 11. *Stages in the fragmentation of 1.4-mm-diam waterdrops.*

Mach number of the air shock was 1.5. × 1.46.

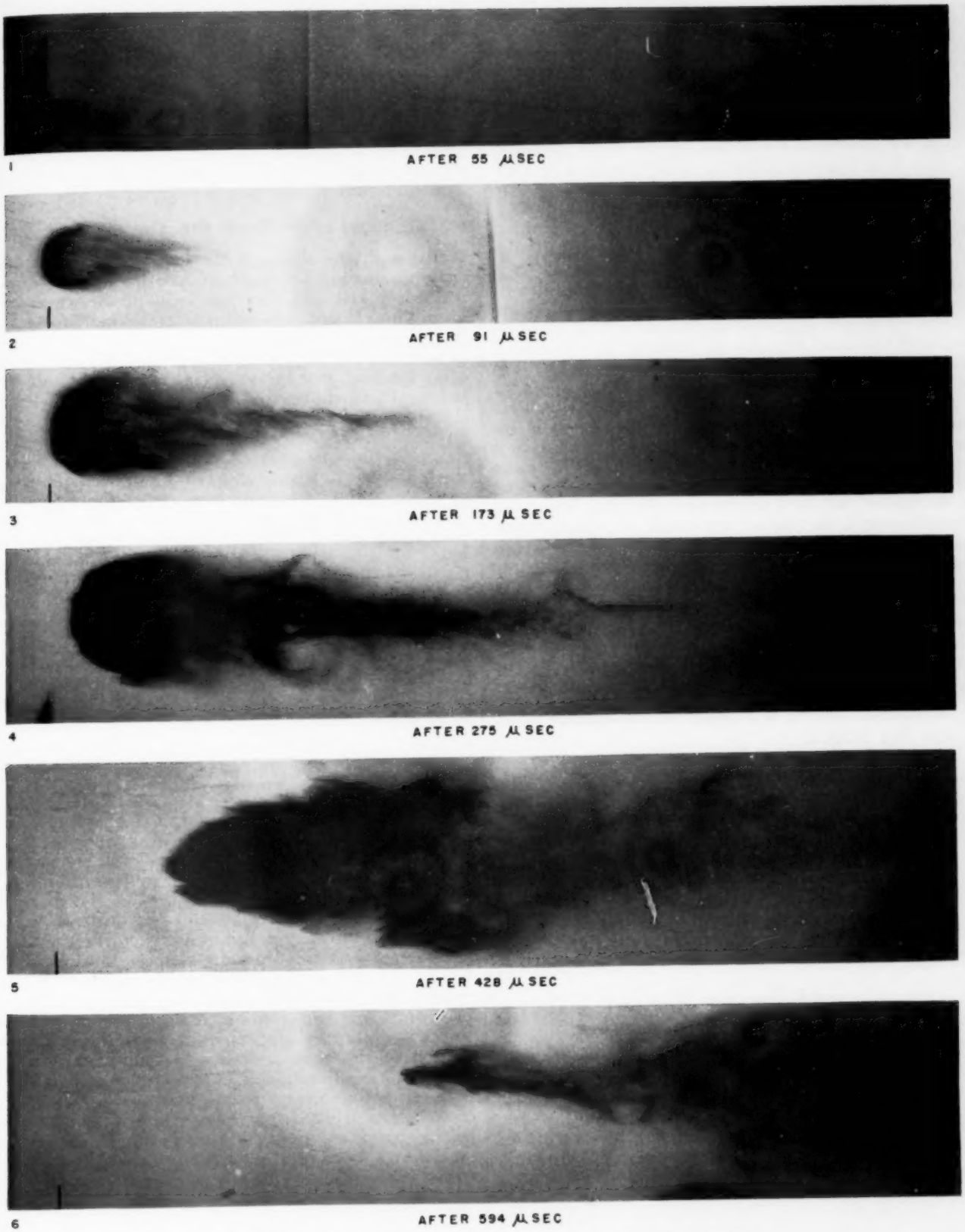

FIGURE 12. *Stages in the fragmentation of 2.7-mm-diam waterdrops.*

Mach number of the air shock was 1.7. × 1.44.

several instances in section 3 a comparison was made of the time required to produce a comparable stage of development in the course of the fragmentation of the waterdrops. The required time for three of these stages of development is plotted against the shock velocity in figure 8. Curve A in figure 8 gives the time required to extinguish the high light in the large waterdrop as a function of the shock velocity. Curve B in figure 8 gives the time required to form a cone of mist having a width-to-length ratio of 1 to 3 downstream from the leeward face of the disintegrating waterdrop as a function of the Mach number of the shock. Data for both the large and for the small waterdrop are given for this stage of fragmentation, and horizontal tie-lines have been drawn between the large-drop and the small-drop values. From curve B it appears that the increment of shortening of the time required to produce this configuration that results on replacing the large waterdrop with the small waterdrop (reduction of the diameter by a factor of 2) is about the same as that which results when the Mach number of the shock is increased by 0.2 in the range of 1.3 to 1.7; that is, a change in the Mach number of the shock is more effective in the rate of waterdrop fragmentation than a change in the drop diameter. Curve C gives the time required to reduce the small waterdrop completely to a trail of mist as a function of the Mach number of the shock. Visual extrapolation of these curves indicates that complete reduction of a small waterdrop to mist may occur within a time interval of the order of 100 μsec when the Mach number of the shock is as high as 3.

4. Mechanism of the Fragmentation of Waterdrops as a Result of Collision With an Air Shock

The data reported in section 3 show only the variation of fragmentation time with drop size and with shock velocity for drops of water in the velocity range that was investigated. The effect of changing the surface tension, viscosity, and density of the liquid of the drop was not explored. Therefore, the information available for deducing the mechanism by which fragmentation occurred is limited. However, in this section, an attempt is made to interpret the observations that were reported in section 3.

4.1. Reaction Time

The 2.7-mm-diam waterdrop showed no visible change in shape immediately after it was struck by an air shock that had a Mach number of 1.3 and, in fact, it existed in the airstream (499 ft/sec) that was flowing behind the shock for nearly 90 μsec before it showed a visible response by change of shape. See section 3.1.a. This behavior is in agreement with the idea that a reaction time is associated with every conceivable movement of matter. During the reaction time, the signal for movement is received and the mechanism of movement is set into operation. An aggregate of molecules of any kind is a coupled system and this is especially the case with water because of the high degree of hydrogen bonding to which it is subject. Therefore it can be expected that the reaction time should be shorter the smaller the mass of water that is involved (drop size) and the stronger the signal for flow that is given (velocity of the shock and of the airflow behind it). This is in agreement with the observed response of two waterdrop sizes after collision with air shocks of three different velocities. See section 3.

4.2. Changes in the Appearance of the High Light

Although the shape of the waterdrop was apparently unaffected for short times after the air-shock-waterdrop collision, the high light in the waterdrop after the collision was noticeably different from the high light in an undisturbed drop. The high light in each of the pictures of waterdrops that were taken after the drop had been struck by the air shock, but before it had shown a visible response by flow, consists of a starlike cluster of prongs or points of light. In some cases, the high light is a double star. See figure 7. It was pointed out in section 3.2.a that the high light in a waterdrop that had been disturbed to the extent of breaking away from the tip of the hypodermic needle and then passing through the hole in the top of the shock tube had some structure in it. The high light in a drop that had fallen freely for several inches, which was contained in the same spark picture, was only a circular pinpoint of light. It seems reasonable to suppose that the structure on the high light is the result of some disturbance of the drop.

The time, τ_n, required for a complete oscillation of a liquid drop for the nth spherical function has been found by Rayleigh [5] to be

$$\tau_n = 2\pi\sqrt{\frac{\rho r^3}{T[n(n-1)(n+2)]}} \tag{25}$$

where r is the radius of the drop; ρ, T are the density and surface tension, respectively, of the liquid of which it is composed. See reference [5], article 364, Vibration of Drops. According to Lenard [6] the case $n=1$ results in no motion, that is, the shape of the drop is spherical; the case $n=2$ is that of the slowest vibration and represents deformation into what is close to an ellipsoidal shape; the cases $n=3$, 4, . . . correspond to more rapid partial vibrations toward the ellipsoidal shape which are anharmonic because their periods do not have a rational relation to the period of the ellipsoidal deformation. A cross section of the solid shapes corresponding to $n=1$, $n=2$, and $n=3$ is in each case a circle when the cut is taken perpendicular to the axis of symmetry. A cross-sectional cut from these shapes taken parallel to the axis of symmetry is a circle for the case $n=1$, an ellipse for the case $n=2$, and a pear shape for the case $n=3$. Models of these shapes were molded of Plasticine and glass models of them were made.[3] Spark pictures of some of these models were taken. Inferences drawn from these pictures must be qual-

[3] These models were made by L. Testa of NBS glassblowing shop.

ified by the fact that the models were about three times larger than the real waterdrops and that they were photographed in the center of the shock-tube window rather than at the extreme left of it as the real waterdrops were so that the optical system was not equivalent.

A high light could be seen in the picture of the glass ellipsoid when viewed through the end and when viewed through the side; it was, in each case, less symmetric than the high light in the picture of the glass sphere. The high light in the picture of the glass ellipsoid that was viewed from the side contained a dim structure somewhat similar to the prongs of light seen on the high lights in pictures of waterdrops that had been struck by an air shock, but it was very much less pronounced. A very dim pinpoint high light that had no structure could be seen in the enlarged end of the pear shape in a picture of this glass model that was viewed from the side; an end view of the glass pear-shaped model was not made. Very little can be concluded from the pictures that were taken of these models; however, a calculation of the period of vibration for the 2.7-mm-diam waterdrop using eq (25) gave the result: for $n=2$, $\tau_2=0.014$ sec; for $n=3$, $\tau_3=0.007$ sec. Because the appearances that were observed in the high lights of waterdrops that were struck by air shocks were all realized in times of less than 100 μsec, it is out of the question to ascribe their existence to oscillations of the waterdrop to these shapes.

In the spark picture of the opaque spherical model that was made of Plasticine, there was no high light, but in the spark picture of the spherical model that was made of glass there was a central pinpoint of light. That the high light is formed by transmitted rather than by diffracted light can be inferred from this observation; the inference must be qualified by the fact that the optical system was not equivalent. If the observed high lights are produced because the waterdrop acts as a lens to the light from the spark, a sharp circular pinpoint of light will form at the focus of the water sphere if the sphere is essentially undeformed. Two modifications of the water sphere that would be capable of causing prongs of light at its focus are the existence of surface ripples and changes in the density of the water of the drop. Either one or both of these disturbances could be caused by the air-shock-waterdrop collision. The passing of the air shock over the waterdrop could conceivably result in microscopic ripples on the surface of the waterdrop; it is also possible that a pulse of compression may be initiated in the waterdrop over the time interval from the first instant that the air shock strikes the center of the windward face of the drop until it passes the center of the leeward face. It would be very difficult to distinguish between these two possibilities even with glass models that were the same size as the waterdrops and that were photographed in the same optical system.

The existence of some structure on the high light of the waterdrop shown in figure 7, picture 1′, indicates that the effect can be produced by ripples alone. This waterdrop was only disturbed to the extent of having just broken away from the hypodermic needle and of just having passed through the hole in the top of the shock tube. It would seem that the possibility of density differences in this drop is remote in comparison with the possibility of surface ripples which should have formed when the residue of the stem of water that was produced as the drop broke away from the hypodermic needle was drawn into the drop under the force of surface tension. The structure on drops that were struck by air shocks is very much more pronounced, however, especially at times after the collision that were of the order of 20 μsec. This could be construed to indicate that density differences may play some role.

The pictures in figure 7 show that while the waterdrop appears to be quiescent during the first 100 μsec after the air-shock-waterdrop collision, it is responding to the collision blow.

4.3. Windward Face Remains Spherical; Leeward Face Becomes Flat

Although the windward face of the 2.7-mm-diam waterdrop was essentially undeformed at the end of nearly 100 μsec after the collision with an air shock that had a Mach number of 1.3, the leeward face appeared flat at the end of 93 μsec after the collision. See figure 3. It has been pointed out [7,8] that a large air bubble rising in water is spherical on top, that is, has a spherical leading surface in the direction of motion, but is flat on the bottom. Taylor [7] has postulated that this shape results as the pressure due to the hydrodynamic flow around the bubble exactly neutralizes the variations in pressure due to gravity at all points on the upper surface of it. The Bernoulli equation is

$$p+\tfrac{1}{2}\rho v^2+\rho g z=\text{constant}, \qquad (26)$$

where p is the pressure, v is the flow velocity, ρ is the density of the liquid, and z is an axis of the coordinate system which is taken in the direction of rise through the liquid. The stagnation point of the flow of liquid around the rising bubble is at the center of its spherical leading surface. Here z is at a maximum but v is zero. If points are considered along any of the streamlines that run radially from the stagnation point around the surface of the bubble, z decreases and v increases. Taylor [7] thought that the net effect is that the second and third terms of eq (26) cancel so that the pressure along a streamline remains constant, that roughly the flat bottom of the bubble occupies the plane at which the pressure on the upper surface is equal to the pressure at the same level far from the bubble, and that surface tension plays no part in producing the observed shape.

Taylor [7] applied the same theory to the shape that should be assumed by a liquid drop in a high speed air blast for the case that the surface of the drop does not disintegrate. On this picture the forces acting to accelerate the waterdrop in the direction of the airflow replace the force of gravity. It is noteworthy in this connection that there is no

apparent drift of the waterdrop during the time interval during which the flattening of the leeward face of the waterdrop is observed. See figure 6, A and B. It is possible, however, that a very small drift does occur.

4.4. Formation of Mist

In deducing a mechanism for the origin of the mist which is observed downstream from the leeward face of fragmenting waterdrops after the air-shock-waterdrop collisions, it is essential to account for all the details that can be observed. The mist appears to emanate from the leeward face of the waterdrop, while the remaining portion of the waterdrop itself remains essentially intact. The mist may, however, actually form on the windward face of the drop and be carried around the drop by the airflow, or it may form at the periphery of the drop between the windward and leeward faces. Viewed from the side, the mist structure has its greatest density at the top and bottom for relatively short periods after the air-shock-waterdrop collision. If a hoop or circle of fringe is viewed edge-on, the observer sees a straight line of fringe with maximum density at either end. In the light of these observations the cone-shaped structure of mist that forms downstream from a fragmenting waterdrop is a hollow funnel. In the case of the 2.7-mm-diam waterdrop, no mist was produced up to 100 μsec after the collision when the Mach number of the shock was 1.3. See figure 3. As the air-shock velocity was increased, the mist formed sooner and more copiously; as the waterdrop diameter was decreased the mist also formed sooner. In the following sections, possible sources of the mist are considered; in the final section an evaluation of the most probable of the sources is made.

a. Vaporization

The appearance of the water mist suggests the possibility of a hot-water-vaporization-to-form-steam mechanism. As soon as the air shock passes the waterdrop, the waterdrop exists in the airstream that is flowing behind the shock. The temperature in this airstream is considerably higher than the room temperature of the undisturbed air in front of the shock. For air shocks having Mach numbers of 1.3, 1.5, and 1.7, the temperature in the airstream behind the shock is 84° C, 123° C, and 165° C, respectively, if the initial temperature was 27° C. See table 1. There is, furthermore, an elevated temperature at the stagnation point of the airflow in the center of the windward face of the waterdrop. This temperature was found in section 2.6 to be 95° C when the air shock had a Mach number of 1.3. In section 2.5.a, the pressure at this point for the same air-shock velocity was found to be 1.99×10^6 d/cm^2 (1.96 atm). Because water boils at 100° C at 1 atm, no vaporization would be expected on the windward face in terms of an equilibrium picture. On the leeward face, the pressure is reduced only to 1.69 atm and the temperature on this face is 80° C when the air shock has a Mach number of 1.3. See sections 2.5.b and 2.6. Consequently, in terms of the equilibrium picture, no vaporization would be expected on this face either. Although equilibrium conditions have certainly not been reached in the order of 100 μsec, which is the time after the air-shock-waterdrop collision at which mist was first seen, it seems doubtful if a hot-water-to-form-steam mechanism is the source of it.

To determine whether or not clouds of mist form behind a waterdrop that is falling through a layer of hot air, high speed moving pictures were taken of incidents of this kind. Glass windows were installed in the ends of a heavily insulated electric oven which contained a small electric fan to distribute the hot air. Light from a carbon arc was passed through a collimating lens and then through the windows of the oven. Drops of distilled water were allowed to fall from the large-bore hypodermic needle through a hole in the top of the oven located at the focal point of the lens of the 15,000-frame/sec camera that was used to take pictures of the falling drops. The camera was placed at the end of the oven opposite the arc light so that the pictures of the falling waterdrops were shadowgraphs.[4]

Moving pictures of waterdrops were taken both after a short and after approximately the longest possible distance of fall through the oven (6.1 in.) at oven temperatures of about 80° C, 125° C, 160° C, and 260° C. Still enlargements of consecutive frames from the movie films show that no cloud of mist was trailing the falling drop at any of the oven temperatures for which observations were made either for the short or for the long distance of fall through the oven. Because the time of fall of the waterdrops through the oven was of the order of tenths of a second, it was concluded from these pictures that the time required for heat transfer to and subsequent vaporization of water from the surface of a falling drop is too long to account for the formation of the water mist which was detected 100 μsec after a waterdrop was hit by an air shock that had a Mach number of 1.3. Consequently a hot-water-vaporization-to-form-steam mechanism based on the elevated temperature of the air that is flowing past the waterdrop after it has been struck by the air shock cannot be a correct explanation of the water mist that emanates from it.

b. Mechanical Origins

The circumstances under which the water mist is formed suggest that the mechanism by which it is produced is mechanical. Mechanisms in this category are that by which mist is produced as a result of sound waves, the stripping off of a surface layer of water by the rapid airflow around the drop, and the breaking of the crests of surface waves. These possible mechanisms are discussed and evaluated below.

(1) *Sound Waves as a Source of Water Mist.* It is known that liquids can be converted to mist by sound waves [9]. In the case of liquids of low viscosity, at a liquid-air interface, the forces in play drive the liquid into the air in the form of a spray

[4] Lee Dunlap and W. K. Stone assisted in these experiments.

of minute droplets to form a fog [9]. Because sound waves may be initiated in a waterdrop that has been struck by an air shock, it is possible that the mist that is carried downstream from waterdrops that have been struck by an air shock could have this origin.

Two experiments were made by Martin Greenspan and Max Swerdlow of the Bureau, to observe directly the reduction of a liquid to mist by means of ultrasonic waves. Drops of ethyl alcohol were placed on the bottom of a glass vessel which was then set into rapid vibration by an oscillating crystal. Clouds of white fog rose from the drops of alcohol and the small drops of alcohol emitted mist more copiously than the large drops did.

A second demonstration of the effect was made using a powerful Crystalab Ultrasonorator. This instrument consists essentially of a crystal that is driven at high frequency while it remains submerged in an oil bath. A beaker containing a small amount of water was placed so that the bottom of it was in contact with the surface of the oil. When the crystal was set into oscillation, a small and rapidly fluctuating mound of water rose above the surface of the water in the beaker. It gave the appearance of what might be expected if a water nozzle, located below the surface of the water in the beaker and pointed toward the surface, were delivering a jet of water through the surface. Periodically dense clouds of mist rose from the head of the water jet. A moving picture was taken of the phenomenon. The fluctuating action of the jet on the surface of the water can be seen in a still enlargement of consecutive frames from this movie. Mist was thrown off wildly in various directions as the jet of water thrashed about. To establish whether this mist is produced mechanically, or as a result of local heating, a small quantity of Ascarite was added to the water in the beaker. A piece of pink litmus paper that was held in the mist underwent a definite though slight color change. This would have been impossible if the mist had consisted of distilled water. However, it seems that the presence of hydroxyl ion in the vapor above the water could be accounted for as a result of cavitation in the water itself [5] which destroys the conclusiveness of this evidence that the origin of the mist was mechanical.

In the case of the evolution of water mist from waterdrops after they have been struck by an air shock, it seems that the actual process could consist of a spalling of water from the free surface of the leeward face of the drop after a pressure pulse reverses there in tension because water, except under very special conditions, has very little tensile strength. On the other hand, it could consist of the breaking of the crests of waves that may be produced by the successive reflection of an initial pressure pulse from the two faces of the drop. These two possibilities are discussed in the following paragraphs.

The spalling mechanism is briefly as follows [10]. When a pressure pulse of steep front reverses in tension at a free surface, interference occurs at first between the incident compressional wave and the reflected tension wave. Tension increases as the reflected wave moves away from the surface. When the medium in which the wave is moving is no longer able to withstand the tension, fracture occurs, and a scab or thin layer is thrown off the free surface. Because water has such low tensile strength, this layer, in the case of a water scab, should be vanishingly thin. It is possible for a second scab to form as the remainder of the pressure pulse reflects in tension from the fresh surface produced by the formation of the first scab. In this way, multiple scabbing can be accounted for [11]. These scabs or thin sheets of water would break up into droplets of very small size [12].

Compressional waves which may be initiated on the windward face of the waterdrop at the instant that the air shock strikes it would reflect in tension from the leeward face of the drop which is a free surface. After the reflected tension wave returned to the windward face of the drop, it would reflect there as a compressional wave because the windward face is also a free surface (reflection occurs with change of sign at a free surface). The process of successive transits of the waves through the waterdrop at the speed of sound in water, and of their successive reflection, would continue until the waves were damped out. The attenuation of sound in water is low.

It has been shown that the thickness of an air shock that has a Mach number of 1.7 is 0.000031 cm. Because this is approximately 1/10,000 the diameter of the waterdrop, the initiation of a pulse of compression in the waterdrop is possible. The amplitude of it may not be large. However, there is no clear evidence of mist formation up to 100 μsec after a 2.7-mm-diam waterdrop has been struck by an air shock having a Mach number of 1.3, although the time that is required for a pressure pulse to make one trip through a 2.7-mm-diam waterdrop at the speed of sound in water is about 2 μsec. There does not seem to be an answer to this discrepancy other than the observation that it is hard to decide just when mist can first be detected in the spark pictures of waterdrops that have been struck by air shocks and that there are periods of quiescence even in the case where water is exposed to ultrasonic waves.

If reflecting waves are the cause of the mist, there should be a more or less even density of mist formation over the whole leeward face of the waterdrop and the mist structure that forms downstream from the leeward face should have its greatest density in the center when it is viewed from the side. However, it can be seen from the spark pictures that for relatively short times after the air-shock-waterdrop collision, the greatest density of the mist structure is not at the center but at the top and bottom as the mist structure is viewed from the side. This certainly seems to indicate that the mist structure is hollow which would lead to the conclusion that the mist is not being formed on the leeward face but, instead, is being formed on the windward face and is being carried around the drop by the airflow or is being formed at the periphery of the drop between the windward and leeward faces. Furthermore, if the reflection of pressure waves as tension waves at

[5] Suggested by Virginia Griffing of the Catholic University.

the leeward face of the drop is the source of the mist, the greatest density of mist formation should occur at short times after the air-shock-waterdrop collision, that is, before the traveling wave has time to become attenuated. However, from the spark pictures of fragmenting waterdrops it appears that the density of mist production increases with time elapsed since the collision incident until quite long periods of time have elapsed. For these reasons it seems very doubtful that the observed water mist is produced from water scabs formed at the leeward face of the waterdrop as a pressure pulse reverses in tension.

It is possible that a pressure pulse may be initiated but that the ultimate effect of its subsequent reflections from the faces of the waterdrop may not be to spall mist from the leeward face of the drop. The successive reflection of the pressure pulse may result in waves on the surface of the drop; the crests of these waves may break, or may be whipped off by the rapid airflow around the drop. Because such waves could form on the windward face of the waterdrop, this view of the function of the pressure pulse, if one is formed in the waterdrop, would be in agreement with the observation that the mist density behind the leeward face is not uniform, but is greatest at the top and bottom when the fragmenting waterdrop is viewed from the side. On this picture the formation of the mist would also be delayed until the waves were set up on the surface of the drop. This would be in agreement with the observation that the mist does not form immediately after the air-shock-waterdrop collision.

(2) *Surface Waves as a Source of Water Mist.* It was pointed out in the preceding discussion that waves may be produced on the surface of a waterdrop as a consequence of a successively reflecting pressure pulse which may have been initiated by the air-shock-waterdrop collision and that these waves may break or that the crests of these waves may be blown off by the rapid airflow around the drop to produce the water mist. It is also possible that surface waves may be produced by the wind that is blowing out radially around the stagnation point in the center of the windward face of the waterdrop and that crests of these wind waves may break or be blown off.

Whatever may be their origin, surface waves certainly appear on the windward face of a waterdrop after it has been struck by an air shock and exists in the high-speed stream of air that flows behind the shock. The development of windward-face corrugations with time is shown in figure 9 for waterdrops that were struck by air shocks that had a Mach number of 1.5. For short times after the collision incident they are only rounded mounds on the surface as in figure 9, picture 2; later they become choppy or sharp-pointed waves as in figure 9, picture 4.

There is some evidence for identifying the waves seen in the profile of the windward face of the waterdrop in figure 9, picture 4, as wind waves. In general, in the presence of gravity two sets of waves are produced by a given wind velocity. It can be seen that very small ripples are superimposed on larger waves in the profile of the windward face of the waterdrop in figure 9, picture 4. The evidence can be further confirmed by calculating the ratios of the values of the allowed wavelengths that capillary waves should have under the experimental conditions and by noting if the observed wavelengths are in approximately this ratio.

The theory of waves produced by wind under the condition that surface tension and the field of gravity are both acting is known [13]. The case being considered here is that a freely falling waterdrop is struck by an air shock in a shock tube. The waterdrop is then accelerated downstream in the rapid airflow in the tube behind the shock. For this case the acceleration due to gravity is negligible in comparison with the horizontal downstream acceleration that, neglecting the drag of the flowing air, is due to the pressure difference between the windward and leeward faces of the drop. For this case the air-water interface is the windward face of the waterdrop and it is perpendicular to rather than parallel with the surface of the earth. The theory for this case is the same as that for waves produced by wind on a body of water under the condition that surface tension and the gravitational field of the earth are both acting. See Lamb, [13], chapter IX, Surface Waves, article 246.

It leads to the equations

$$c_m^2=\frac{2\sqrt{\rho_w-\rho_a}\sqrt{\alpha T}}{\rho_w+\rho_a}, \tag{27}$$

$$\lambda_m=2\pi\sqrt{\frac{T}{\alpha(\rho_w-\rho_a)}}, \tag{28}$$

$$\frac{c^2}{c_m^2}=\frac{1}{2}\left[\frac{\lambda}{\lambda_m}+\frac{\lambda_m}{\lambda}\right], \tag{29}$$

where c is the velocity of the waves, λ is the wavelength, T is the surface tension, ρ_w, ρ_a are the densities of water and of the air flowing behind the shock, respectively, α is the acceleration of the waterdrop in the airflow behind the shock, and the sub-m notation indicates the minimum value of the quantity.

For every value of $c^2/c_m^2>1$, there are two values of λ/λ_m, that is, there are two values of the wavelength as was noted above. Two values of these ratios given by Lamb [13] are: $c/c_m=1.2$, $\lambda/\lambda_m=2.476$ and 0.404; $c/c_m=1.4$, $\lambda/\lambda_m=3.646$ and 0.274. From these ratios, the equations for c_m^2 and λ_m, and taking the average value of α, the slope of the drift-velocity-against-time curve for the time interval up to 400 μsec to be 6×10^6 cm/sec^2 for the case that the Mach number of the shock is 1.5 (see fig. 6, C), and $\rho_a=\rho_2$ for the airflow behind shocks that have a Mach number of 1.5 (see table 1), it is possible to calculate the ratio of the wavelengths that should be observed on the windward face of the waterdrop shown in figure 9, picture 4. From eq (27)

$$c_m=\left[\frac{2\sqrt{1-0.00218}}{1.00218}\sqrt{72(6\times10^6)}\right]^{1/2}=203.6 \text{ cm/sec}$$

and from eq (28),

$$\lambda_m=\frac{2(3.1416)\sqrt{72}}{\sqrt{(6\times10^6)(1-0.00218)}}=0.02179 \text{ cm}.$$

By use of the ratios given above, when $c=244.3$ cm/sec, $\lambda_1=0.05395$ cm, $\lambda_2=0.008803$ cm, and when $c=285$ cm/sec, $\lambda_1=0.07945$ cm, $\lambda_2=0.00597$ cm. The calculated values of the wavelength, λ, are plotted against the values of the wave velocity, c, in figure 13. The measured wavelength of the coarse waves on the windward face of the waterdrop shown in figure 9, picture 4, is roughly 0.06 cm. From figure 13 the wavelength of the ripples between the coarse waves should be 0.0082 cm. Measurements indicate a value of 0.014 cm.

The evidence seems to indicate that surface waves do form, that two wave lengths exist as is to be expected from theory, and that the ratio of the wavelengths is roughly what should be expected from theory. Waves are observed on the windward face of waterdrops before the waterdrops are accelerated downstream. See figure 9, pictures 1 and 2. Wind waves can form in the absence of a gravitational field; under this condition, however, only one wavelength is to be expected.

(3) *Unstable Waves.* Taylor [7] (see also Lane and Green [14]) suggested that the formation of unstable waves might constitute a mechanism of fragmentation. The crests of the waves may blow off to form droplets. The diameters of the droplets produced in this way are likely to be of the same order as the wavelength of the most unstable wave. For high airflow rates, calculations based on this hypothesis produce much smaller values for the size of the droplets than are found experimentally. Taylor [7] has suggested that it is possible that the discrepancy may result from the fact that the air close to the fluid surface is moving slower than the air outside the boundary layer and is therefore less effective in producing waves.

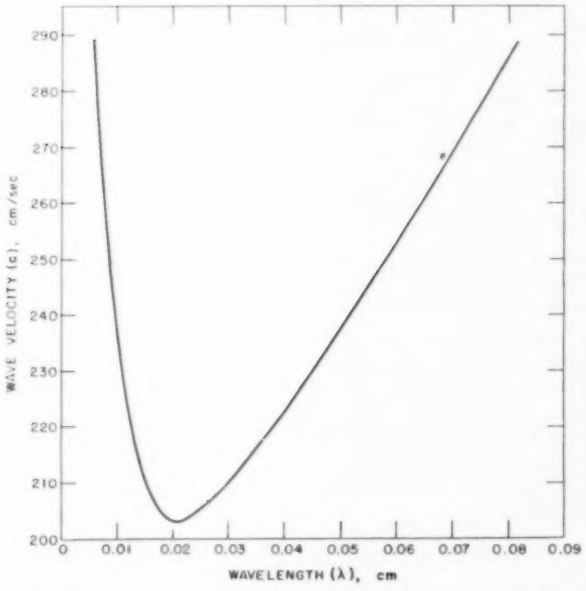

FIGURE 13. *Corresponding values of the wavelength and wave velocity for a water surface that is being accelerated at the average rate of 6×10^6 cm/sec^2.*

(4) *Stripping of a Surface Layer of Water by the Airflow.* Taylor [7] has considered the possibility that waterdrops may disintegrate in a high-velocity airstream by means of the stripping off of a surface layer of water which then breaks up. Air is flowing radially from the stagnation point on the windward face to the equator of the waterdrop midway between the windward and leeward faces of it. The motion of the air sets the surface layer of the water on the windward face of the drop into motion. This thin moving layer of water spills off the drop at the equatorial belt that separates the windward and leeward faces of the drop and breaks up to form the mist that is observed downstream from the leeward face.

It can be shown (see appendix A) that the total efflux or total loss of volume from the boundary layer per unit time is

$$\frac{dV}{dt}=4\pi r\left(\frac{\rho_a}{\rho_w}\right)^{1/3}\left(\frac{\nu_a}{\nu_w}\right)^{1/6}\sqrt{U_2-W}\sqrt{\nu_w}\sqrt{x} \qquad (30)$$

where ρ is the density, ν is the kinematic viscosity, U_2 is the velocity of the airflow, W is the drift velocity of the waterdrop, and x is a distance along a radius of the windward face of the waterdrop measured from the center of the windward face. The sub-a notation refers to the air and the sub-w notation refers to the water. Taylor [7] used eq (30) to develop an expression that was intended to give the decay of a lenticular drop from the time that it had undergone maximum flattening (see section 4.6) to the time of complete disintegration by means of efflux of liquid at the periphery between the windward and leeward faces and found the condition that the drift velocity, W, should have reached the airflow velocity, U, at the time that complete disintegration was accomplished. He later [14] modified this conclusion. At the time that fragmentation of the 2.7-mm-diam waterdrop was essentially complete, the drift velocity was about 33 percent of the airflow velocity when the Mach number of the shock was 1.5, and about 50 percent of the airflow velocity when the Mach number of the shock was 1.7. See section 4.7. The condition that the waterdrop should acquire the airflow velocity before fragmentation is complete may possibly be realized when the fragmentation of waterdrops in the airflows behind shocks having Mach numbers greater than 1.7 is investigated. Lane and Green [14] report that a 0.5-cm drop of dibutyl phthalate disintegrating in a 3.4×10^4 cm/sec air blast had attained 90 percent of the airflow velocity at the time that the drop was essentially completely fragmented.

Results of the present investigation seem to indicate that a marked reduction in the drag force of a waterdrop occurs between 100 and 200 μsec

after the air-shock-waterdrop collision (see section 4.7). The fragmentation mechanism may be more complicated than was assumed by Taylor [7] when he wrote the expression that was intended to give the decay of a lenticular drop from the time of maximum flattening to the time of complete disintegration by means of the efflux of liquid at the periphery between the windward and leeward faces. It is possible that instead of remaining in the form of a water disk during the disintegration process the water disk is converted to a ring of water when a hole forms at the center of the windward face and that eventually the water ring segments into a chain of water beads. To evaluate surface-layer stripping as a possible mechanism for liquid-drop fragmentation by determining what the drift velocity should be at the time that fragmentation is complete, it is necessary to determine experimentally whether these large changes in the form of the liquid mass that remains of the drop actually do take place. If they do occur, it will be necessary to apply the surface layer stripping mechanism to these forms of the water mass in an equation designed to trace the complete decay of the liquid drop to mist. For a further discussion of this point, see section 4.7. However, there may be a Mach number of the air shock considerably higher than 1.7 for which the airflow behind the shock would have a sufficiently high velocity to reduce the waterdrop radius to zero by a surface-layer stripping mechanism before the complication of hole formation or of segmentation of the remaining water ring would have time to occur.

(5) *Turbulence as a Source of Mist.* Potential flow exists around the waterdrop immediately after the air shock has struck it. This means that there are no vortices in the flow and that the stagnation pressure at the center of the leeward face is equal to the stagnation pressure at the center of the windward face. Vortices will form, however, in a time interval of the order of 100 μsec after the air-shock-waterdrop collision and as the vortices form, the pressure on the leeward face will drop. The vortices themselves may be a source of the water mist, that is, they may gradually eat away the leeward face of the waterdrop.

Because the direction of the airflow in the vortices is toward the equator of the drop, the mist that may be produced as a result of the vortex motion would be carried back toward the equator of the drop before it entered the airflow downstream from the leeward face. This would require that the mist cone should be a hollow funnel as is observed.

The time that is needed for the formation of the vortices would require that there should be a time interval after the air-shock-waterdrop collision in which no mist is formed. This is the case where the air shock had a Mach number of 1.3, but for this air-shock velocity there is no evidence of turbulence in the mist structures that form downstream from the leeward face of the fragmenting drops for any time after the collision incident at which pictures were taken. See figure 4, pictures 1 through 6. On the other hand, in the case of collisions of waterdrops with air shocks that had a Mach number of 1.5, there is already a well-developed mist-cone in pictures that were taken at about 85 μsec after the collision incident (see fig. 10) and in the case of collision of a waterdrop with an air shock that had a Mach number of 1.7 there is a mist structure behind the leeward face of the drop at the end of about 55 μsec. See figure 12. Furthermore, in pictures of waterdrops that were taken at time intervals less than 100 μsec after the waterdrops were struck by air shocks that had Mach numbers of 1.5 and 1.7, there was no evidence of swirling in the mist structure downstream from the leeward face, but in pictures that were taken at the end of longer time intervals after the collision of a waterdrop with air shocks that were moving at these velocities, strong evidence of swirling exists.

These observations seem to indicate that mist can be produced in the absence of vortices, that is, that the mist has an origin other than the vortices. The existence of vortices may, however, contribute to the production of mist after they form. This is in agreement with the observation that the mist density is greater for comparable times after the air-shock-waterdrop collision as the air-shock velocity was increased.

(6) *Most Probable Sources of the Water Mist.* From a consideration of the evidence for and against the various postulated mechanisms for mist production that have just been given, it seems that the most likely mechanisms are those which take into account the effect of the rapid airstream on the waterdrop. The mist that is observed is probably made up of contributions from the whipping off or from the breaking of the crests of waves, from the spill-off at the equatorial belt of the moving boundary layers on the windward face, and from the stripping of water from the leeward face by the vortices that form there in the airflow. It seems unlikely that one of these mechanisms operates to the complete exclusion of the others.

4.5. Radial Water Flow

The start of evolution of water mist from the leeward face of a waterdrop after it has been struck by an air shock is accompanied by the first evidence of a radial flow of water from the drop. The thin sheet of water that is just beginning to move out radially at the equator of the drop appears only as a protrusion from the upper and lower surface of the silhouette of the drop as it is seen in the spark pictures. The gradual development of it over a period of about 70 μsec can be seen in figure 3, pictures 1 through 8, for the 2.7-mm-diam waterdrop after collisions with air shocks that had Mach numbers of 1.3.

To determine the cause of this radial flow, it is necessary to account for all the variations of it with the conditions under which it forms. From the pictures that were just referred to, it is seen that (A) when it is produced as a result of collision of a waterdrop with an air shock it moves out of the drop on a plane that extends through the center of the drop and that is perpendicular to the direction of motion of the air shock that struck the waterdrop. Com-

parison of spark pictures of the large and of the small waterdrop at various times after the air-shock-waterdrop collision shows that (B) the radial flow forms sooner for a small than for a large waterdrop. When the Mach number of the shock is 1.3 the formation time for the 2.7-mm-diam waterdrop is of the order of 100 μsec, but for the 1.4-mm-diam waterdrop it is much less than 75 μsec, because for this size of waterdrop the radial flow is already well developed 75 μsec after the air-shock-waterdrop collision. A comparison of the size of the radial flow with the diameter of the residue of the drop seems to indicate that (C) the radial flow may be larger the smaller the diameter of the drop.

This interesting phenomenon also results if liquid drops are suspended in a sound field. It is very evident, for example, in pictures taken by Hanson, Domich, and Adams [15]. In this case (A′), the radial flow forms perpendicular to the direction of the sound field. For drops of methyl alcohol of different sizes which Hanson, Domich, and Adams [15] suspended in a sound field, only drops having a diameter of 0.0334 cm or less, have the radial flow. The high light in the drops that have the radial flow is completely extinguished whereas the larger drops that have no radial flow have distinct high lights. It is noteworthy that the limiting size of drop that will develop a radial flow in the sound field that was used by Hanson, Domich, and Adams is lower for drops of water than for drops of methyl alcohol because a 0.0315-cm waterdrop suspended in the sound field has a distinct high light and no radial flow. There is no way of knowing (B′) the rate at which the radial flow formed on these drops. However, (C′) among the drops of methyl alcohol that have a diameter of 0.0334 cm or less, the smaller the drop is, the more extensive is the radial flow. A 0.0168-cm drop has a large radial flow, a 0.0334-cm drop has a small radial flow, and 0.0511- to 0.0793-cm drops have no radial flow. Although the sound frequency is not indicated on the picture given by Hanson, Domich, and Adams [15], it appears probable from their discussion that a 50-kc field was used. After these drops were struck by an air blast that had a velocity of 60 ft/sec, the radial flow was blown off the drop and existed as a mist structure downstream from the leeward face of it [15]; this appears to be evidence to indicate that the water mist, which was discussed in section 4.4, had its origin at least partly in protrusions of one kind or another that formed on the surface of the drop. The cause of the radial flow is undoubtedly the same regardless of whether it occurs as a result of collision of a drop with an air shock or as a consequence of supporting a drop in a sound field.

The lowest pressure that occurs around a sphere that is located in an airflow exists in a belt around it that separates the windward from the leeward face. The pressures that were found by Fage [4] to exist at all points from the center of the windward face to the center of the leeward face for a 6-in.-diam sphere in a 35 ft/sec airflow are given in figure 14, B. From these data the low-pressure belt be-

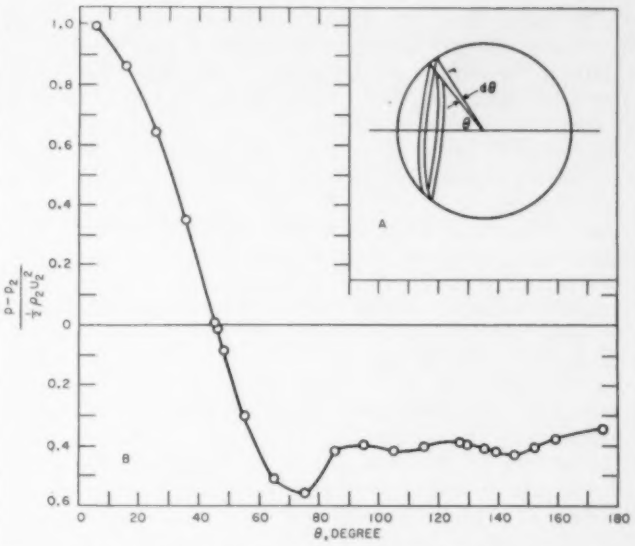

FIGURE 14. *A, Differential area; B, distribution of pressure around a 6-in.-diam sphere in a 35-ft/sec airflow.*

Reynolds number 110,000. Data of Fage [4].

tween the windward and the leeward face exists from 60° to 85°. It can be expected that the high pressures that exist on the windward and leeward faces of a deformable water sphere during the period when potential flow occurs, that is, when the stagnation pressure on the leeward face is the same as the stagnation pressure on the windward face, will drive water out through the low-pressure belt. This water flow, however, occurs throughout the drop and is not restricted to a very narrow zone at the equator. These exterior pressure differences are the cause of the gradual flattening of the drop, which is discussed in section 4.6, but they are not the cause of the very localized thin circular sheet of water that moves out of the equatorial belt of the drop.

It is shown in section 4.6 that a memory of some kind may exist in the water of the drop. This memory may be a pulse of compression. It is seen from figure 3 that an air shock that is moving at supersonic velocity can collide with a waterdrop without producing an immediate distortion of it. However, a layer of water on the windward face of the drop may be given an almost instantaneous acceleration at the instant that the shock wave passes over the drop, that is, a pulse of compression could be initiated. This pressure pulse would move at the speed of sound in water from all points on the hemispherical windward face through the geometrical center of the drop and would be reflected as a tension pulse from the mirror-image points on the hemispherical leeward face of the drop. The center of the drop which is the point of intersection of the reverberating pulse, may be the point where maximum pressure amplitude occurs because maximum superposition occurs there.

The radial flow of water that moves out of a waterdrop that has been struck by an air shock, comes out

on a plane that is perpendicular to the direction in which the air shock was moving and that runs through the center of the drop. Likewise, the radial flow that comes out of a drop of methyl alcohol that is suspended in a sound field also moves out on a plane that is perpendicular to the direction in which the sound pulses strike the liquid sphere and that runs through the center of the drop. This is in agreement with observations (A and A′) cited above. The maximum pressure that would result from superposition of waves would develop sooner in a small waterdrop than in a large waterdrop because the time required for the pressure pulse to make a trip across the drop would be shorter. This would also be the case for pressure pulses set up in waterdrops suspended in a sound field. This is in agreement with observation (B) cited above. Finally, the pressure that would be developed in the center of the drop as a result of collision of the drop with an air shock moving at a given velocity or as a result of a sound field of specified intensity would be capable of driving a radial flow of water a certain distance. Compared with the diameter of the drop, this distance would be larger for a small drop than for a large drop. This is in agreement with observations (C and C′) cited above. If the pressure developed is incapable of driving a water flow to a distance larger than the diameter of the drop itself, no flow would be observed. This is in agreement with the observation that in the case of drops of methyl alcohol that were suspended in a sound field, no radial flow at all was observed on the largest of the drops. To make a comparable statement for waterdrops that were struck by air shocks, it would be necessary to observe the behavior of waterdrops that had a diameter larger than 2.7 mm after they were struck by an air-shock that had a Mach number of 1.3 or to observe the behavior of the 2.7-mm-diam waterdrops after collision with air shocks that have Mach numbers less than 1.3.

On the other hand, it is possible that this radial flow may be produced by instability on the surface of the drop. The airflow, which follows the air shock, blows against the windward face of the drop and water waves are initiated by it. Similarly, there is a periodic movement of air past a liquid drop that is suspended in a sound field and this air movement could have the same effect. The stability of waves on the surface of a liquid drop is a function of their latitude on the sphere with respect to the stagnation point in the center of the windward face which may be considered as a pole. The line of maximum instability is at the equator of the drop and it is possible that surface waves may grow to a very high amplitude at the equator to give the appearance of a radial flow. This would be in agreement with observations (A, A′) cited above.

The growth of an unstable wave on the surface of a spherical body is mathematically an extremely difficult problem. This is especially the case at the later stages of the growth of instability when the radial flow develops. However, from stability theories on simple models, it is to be expected that waves of small wavelength, produced as the result of eigenvibrations, are likely to be associated with small bodies and that, under many circumstances, waves of small wavelengths are more unstable than waves of large wavelengths [16]. Small bodies also respond readily to the influence of an external unsteady field because of their small inertia. This evidence may provide an explanation of observations (B) and (C, C′) cited above.

4.6. Flattening of the Waterdrop in the Airflow

The flattening of the waterdrop perpendicular to the direction of the airflow in the shock tube is the result of the pressure difference that exists around it in the airflow behind the shock. Burgers [17] has accounted for the flattening with time by use of a simple model, namely, that at the instant that the air shock has just passed the waterdrop streamlines converge at the center of both the windward and leeward face of it and the pressure at the center of each of these faces is the stagnation pressure. See appendix B. The outward displacement d at the equator of the drop and perpendicular to the direction of the airflow is found to be given by

$$d=\frac{1}{3}\frac{\Delta p}{\rho r}t^2 \tag{31}$$

where Δp is the pressure difference between either the windward- or the leeward-face stagnation point and points along the equator of the drop, r is the drop radius, ρ is the density of the liquid of the drop, and t is the time. The increase in the diameter of the waterdrop perpendicular to the direction of the airflow is $2d$.

From eq (31) it can be seen that the smaller the waterdrop is, the larger is the increase in its diameter perpendicular to the direction of the airflow for any given time after the air-shock-waterdrop collision. This is in agreement with observation. See section 3.1.b. It appears that with a constant pressure difference between the poles and equator of a liquid sphere, the pressure gradient inside the sphere becomes larger with decreasing radius so that the acceleration of the water also becomes larger.

The curves of the equatorial diameter (maximum diameter) of the 2.7-mm-diam waterdrop at time intervals up to 200 μsec after the collision incident calculated by use of eq (31) for the three air-shock velocities for which experimental data were obtained are shown in figure 5 with the empirical curves. For the case that the Mach number of the shock was 1.3, the calculated curve lies above the empirical curve; for the case that the Mach number of the shock was 1.5, the calculated curve lies below the empirical curve; for the case that the Mach number of the shock was 1.7 the calculated curve lies very much below the empirical curve. In calculating points for the theoretical curves, the value of p_t, the stagnation pressure at the center of the windward face, was used for Δp. This is the very highest pressure that could be used for Δp. Actually, it may be a larger value than should be used and may account for the fact that the calculated curve for

the case that the Mach number of the shock was 1.3, the shape of which is closely similar to that of the empirical curve, lies above the empirical curve. However, if some fraction of p_t were used for Δp, the calculated curves for the cases that the Mach number of the shock was 1.5 and 1.7 would lie even further below the respective empirical curves. This observation leads to the thought that it may not be possible to explain the flattening of the waterdrop wholly in terms of the pressure difference which is set up between the poles and equator of the drop as a result of the airflow around it.

One possible explanation of the discrepancy may be that the waterdrop remembers the collision. If this is the case, the memory is a function of the air-shock velocity, and the memory is greater the higher the air-shock velocity is because the curves calculated by use of eq (31) have an increasingly poorer fit to the empirical curves for the case that the Mach number of the shock is 1.5 and 1.7, respectively. The memory may be a pressure pulse that is initiated in the water of the drop as the air shock passes and that subsequently undergoes successive reflection from the windward and leeward faces of the drop. As has been noted, because both faces of the waterdrop are free surfaces, this pulse will always reflect as a tension pulse from the leeward face and will always reflect as a pressure pulse from the windward face. In this way the value of Δp could become larger than p_t in air-shock-waterdrop collisions where a shock effect occurs.

There is another possible explanation. Attempts to calculate the acceleration of the 2.7-mm-diam waterdrop in the airflow behind shocks for which the Mach number is 1.5 (see section 4.7) indicate strongly that a central hole may form through the water disk to which the waterdrop flattens. The gradual development of this hole (see section 4.8) may account for an increase in the observed diameter of the water disk in excess of what can be accounted for by the pressure difference between the poles and equator of it alone.

4.7. Drift Velocity

Measurements of the distance from the edge of the fiducial marker to the leading edge of the waterdrop at various time intervals after the air-shock-waterdrop collision were made for three air-shock velocities. The fact that the waterdrops fell from the tip of the hypodermic needle with a slight scatter, and that the hypodermic needle itself was adjusted from time to time to insure that the waterdrops would fall through the hole in the floor of the shock tube, introduced a considerable amount of variation in the drift distances. It was arbitrarily decided that all negative values of drift should be recorded as zero drift and that wherever two consecutive spark pictures showed a zero or a negative value of drift all positive values for earlier periods of time should be disregarded. The measured distances of drift at various time intervals after the air-shock-waterdrop collision are plotted against the time elapsed since the collision in figures 6,A and 6,B for the case that the Mach number of the shock is 1.5 and 1.7, respectively. The slope of the drift-time curves of figures 6,A and 6,B were determined at 100-μsec intervals and these values, which are the drift velocities, are plotted against the time elapsed since the collision in figure 6,C. From figure 6,C it can be seen that the slope of the drift-velocity-against-time curve increases as the air-shock velocity increases. This is logical because the velocity of the airflow behind the shock is higher the higher the air-shock velocity.

From figure 6,C and table 1 it can be seen that 750 μsec after the air-shock-waterdrop collision, the drift velocity of the 2.7-mm-diam drop is about one-third of the airstream velocity for the case that the Mach number of the shock was 1.5. Reference to figure 10, picture 6, shows that at approximately this time after the air-shock-waterdrop collision the 2.7-mm-diam waterdrop was almost completely reduced to mist. Also, from figure 6,C and table 1 it can be seen that 600 μsec after the air-shock-waterdrop collision the drift velocity of the 2.7-mm-diam waterdrop is approximately one-half the airstream velocity for the case that the Mach number of the shock was 1.7. Reference to figure 12, picture 6, shows that 594 μsec after the air-shock-waterdrop collision the 2.7-mm-diam waterdrop is essentially a trail of mist. These observations show that the waterdrop does not acquire the airstream velocity before fragmentation is complete. This condition is more nearly realized when the Mach number of the shock is 1.7 than when it is 1.5. It may be found to be true for Mach numbers of the shock higher than 1.7. See section 4.4.b.

The slope of the curve of drift velocity plotted against the time elapsed since the air-shock-waterdrop collision is the acceleration given to the waterdrop. It is possible to calculate the acceleration for comparison with the observed slopes. In the case where there is relative accelerated motion between an object and a fluid there is an apparent change in the mass (M) of the object. The apparent addition to the mass (M) of the object is (M′) and in this paper is referred to as the additional mass. The force acting on the object is given by $(M+M')(dU/dt)$ where U is the relative motion between the object and the fluid. See reference [13]. The force on a water sphere that is moving in an infinite body of air is, assuming potential flow,

$$F=\frac{2}{3}\pi\rho_a r^3\alpha+\frac{4}{3}\pi r^3\rho_w\alpha, \tag{32}$$

where ρ_a, ρ_w are the densities of the airstream and of water, respectively, r is the radius of the sphere, and α is its acceleration. See reference [13]. The force can be evaluated from the distribution of pressure around a sphere in an airflow. Fage [4] has measured this pressure distribution for a 6-in.-diam sphere when the airflow velocity was 35 ft/sec. A graph of his measured values of the pressure on the sphere, p, above the free-stream pressure, p_2, is given in figure 14, B. The Reynolds number for his measurements was 110,000. Because the Reynolds numbers for the 2.7-mm-diam waterdrop in the flow

behind air shocks that had Mach numbers of 1.7, 1.5, and 1.3 were 89,000, 61,000, and 35,000, respectively, the pressure distribution around the waterdrop will be most nearly like that found by Fage [4] for the case that the Mach number of the shock was 1.7. However, the variation of the pressure distribution over this range of the Reynolds number should not be important. From the data of Fage [4], it appears that the minimum in the curve at 75° tends to be less marked as the Reynolds number is reduced. For the purpose of evaluating the acceleration of the waterdrop in the airflow behind a shock, it was assumed that the pressure follows the experimental curve of figure 14, B to 60°, that the minimum in the curve at 75° is absent, and that the pressure is constant over the remainder of the sphere from 60° to 180°. See appendix C. The total force on the sphere found by use of these assumptions is $0.244\ \pi r^2\rho_2 U_2^2$ where r is the radius of the sphere and ρ_2, U_2 are the density and the velocity of the airflow, respectively. Equating this to the force on a sphere in terms of its acceleration, α, given by eq (32) yields

$$\alpha=\frac{0.244 U_2^2\rho_2}{\frac{2}{3}\rho_2 r+\frac{4}{3}\rho_w r}. \tag{33}$$

The velocity of the airflow behind the shock for the case that the Mach number of the shock is 1.5 is 2.37×10^4 cm/sec. Substituting the radius of the 2.7-mm-diam waterdrop for r, the acceleration α is found to be 1.64×10^6 cm/sec² in the airflow behind a shock that has a Mach number of 1.5. An enlarged graph of the waterdrop drift velocity after collision with a shock that has this Mach number is given in figure 15 for small values of time after the collision incident. At the end of 50 μsec after the air-shock-waterdrop collision, at which time the waterdrop is still close to its original spherical shape, the slope of the empirical drift velocity curve is 2×10^6 cm/sec².

A value of the acceleration similar to that obtained in the preceding calculation is found by equating the total force in terms of the acceleration as it is given in eq (32) to the drag resistance, $r^2\pi C_D\rho_2 U_2^2/2$ where C_D is the drag coefficient. From this equality,

$$\alpha=C_D U_2^2\rho_2 r^2/[\tfrac{4}{3}\rho_2 r^3+\tfrac{8}{3}\rho_w r^3]. \tag{34}$$

For a Reynolds number of 100,000, from the data of Wiesselsberger [18] and Allen [19], C_D for a sphere is 0.48. By use of this value of C_D, α is found to be 1.57×10^6 cm/sec² for the 2.7-mm-diam waterdrop in the airflow behind the shock for the case that the Mach number of the shock is 1.5. This is to be compared with the value of 1.64×10^6 cm/sec² obtained by the preceding calculation and with the observed value of 2×10^6 cm/sec².

When, however, an attempt is made to calculate the acceleration of the 2.7-mm-diam waterdrop in the airflow behind a shock that has a Mach number of 1.5 for times longer than 50 μsec after the air-shock-waterdrop collision, the result is found to be very different from the slope of the experimental drift

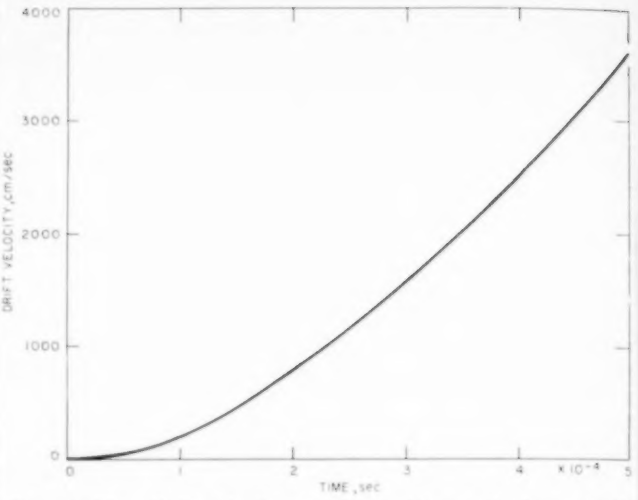

FIGURE 15. *Drift velocity of 2.7-mm-diam waterdrops in the airflow behind shocks for short times after the air-shock-waterdrop collision.*

Mach number of the air shock was 1.5. The slope of the curve at various times after the air-shock-waterdrop collision is as follows:

Time	Slope of curve
μsec	cm/sec²
50	2×10^6
100	4
200	7.5
300	8.3
400	10

velocity curve shown in figure 15. The discrepancy appears to result from the fact that the waterdrop is changing shape. The calculated values of the acceleration should provide some additional evidence for the shape that the waterdrop assumes.

At the end of 94 μsec after the air-shock-waterdrop collison, for the case that the Mach number of the shock was 1.5, the waterdrop has already flattened in all directions perpendicular to the airflow (see fig. 9, picture 2) and at the end of 209 μsec after the collision incident it appears to have flattened into a water disk (see fig. 9, picture 3). The additional mass and the drag coefficient of a disk in an airflow are different from those of a sphere. If the waterdrop has become a water disk, its acceleration, α, should be given by

$$\alpha=\frac{C_D(U_2-W)^2\rho_2\pi r^2}{\frac{16}{3}\rho_2 r^3+\frac{8}{3}\pi\rho_w r_o^3} \tag{35}$$

where r is the radius of the water disk, r_o is the radius of the original water sphere, and W is the waterdrop drift velocity. The drag coefficient C_D for a disk is about unity and does not seem to change with change in the Reynolds number of the flow. Using values of W from the graph of figure 15 and values of r found from eq (31) (see fig. 5), the acceleration of the waterdrop under the assumption that it is a solid disk with a drag coefficient of unity was calculated by use of eq (35) for time intervals of 100, 200, and 300 μsec after the 2.7-mm-diam waterdrop collided with an air shock that had a Mach number

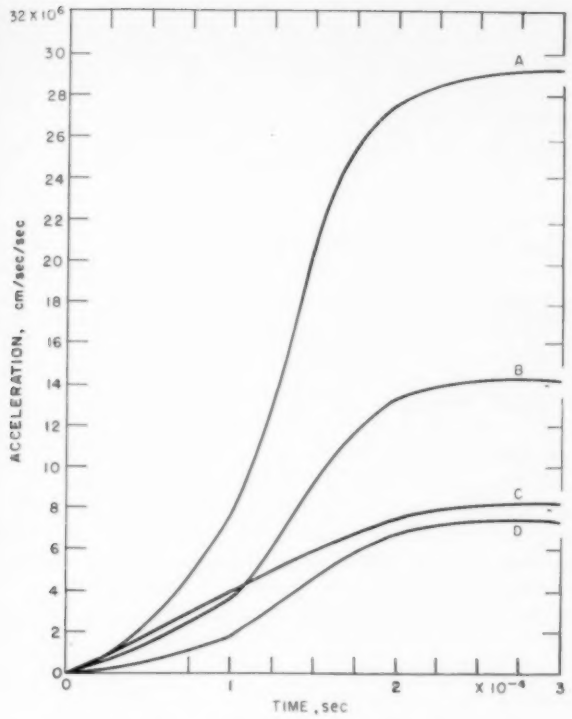

FIGURE 16. *Calculated acceleration of 2.7-mm-diam waterdrops in airflow behind shocks for three assumptions about the waterdrop shape.*

Mach number of the shock was 1.5. A, calculated with $C_D = 1.0$ (solid disk); B, calculated with $C_D = 0.48$ (solid sphere); C, observed; D, calculated with $C_{D,\,eff} = 0.25$ (perforated disk).

of 1.5. The values of the acceleration obtained for this assumption in regard to the waterdrop comprise curve A of figure 16. Curve B of figure 16 is a graph of the values of the acceleration of the waterdrop obtained by use of eq (34) assuming that the waterdrop was a sphere of radius r as far as its drag coefficient ($C'_D = 0.48$), additional mass, and area presented to the flow are concerned, but a sphere of radius r_a as far as its real mass is concerned. It can be seen that the calculated acceleration-against-time curve, assuming that the waterdrop is a sphere, closely resembles the curve of the observed waterdrop acceleration up to 100 μsec after the air-shock-waterdrop collision but deviates sharply from the curve of the observed values of the acceleration for longer time intervals after the collision incident.

Inspection of eq (34) and (35) indicates that consideration of the loss from the original mass of the waterdrop in the form of mist will worsen rather than improve the agreement of the calculated with the observed values of the acceleration. It would appear that somewhere between 100 and 200 μsec after the air-shock-waterdrop collision the drag force is effectively reduced. Calculated values of the acceleration found with use of eq (35) and with an effective drag coefficient, $C'_{D,\,eff}$, arbitrarily taken to be one-fourth, were made and are plotted as curve D in figure 16. It can be seen that the values of the acceleration calculated with this arbitrary assumption about the drag coefficient are in fair agreement with the observed values of the acceleration for time intervals of 200 and 300 μsec after the collision incident but do not fit the experimental curve for smaller intervals of time after the collision incident. It can be deduced from the curves of figure 16 that a 2.7-mm-diam waterdrop remains essentially a sphere up to 100 μsec after collision with an air shock that has a Mach number of 1.5, but that somewhere between 100 and 200 μsec after the collision incident the drag force on it is materially reduced for some reason.

It is useless to look for an explanation of this behavior in the formation of a turbulent boundary layer. A turbulent boundary layer could logically be expected to form because of the irregularities that are observed on the windward face of the waterdrop, and a turbulent boundary layer does markedly reduce the drag coefficient of a sphere by causing the separation of the flow to move further back from the windward face. However, the waterdrop has flattened to a disk and the presence of a turbulent boundary layer does not affect the drag coefficient of a disk for which separation of the flow always occurs at the periphery. It would appear that the only explanation of the effective reduction of the drag force is the presence of a central hole or even of many holes in the disklike shape to which the waterdrop flattens. The presence of holes would reduce the area of the disk that is presented to the airflow and would therefore reduce the drag force.

To hypothesize that a central hole forms in the water disk to which the waterdrop flattens would relate the behavior of waterdrops in airstreams of very high velocity to what has been observed at lower velocities [15, 22]. See section 4.8. In view of the fact that the waterdrop probably does not enlarge by flattening into a solid disk, but that it is reduced to a water ring, the substantiation of Taylor's hypothesis of water loss by the stripping away of a surface layer which then breaks up to form mist (see section 4.4.b) should be reconsidered. An equation designed to trace the history of the waterdrop to the point of complete reduction to mist would have to take into account the loss of water from a moving water boundary layer during the successive stages when: (A) The original drop flattens to a disk and the moving boundary layer spills off the periphery of the water disk, (B) the water disk is perforated to form a water ring and the moving boundary layer spills off both the outer and inner periphery of the ring, and finally, (C) the ring of water eventually segments to form a chain of water beads and the moving boundary layer formed on the windward face of each of the beads spills off the periphery of the bead. After the water ring has segmented to form water beads, the total loss of water per unit time from moving windward-face boundary layers would be the sum of the losses per unit time from the aggregate of the individual small water spheres. In his equation to trace the history of the decay of the drop, Taylor [7] has only considered case (A).

The loss of water from a waterdrop that simply flattened into a coherent solid disk which did not develop holes can be found for various intervals of time after the air-shock-waterdrop collision from

Taylor's treatment. If x is taken to be the radius of the solid water disk, then eq (30) is simply

$$V=\left[4\pi\left(\frac{\rho_a}{\rho_w}\right)^{1/3}\left(\frac{\nu_a}{\nu_w}\right)^{1/6}\sqrt{\nu_w}\right]\int_o^t(U-W)^{1/2}t^{3/2}dt \quad (36)$$

$$V=0.241\int_o^t(U-W)^{1/2}t^{3/2}dt. \quad (37)$$

The lower portion of the drift velocity curve given in figure 15 is quite accurately represented by

$$W=kt^2 \quad (38)$$

where k is a constant which, from the empirical curve, has the value of 2×10^{10}. Using eq (31),

$$r=r_o+\frac{\Delta p}{3\rho_2 r_o}t^2 \quad (39)$$

where r is the radius of the water disk and r_o is the radius of the original undeformed water sphere. Substituting eq (38) and (39) into eq (37),

$$V=0.241\int[U-2\times10^{10}\ t^2]^{1/2}\left[r_o+\frac{\Delta p}{3\ \rho_2 r_o}t^2\right]^{3/2}dt. \quad (40)$$

The value of the right-hand side of eq (40) was found for t equal to 100, 200, and 300 μsec after the air-shock-waterdrop collision, respectively, for the case that the shock had a Mach number of 1.5. These values were plotted against the time and the area under the curve, that is, the total loss of volume of the drop, up to 100, 200, and 300 μsec after the collision incident or time zero was found to be 1.69×10^{-4}, 8.19×10^{-4}, and 18.89×10^{-4} cm^3, respectively.

The calculated acceleration at the end of 100 μsec after the air-shock-waterdrop collision, assuming that the waterdrop was still a sphere with $C_D=0.48$, was found to be 3.74×10^6 cm/sec^2 when no account was taken of the loss of mass by efflux and was found to be 3.83×10^6 cm/sec^2 when the loss of mass by efflux at the periphery was subtracted from the mass of the drop. The observed acceleration at the end of this time interval after the collision incident is 4.0×10^6 cm/sec^2. The acceleration was also calculated for the time intervals of 200 and 300 μsec after the air-shock-waterdrop collision. For these intervals of time after the collision incident, it was assumed that the waterdrop was a perforated disk with an effective drag coefficient $C_{D,eff.}=1/4$ to compensate for the loss of area and for the reduction of the actual drag coefficient and of the additional mass. The calculated acceleration for 200 μsec after the collision incident was found to be 6.94×10^6 cm/sec^2 when no account was taken of the loss of mass by efflux and was found to be 7.19×10^6 cm/sec^2 when the loss of mass by efflux was subtracted from the sum of the real mass and of the additional mass (of a solid disk). The observed acceleration at the end of this time interval after the collision incident is 7.5×10^6 cm/sec^2. The calculated acceleration for 300 μsec after the collision incident was found to be 7.34×10^6 cm/sec^2 when no account was taken of the loss of mass by efflux and was found to be 7.96×10^6 cm/sec^2 when the loss of mass by efflux was subtracted from the sum of the real mass and of the additional mass (of a solid disk). The observed acceleration 300 μsec after the collision incident is 8.3×10^6 cm/sec^2. A summary of the calculated values of the acceleration of a 2.7-mm-diam waterdrop in the airflow behind a shock that has a Mach number of 1.5 for various assumptions in regard to the shape of the drop is given in table 2.

It would appear that the loss of mass by efflux is too low at the end of 200 and of 300 μsec after the air-shock-waterdrop collision because larger values of this loss would improve the agreement between the calculated and observed acceleration for each of these time intervals. However, this is incorrect. For the case that the water disk is really a water ring having a width that would make the area of the ring equal to one-fourth the area of the disk,

$$\pi r^2-\pi R^2=0.25\pi r^2 \quad (41)$$

where r is the radius of the disk and R is the radius of the hole. Therefore, $R=\sqrt{3}\ r/2\sim0.87\ r$, and the width of the ring is $0.13\ r$. The volume loss with time for a solid water disk from eq (30) is

$$\frac{dV}{dt}=2\pi r\cdot\sqrt{x}\cdot K[f(t)] \quad (42)$$

where K is a constant, $f(t)$ is a function of the time,

TABLE 2. *Calculated acceleration for a 2.7-mm-diam waterdrop in the airflow behind a shock ($M_s=1.5$) with various assumption in regard to the shape assumed by the drop*

Drag coefficient, C_D	Acceleration, a		
	After 1×10^{-4} sec	After 2×10^{-4} sec	After 3×10^{-4} sec
	cm/sec²	*cm/sec²*	*cm/sec²*
$C_D=0.48$, solid sphere	3.74×10^6	1.34×10^7	1.42×10^7
$C_D=1$, solid disk	7.78×10^6	2.78×10^7	2.93×10^7
$C_D=0.25$, perforated disk	1.94×10^6	6.94×10^6	7.34×10^6
$C_D=0.48$, solid sphere with Taylor loss	3.83×10^6	7.19×10^6	7.96×10^6
$C_D=0.25$, perforated disk with Taylor loss			
Observed acceleration	4.0×10^6	7.5×10^6	8.3×10^6

r is the radius of the solid water disk, and x is the distance that the wind blows over the water. Because the wind will blow from the stagnation point at the center of the disk to the periphery of the disk, the volume loss per unit time from the boundary layer that will form on the windward face of a solid water disk in an airflow is

$$\frac{dV}{dt}=2\pi r\cdot r^{1/2}\cdot K[f(t)]. \tag{43}$$

In the case of a water ring facing an airflow at 90° incidence, the stagnation point is a stagnation ring located at the center of the water ring. For the case that the water ring has one-fourth the area of a water disk of the same radius, the inner periphery is is $2\pi(0.87r)$, the outer periphery is $2\pi r$, and x is 0.13 $r/2$. Therefore, the volume loss with time for the water ring is

$$\frac{dV}{dt}=1.87(2\pi r)(0.25r^{1/2})K[f(t)]$$

$$\simeq 0.5\{2\pi r\cdot r^{1/2}\cdot K[f(t)]\}. \tag{44}$$

Per unit time, the loss of mass by efflux from a ring that has one-fourth the area of a solid disk of the same radius is only half of that which would occur for the solid disk. The proper correction to bring the calculated values of the acceleration of the waterdrop at the time intervals of 200 and 300 μsec after the air-shock-waterdrop collision into agreement with the observed values should consist of a combination of reduction of the loss of mass by efflux, reduction of the real drag coefficient, and reduction of the additional mass.

4.8. Breakup of the Intact Portion of the Drop

Taylor [20] has shown theoretically that when two superposed fluids of different densities are accelerated in a direction perpendicular to their interface, this surface is unstable if the acceleration is directed from the lighter to the heavier fluid. Lewis [21] has shown experimentally that a layer of water driven by compressed air is unstable and that small disturbances, introduced into its surface against which the air is pressing to drive the liquid, grow so that it appears as though fingers of air move through the water layer. When these fingers reach the opposite surface of the water layer thin bubbles of water blow out ahead of them.

The acceleration of a waterdrop in the high-velocity airflow behind an air shock that has a Mach number of 1.5 is 4×10^6 cm/sec^2 100 μsec after the air-shock-waterdrop collision. Because this acceleration, which is very much greater than the acceleration of gravity, is perpendicular to the air-water interface, and because the acceleration is directed from the low-density air into the high-density water, the accelerating waterdrop is unstable.

Lane [22] and Hanson, Domich, and Adams [15] have observed that a waterdrop in a relatively low-velocity airstream first flattens in a direction perpendicular to that of the airflow and then develops a bubble. The bubble blows out downstream from the leeward face of the flattened waterdrop. In some cases the bubble that forms bursts and the remaining walls of it retract to the supporting ring of water that is left of the waterdrop. In other cases a head of water gathers at the center of the bubble and begins to move back toward and eventually through the water ring that is left of the drop, drawing the remaining walls of the bubble with it. Because bubble formation is in agreement with what Lewis [21] observed to happen in an unstable accelerating layer of liquid, this observation suggests the possibility that a dimple, formed at the stagnation point of the windward face of a waterdrop which is unstable because it is in a very rapid state of acceleration, may move through the drop like the fingers of air described by Lewis [21]. On reaching the leeward face of the waterdrop, it would blow a bubble precisely as the fingers of air observed by Lewis [21] blew out bubbles when they reached the leeward surface of the accelerating water layer. After the bubble burst, the waterdrop would have been reduced to a ring of water. Lewis [21] found that in the case where a layer of water was accelerated without first mechanically introducing surface irregularities on it, the slight surface tension curvature at the sides of the channel he used and other unavoidable sources of small disturbances are sufficient to start the instability. In this case, however, there is a time lag before an appreciable top surface amplitude occurs.

In the present investigation, no evidence of bubble formation was seen in any of the spark pictures that were taken of fragmenting waterdrops in the high-velocity airflows behind air shocks that had Mach numbers of 1.3, 1.5, and 1.7. However, the time interval between spark pictures was not made very small so that it is possible that, if bubble formation occurs very rapidly in these high-velocity airstreams, it could have been missed.

Lewis [21] found that the velocity of penetration of an air finger was given by the expression

$$v_p=C_1[(g_1-g)r_1]^{1/2} \tag{45}$$

where C_1 is a constant which for water has the value of 1.11, g_1 is the acceleration of the water layer, g is the acceleration of gravity, and r_1 is the radius of curvature of the air finger. He states that this equation, with $C_1=1.11$, overestimates the value of the velocity when r_1 is small (~0.25 in.) and underestimates the value of the velocity when r_1 is large (~0.9 in.).

From the requirement that an effective drag coefficient of one-fourth is needed to obtain agreement between calculated and observed acceleration of the waterdrop at the end of the interval of 200 μsec after the air-shock-waterdrop collision, it would seem that the bubble has formed and burst by this time if the process of bubble formation actually occurs. From eq(45) it is possible to estimate very roughly the

time that would be required for an air finger, which may form at the stagnation point of the windward face, to pass through the thickness of the drop. The average value of the acceleration of the waterdrop in the airflow behind a shock that has a Mach number of 1.5 over the first 200 μsec after the air-shock-waterdrop collision is 3.8×10^6 cm/sec^2. The original radius of the waterdrop was 0.14 cm and it can be assumed that the radius of the air finger is about half of this. If these values are substituted into eq(45), the velocity of penetration is found to be 580 cm/sec. From figure 9, picture 2, the thickness of the flattening waterdrop at close to 100 μsec after the air-shock-waterdrop collision is 0.208 cm so that the time required for penetration would be about 360 μsec. This is of the right order of magnitude but is too large because the requirement of an effective drag coefficient of one-fourth is needed to obtain agreement between the calculated and observed value of the acceleration, which was taken to be evidence that a hole has formed in the water disk, 200 μsec after the collision. However, the roughness of the assumption that the radius of curvature of the air finger is about half the radius of the original waterdrop could account for the discrepancy.

If a water ring forms, its diameter should remain constant because the water ring is subject to the check of surface tension and because there is no longer a pressure difference acting between the centers of the faces and the periphery of the water ring that would tend to drive it to larger size. This constant diameter is precisely what is observed in the plateau region in the time interval that extends from about 220 μsec to about 300 μsec in the curves of figure 5. In the pictures obtained by Hanson, Domich, and Adams [15] of the fragmentation of waterdrops in lower velocity airflows, it can be seen that the water ring itself eventually segments into a chain of water beads. It can be assumed that this breakup of the water ring has occurred at the end of the plateau region in the curves of figure 5, that is, 300 μsec after the air-shock-waterdrop collision, because after this there is a further increase of the apparent diameter of the waterdrop perpendicular to the direction of the airflow. This further increase in the diameter of the structure that remains of the waterdrop could be accounted for as a drifting apart of the water beads into which the ring of water that remains of the drop has broken.

For the case of shocks having Mach numbers of 1.3 and 1.5, for which sufficient data exist to identify the plateau region, the formation of the plateau seems to occur in about the same time interval, namely, from about 220 to about 300 μsec after the air-shock-waterdrop collision. It seems reasonable to think that the plateau should be displaced to lower values of the time as the air-shock velocity is increased because the acceleration of the waterdrop is higher as the velocity of the airflow about it is higher, and the time required to pierce the waterdrop with an air finger to form a water ring is proportional to its acceleration. More data than those presented here are needed. It will require taking pictues of fragmenting waterdrops with the camera arranged to look down the length of the shock tube rather than to look through it from the side to determine what actually does occur.

The importance of knowing that segmentation of the water ring occurs at the end of 300 μsec after the air-shock-waterdrop collision and of knowing whether or not it occurs sooner as the shock velocity is increased is the bearing that this information has on the high-speed-rain-erosion problem. Segmentation of the ring of water that remains of the original waterdrop into small water beads would represent a large reduction of its ability to produce erosion damage on striking a solid surface.

It is noteworthy that the small waterdrop started to drift sooner than the large waterdrop. From inspection of either eq (33) or of eq (34), it can be seen that a small waterdrop has a greater acceleration than a large waterdrop in airstreams of the same velocity. It is evident from eq (45), therefore, that the small waterdrop will be pierced to form a water ring sooner than a large waterdrop will. The 1.4-mm-diam waterdrop should be expected, therefore, to become unstable and to undergo ring formation and segmentation before the 2.7-mm-diam waterdrop does.

4.9. Limitations of the Observations

It is noteworthy that Hanson, Domich, and Adams [15], using a 0.3-mm-diam drop of methyl alcohol and an airflow having a velocity of 0.695×10^4 cm/sec, found that the drop of alcohol had reacted to the airflow in a marked way at the end of only 10 μsec; the drop of alcohol was flattened against the wind, streamers of *liquid* were pouring off the periphery of it, and a pointed structure that was oriented in the direction from which the wind was coming had developed in the center of the windward face of it. This evidence indicates that the fragmentation mechanism is dependent on the drop diameter, the velocity of the airflow, and the density, surface tension, and viscosity of the liquid of the drop. The results that were obtained and the conclusions that have been drawn in the study that is reported here apply only to drops of water that have a diameter in the range of 1.4 to 2.7 mm and that disintegrate in airstreams, the velocities of which are in the range of 1.52×10^4 to 3.16×10^4 cm/sec. To extrapolate the conclusions to the fragmentation of liquid drops under conditions for which the values of the variables are outside the range for which the observations of this study were made may result in spurious inferences because it appears that not only the rate of the fragmentation but also the very mechanism by which it occurs is strongly dependent on these variables. The mechanism by which the fragmentation occurs for various sized drops of liquids of different properties in airstreams of different velocities has many aspects of basic interest. Much more experimental work will be required to show the correct interdependence of the variables that are involved.

5. Importance of the Fragmentation Time of Waterdrops to the Problem of Collision With Rain of Objects Moving at Supersonic Velocities

A blunt object moving through air at supersonic velocity is accompanied by a shock wave that is separated from the leading surface of the object by a zone in which air is moving at high velocity ahead of the object. The width of the zone of separation between the shock wave and the leading surface of the object that is producing it depends on the radius of curvature of the object and on the velocity at which it is moving. It was pointed out earlier that the existence of this phenomenon might prove to be of considerable importance to the high-speed rain-erosion problem for objects moving at supersonic velocities. If a waterdrop would be shattered under the conditions that exist in the zone by which a shock is separated from the leading surface of the object that is producing it, and if this fragmentation of the waterdrop would have time to occur before the surface of the object collided with the waterdrop, the erosion problem might be much less serious at supersonic velocities than at subsonic velocities. It seemed possible that it might be bypassed entirely. It was to determine whether or not such an escape from the problem of rain erosion exists at supersonic velocities that the present investigation of the time required for the fragmentation of waterdrops was undertaken.

The distance by which the detached shock, formed in front of a sphere that is moving at supersonic velocity, is separated from the sphere that is producing it, is plotted against the Mach number at which the sphere is moving for four sphere diameters in figure 17. The time required to traverse, at the sphere velocity itself, the distance by which the shock is separated from the sphere is plotted against the Mach number at which the sphere is moving for four sphere diameters in figure 18. The velocity of the sphere is the same as the velocity of the shock. The data used to produce these curves are those of Heybey [23] for shocks having Mach numbers of 2 and 3 and those given by Shapiro [24] for shocks having Mach numbers less than 2. See table 3.

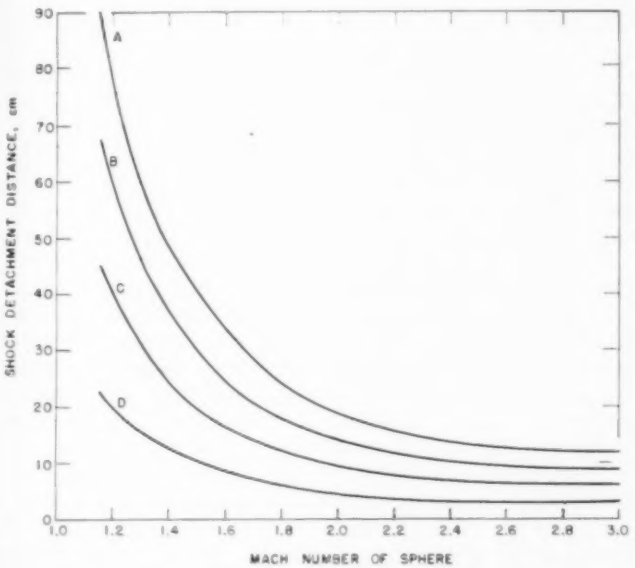

FIGURE 17. *Shock detachment distance for spheres.*

A, 4-ft-diam sphere; B, 3-ft-diam sphere; C, 2-ft-diam sphere; D, 1-ft-diam sphere.

TABLE 3. *Shock-detachment distance, d_s, for various shock velocities*

Shock velocity	d_s/sphere radius [a]
1.15 Mach	1.48
1.3	1.0
1.36	.84
1.62	.54
1.8	.40
2.0	.31
3.0	.20

[a] See references [23, 24].

If a sphere moving at a Mach number of 1.3 were to encounter rain, the detached shock preceding it, and the zone of separation between this shock and the sphere, would run over the raindrops. From the graph of figure 18, the time that the raindrops would have to become completely fragmented so as not to damage the sphere at all on colliding with the leading surface of it is 345 μsec if the sphere diameter is 1 ft, 670 μsec if the sphere diameter is 2 ft, and 1,025 μsec if the sphere diameter is 3 ft. The stage of

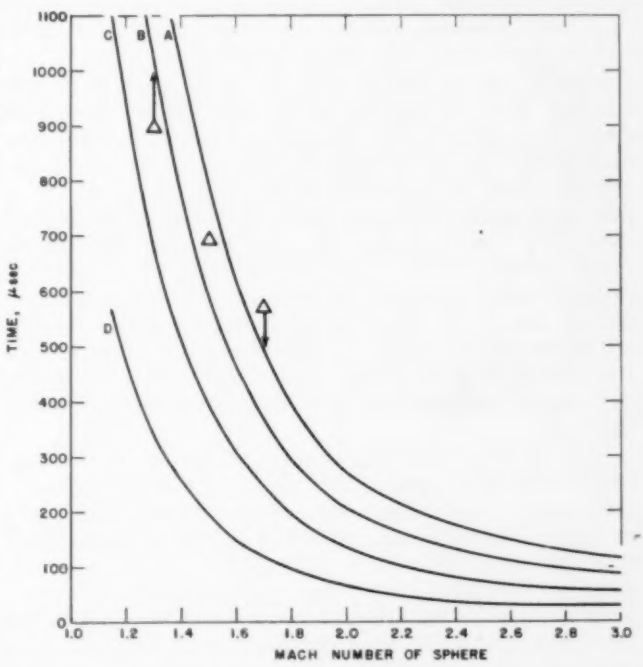

FIGURE 18. *Time during which fragmentation must occur to prevent a waterdrop-sphere collision.*

A, 4-ft-diam sphere; B, 3-ft-diam sphere; C, 2-ft-diam sphere; D, 1-ft-diam sphere. Observed time required to reduce a small waterdrop to a trace of mist is indicated with triangular points.

disintegration that a 2.7-mm-diam waterdrop would have reached at the end of the protection time afforded by a 1-ft-diam sphere moving at a Mach number of 1.3 is between that shown in pictures 2 and 3 of figure 4. The stage of disintegration that a 2.7-mm-diam waterdrop would have reached at the end of the protection time afforded by a 2-ft-diam sphere moving at a Mach number of 1.3 is between that shown in pictures 5 and 6 of figure 4. That is, the waterdrop residues shown in figure 4, pictures 2 and 3, and those shown in figure 4, pictures 5 and 6, are about representative of the waterdrop fragments that would strike the leading surface of a 1-ft-, and of a 2-ft-diam sphere that was moving at a Mach number of 1.3, respectively. It can be seen that the waterdrop is not reduced completely to a trace of mist at the end of the allowed times when the Mach number of the shock is 1.3. However, from a comparison of the degree of fragmentation of 1.4-mm-diam waterdrops, it appears that this condition may be realized within the protection time afforded by a 4-ft-diam sphere, which on extrapolation of curve *A* of figure 18, might be as much as 1,200 μsec.

Similarly, if the Mach number of the sphere were 1.5 when it intercepted rain, the time interval in which the raindrops must fragment if they are not to damage the leading surface of the sphere when they collide with it is 200 μsec for a 1-ft-diam sphere, 390 μsec for a 2-ft-diam sphere, 600 μsec for a 3-ft-diam sphere, and 780 μsec for a 4-ft-diam sphere. By inspection of figures 10 and 11 it can be seen that both 3-ft- and 4-ft-diam spheres would be completely protected from 1.4-mm-diam waterdrops and that the 4-ft-diam sphere would be fairly well protected against 2.7-mm-diam waterdrops.

Finally, if the sphere were moving at a Mach number of 1.7 when it intercepted rain, the time interval in which the waterdrops must disintegrate if they are not to damage the leading surface of the sphere when they collide with it is 120 μsec for a 1-ft-diam sphere, 245 μsec for a 2-ft-diam sphere, 365 μsec for a 3-ft-diam sphere, and 495 μsec for a 4-ft-diam sphere. From the appearance of waterdrop residues seen in spark pictures when the Mach number of the shock was 1.7, it seems probable that a 4-ft-diam sphere would be completely protected from 1.4-mm-diam waterdrops and that it may be fairly well protected from 2.7-mm-diam waterdrops. See figure 12.

The sphere diameters required in order to provide sufficiently long protection times to reduce 1.4-mm-diam and 2.7-mm-diam waterdrops to mist are listed in table 4 for the case that the sphere is moving at a Mach number of 1.3, 1.5, and 1.7. How much damage will be done by the impingement of waterdrop fragments on spheres having diameters smaller than the minimum required for complete protection can only be a matter for conjecture until an actual test is made. Certainly, the damage will be found to be very much less severe than would be expected if the entire waterdrop should impinge as a spherical projectile at these velocities.

TABLE 4. *Sphere diameters that will afford sufficiently long protection time to reduce waterdrops of two sizes to mist*

Velocity of shock or of sphere	Minimum sphere diameter required so that water mist only will impinge on the leading surface of the sphere
	ft
$M_s=1.3$	
1.4-mm waterdrop diameter	4
2.7-mm waterdrop diameter	$>>4$
$M_s=1.5$	
1.4-mm waterdrop diameter	3
2.7-mm waterdrop diameter	$\lesssim 4$
$M_s=1.7$	
1.4-mm waterdrop diameter	4
2.7-mm waterdrop diameter	$\lesssim 4$

It is important to know whether the degree of fragmentation reached at the end of the protection time afforded by any sphere diameter is greater or less as the velocity of the shock is increased. For the case of the 1-ft-diam sphere it is a question of evaluating the degree of waterdrop fragmentation 345 μsec after collision with a shock moving at a Mach number of 1.3 (fig. 4), 200 μsec after collision with a shock having a Mach number of 1.5 (fig. 10), and 120 μsec after collision with a shock moving at a Mach number of 1.7 (fig. 12). For the case of the 2-ft-diam sphere it is a question of comparing the extent of waterdrop fragmentation 670 μsec after collision with a shock moving at a Mach number of 1.3, 390 μsec after collision with a shock moving at a Mach number of 1.5, and 245 μsec after collision with a shock moving at a Mach number of 1.7. For the case of the 3-ft-diam sphere, comparison must be made of the observed fragmentation 1,025 μsec after collision with a shock moving at a Mach number of 1.3, 600 μsec after collision with a shock moving at a Mach number of 1.5, and 365 μsec after collision with a shock moving at a Mach number of 1.7. From a comparison of the degree of fragmentation observed at approximately the end of the allowed protection time for three sphere diameters at each of the three air shock velocities, it appears that the degree of fragmentation of waterdrops that exist within the zone of detachment within the protection time afforded by a detached shock will be found to be either about comparable for shocks of different velocities or may be somewhat greater the higher the velocity of the shock.

Finally, it may be asked whether there is a basis for assuming that at some much higher velocity than any used in this investigation the waterdrop will be completely reduced to a trace of mist within the protection time available for 1-ft- or 2-ft-diam spheres before the residue of the drop will strike the leading surface of the sphere at that velocity. The data at hand are not sufficient to answer this question. It is not even known that it is necessary to reduce the waterdrop completely to mist before the damage done by it on impingement will be negligible. A rough answer can be attempted on the assumption that complete reduction to mist is necessary. Because only the 1.4-mm-diam waterdrops were completely reduced to mist after collision with shocks

moving with Mach numbers of 1.3, 1.5, and 1.7 within the time intervals that were investigated, an answer can only be attempted for waterdrops of this size. The approximate time required to reduce a 1.4-mm-diam waterdrop to a trail of mist is plotted in figure 18 against the Mach number of the shock with which it collided. The arrow drawn down from the time required when the shock had a Mach number of 1.7 indicates that it may be lower than 574 μsec. The arrow drawn upward from the point on the graph for the time required when the shock had a Mach number of 1.3 indicates that the time actually required to reduce a 1.4-mm-diam waterdrop to mist is greater than 901 μsec. The fewness of the points and the ambiguity in them leave unanswered the question as to whether at some high Mach number of the shock the curve on which these three points lie will ever intersect and drop below curve C or curve D of figure 18. It is conceivable that at a Mach number of the shock greater than 3 this condition may be realized, but further observations at Mach numbers of the shock higher than 1.7 will be needed to justify such an extrapolation.

Even if it is found that there is no high Mach number of the shock at which 1.4-mm-diam waterdrops are completely reduced to mist before they impinge against spheres of small diameters, there is another means which may be used to accomplish this. By proper design, the detached shock wave produced by a blunt object moving through air at supersonic velocity can be pushed out to increase the detachment distance and hence to increase the time during which fragmentation of waterdrops may occur before they impinge against the leading surface of the object. Construction of a retractable cowl around a sphere, for example, would have this effect, and the increased aerodynamic drag need only be a disadvantage during actual flight through rain. It appears that recourse to such a device will bypass the high-speed rain-erosion problem completely at supersonic velocities. Use of such a device to insure complete immunity from rain-erosion damage at supersonic velocities could only be justified, however, if the aerodynamic disadvantage is preferable to the impaired performance of pointed radomes which are only slightly vulnerable to rain erosion attack.

The author thanks J. M. Burgers, Z. I. Slawsky, W. H. Heybey, Edward F. Smiley, Adolf H. Lange, Chan Mou Tchen, and John Mandel for contributions to theoretical aspects of the problem and Ben Crapo, Harriet A. Baker, and Robert R. Pizer for assistance with the optics, electronics, and photography.

6. Appendix A. Loss of Water Per Unit Time From the Moving Boundary Layer [6]

Consider that air (sub-a notation) in the airflow behind an air shock is moving at velocity U_2 over the water (sub-w notation) of the windward face of a waterdrop. A boundary layer is set up in the water and in the air on either side of the interface. The velocity in the boundary layer is u. In the water boundary layer, $u=u_wU_2$; in the air boundary layer, $u=u_aU_2$; u_w and u_a are dimensionless coefficients. At the interface, $u_w=u_a$; at some depth below the surface, $u_w=0$; at some height above the air-water interface, $u_a=1$. If the x-axis lies in the air-water interface of the windward face of the waterdrop, and the y-axis, perpendicular to it, is positive both upstream in the air and downstream in the water, the boundary layer velocities may be expressed as

$$u_a=u/U_2=1-Ae^{-y/(\alpha_a\sqrt{x})}$$

$$u_w=u/U_2=(1-A)e^{-y/(\alpha_w\sqrt{x})}$$

where A, α_a, and α_w are quantities that must be determined. This choice satisfies the boundary conditions that as $y\to\infty$, $u_a\to1$, and $u_w\to0$, and that for $y=0$, $u_a=u_w$. This choice also satisfies Karman's boundary layer momentum equations. The Karman equation for air is

$$\frac{d}{dx}\int_0^\infty u(U_2-u)dy=-\nu_a\left[\frac{\partial u}{\partial y}\right]_{y=0} \tag{A1}$$

where ν is the kinematic viscosity.

Dividing both sides by U_2^2 gives the form

$$\frac{d}{dx}\int_0^\infty \frac{u}{U_2}\left[1-\frac{u}{U_2}\right]dy=-\frac{\nu_a}{U_2}\left[\frac{\partial(u/U_2)}{\partial y}\right]_{y=0}. \tag{A2}$$

or

$$\frac{d}{dx}\int_0^\infty\left[Ae^{\frac{-y}{\alpha_a\sqrt{x}}}-A^2e^{\frac{-2y}{\alpha_a\sqrt{x}}}\right]dy=-\frac{\nu_a}{U_2}\left[\frac{\partial}{\partial y}\left(1-Ae^{\frac{-y}{\alpha_a\sqrt{x}}}\right)\right]_{y=0}. \tag{A3}$$

Performance of the indicated operations produces the result

$$\alpha_a{}^2=\frac{2\nu_a}{U_2\left[1-\frac{A}{2}\right]}. \tag{A4}$$

The Karman equation for the water is

$$\frac{d}{dx}\int_0^\infty u^2\,dy=-\nu_w\left[\frac{\partial u}{\partial y}\right]_{y=0}. \tag{A5}$$

Dividing through by U_2^2 gives the form

$$\frac{d}{dx}\int_0^\infty (u/U_2)^2\,dy=-\frac{\nu_w}{U_2}\left[\frac{\partial}{\partial y}(u/U_2)\right]_{y=0}, \tag{A6}$$

or

$$\frac{d}{dx}\int_0^\infty (1-A)^2e^{\frac{-2y}{\alpha_w\sqrt{x}}}dy=-\frac{\nu_w}{U_2}\left[\frac{\partial}{\partial y}(1-A)e^{\frac{-y}{\alpha_w\sqrt{x}}}\right]_{y=0}. \tag{A7}$$

[6] With minor changes, the treatment presented here is that given by Taylor in reference [7].

Performance of the indicated operations produces the result

$$\alpha_w^2=\frac{4}{U_2}\frac{\nu_w}{(1-A)}. \tag{A8}$$

The condition of continuity of tangential stress, F, imposes the condition that

$$\begin{aligned}\frac{F}{U_2}&=\rho_a\nu_a\left[\frac{\partial}{\partial y}\left(\frac{u}{U_2}\right)\right]_{y=0}=-\rho_w\nu_w\left[\frac{\partial}{\partial y}\left(\frac{u}{U_2}\right)\right]_{y=0}\\&=\rho_a\nu_a\left[\frac{\partial}{\partial y}\left\{1-Ae^{\frac{-y}{\alpha_a\sqrt{x}}}\right\}\right]_{y=0}\\&=-\rho_w\nu_w\left[\frac{\partial}{\partial y}\left\{(1-A)e^{\frac{-y}{\alpha_w\sqrt{x}}}\right\}\right]_{y=0}\\&=\rho_a\nu_a\left[\frac{A}{\alpha_a\sqrt{x}}\right]=\rho_w\nu_w\left[\frac{(1-A)}{\alpha_w\sqrt{x}}\right].\end{aligned} \tag{A9}$$

From eq (A8),

$$A=1-[4\nu_w/(\alpha_w^2U_2)], \tag{A10}$$

and by substitution of the expression for $(1-A)$ in eq (A9)

$$\frac{F\sqrt{x}}{U_2}=\frac{\rho_w\nu_w}{\alpha_w}\left[\frac{4\nu_w}{\alpha_w^2U_2}\right]. \tag{A11}$$

Similarly from eq (A4)

$$A=2-[4\nu_a/(\alpha_a^2U_2)] \tag{A12}$$

and by substituting eq (A12) into eq (A9)

$$\frac{F\sqrt{x}}{U_2}=\frac{\rho_a\nu_a}{\alpha_a}\left[2-\frac{4\nu_a}{\alpha_a^2U_2}\right]. \tag{A13}$$

Equating the expression for A given by eq (A10) and (A12)

$$\frac{4\nu_w}{\alpha_w^2U_2}=\frac{4\nu_a}{\alpha_a^2U_2}-1 \tag{A14}$$

and by equating the expressions for $F\sqrt{x}/U_2$ given by eq (A11) and (A13)

$$\frac{\rho_w\nu_w}{\alpha_w}\left[\frac{4\nu_w}{\alpha_w^2U_2}\right]=\frac{\rho_a\nu_a}{\alpha_a}\left[2-\frac{4\nu_a}{\alpha_a^2U_2}\right]. \tag{A15}$$

From eq (A14) and (A15) by use of the condition that when $\nu_w/(\alpha_w^2U_2)$ is small, $\nu_a/(\alpha_a^2U_2)\cong 1/4$, it can be shown that

$$\frac{\nu_w}{\alpha_w^2U_2}\simeq\frac{1}{4}\left(\frac{\rho_a}{\rho_w}\right)^{2/3}\left(\frac{\nu_a}{\nu_w}\right)^{1/3}. \tag{A16}$$

Substituting the values of ρ_a, ν_a for the airstream flowing behind an air shock that has a Mach number of 1.5 (see table 1) and the values of $\rho_w=0.998$, $\nu_w=0.01$, produces the result that $\nu_w/(\alpha_w^2U_2)\cong 0.009187$, from which $\alpha_w=10.43\ (\nu_w/U_2)^{1/2}$. From eq (A14) and the value of $\nu_w/(\alpha_w^2U_2)$, it is found that $\nu_a/(\alpha_a^2U_2)=0.2592$, and $\alpha_a=1.964\ (\nu_a/U_2)^{1/2}$. Using these expressions for α_a and α_w, values of the dimensionless quotient of the boundary layer velocity divided by the free-stream velocity, u/U_2, were calculated from the exponential expressions for u_a and u_w that were chosen initially. The kinematic viscosity of the airflow behind an air shock that has a Mach number of 1.5 was used for ν_a in the expression for α_a. The calculated values of u/U_2 are plotted in figure 19.

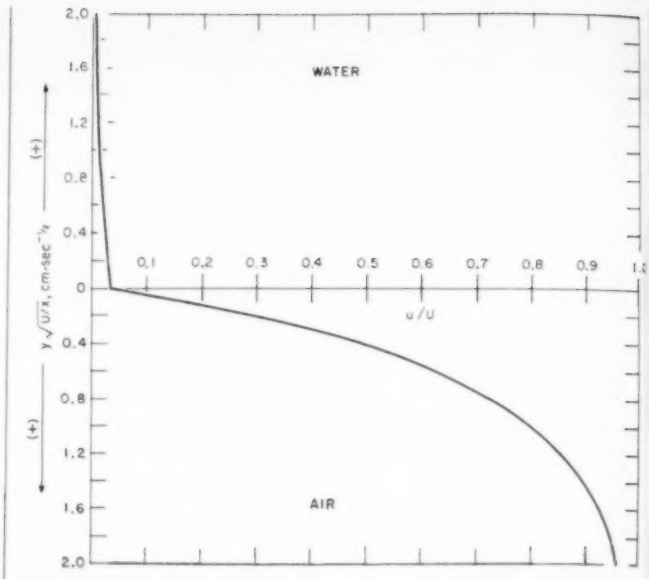

FIGURE 19. *Boundary layers in air and water under the conditions that exist in the airstream flowing behind a shock.*

Mach number of the air shock is 1.5.

The efflux of water out of the boundary layer per unit length of periphery when the mass of water itself has velocity W is

$$\int_0^\infty (U_2-W)(1-A)e^{\frac{-y}{\alpha_w\sqrt{x}}}dy=(U_2-W)(1-A)\alpha_w\sqrt{x}. \tag{A17}$$

By use of eq (A10) and of eq (A16) and by multiplying by the periphery, $2\pi r$, the total efflux or total loss of volume per unit time is

$$\frac{dV}{dt}=4\pi r\left(\frac{\rho_a}{\rho_w}\right)^{1/3}\left(\frac{\nu_a}{\nu_w}\right)^{1/6}\sqrt{U_2-W}\sqrt{\nu_w}\sqrt{x}. \tag{A18}$$

7. Appendix B. Flattening of the Waterdrop With Time

The sphere of liquid is located at the origin of a rectangular coordinate system in which the x-axis runs parallel to the direction of the airflow in the shock tube. The stagnation pressure exists at $x=\pm r$ where r is the radius of the liquid sphere. It

[7] This solution of the time dependence of the flattening of a waterdrop in an air flow was developed by J. M. Burgers.

is assumed that the liquid in the sphere is incompressible and that motion throughout the whole volume of the sphere as a result of the pressure distribution begins instantaneously.

The continuity equation is

$$\frac{\partial u}{\partial x}+\frac{\partial v}{\partial y}+\frac{\partial w}{\partial z}=0, \tag{B1}$$

where u, v, w are the velocities along the x-, y-, and z-axis, respectively. To satisfy the continuity equation

$$u=-2bx,\ v=by,\ w=bz, \tag{B2}$$

where b is a function of the time that must be determined. Also, because

$$u=-\frac{\partial \phi}{\partial x},\ v=-\frac{\partial \phi}{\partial y},\ w=-\frac{\partial \phi}{\partial z}, \tag{B3}$$

where ϕ is the velocity potential, it follows that [8]

$$\phi=b\left[-x^2+\frac{1}{2}y^2+\frac{1}{2}z^2\right]. \tag{B4}$$

The equation of motion is

$$p=-\rho\frac{\partial \phi}{\partial t}+\text{constant} \tag{B5}$$

where ρ is the density of the liquid and t is the time. The term $\frac{1}{2}\rho(u^2+v^2+w^2)$ is neglected as small for short times after the air-shock-waterdrop collision. Applying the equation of motion at the points $x=\pm r$ on the surface of the sphere

$$p_x=\rho r^2\frac{db}{dt}+\text{constant} \tag{B6}$$

and applying the equation at the points $y=\pm r$, $z=\pm r$ on the surface of the sphere

$$p_{y,z}=-\frac{1}{2}\rho r^2\frac{db}{dt}+\text{constant}. \tag{B7}$$

The pressure difference is

$$\Delta p=p_x-p_{y,z}=\frac{3}{2}\rho r^2\frac{db}{dt} \tag{B8}$$

and therefore

$$\frac{db}{dt}=\frac{2}{3}\frac{\Delta p}{\rho r^2}. \tag{B9}$$

If the pressure difference is independent of the time,

$$b=\frac{2}{3}\frac{\Delta p}{\rho r^2}t. \tag{B10}$$

The outward velocity of liquid at the equator of the sphere is given by $v=by$, $w=bz$ from eq (B2), and at the points where $y=\pm r$, $z=\pm r$,

$$v=w=\frac{2}{3}\frac{\Delta p}{\rho r}t. \tag{B11}$$

The outward displacement d at the points $y=\pm r$, $z=\pm r$ is

$$d=\frac{2}{3}\frac{\Delta p}{\rho r}\int_0^t t\,dt$$

$$=\frac{1}{3}\frac{\Delta p}{\rho r}t^2. \tag{B12}$$

The increase in the diameter of the waterdrop perpendicular to the direction of the airflow is $2d$.

8. Appendix C. Total Force Acting on the Waterdrop

Consider the differential area to be a narrow band around the sphere. See inset, figure 14, A. The width of the differential area is the arc subtended by the angle $d\theta$ and is $rd\theta$ where r is the radius of the sphere. The radius of the band of differential area is $r\sin\theta$, the circumference of the band is $2\pi r\sin\theta$, and the area of the band is $2\pi r^2\sin\theta\,d\theta$. Because the pressure curve of figure 14, B is quite accurately given by $\frac{1}{2}\rho_2 U_2^2(1-2\sin^2\theta)$ up to 60°, the horizontal component of the force on the differential area at any angle θ is $\frac{1}{2}\rho_2 U_2^2(1-2\sin^2\theta)(\cos\theta)$, and the differential force, dF_θ, is

$$dF_\theta=\frac{1}{2}\rho_2 U_2^2(1-2\sin^2\theta)(\cos\theta)(2\pi r^2\sin\theta d\theta). \tag{C1}$$

Hence, the force, F_θ, is

$$\overset{\theta=\pi/3}{\underset{\theta=0}{F}}=\pi r^2\rho_2 U_2^2\left[\int_0^{\pi/3}\sin\theta\cos\theta d\theta-2\int_0^{\pi/3}\sin^3\theta\cos\theta d\theta\right], \tag{C2}$$

$$\overset{\theta=\pi/3}{\underset{\theta=0}{F}}=\pi r^2\rho_2 U_2^2\left|\frac{\sin^2\theta}{2}-\frac{2\sin^4\theta}{4}\right|_0^{\pi/3}, \tag{C3}$$

$$=0.094\,\pi r^2\rho_2 U_2^2. \tag{C4}$$

The horizontal component of the force on the differential element in the region $\pi/3\leq\theta\leq\pi$ is given by $-0.4(\frac{1}{2}\rho_2 U_2^2)\cos\theta$, so the force on this part of the sphere is given by

$$\overset{\theta=\pi}{\underset{\theta=\pi/3}{F}}=-0.4\left(\frac{1}{2}\rho_2 U_2^2\right)\int_{\pi/3}^{\pi}2\pi r^2\sin\theta\cos\theta d\theta \tag{C5}$$

$$=-0.4\,\pi r^2\rho_2 U_2^2\left|\frac{\sin^2\theta}{2}\right|_{\pi/3}^{\pi} \tag{C6}$$

$$=0.15\,\pi r^2\rho_2 U_2^2. \tag{C7}$$

Therefore, the total force on the sphere is $0.244\,\pi r^2\rho_2 U_2^2$.

[8] The solution given is not unique but consideration of the general case shows that an equation of the form of eq (B9) should be found except that the dimensionless coefficient 2/3 may be different.

9. References

[1] Edward F. Smiley and Ernst H. Winkler, J. Chem. Phys. **22,** 2018 (1954).
[2] Ames Research Staff, NACA Report 1135 (1953).
[3] J. M. Burgers, Ned. Akad. v. Wetensch. Afd. Natuurkunde, LII, No. 8 en 9 (1943).
[4] A. Fage, Aeronautical Research Committee Reports and Memoranda, R and M No. 1766, ARC Technical Report (1937).
[5] John W. Strutt, Baron Rayleigh, Theory of sound (Dover Publications, New York, N. Y., 1945).
[6] P. Lenard, Ann. phys. **266,** 209, Neue Folge Band XXX (1887).
[7] Sir Geoffrey Taylor, Porton Paper 6600/5278/49.
[8] Robert H. Cole, Underwater explosions (Princeton Univ. Press, Princeton, N. J., 1948).
[9] Robert Williams Wood, Supersonics (Brown Univ., Providence, R. I., 1939).
[10] John S. Rhinehart, J. Appl. Phys. **22,** 555 (1951).
[11] John S. Rhinehart, NOTS TM No. 348 (May 1952).
[12] Joseph B. Keller and Ignace Kolodner, J. Appl. Phys. **25,** 918 (1954).
[13] Sir Horace Lamb, Hydrodynamics, 6th ed. (Cambridge Univ. Press, New York, N. Y., 1932).
[14] W. R. Lane and H. L. Green, The mechanics of drops and bubbles in Surveys of mechanics, edited by G. K. Batchelor and R. M. Davies (Cambridge Univ. Press, New York, N. Y., 1956).
[15] A. R. Hanson, E. G. Domich, and H. S. Adams, Research Report No. 125, Univ. Minn. Inst. Technol., Dept. of Aeronaut. Eng., Rosemount Aeronaut. Labs., Minneapolis, Minn. (January 1956).
[16] C. M. Tchen, J. Appl. Phys. **27,** 1533 (1956).
[17] J. M. Burgers, Communicated by letter.
[18] C. Wieselsberger, Physik. Z. **23,** 219 (1922).
[19] H. S. Allen, Phil. Mag. **50,** 323 (1900).
[20] Sir Geoffrey Taylor, Proc. Roy. Soc. London **[A]201,** 192 (1950).
[21] D. J. Lewis, Proc. Roy. Soc. London **[A]202,** 81 (1950).
[22] W. R. Lane, Ind. Eng. Chem. **43,** 1261 (1951).
[23] W. H. Heybey, Navord Report No. 3594 (December 1953).
[24] A. H. Shapiro, Compressible fluid flow, p. 886 (Ronald Press Co., New York, N. Y., 1954).

WASHINGTON, February 1, 1957.

U. S. GOVERNMENT PRINTING OFFICE: 1958

THE NATIONAL BUREAU OF STANDARDS

The scope of activities of the National Bureau of Standards at its headquarters in Washington, D. C., and its major laboratories in Boulder, Colorado, is suggested in the following listing of the divisions and sections engaged in technical work. In general, each section carries out specialized research, development, and engineering in the field indicated by its title. A brief description of the activities, and of the resultant publications, appears on the inside of the front cover.

WASHINGTON, D. C.

Electricity and Electronics. Resistance and Reactance. Electron Devices. Electrical Instruments. Magnetic Measurements. Dielectrics. Engineering Electronics. Electronic Instrumentation. Electrochemistry.

Optics and Metrology. Photometry and Colorimetry. Optical Instruments. Photographic Technology. Length. Engineering Metrology.

Heat. Temperature. Physics. Thermodynamics. Cryogenic Physics. Rheology. Engine Fuels. Free Radicals Research.

Atomic and Radiation Physics. Spectroscopy. Radiometry. Mass Spectrometry. Solid State Physics. Electron Physics. Atomic Physics. Neutron Physics. Nuclear Physics. Radioactivity. X-rays. Betatron. Nucleonic Instrumentation. Radiological Equipment.

Chemistry. Organic Coatings. Surface Chemistry. Organic Chemistry. Analytical Chemistry. Inorganic Chemistry. Electrodeposition. Molecular Structure and Properties of Gases. Physical Chemistry. Thermochemistry. Spectrochemistry. Pure Substances.

Mechanics. Sound. Mechanical Instruments. Fluid Mechanics. Engineering Mechanics. Mass and Scale. Capacity, Density, and Fluid Meters. Combustion Controls.

Organic and Fibrous Materials. Rubber. Textiles. Paper. Leather. Testing and Specifications. Polymer Structure. Plastics. Dental Research.

Metallurgy. Thermal Metallurgy. Chemical Metallurgy. Mechanical Metallurgy. Corrosion. Metal Physics.

Mineral Products. Engineering Ceramics. Glass. Refractories. Enameled Metals. Concreting Materials. Constitution and Microstructure.

Building Technology. Structural Engineering. Fire Protection. Air Conditioning, Heating, and Refrigeration. Floor, Roof, and Wall Coverings. Codes and Safety Standards. Heat Transfer.

Applied Mathematics. Numerical Analysis. Computation. Statistical Engineering. Mathematical Physics.

Data Processing Systems. SEAC Engineering Group. Components and Techniques. Digital Circuitry. Digital Systems. Analog Systems. Application Engineering.

• Office of Basic Instrumentation.

• Office of Weights and Measures.

BOULDER, COLORADO

Cryogenic Engineering. Cryogenic Equipment. Cryogenic Processes. Properties of Materials. Gas Liquefaction.

Radio Propagation Physics. Upper Atmosphere Research. Ionospheric Research. Regular Propagation Services. Sun-Earth Relationships. VHF Research.

Radio Propagation Engineering. Data Reduction Instrumentation. Modulation Systems. Navigation Systems. Radio Noise. Tropospheric Measurements. Tropospheric Analysis. Radio Systems Application Engineering. Radio Meteorology.

Radio Standards. High Frequency Electrical Standards. Radio Broadcast Service. High Frequency Impedance Standards. Calibration Center. Microwave Physics. Microwave Circuit Standards.

Recent Publications of the National Bureau of Standards

Periodicals

Journal of Research of the National Bureau of Standards, Volume 60, No. 1, January 1958 (RP2815 to RP2823 incl.). 60 cents. Annual subscription $4.00, $1.25 additional for foreign mailing.

Technical News Bulletin, Volume 42, No. 1, January 1958. 10 cents. Annual subscription $1.00, 35 cents additional for foreign mailing.

Basic Radio Propagation Predictions for April 1958. Three months in advance. CRPL-D 161. Issued January 1958. 10 cents. Annual subscription $1.00, 25 cents additional for foreign mailing.

Applied Mathematics Series

AMS49. Further contributions to the solution of simultaneous linear equations and the determination of eigenvalues. 50 cents.*

Handbooks

H63. Protection against neutron radiation up to 30 million electron volts. 40 cents.*

H64. Design of free-air ionization chambers. 20 cents.*

Available from the Superintendent of Documents, U. S. Government Printing Office, Washington 25, D. C. The three NBS periodicals are available on a 1-, 2-, or 3-year subscription basis, although no reduction in rates can be made.

**Foreign postage, one-fourth additional.*

UNITED STATES
GOVERNMENT PRINTING OFFICE
DIVISION OF PUBLIC DOCUMENTS
WASHINGTON 25, D. C.

OFFICIAL BUSINESS

PENALTY FOR PRIVATE USE TO AVOID PAYMENT OF POSTAGE, $300 (GPO)

Journal of Research of the National Bureau of Standards | Vol. 60, No. 3 | March 1958

Contents

		Page
Current and potential relations for the cathodic protection of steel in salt water. W. J. Schwerdtfeger.	RP2833	153
Joule-Thomson process in the liquefaction of helium. Edmund H. Brown and John W. Dean.	RP2834	161
Changes in the properties of an asphalt during the blowing operation. L. R. Kleinschmidt and H. R. Snoke.	RP2835	169
Creep of annealed nickel, copper, and two nickel-copper alloys. William D. Jenkins and Carl R. Johnson.	RP2836	173
Stress-strain relation of pure-gum rubber vulcanizates in compression and tension. Lawrence A. Wood.	RP2837	193
Tables for diagonalizing second-order matrices. R. E. Trees and C. DeW. Coleman.	RP2838	201
Effects of capillary shape on flow characteristics and degradation of polymer solutions. Hobart S. White and Harriet V. Belcher.	RP2839	215
Ortho-para catalysis in liquid-hydrogen production. D. H. Weitzel, W. V. Loebenstein, J. W. Draper, and O. E. Park.	RP2840	221
Degradation of cellulose in a vacuum with ultraviolet light. Joseph H. Flynn, William K. Wilson, and William L. Morrow.	RP2841	229
Cavity ionization as a function of wall material. Frank H. Attix, LeRoy DeLaVergne, and Victor H. Ritz.	RP2842	235
Fragmentation of waterdrops in the zone behind an air shock. Olive G. Engel.	RP2843	245

[A list of recent NBS publications is given on page 3 of the cover.]

For sale by the Superintendent of Documents, U. S. Government Printing Office, Washington 25, D. C. Price 60 cents (single copy). Subscription price: $4.00 a year; $1.25 additional for foreign mailing.

UNITED STATES GOVERNMENT PRINTING OFFICE, WASHINGTON : 1958